Computational Modelling of Helicopter High-Frequency Dynamics

by

Andrew J. Line

Department of Aeronautics
Imperial College London
Prince Consort Road
London SW7 2BY

This thesis is submitted for the degree of Doctor of Philosophy of the University of London

Abstract

In order to improve the hover performance and maximum lift capabilities of the helicopter, modern rotor designs are incorporating high levels of blade twist - a design parameter which is known to have a significant effect on the aerodynamic loading and vibration levels of the rotor. The helicopter industry as a whole is currently unable to predict rotor vibration to acceptable levels of accuracy, nor is it able to capture the effects of blade twist on vibration levels - severely limiting its ability to exploit twist fully within new rotor designs.

Recent literature has highlighted the potentially powerful effect that improved wake modelling could have on the prediction of vibrational loads. The primary aim of this research has been to assess the benefits of improved wake modelling, both in terms of the accuracy of predicted vibratory loads and in terms of sensitivity to blade twist.

The Vorticity Transport Model (VTM), developed by Brown, is a grid-based computational fluid dynamic code which provides a comprehensive description of the generation and evolution of helicopter wakes. Integration of the VTM with an industry-standard structural dynamics code has allowed the benefits of improved wake modelling to be explored.

The capabilities of the VTM itself have also been enhanced with the introduction of a new adaptive grid system and Fast Multipole algorithm for evaluating the velocity field throughout the computational domain. The predicted wake geometries, aerodynamic loading and rotor dynamics have been validated against experimental data for both hovering and forward flight. A detailed study of Harris' experimental work using the VTM has provided further insight into the primary physical mechanisms that control the evolution of rotor wakes in forward flight.

Acknowledgements

Firstly, I would like to thank my PhD supervisor, Dr. Richard Brown, for his flawless guidance, support and insight. I would also like to thank Nick Griffiths, Robert Hansford and Rob Harrison at Westland Helicopters Ltd. - this work would not have been possible without their invaluable help and advice. Finally, I would like to thank my family and friends for their continuous encouragement and support.

This research was sponsored by an EPSRC Industrial Case award (No. 01305179) in conjunction with Westland Helicopters Ltd.

To those who have inspired me.

Contents

Abstract 1

Acknowledgements 2

Dedication 3

Table of Contents 4

List of Figures 7

List of Tables 13

Nomenclature 14

1 Introduction 19

1.1 Synopsis 21

1.2 Publications 23

2 Model Description 24

2.1 Introduction 24

2.2 Governing Equations 25

2.3 Vorticity Transport Model 26

2.4 Numerical Implementation 27

2.4.1 Grid Structure 28

2.4.2 Flow Variables 30

2.4.3 Weighted Average Flux Scheme 31

2.4.4 Vorticity-Velocity Coupling 34

2.4.5 Boundary Conditions 34

2.5 Structural Dynamics 36
2.6 Blade Aerodynamics 39
2.7 Proposed Model Improvements 42
2.7.1 Semi-Lagrangian Adaptive Grid 42
2.7.2 Cartesian Fast Multipole Method 43
2.8 Summary 44

3 Semi-Lagrangian Adaptive Grid **45**
3.1 Introduction 45
3.2 Boundary-Free Formulation 46
3.3 Octree Data Structure 48
3.4 Nested Grids 50
3.4.1 Courant-Friedrichs-Lewy Condition 51
3.4.2 Grid Level Boundaries 53
3.5 Grid Performance 55
3.6 Summary 59

4 Cartesian Fast Multipole Method **60**
4.1 Introduction 60
4.2 Theory 62
4.2.1 The Rosenhead-Moore Kernel 64
4.2.2 Point-Particle Interactions 66
4.2.3 Point-Cluster Interactions 66
4.2.4 Error Analysis 67
4.2.5 Tensor Calculation 68
4.2.6 Moment Calculation 69
4.2.7 Cluster-Cluster Interactions 69
4.3 Implementation 71
4.3.1 Octree Data Structure 71
4.3.2 Well Separated Interactions 72
4.3.3 Fast Treecode 73
4.3.4 Fast Multipole Method 75
4.3.5 Mutual Cluster-Cluster Interactions 78

4.4 Computational Cost 79
4.5 Summary 80

5 Model Validation **81**
5.1 Introduction 81
5.2 Caradonna & Tung's Experimental Data 82
5.2.1 Experimental Setup 82
5.2.2 Numerical Simulations 82
5.2.3 Blade Loading 83
5.2.4 Wake Geometry 84
5.3 Harris' Experimental Data 87
5.3.1 Experimental Setup 87
5.3.2 Numerical Simulations 87
5.3.3 Disc Tilt 88
5.4 Summary 90

6 A Detailed Study of Harris' Experimental Work **93**
6.1 Introduction 93
6.2 Flap Dynamics 96
6.3 Inflow Distribution 99
6.4 Linear Inflow Models 111
6.5 Wake Topology 114
6.6 Summary 119

7 Vibration Prediction **120**
7.1 Sensitivity to Blade Twist 122
7.2 Model Development 128
7.2.1 Structural Dynamic Model 129
7.2.2 R150-VTM Integration 130
7.2.2.1 Implementation 130
7.2.2.2 Blade Aerodynamics 131
7.2.2.3 Fuselage Aerodynamics 132
7.3 AHS Dynamics Workshop 132

7.3.1 Convergence Study 133
7.3.2 High Speed Case 137
7.3.3 Low Speed Case 140
7.4 Model Evaluation 143
7.5 Summary 146

8 Conclusions **147**

Bibliography **151**

Appendix A: VTM-R150 Twist Study **161**
A1. High Speed Case $\mu = 0.37$ 162
A2. Low Speed Case $\mu = 0.15$ 166

Appendix B: VTM-R150 Convergence Study **170**
B1. High Speed Case $\mu = 0.37$ 170
B2. Low Speed $\mu = 0.15$ 175

Appendix C: AHS Workshop Results **180**
C1. High Speed Case $\mu = 0.37$ 180
C2. Low Speed Case $\mu = 0.15$ 185

List of Figures

2.1 *Definition of solution domain.* 29

2.2 *Wake visualisation of a 4-bladed rotor at* $\mu_x = 0.147$. 30

2.3 *Staggered arrangement (left) and collocated arrangement (right) of the velocity field.* 31

2.4 *Stencil for calculation of intercell vorticity fluxes.* 32

2.5 *Evolution of a solution contaminated by invalid boundary conditions.* 35

2.6 *Simplified representation of an articulated rotor.* 37

2.7 *Blade aerodynamic and inner wake model.* 40

3.1 *Adaptive grid generation and destruction tracks regions of vorticity within the flow.* 46

3.2 *Adaptation of the grid structure as the rotor wake evolves.* 47

3.3 *Cell locations organised into an octree data structure.* 49

3.4 *The rotor is embedded within a nested grid structure that decreases in resolution with distance from the hub.* 51

3.5 *Overlapping of adjacent grid levels for a one-dimensional grid; shaded cells represent ghost cells.* 53

3.6 *Overlapping of the grid level boundaries provides both second order accuracy and monotonicity; shaded cells represent ghost cells.* 54

3.7 *Strategy for preserving vorticity conservation, second order accuracy and the TVD properties of the solution at grid interfaces. Shaded cells denote ghost cells.* 55

3.8 *Use of nested grid levels to reduce progressively the resolution into the far wake;* $\mu = 0.12, \Delta x_0 = 0.016R$ 57

3.9 *Visualisation of the wake of a two-bladed teetering rotor in vortex ring conditions.* 58

4.1 *Comparison of the Biot-Savart and Rosenhead-Moore kernels.* 65
4.2 *Point-cluster interaction.* 66
4.3 *Use of multipole expansions of vorticity and velocity field in a cluster-cluster interactions.* 70
4.4 *Region of convergence of multipole series.* 72
4.5 *Decomposition of the vorticity field in to the far field (white), intermediate field (dark grey), near field (light grey) of cluster i.* 76
4.6 *Refinement of velocity field through hierarchical decomposition.* 77
4.7 *Effective interaction list of the shaded cell* 77
4.8 *Evaluation of the mutually induced velocity fields generated by two clusters.* 78
4.9 *Interaction list for cluster i using mutual cluster-cluster interactions; far field (white), intermediate field (dark grey), and near field (light grey).* . . . 79
4.10 *Computational cost of the FMM.* 80

5.1 *Comparison between experimental and calculated lift coefficient:* $C_T = 0.0079, \Omega R = 150ms^{-1}$. 83
5.2 *Comparison between experimental and calculated loading coefficient:* $C_T = 0.0079, \Omega R = 150ms^{-1}$. 84
5.3 *Comparison in wake geometry between Caradonna & Tung's experimental data and VTM prediction.* 85
5.4 *Comparison between Caradonna & Tung's experimental data and Kocurek & Tangler's empirical model - taken from Caradonna & Tung's original paper [79].* 86
5.5 *Visualisations of the predicted wake geometry.* 86
5.6 *Comparison of new and old versions of the VTM against Harris' experimental data: lateral disc tilt (top), longitudinal disc tilt (bottom).* 88
5.7 *Wake structure for the* $\mu = 0.12$ *case, resolved using cell sizes of (a)* $\Delta x = 0.04R$*, and (b)* $\Delta x = 0.016R$. 90
5.8 *Comparison of predicted blade loading using grid resolutions of (a)* $\Delta x = 0.04R$*, and (b)* $\Delta x = 0.016R$. 91

6.1 *Lateral disc tilt predictions using a uniform inflow model and a three-mode dynamic inflow model.* 94
6.2 *Definition of aerofoil flow angles.* 97
6.3 *Components of lateral flapping according to equation 6.13.* 99
6.4 *Calculated mean inflow compared to Glauert's inflow model.* 100
6.5 *Integrated inflow plotted as a function of azimuth,* $0 \leq \mu \leq 0.08$. 102
6.6 *Integrated inflow plotted as a function of azimuth,* $0.08 \leq \mu \leq 0.20$. 102
6.7 *Variation in* $J(\psi)$ *over a rotor revolution,* $0.0 \leq \mu \leq 0.08$. 103
6.8 *Variation in* $J(\psi)$ *over a rotor revolution,* $0.08 \leq \mu \leq 0.20$. 104
6.9 *Distribution of (a) inflow and (b)* $I(r, \psi)$ *for* $\mu = 0.0$. 105
6.10 *Distribution of (a) inflow and (b)* $I(r, \psi)$ *for* $\mu = 0.02$. 105
6.11 *Distribution of (a) inflow and (b)* $I(r, \psi)$ *for* $\mu = 0.04$. 105
6.12 *Distribution of (a) inflow and (b)* $I(r, \psi)$ *for* $\mu = 0.06$. 106
6.13 *Distribution of (a) inflow and (b)* $I(r, \psi)$ *for* $\mu = 0.08$. 106
6.14 *Distribution of (a) inflow and (b)* $I(r, \psi)$ *for* $\mu = 0.10$. 106
6.15 *Distribution of (a) inflow and (b)* $I(r, \psi)$ *for* $\mu = 0.12$. 107
6.16 *Distribution of (a) inflow and (b)* $I(r, \psi)$ *for* $\mu = 0.16$. 107
6.17 *Distribution of (a) inflow and (b)* $I(r, \psi)$ *for* $\mu = 0.20$. 107
6.18 *Distribution of (a) inflow and (b)* $I(r, \psi)$ *for* $\mu = 0.24$. 108
6.19 *Visualisations of the wake geometry on a vertical slice through rotor hub at various advance ratios: (a)* $\mu = 0.04$ *(b)* $\mu = 0.06$ *(c)* $\mu = 0.08$ *(d)* $\mu = 0.10$. 110
6.20 *Comparison between the predictions of the VTM and Glauert's model (*$k_x = 1.35$, $k_y = 0.0$*).* 111
6.21 *Comparison of* k_x *for the methods presented in table 6.1.* 113
6.22 *Visualisation of wake structure at* $\mu = 0.02$. 114
6.23 *Visualisation of wake structure at* $\mu = 0.04$. 115
6.24 *Visualisation of wake structure at* $\mu = 0.08$. 116
6.25 *Visualisation of wake structure at* $\mu = 0.10$. 117
6.26 *Visualisation of wake structure at* $\mu = 0.12$. 118
6.27 *Visualisation of wake structure at* $\mu = 0.16$. 118

7.1 *Variation in rotor thrust due to changes in blade twist,* $\mu = 0.15$. 124
7.2 *Harmonic content of rotor thrust relative to* 8° *blade,* $\mu = 0.15$. 124

7.3 *Variation in rotor thrust due to changes in blade twist,* $\mu = 0.37$. 125
7.4 *Harmonic content of rotor thrust relative to 8° blade,* $\mu = 0.37$. 125
7.5 *Effect of blade twist on blade loading* $\mu = 0.15$*; (a) 8° twist, (b) 12° twist, (c) 16° twist, and (d) 20° twist.* 126
7.6 *Effect of blade twist on blade loading* $\mu = 0.37$*; (a) 8° twist, (b) 12° twist, (c) 16° twist, and (d) 20° twist.* 127
7.7 *Sensitivity of blade loading to grid resolution* $\psi = 135$, $\mu = 0.37$. 134
7.8 *Sensitivity of blade loading to grid resolution* $\psi = 45$, $\mu = 0.37$. 134
7.9 *Sensitivity of flapwise bending moment to grid resolution at 64% radius,* $\mu = 0.37$. 135
7.10 *Flap components of the R150 mode shapes.* 136
7.11 *Flap moment at 3.2% Radius* $\mu = 0.37$. 138
7.12 *Lag moment at 64.0% Radius* $\mu = 0.37$. 139
7.13 *Control loads* $\mu = 0.37$. 140
7.14 *Flap moment at 64.0% Radius* $\mu = 0.15$. 141
7.15 *Flap moment at 31.0% Radius* $\mu = 0.15$. 142
7.16 *Control loads* $\mu = 0.15$. 142

A.1 *Normal force distribution* $\psi = 0°$, $\mu = 0.37$. 162
A.2 *Normal force distribution* $\psi = 45°$, $\mu = 0.37$. 162
A.3 *Normal force distribution* $\psi = 90°$, $\mu = 0.37$. 163
A.4 *Normal force distribution* $\psi = 135°$, $\mu = 0.37$. 163
A.5 *Normal force distribution* $\psi = 180°$, $\mu = 0.37$. 164
A.6 *Normal force distribution* $\psi = 225°$, $\mu = 0.37$. 164
A.7 *Normal force distribution* $\psi = 270°$, $\mu = 0.37$. 165
A.8 *Normal force distribution* $\psi = 315°$, $\mu = 0.37$. 165
A.9 *Normal force distribution* $\psi = 0°$, $\mu = 0.15$. 166
A.10 *Normal force distribution* $\psi = 45°$, $\mu = 0.15$. 166
A.11 *Normal force distribution* $\psi = 90°$, $\mu = 0.15$. 167
A.12 *Normal force distribution* $\psi = 135°$, $\mu = 0.15$. 167
A.13 *Normal force distribution* $\psi = 180°$, $\mu = 0.15$. 168
A.14 *Normal force distribution* $\psi = 225°$, $\mu = 0.15$. 168
A.15 *Normal force distribution* $\psi = 270°$, $\mu = 0.15$. 169

A.16 *Normal force distribution* $\psi = 315^{\circ}$, $\mu = 0.15$. 169
B.17 *Predicted flap moment at 81.0% Radius* $\mu = 0.37$. 170
B.18 *Predicted flap moment at 64.0% Radius* $\mu = 0.37$. 171
B.19 *Predicted flap moment at 48.0% Radius* $\mu = 0.37$. 171
B.20 *Predicted flap moment at 31.0% Radius* $\mu = 0.37$. 172
B.21 *Predicted flap moment at 3.2% Radius* $\mu = 0.37$. 172
B.22 *Predicted lag moment at 64.0% Radius* $\mu = 0.37$. 173
B.23 *Predicted lag moment at 31.0% Radius* $\mu = 0.37$. 173
B.24 *Predicted lag moment at 6.8% Radius* $\mu = 0.37$. 174
B.25 *Predicted control loads* $\mu = 0.37$. 174
B.26 *Predicted flap moment at 81.0% Radius* $\mu = 0.15$. 175
B.27 *Predicted flap moment at 64.0% Radius* $\mu = 0.15$. 175
B.28 *Predicted flap moment at 48.0% Radius* $\mu = 0.15$. 176
B.29 *Predicted flap moment at 31.0% Radius* $\mu = 0.15$. 176
B.30 *Predicted flap moment at 3.2% Radius* $\mu = 0.15$. 177
B.31 *Predicted lag moment at 64.0% Radius* $\mu = 0.15$. 177
B.32 *Predicted lag moment at 31.0% Radius* $\mu = 0.15$. 178
B.33 *Predicted lag moment at 6.8% Radius* $\mu = 0.15$. 178
B.34 *Predicted control loads* $\mu = 0.15$. 179
C.35 *Flap moment at 81.0% Radius* $\mu = 0.37$. 180
C.36 *Flap moment at 64.0% Radius* $\mu = 0.37$. 181
C.37 *Flap moment at 48.0% Radius* $\mu = 0.37$. 181
C.38 *Flap moment at 31.0% Radius* $\mu = 0.37$. 182
C.39 *Flap moment at 3.2% Radius* $\mu = 0.37$. 182
C.40 *Lag moment at 64.0% Radius* $\mu = 0.37$. 183
C.41 *Lag moment at 31.0% Radius* $\mu = 0.37$. 183
C.42 *Lag moment at 6.8% Radius* $\mu = 0.37$. 184
C.43 *Control loads* $\mu = 0.36$. 184
C.44 *Flap moment at 81.0% Radius* $\mu = 0.15$. 185
C.45 *Flap moment at 64.0% Radius* $\mu = 0.15$. 185
C.46 *Flap moment at 48.0% Radius* $\mu = 0.15$. 186
C.47 *Flap moment at 31.0% Radius* $\mu = 0.15$. 186

C.48 *Flap moment at 3.2% Radius* $\mu = 0.15$. 187
C.49 *Lag moment at 64.0% Radius* $\mu = 0.15$. 187
C.50 *Lag moment at 31.0% Radius* $\mu = 0.15$. 188
C.51 *Lag moment at 6.8% Radius* $\mu = 0.15$. 188
C.52 *Control loads* $\mu = 0.15$. 189

List of Tables

3.1 *Cell count comparison between old and new grid systems.* 56

3.2 *Distribution of cells throughout grid levels.* 57

5.1 *Description of Caradonna and Tung's experimental setup.* 82

5.2 *Description of Harris' experimental setup.* 87

6.1 k_x *and* k_y *factors for Glauert's inflow model.* 112

7.1 *Description of the rotor of the Lynx XZ170 Main Rotor.* 122

7.2 *Trim conditions for each of the flight conditions used by the AHS dynamics workshop.* 122

Nomenclature

Rotor System

A	: rotor disc area, πR^2
c	: blade chord
C_{BL}	: blade loading coefficient
C_D	: drag, scaled by $\frac{1}{2}\rho(\Omega R)^2 c$
C_L	: lift, scaled by $\frac{1}{2}\rho(\Omega R)^2 c$
C_M	: moment, scaled by $\frac{1}{2}\rho(\Omega R)^2 c^2$
C_T	: rotor thrust, scaled by $\rho A(\Omega R)^2$
$\dot{h}$	: aerofoil plunge velocity
M	: hub moment $M = M_0 + M_{1c}\cos\psi + M_{1s}\sin\psi$
M_0	: mean hub moment
M_{1c}	: cosine component of hub moment
M_{1s}	: sine component of hub moment
N_b	: number of blades on rotor
r	: radial position, scaled by R
q	: aerofoil pitch rate
R	: rotor radius
α	: aerofoil incidence
β	: rotor flapping $\beta = \beta_0 + \beta_{1c}\cos\psi + \beta_{1s}\sin\psi$
β_0	: rotor coning
β_{1c}	: rotor longitudinal flapping
β_{1s}	: rotor lateral flapping
λ	: rotor inflow scaled by ΩR

θ : control angle $\theta = \theta_0 + \theta_{1c}\cos\psi + \theta_{1s}\sin\psi$

θ_0 : collective

θ_{1c} : lateral cyclic

θ_{1s} : longitudinal cyclic

μ_x : rotor forward speed scaled by ΩR

μ_z : rotor vertical speed scaled by ΩR

σ : rotor solidity

Ω : rotor rotational speed

ψ : azimuthal location

Fluid Dynamic Model

F : intercell vorticity flux

M : Mach number

N : number of grid cells

p : pressure in the flow

S : vorticity source

t : time

u : flow velocity

u_b : flow velocity relative to blade

V : cell volume

Δt : timestep

Δx : cell edge-length

ν : kinematic viscosity of the flow

ρ : flow density

ω : vorticity

ω_b : bound vorticity

Ω : solution domain

Structural Dynamics

D	: dissipation
$\mathcal{L}$	: Lagrangian of the system
q	: generalised coordinates
T	: kinetic energy
U	: potential energy
W	: work

Fast Multipole Method

a_k	: k^{th} Taylor coefficient of K_δ
b_k	: k^{th} Taylor coefficient of ϕ_δ
K	: Biot-Savart kernel
K_δ	: regularised Biot-Savart Kernel
L	: Interaction List
m_k	: k^{th} moment of vorticity
δ	: kernel smoothing parameter
ε	: error
ϕ_δ	: regularised Newtonian potential

Mathematical Notation

$a \cdot b$	: scalar product of a and b
$a \times b$	: vector product of a and b
$A \in B$	: member A of B
$A \subset B$	: subset A of B
$A \cap B$	: intersection of A and B
$A \cup B$	: union of A and B

Abbreviations

BVI	: Blade Vortex Interaction
CFD	: Computational Fluid Dynamics
FMM	: Fast Multipole Method
TVD	: Total Variation Diminishing
VTM	: Vorticity Transport Model
WAF	: Weighted Average Flux
WHL	: Westland Helicopters Ltd.

Chapter 1

Introduction

Helicopters are, in general, plagued by high levels of vibration. The magnitude and frequency of the vibration can seriously degrade the working life of the components of the aircraft, not to mention the ride quality experienced by the passengers. The primary source of vibration on helicopters originates from the aerodynamic loads generated by the rotor. The prediction of the vibratory loads generated by the rotor system is further complicated by the complex dynamic response of the rotor system and fuselage, and the coupling of this response back into the aerodynamic forcing of the rotor. Indeed, an industry-wide survey, performed by Hansford and Vorwald [1] in 1996, showed that the helicopter industry as a whole was unable to predict vibration levels to an accuracy greater than 50%. In order to minimise the effects of vibration, industry has been forced to integrate vibration suppression devices into the helicopter, incurring significant penalties in terms of cost, weight and the performance of the aircraft. Although the capability of these vibration suppression devices has improved greatly in recent years, with the technologies evolving from simple passive mechanical devices to the sophisticated, actively controlled, vibration suppression devices used on modern helicopters, these devices are essentially parasitic devices whose only purpose is to ameliorate deficiencies elsewhere in the rotor system.

Accurate prediction of the vibratory loads generated by the rotor would allow the rotor to be designed to minimise vibration at the source, thereby reducing, or even eliminating, the need for vibration suppression devices. Any improvements in vibration prediction has the potential therefore to bring about significant improvements in the overall performance, cost and reliability of helicopters.

The problem is further compounded by the conflicting requirements placed on helicopter manufacturers for improved rotor performance. The demand for improved hover performance has forced manufacturers to integrate increased levels of twist into their blade designs. However, the optimisation of the rotor in hover leads to a degradation of performance in forward flight, most significantly in the form of increased vibration levels. Furthermore, the link between blade twist and rotor vibration is not fully understood, nor can it be modelled accurately using the methods currently employed by industry.

The study by Hansford and Vorwald suggested that the current inability of the methods used by industry to predict the vibratory loading of the rotor system stemmed principally from an overly simple description of the rotor aerodynamics and the structure of the rotor wake. Since the major source of vibration in the rotor system originates from the aerodynamic loading of the rotor blades, a comprehensive description of the aerodynamic environment surrounding the rotor is therefore required for the accurate prediction of vibration [2]. The aerodynamic models used within most industrial vibration prediction codes generally employ a number of simplifying assumptions, regarding the structure and evolution of the wake, in order to reduce the computational cost of simulations. However, with the increases in computational processing power provided by modern computer hardware, it is now feasible to remove many of these assumptions, and to assess the potential benefits of improved wake modelling on the accuracy of vibration predictions.

Computational Fluid Dynamic (CFD) models, through their fundamental treatment of the flow physics, present a unique and powerful tool for analysing the aerodynamics of helicopter rotors. CFD methods do, however, have limitations which, if not properly addressed, limit the success of these techniques in modelling rotorcraft related flows. Given that the environment in which a helicopter rotor operates is dominated by complex and persistent vortical structures, any method selected to model a rotor wake needs to preserve the integrity of the vortical structure of the wake over significant periods of time. Standard CFD methods, that rely upon a primitive variable formulation of the Navier-Stokes equations, i.e. in terms of velocity and pressure, are susceptible to excessive numerical dissipation of vorticity [3]. If not controlled, this dissipation leads ultimately to the loss of coherence of vortical structures within the flow. A further limitation of CFD methods lies in their rather intensive use of computational resources. Excessive use of the available computational resources constrains the maximum resolution, and hence the range of flow-

scales, that can be simulated. This limits the accuracy that can be achieved using these methods - an issue which becomes particularly relevant for problems, such as vibration and acoustics, which are dependent on the fine-scale features of the flow.

This thesis describes the development of a CFD-based method for modelling rotor aerodynamics. The method is based upon the Vorticity Transport Model (VTM), originally developed by Brown [4]. By describing the flow in terms of a time-dependent vorticity distribution, rather than in terms of the primitive variables, velocity and pressure, the VTM is able to conserve implicitly the vorticity of the flow. The VTM is therefore able to preserve indefinitely the strength of vortical structures in the flow, making it particularly suited to the modelling of rotor aerodynamics.

However, the implementation used by the original version of the VTM places significant demands on the available computational resources, and forces concessions to be made regarding the resolution at which the model can be run. This diminishes the effectiveness of the model when analysing problems which require the flow to be resolved to very fine length scales, as is required for vibration prediction. A key element of the work presented in this thesis relates to the development of efficient algorithms and modelling strategies for the purpose of improving the computational efficiency of the VTM. These improvements permit the VTM to exploit the available computational resources more efficiently, and hence increases the range of flow-scales that can be resolved by the model.

The enhanced VTM code provides a level of fidelity which has the potential to significantly improve upon the description of the rotor aerodynamics provided by the aerodynamic models currently employed by the helicopter industry for vibration prediction. The latter half of this thesis is devoted to an evaluation of the capabilities of the enhanced VTM, particularly in terms of its potential to improve the accuracy of vibration predictions.

1.1 Synopsis

The structure of the thesis is arranged as follows. Chapter two presents a comprehensive description of the theory and implementation used by the original version of the VTM. A number of deficiencies and limitations in the original formulation are highlighted. These relate mainly to the model's inefficient use of computational resources, as well as its

treatment of far-field boundary conditions.

Chapters three and four address the excessive computational cost of the original formulation of the VTM. Chapter three presents a new semi-Lagrangian adaptive grid system which permits significant increases in grid resolution, with minimal impact on computational cost. The method relies upon the fact that, when modelling using the vorticity-velocity form of the Navier-Stokes equations, only those regions of the flow that contain vorticity need to be retained within the computational domain. The new grid system uses adaptive cell generation and destruction to track regions of vorticity in the flow as it evolves through time. This approach minimises the number of grid cells, and hence the computational resources, required to model the rotor and its wake. A powerful feature of the new grid system is that the solution domain is essentially unbounded - the grid is free to expand in size with the rotor wake, thereby eliminating the need for far-field boundary conditions.

Chapter four describes the development of a highly efficient algorithm, based on the Cartesian Fast Multipole Algorithm, which is used to evaluate the velocity field throughout the computational domain. The similarities in the algorithmic structures of the Fast Multipole Method and the adaptive grid system lead to a particularly efficient numerical implementation. In particular, both methods use an octree-based hierarchical decomposition of the computational domain and therefore can share common data-structures, yielding considerable savings in terms of memory usage and computation time.

Having integrated the new grid system and velocity calculation into the VTM, the performance of the new code is assessed in chapter five. The code is validated against the well known experimental data of Harris [5] and of Caradonna and Tung [6]. These data sets allow the accuracy of the predicted wake structure, aerodynamic loading, and low-frequency dynamics of the rotor, in hover and forward flight, to be analysed.

In chapter six, the analysis of Harris' experimental data is extended in some detail in an attempt to understand the origins of some interesting features contained in the experimental data. From a detailed analysis of the predicted wake structures and inflow distributions, the study provides significant insight into the structure and evolution of rotor wakes in forward flight.

In chapter seven, the potential of the VTM to improve the accuracy of vibration prediction is assessed. The ability of the VTM to capture the effects of blade twist on the

aerodynamic forcing of the rotor is confirmed. In an attempt to quantify the improvements in vibration prediction that can be realised using the VTM, the model is integrated with an industry-standard structural dynamics code. The performance of the resulting code is evaluated by comparing its predictions against flight test data.

Finally, in chapter eight the thesis concludes with a discussion and suggestions for future work.

1.2 Publications

A number of elements of the work presented within this thesis have been published previously.

In September 2003, a paper [7] outlining the use of the Semi-Lagrangian adaptive grid and Fast Multipole Method (FMM) for modelling rotor wakes was presented at the 29^{th} European Rotorcraft Forum in Friedrichshafen, Germany. The paper described the basic theory and implementation of the new version of the VTM and presented the validation of the code in forward flight.

In June 2004, two papers [8] [9] were presented at the 60^{th} Annual Forum of the American Helicopter Society in Baltimore, USA. The first paper presented the ongoing work on the development of the VTM, including the use of the adaptive grid and FMM for high resolution wake modelling, the validation of the code in hovering flight and several examples of the code's capabilities and performance. The second paper presented the preliminary results from numerical simulations of full aircraft simulations in descending flight. The work examined the interference effects of the fuselage and tail rotor aerodynamics on the performance of the aircraft upon entering vortex ring conditions.

Finally, a further paper has been submitted for publication in the AIAA journal. This paper provides a complete and comprehensive description of the new version of the VTM, including validation of the wake geometries, blade loading and low-frequency blade dynamics predicted by the code. The paper also presents several extensions to the model, including an efficient approach to modelling rotors in ground effect using a simple modification to the FMM, and the introduction of a simple panel-based description of the fuselage aerodynamics to the VTM for modelling rotor-fuselage interference effects.

Chapter 2

Model Description

2.1 Introduction

The wake of a helicopter rotor is a particularly challenging flow to model. Even in the simplest of flight conditions, the highly interactive nature of the vorticity contained in the rotor wake leads to the creation of exceptionally complex flow structures. In terms of rotor vibration, possibly the most significant source of vibration occurs when a blade impacts directly with the vortical structures in the wake. Accurate modelling of these so-called Blade Vortex Interactions (BVI) places significant demands upon any model employed to investigate rotor vibration. Not only must the model be capable of predicting the unsteady aerodynamics of the rotor blades from low-speed reverse flow conditions up to transonic speeds, but it must also capture the non-linear structural dynamics of the entire rotor system, whilst simultaneously modelling the evolution of the rotor wake. The task of developing such a numerical model is further complicated by the inherent differences in time scales between that of the motion of the rotor and that of the evolution of the wake.

Arguably the most rigorous numerical approach for modelling fluid flows are provided by grid-based Computational Fluid Dynamic (CFD) models. By solving directly the equations that govern the fundamental physical processes via which the flow evolves, CFD methods present a particularly faithful and general description of the flow physics. The vast majority of CFD methods use a primitive variable formulation, in which the flow is described in terms of a velocity and pressure field. Although primitive variable schemes are by far the most mature, they do not, in general, explicitly conserve vorticity. Indeed,

the presence of numerical diffusion in such schemes will ultimately lead to the destruction of vorticity. It is therefore unlikely that a scheme which does not address the issues of vorticity conservation will be able to preserve the strength of vortical structures in the flow for the lengths of time required for rotor wake modelling.

2.2 Governing Equations

The Navier-Stokes Equations governing the flow surrounding the rotor can be written in primitive variable (velocity-pressure) form as

$$\frac{\partial}{\partial t}u + u \cdot \nabla u = -\frac{1}{\rho}\nabla p + \nu \nabla^2 u \tag{2.1}$$

$$\nabla \cdot u = 0 \tag{2.2}$$

if it is assumed that the flow is incompressible. This assumption is reasonably well justified, except perhaps near to the tips of the blades or in the cores of the wake vortices where higher flow velocities may introduce compressibility effects.

Taking the curl of equation 2.1 yields the unsteady vorticity transport equation

$$\frac{\partial}{\partial t}\omega + u \cdot \nabla\omega - \omega \cdot \nabla u = \nu \nabla^2 \omega \tag{2.3}$$

where the vorticity, ω, is defined as $\omega = \nabla \times u$. Equation 2.3 describes the flow as a vorticity distribution which evolves under the influence of the velocity field, u. The vorticity and velocity fields are coupled by the Biot-Savart relationship, which can be expressed in its differential, or Poisson, form as

$$\nabla^2 u = -\nabla \times \omega \,. \tag{2.4}$$

In the limit of zero viscosity, the viscous term on the right hand side of equation 2.3 becomes non-zero only on surfaces immersed in the flow, and can be replaced by a local vorticity source.

Hence, for the high Reynolds number flows relevant to most rotor aerodynamic problems, the vorticity transport equation can be written as

$$\frac{\partial}{\partial t}\omega + u \cdot \nabla\omega - \omega \cdot \nabla u = S \,, \tag{2.5}$$

where the source term S accounts for the vorticity production accompanying the generation of aerodynamic loads on the rotor blades.

2.3 Vorticity Transport Model

The Vorticity Transport Model (VTM), developed by Brown [4], is a grid-based CFD model for simulating the aerodynamic evolution of rotor wakes and associated flows. Unlike primitive variable approaches, the VTM describes the aerodynamic environment surrounding the rotor in terms of vorticity and velocity. Since the rotor wake is a vorticity dominated flow, it seems reasonable to represent the flow as a time-dependent vorticity distribution. Indeed, for the purposes of simulating rotor wakes, this approach presents a number of practical and numerical benefits over primitive variable schemes.

Most significantly, vorticity is explicity preserved within the vorticity-velocity formulation. Numerical diffusion and dissipation can in no way lead to the destruction of vorticity, allowing the strength of vortical structures in the flow to be preserved indefinitely. Any numerical diffusion present within the scheme will however lead to the spatial smoothing of the vorticity distribution, thereby reducing the compactness of vortical structures. These effects are minimised within the VTM through the introduction of appropriate flux limiter functions to yield a scheme with Total Variation Diminishing (TVD) properties.

Since the vorticity conserving properties of the vorticity transport approach are explicit within the formulation itself, the strength, or circulation, of the wake is independent of grid resolution. Consequently, the VTM has the flexibility to run at a resolution relevant to a given problem. Situations requiring only the prediction of gross flow features, such as flight mechanics simulations, can be modelled successfully using very coarse grid resolutions [10]. Conversely, in cases where small-scale flow features become significant, such as in the modelling of blade-vortex interactions for acoustics or vibration prediction, the code can be run at higher resolution to expose the detail of those fine vortical structures.

The model has been used previously to investigate a variety of rotorcraft problems, including the generation of linearised models for flight mechanics [10], the onset of the vortex ring state [11],[12], and the sensitivity of rotorcraft to encounters with aircraft wakes [13].

Unless otherwise stated, all results presented throughout this thesis can be assumed to have been produced using the VTM. In addition, the original version of the VTM, as developed by Brown in [4] will be referred to simply as the 'original VTM'.

2.4 Numerical Implementation

The following section describes the finite volume formulation used by the VTM to numerically solve the vorticity transport equation given in equation 2.3.

The governing equations are solved from an Eulerian frame of reference, upon a structured grid which is fixed with respect to the hub of the helicopter's main rotor. The grid is created by partitioning the solution domain into a finite number of control volumes, or cells. Each cell contains a distribution of vorticity along with a description of the local velocity field. The evolution of the solution through time is discretised into contiguous timesteps of duration Δt, such that the time at the start of timestep $n \in \mathbb{N}$ is given by $t = n\Delta t$.

Integration of equation 2.3 over a cell with volume, V, yields

$$[\omega]^{n+1} - [\omega]^n = [\omega.\nabla u]^n_{\Delta t} - [u.\nabla\omega]^n_{\Delta t} + [\nu.\nabla^2 u]^n_{\Delta t} + [S]^n_{\Delta t} \,, \tag{2.6}$$

where the operators

$$[q]^n = \int_V q(x, n\Delta t)\ dV \tag{2.7}$$

and

$$[q]^n_{\Delta t} = \int_n^{n+1} [q]^n\ dt \tag{2.8}$$

perform the integration of a flow variable, $q(x,t)$, over the cell volume and timestep respectively. Approximation of each operator using a suitable numerical method yields a set of algebraic equations in terms of local flow variables, which then allow the solution to be

evolved through time. In the current formulation of the VTM, all operators, except the vorticity source, are approximated using explicit numerical methods.

Starting from the vorticity distribution at time $t = n\Delta t$, the velocity field $u^n = u([w]^n)$ is first evaluated by inversion of equation 2.4. Each integration operator in equation 2.6 is then applied sequentially using the operator splitting approach to construct the vorticity field at time $t = (n+1)\Delta t$:

$$\begin{aligned} [\omega]^{*} &= [\omega]^{n} + [S]^{n}_{\Delta t} \\ [\omega]^{**} &= [\omega]^{*} + [\omega.\nabla u]^{n}_{\Delta t} \\ [\omega]^{***} &= [\omega]^{**} - [u.\nabla\omega]^{n}_{\Delta t} \\ [\omega]^{n+1} &= [\omega]^{***} + [\nu.\nabla^2 u]^{n}_{\Delta t} \ . \end{aligned} \tag{2.9}$$

The stretching operator, $[\omega.\nabla u]^n_{\Delta t}$, is evaluated using Runge-Kutta integration, and the advection operator, $[u.\nabla\omega]^n_{\Delta t}$, is evaluated using the Weighted-Average-Flux (WAF) scheme of Toro [18]. A full description of the WAF scheme is presented in section 2.4.3. The diffusion term is included here solely for completeness. In practice the diffusion term is neglected for the reasons described previously in section 2.2. The operator splitting approach was shown by Brown [14] to be second order accurate as long as the numerical approximation of each integration operator is of at least second order accuracy.

2.4.1 Grid Structure

The grid system employed by the original version of the VTM is a simple, uniform resolution, Cartesian grid. As illustrated by figure 2.1, the solution domain, $\Omega \subset \mathbb{R}^3$, is defined by a regular cuboid which contains the helicopter and the surrounding flow. The domain is populated throughout with cubic cells with edge-length Δx and volume V. The edges of the cuboid are aligned with the Cartesian directions and have an edge length equal to $N_i\Delta x$, where $i \in [x, y, z]$ is the relevant Cartesian direction. The resulting grid therefore contains a total of $N = N_x N_y N_z$ cells.

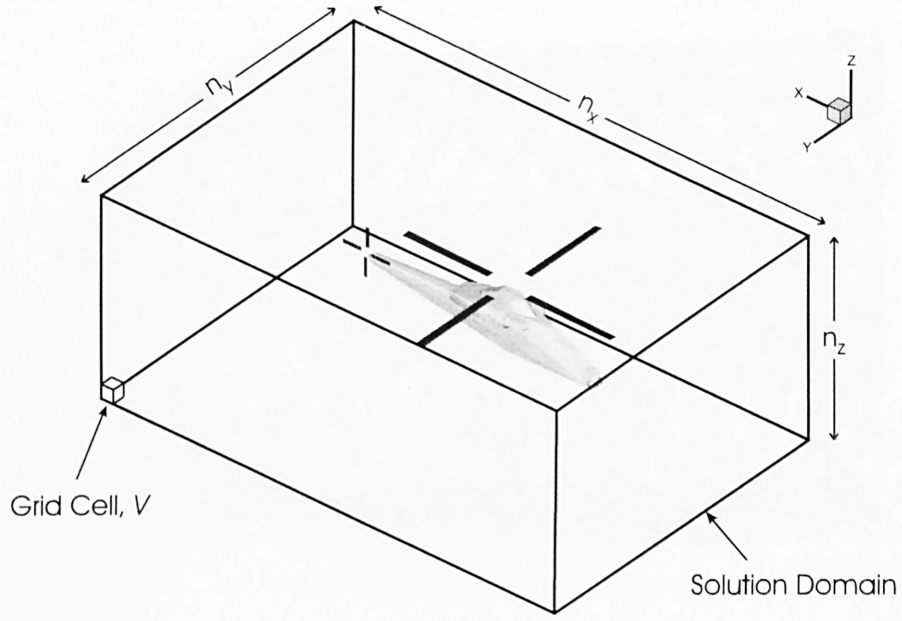


Figure 2.1: *Definition of solution domain.*

When modelling a flow via a vorticity transport approach, only those regions of the flow that contain vorticity need to be included within the solution domain. The grid system described above however, does not exploit this feature, resulting in a particularly inefficient implementation in terms of storage requirements.

Figure 2.2 shows an example wake geometry, calculated using the original version of the VTM, generated by a 4-bladed rotor in forward flight. The grid used for this calculation contained a total of 8.07 million cells of width $\Delta x = 0.0175R$, where R is the rotor radius. However, the number of cells that actually contained vorticity was just 1.2 million (14.8% of the total number of cells). This clear inefficiency severely limits what can be achieved, in terms of grid size and resolution, using the available computational resources. The non-vorticity-containing cells present within the grid serve only to (a) provide space for the future evolution of the wake, and (b) to fill the solution domain to allow the application of boundary conditions at its edges. The uniform-resolution nature of the grid also prevents any adaptation or refining of the solution, limiting the ability of the model to expose the fine-scale flow features which are crucial for accurate prediction of rotor vibration and acoustics.

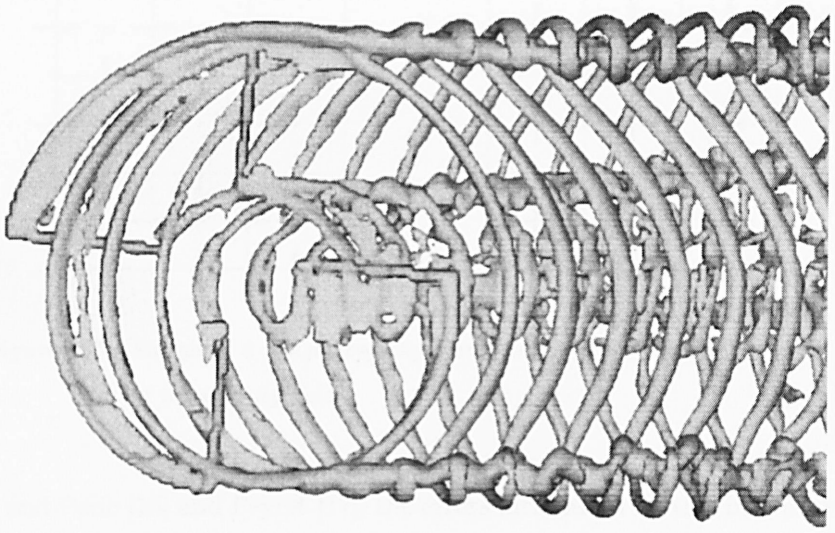


Figure 2.2: *Wake visualisation of a 4-bladed rotor at* $\mu_x = 0.147$.

These limitations of the original grid system, along with other deficiencies to be described in section 2.4.5, have motivated the development of an alternative grid system which will be presented in Chapter 3.

2.4.2 Flow Variables

The VTM uses a staggered arrangement of flow variables throughout the grid, an approach first introduced by Harlow and Welsh [15]. As described by Figure 2.3, the velocity field is evaluated at the centre of the rear faces of each cell rather than at the cell centre as in a collocated arrangement. In addition, each cell contains a uniform distribution of vorticity, leading to a piecewise constant description of the global vorticity field.

Use of the staggered arrangement presents a number of benefits, both in terms of accuracy and convenience, over the collocated arrangement. Evaluation of the intercell vorticity fluxes requires the velocity normal to each cell face. For the staggered arrangement, these velocities are readily available, whereas for the collocated arrangement they must be interpolated from the cell centres of neighbouring cells. As discussed in the texts

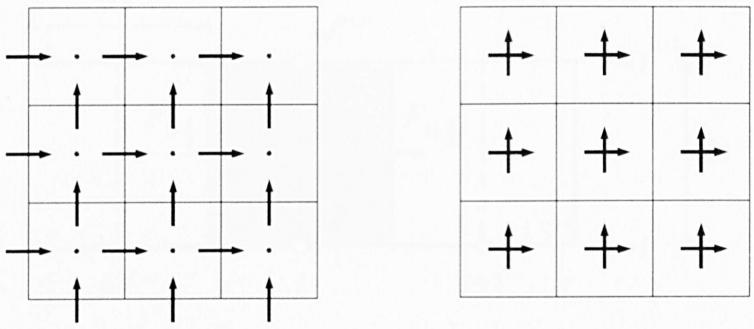


Figure 2.3: *Staggered arrangement (left) and collocated arrangement (right) of the velocity field.*

of Ferziger and Peric [16] and Peyret [17], the errors introduced by this interpolation procedure can develop into spurious oscillations in the velocity and vorticity fields. Indeed, previous experience using the collocated arrangement within the VTM has resulted in oscillatory solutions.

2.4.3 Weighted Average Flux Scheme

The advection operator introduced in equation 2.6, which accounts for advection of vorticity through the interface between two adjacent cells, is evaluated using the Weighted-Average-Flux (WAF) method of Toro [18]. The WAF method is a second-order accurate, one-dimensional Riemann solver for hyperbolic conservation laws. It was developed primarily for shock-capturing in compressible gas dynamic problems [19]. However, its ability to resolve the steep gradients in flow properties in the neighborhood of shocks makes it equally suitable for resolving the steep vorticity gradients found within the rotor wake.

Consider the cell i shown in figure 2.4. In the absence of diffusion and vorticity sources, any variation in the vorticity contained in i must be due to the advective flux, F, of vorticity through cell i's boundaries.

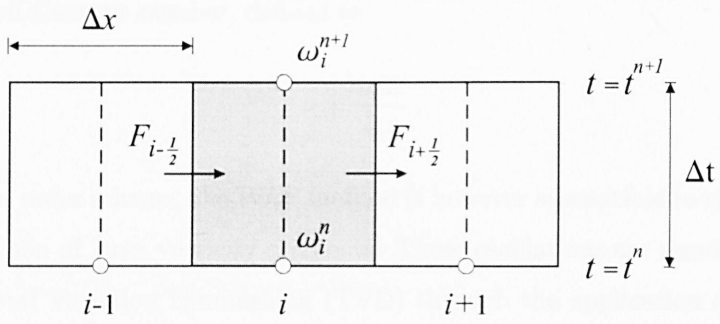


Figure 2.4: *Stencil for calculation of intercell vorticity fluxes.*

A numerical scheme for the calculation of the advective fluxes can be derived directly from the non-linear advection equation

$$\frac{\partial}{\partial t}\omega + u \cdot \nabla\omega = 0 \,, \tag{2.10}$$

obtained from equation 2.5 by omitting the stretching and source terms. Integration of equation 2.10 over the cell volume and again over a time interval of size Δt leads to

$$[\omega_i]^{n+1} = [\omega_i]^n - \frac{\Delta t}{\Delta x}(F_{i+\frac{1}{2}} - F_{i-\frac{1}{2}}) \,, \tag{2.11}$$

where $F_{i+\frac{1}{2}}$ is the vorticity flux through the interface between cells i and $i+1$. The advection operator therefore becomes

$$[u.\nabla\omega_i]^n_{\Delta t} = \frac{\Delta t}{\Delta x}(F_{i+\frac{1}{2}} - F_{i-\frac{1}{2}}) \,. \tag{2.12}$$

The intercell flux can be evaluated using the solution to the piece-wise constant Riemann problem at the cell interface.

The WAF scheme constructs the intercell flux as

$$F_{i+\frac{1}{2}} = W_1 F^{(1)}_{i+\frac{1}{2}} + W_2 F^{(2)}_{i+\frac{1}{2}} \,, \tag{2.13}$$

where

$$W_1 = \frac{1}{2}(1+\nu) \quad ; \quad W_2 = \frac{1}{2}(1-\nu) \tag{2.14}$$

$$F^{(1)}_{i+\frac{1}{2}} = u[\omega_i]^n \quad ; \quad F^{(2)}_{i+\frac{1}{2}} = u[\omega_{i+1}]^n \,, \tag{2.15}$$

and ν is the cell Courant number, defined as

$$\nu = \frac{u\Delta t}{\Delta x} \, . \tag{2.16}$$

As a second order scheme, the WAF method is however susceptible to spurious oscillations in the region of large vorticity gradients. These oscillations are removed by making the scheme Total Variation Diminishing (TVD) through the application of suitable flux limiter, or wave amplification, functions to the fluxes defined in equation 2.15. The Total Variation, $TV^n(\omega) = TV([\omega]^n)$, of the vorticity field is defined by Harten [20] as

$$TV^n(\omega) = \int_{-\infty}^{+\infty} \left| \frac{\partial \omega}{\partial x} \right| \, dx \, . \tag{2.17}$$

For a discretised representation of the vorticity field, equation 2.17 can be written as

$$TV^n(\omega) = \sum_{i \in \Omega} | \, [\omega_{i+1}]^n - [\omega_i]^n \, | \, , \tag{2.18}$$

leading to the requirement that

$$TV^{n+1}(\omega) \leq TV^n(\omega) \tag{2.19}$$

for a fully TVD scheme. The derivation of a number of wave amplification functions which satisfy equation 2.19 is presented by Toro [21] and [22].

Introduction of flux limiter functions does however increase the size of the stencil to include the two cells either side of the interface. The relevance of this observation will become clear when the adaptive grid system for the new VTM is developed in Chapter 3.

The scheme is extended to three dimensions using the space-operator splitting approach of Strang [23], in which the three-dimensional problem is decomposed into three one dimensional problems. Full multi-dimensional versions of the WAF scheme have been developed recently by Billett and Toro [24], [25]. However, these schemes are not strictly TVD and hence do not guarantee a compact representation of the vortical structures in the flow.

2.4.4 Vorticity-Velocity Coupling

In incompressible flow the velocity and vorticity fields are coupled by the Biot-Savart relationship, the differential form of which is given by equation 2.4. From a known vorticity distribution, inversion of equation 2.4 provides the required velocity field.

In the original version of the VTM, the inversion process is implemented by first applying a finite-difference approximation to equation 2.4 on each cell to produce a system of linear equations. This system of equations is then solved using the method of Cyclic Reduction, developed by Schumann and Sweet [26], [27], to yield the velocity field. For a grid containing N cells, the method of Cyclic Reduction performs the inversion procedure in $O(N \log N)$ operations.

An alternative approach can be derived by integrating equation 2.4 over the solution domain, Ω, using the integral form of the Biot-Savart relationship

$$u(x) = \int_{\Omega} K(x,y) \times \omega(y)\, dy\,, \tag{2.20}$$

with the Biot-Savart kernel defined by

$$K(x,y) = -\frac{1}{4\pi} \frac{(x-y)}{|x-y|^3}\,. \tag{2.21}$$

The integral formulation is presented here as it forms the basis of a family of solution methods, called Multipole methods, which will be developed in chapter 4 as an alternative to Cyclic Reduction.

2.4.5 Boundary Conditions

Due to the elliptic nature of the Biot-Savart relationship, all vorticity present in the flow has an influence, via the velocity field, everywhere throughout the flow. However, for standard grid-based CFD approaches it is rarely practical to generate solution domains which contain the entire vorticity field of the flow.

As described in section 2.4.1, the solution domain employed by the original version of the VTM is constrained to contain only a finite region of the flow. Consequently, for non-trivial flows it is inevitable that vorticity will be lost from the solution domain. Since it is, by definition, impossible to model the evolution of vorticity that is located

outside of the solution domain, its whereabouts and strength are essentially unknown. Hence, any vorticity that passes out of the solution domain is forbidden from re-entering. Furthermore, failure to reconstruct the velocity field induced by any *external* vorticity on the rest of the flow will result in non-physical solutions. It is therefore essential that suitable far-field boundary conditions are applied to the solution domain. Within the original VTM, the velocity field induced by vorticity outside of the solution domain is reconstructed approximately by forcing zero-curvature of the velocity and vorticity fields at the domain boundary.

Although experience has shown this approach to be very effective for the majority of flight conditions, it does have its limitations. Indeed, spurious flow features are known to be produced by the boundary conditions when the wake-induced velocities are similar, or greater, in magnitude compared to the freestream velocity, i.e. in low speed flight and in hover.

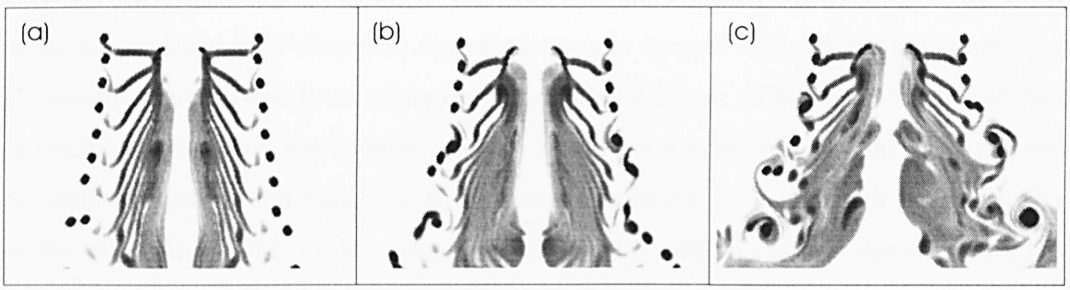


Figure 2.5: *Evolution of a solution contaminated by invalid boundary conditions.*

An example of a solution which has become contaminated by the boundary conditions is illustrated in 2.5, in which the wake is visualised as contours of vorticity magnitude on a vertical slice through the rotor hub. The simulation begins with the rotor in a low-speed vertical climb (a) before slowing into a hover. During the transition from axial flight to hover, (b), the far wake is destabilised, producing a net up-flow at the lower grid boundary. This up-flow attempts to draw vorticity back into the domain from the outside - vorticity that can in no way be reconstructed. From this point onwards, the VTM is unable to describe accurately the vorticity field close to the lower boundary. The resulting velocity field forces the far-wake sideways and upwards, as shown in (c), to produce a wake structure which resembles the wake produced by a rotor hovering in ground effect, rather

than out of ground effect.

This deficiency of the model has motivated the development of a fully boundary-free grid formulation which eliminates the need for any explicit far-field boundary conditions. The introduction of such a boundary-free approach into the VTM is presented in Chapter 3.

2.5 Structural Dynamics

Modern helicopter rotor systems consist of a highly complex arrangement of hinges, linkages, springs and dampers. Accurate modelling of the structural dynamics of such systems is therefore particularly challenging and numerically expensive. The problem is further complicated by the coupling of the rotor and fuselage dynamics.

To limit the complexity and cost of the structural dynamic model, the VTM employs a somewhat simplified description of the rotor system, in which many of the hub components are replaced with simplified representations or ignored completely. For example, a conventional articulated rotor system is described within the VTM as a collection of rigid or flexible blades, each free to move about a number of hinges, accompanied by a number of idealised springs and dampers, as illustrated in figure 2.6. Although the capability exists within the VTM, for the sake of simplicity the coupled fuselage dynamics are not included in the calculations presented here. Instead, the rotor hub is simply assumed to remain fixed with respect to the aircraft trajectory.

Of course, there exists a wide variety of rotor designs, from the relatively simple teetering rotors to the more complex articulated and elastomeric designs. Furthermore, seemingly subtle changes to a design, such as the reordering of the flap-lag-feather hinges along the rotor radius, can have a significant effect on the dynamical nature of the system. With this in mind, it seems sensible to adopt a flexible and generalised approach to the modelling of the structural dynamics. Consequently, within the VTM the structural dynamics are modelled using an approach derived using Lagrangian dynamics.

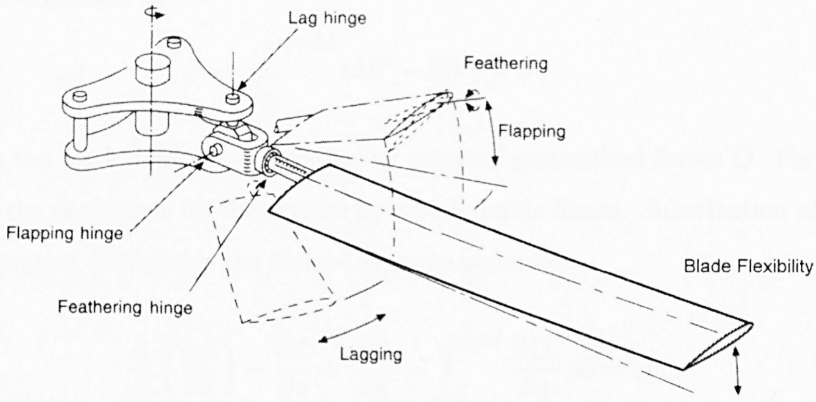


Figure 2.6: *Simplified representation of an articulated rotor.*

For a system with $n \in \mathbb{N}$ degrees of freedom, the problem can be completely defined in terms of n generalised coordinates, $q = q(q_1, q_2, ..., q_n, t)$ and their time derivatives, $\dot{q} = dq/dt$, from which the total kinetic and potential energy, the dissipation and work done on the system can be constructed.

$$\text{Kinetic Energy} = T(q, \dot{q}) \tag{2.22}$$

$$\text{Potential Energy} = U(q, \dot{q}) \tag{2.23}$$

$$\text{Dissipation} = D(q, \dot{q}) \tag{2.24}$$

$$\text{Work} = W(q, \dot{q}) \, . \tag{2.25}$$

For a rigid blade, the generalised coordinates are taken to be the azimuth angle of the blade, along with the flap, lag and feather angles. For a flexible blade, additional coordinates must be introduced to capture the additional torsional and bending degrees of freedom.

The modified Lagrangian of the system at time t is defined as

$$\mathcal{L}^* = T - U + \int_{t_0}^{t_0+t} D_\tau \, d\tau \, , \tag{2.26}$$

where $D_t = \partial D / \partial t$ is the rate of dissipation in the system and t_0 is the time at which the system was initialised. Hamilton's principle of minimisation of action states that the

variation of $\mathcal{L}^* - W$ is minimised along any trajectory of the system on the manifold $(q, \dot{q})$. This can be expressed as

$$\int_{t_0}^{t_0+\Delta t} (\delta\mathcal{L}^* - \delta W) = 0 \,, \tag{2.27}$$

where W is the work done on the system by external generalised forces Q. For example, Q could be the work done on the system by aerodynamic forces. Substitution of equation 2.26 into equation 2.27 yields the Euler-Lagrange equations

$$\frac{d}{dt}\left(\frac{\partial\mathcal{L}}{\partial\dot{q}}\right) - \frac{\partial\mathcal{L}}{\partial q} + \frac{\partial D_t}{\partial\dot{q}} - \int_{t_0}^{t_0+t} \frac{\partial D_t}{\partial q}\, dt = Q \,, \tag{2.28}$$

where $\mathcal{L} = T - U$ is the conventional Lagrangian of the system in the absence of dissipation. Expanding the first term of equation 2.28 as

$$\frac{d}{dt}\left(\frac{\partial\mathcal{L}}{\partial\dot{q}}\right) = \frac{\partial^2\mathcal{L}}{\partial\dot{q}_i\partial q_j}\,\dot{q}_j + \frac{\partial^2\mathcal{L}}{\partial\dot{q}_i\partial\dot{q}_j}\,\ddot{q}_j \tag{2.29}$$

produces a system of equations

$$\frac{\partial^2\mathcal{L}}{\partial\dot{q}_i\partial\dot{q}_j}\,\ddot{q}_j + \frac{\partial^2\mathcal{L}}{\partial\dot{q}_i\partial q_j}\,\dot{q}_j - \frac{\partial\mathcal{L}}{\partial q_i} + \frac{\partial D_t}{\partial\dot{q}_i} - \int_{t_0}^{t_0+t} \frac{\partial D_t}{\partial q_i}\, dt = Q_i \,, \tag{2.30}$$

which, after evaluating all the derivatives and the integral numerically, can be solved directly for the accelerations $\ddot{q}$. Finally, the generalised coordinates at the next timestep are evaluated using Euler integration:

$$q^{n+1} = q^n + \dot{q}^n\Delta t \tag{2.31}$$

$$\dot{q}^{n+1} = \dot{q}^n + \ddot{q}^n\Delta t \,. \tag{2.32}$$

The power of the Lagrangian approach lies in its generality. Not only is it capable of handling complex, highly coupled non-linear systems, but its formulation makes it very easy to accommodate changes in the mechanical design of the system. In contrast to standard approaches, which require the full equations of motion to be derived for each new system, only a straightforward modification of the generalised coordinates and associated energy of the system is required by the Lagrangian approach.

2.6 Blade Aerodynamics

The vorticity source operator in equation 2.6 models the generation of vorticity by the surfaces immersed within the flow, in other words by the rotor blades. However, evaluation of the vorticity source is complicated by the fact that the timestep used to evolve the dynamics of the wake is typically several times larger than that required to capture the unsteady aerodynamics and high-frequency structural dynamics of the rotor. To accommodate this disparity in timescales, a substepping approach is introduced. The global timestep, Δt is first partitioned into $m \in \mathbb{N}$ contiguous substeps, such that

$$\Delta t = \sum_{i=0}^{m-1} \Delta t_i \, . \tag{2.33}$$

The vorticity generated over each of the substeps is then summed to give the vorticity source for the global timestep

$$[S]^n_{\Delta t} = \sum_{i=0}^{m-1} [S]^{n+i/m}_{\Delta t_i} \, . \tag{2.34}$$

The number of substeps is chosen to (a) ensure that all required timescales of the rotor aerodynamics and dynamics are captured accurately, and (b) to satisfy any stability and accuracy requirements of the numerical method employed to model the blade aerodynamics.

A variety of methods can, of course, be utilised to evaluate the vorticity source S. At present, the VTM employs a single-panel lifting surface model of the blade aerodynamics, based upon the Weissinger-L method [28]. The method was developed as a computationally efficient alternative to panel methods for the analysis of swept wings. The method was later extended to include compressibility corrections by DeYoung [29] and Stevens [30], who both used the method to analyse wings with arbitrary sweep, planform and twist.

The method is implemented by first partitioning the blade into a finite number of discrete panels along the span of the blade. As illustrated in figure 2.7, each panel consists of a bound horseshoe vortex attached at the 1/4-chord, a collocation point at the 3/4-chord and a separation line. As the blade sweeps through the flow over the course of a substep, a vortex panel containing trailed and shed vorticity is deposited into the flow from the separation line. The resulting vortex lattice grows over subsequent substeps, whilst being

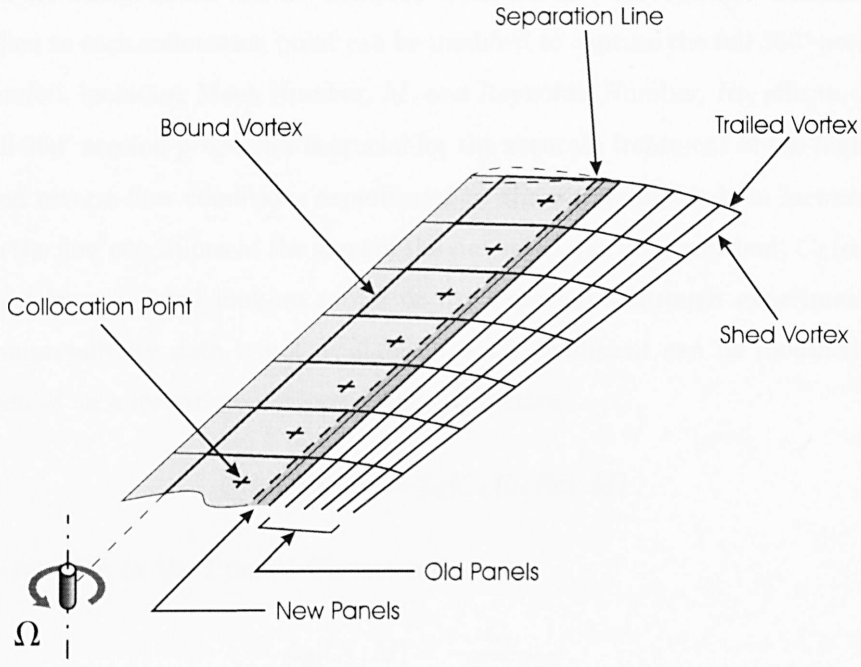


Figure 2.7: *Blade aerodynamic and inner wake model.*

freely convected by the local flow velocity. At some distance downstream of the blade, the vorticity on the rearmost panels of the lattice is interpolated into the grid, forming the vorticity source S.

The strength of both the bound vortex and the newly created panels is evaluated as follows. The local flow velocity, u_b, at each collocation point is calculated as the sum of the wake induced velocity, the free-stream velocity and the structural motion of the blade. Setting the velocity component normal to each collocation point equal to zero yields a set of algebraic equations that can be solved for the strength of the bound vorticity, ω_b, and the strength of the trailed and shed vorticity produced over that substep. The vorticity generated by the blade can then be expressed in terms of the shed and trailed vorticity as

$$S = -\frac{d}{dt}\omega_b + u_b \nabla \cdot \omega_b \,, \tag{2.35}$$

where the first term represents the shed vorticity and the second term the trailed vorticity. Locating the bound vortex and collocation point at the 1/4- and 3/4-chord respectively leads to the idealised lifting-line lift-curve slope for an infinite aspect ratio panel of exactly



*This approach accounts only for the circulatory component of the loading. Any non-circulatory contribution to the loading is calculated independently of the Weissinger-L blade model.

2π. From knowledge of the real aerofoil properties, the zero through-flow boundary condition applied to each collocation point can be modified to capture the full 360° performance of the aerofoil, including Mach Number, M, and Reynolds Number, Re, effects. Inclusion of the full 360° aerofoil properties is crucial for the accurate treatment of the high angle of attack and reverse-flow conditions experienced by the retreating blade in forward flight.

From the flow conditions at the start of the time-step, the lift-coefficient, $C_L(\alpha, Re, M)$, is obtained from aerofoil look-up tables or from curve-fits through experimental data. When compressibility data is not available, the lift coefficient can be modified through application of an appropriate compressibility correction

$$C_L(\alpha, Re, M) = L_\beta[C_L(\alpha, Re), M] \,, \tag{2.36}$$

normally taken to be the Prandtl-Glauert correction

$$L_\beta[C_L, M] = \frac{C_L}{\sqrt{1 - M^2}} \,. \tag{2.37}$$

The resulting lift coefficient can then be used to pre-condition the collocation point boundary condition, before calculating the bound vorticity as described previously. Aerofoil look-up tables, or curve fits through experimental data, are again used to evaluate sectional drag and pitching-moment coefficients.

This approach does however rely upon the use of two-dimensional aerofoil data, and is therefore incapable of capturing certain three-dimensional flow features, such as the effect of blade rotation on the boundary layer profile and the associated stall-delay. A number of empirical stall models have been developed to account for these three-dimensional effects (primarily for the analysis of wind-turbine blades), such as the models of Corrigan [31], Du and Selig [32],[33], and Corten [34]. Although not implemented within this work, introduction of such a model may be beneficial, particularly for the analysis of highly loaded or highly twisted rotors.

The blade aerodynamic model must also be capable of capturing dynamic stall, a separated flow regime associated with the shedding of a vortex from the leading edge of an aerofoil under conditions of high incidence and rapid pitch rate. The presence of the vortex above the aerofoil's upper surface postpones the stall of the aerofoil, leading to lift coefficients in excess of the maximum lift coefficient experienced under static conditions. Dynamic stall also introduces significant pitching-moment variations which can be

a significant driver of vibration in the rotor system. The dynamic stall model used by the VTM is based on the model of Beddoes [35], [36] and [37], in which a first-order time delay postpones the loss of lift above the stall angle-of-attack. In spite of the model's simplicity, it is capable of capturing the primary loading features induced by dynamic stall.

2.7 Proposed Model Improvements

As highlighted at various points throughout this chapter, the original VTM suffers from a number of deficiencies which may limit the model's ability to tackle the particularly challenging problem of vibration prediction.

As discussed in Chapter 1, successful prediction of vibration is likely to require a significant increase in grid resolution such that the fine-scale flow features, such as vortex cores and BVI, can be captured. The current grid system, employing a fixed, uniform resolution grid does not present the most efficient means with which to obtain such resolutions. This certainly motivates the development of a more efficient grid system which will facilitate such increases in grid resolution.

It is also crucial that the wake system is free to evolve naturally under the wake's own self-induced velocity field. As discussed in section 2.4.5, it is possible for the solution to become contaminated as a result of poorly posed boundary conditions. Although it may be possible to derive more representative boundary conditions, this approach would not eliminate the problem entirely since it is, by definition, impossible to reconstruct the velocity field induced by vorticity located outside of the solution domain. A more effective and justifiable strategy would be to develop an approach in which the entire vorticity field of the flow is retained within the solution domain, removing the need to provide far-field boundary conditions.

2.7.1 Semi-Lagrangian Adaptive Grid

A new grid system, the Semi-Lagrangian Adaptive Grid, has been developed to address the deficiencies of the grid system employed in the original VTM. The system exploits a useful feature of the vorticity transport approach, which requires that only those regions of the flow which contain vorticity need to be represented explicitly within the solution

domain. A process of adaptive cell generation and destruction is used to create cells around these vorticity-containing regions, and to track them as the flow evolves. This approach minimises the number of cells required to enclose the vorticity present in the flow, leading to a reduction in cell count by roughly one order of magnitude compared to the original grid system. The new grid system also permits the use of nested grids of varying resolution to focus computational effort into particular areas of the flow, i.e. near to the rotor. The adaptive cell generation and nested grid features of the new system together present the flexibility to generate unbounded solution domains, thus removing the requirement for far-field boundary conditions. A full description of the new grid system is presented in Chapter 3.

2.7.2 Cartesian Fast Multipole Method

A drawback of the adaptive, unbounded nature of the new grid system lies in the added complexity introduced when evaluating the velocity field using the Method of Cyclic Reduction (described in section 2.4.4). The Method of Cyclic Reduction is at its most efficient when applied to a uniform, structured domain with simple boundaries. Although, it is possible to use the method with the Semi-Lagrangian adaptive grid system, it would require a separate solution domain to be defined and initialised at every timestep, incurring a considerable cost penalty.

As a result, the Method of Cyclic Reduction has been replaced with the Fast Multipole Method (FMM). The FMM can be applied easily to unstructured and unbounded grids, and has been demonstrated to yield large improvements in efficiency over the Method of Cyclic Reduction. For a grid containing N grid cells, the velocity field can be evaluated in $O(N)$ operations using the FMM, compared to $O(N \log N)$ operations for the Method of Cyclic Reduction. A full description of the Fast Multipole Method is presented in Chapter 4.

2.8 Summary

The VTM is a comprehensive rotor code for modelling the dynamics and aerodynamics of a rotor system. The evolution of the rotor wake is modelled via a numerical solution of the vorticity transport equation using a TVD finite-volume scheme. Representation of the flow field in terms of a time-varying vorticity field bypasses the issue of vorticity conservation which is often problematic for primitive variable formulations. The rotor blades are treated as sources of vorticity, and are modelled using a variation of the Weissinger-L method along with look-up tables of aerofoil performance data. The dynamics of the rotor system are captured using a Lagrangian dynamics approach, which provides a particularly flexible framework that can be used to model a variety of rotor configurations.

A number of deficiencies of the original VTM have been identified which are likely to limit the model's ability to simulate accurately the evolution of the rotor wake at the very high resolutions required for vibration prediction. These include the potential contamination of the solution due to inappropriate far-field boundary conditions and the inefficiency of the existing grid system. These limitations will be addressed through the introduction of a new boundary-free grid system and velocity calculation using the Fast Multipole Method.

Chapter 3

Semi-Lagrangian Adaptive Grid

3.1 Introduction

As described in the previous chapter, the existing grid system suffers from a number of deficiencies, namely the excessive cost of the grid system when using very high resolutions, and the potential contamination of the solution as a consequence of the truncation of the wake at the grid boundaries. The grid system described within this chapter has been developed to eliminate these deficiencies and to provide an efficient, flexible and reliable formulation capable of modelling a wide range of rotor flows.

The Semi-Lagrangian Adaptive Grid system, through its boundary-free formulation and use of adaptive cell generation, provides all the necessary structure to eliminate the aforementioned problems. Since the evolution of the flow is modelled using equation (2.5), only regions of the flow that actually contain vorticity need to be contained within the computational domain. The number of computational cells, and hence the the memory required by the calculation, can be minimised by using a grid that contains a variable number of cells that are adaptively generated and destroyed to allow the vorticity-containing regions of the flow to be tracked as the solution evolves through time.

3.2 Boundary-Free Formulation

The method employs a virtual Cartesian stencil or framework, upon which cells can be created and destroyed. Each location on the stencil is a cube, with edge-length Δ_0, that can be occupied by a single computational cell. The stencil is fixed in the frame of reference of the rotor hub and extends to infinity in all directions to encapsulate the entire space surrounding the rotor. The stencil thus provides an infinite number of discrete locations that can be occupied by cells at any given time. Crucially, since the stencil is entirely boundary-free, the grid can enclose all of the vorticity present in the flow throughout the entirety of the simulation. The rotor wake can therefore grow in size arbitrarily, without the vorticity field being truncated by grid boundaries, thereby eliminating the need for any far-field boundary conditions on the vorticity field.

The vorticity generated by a vorticity source, S, (assumed here to be the rotor blades), is captured within the grid by creating cells at the appropriate locations on the stencil. To allow the vorticity to advect through the grid during the next timestep, the immediate neighbours of any newly created cells must also be created, as shown in figure 3.1.

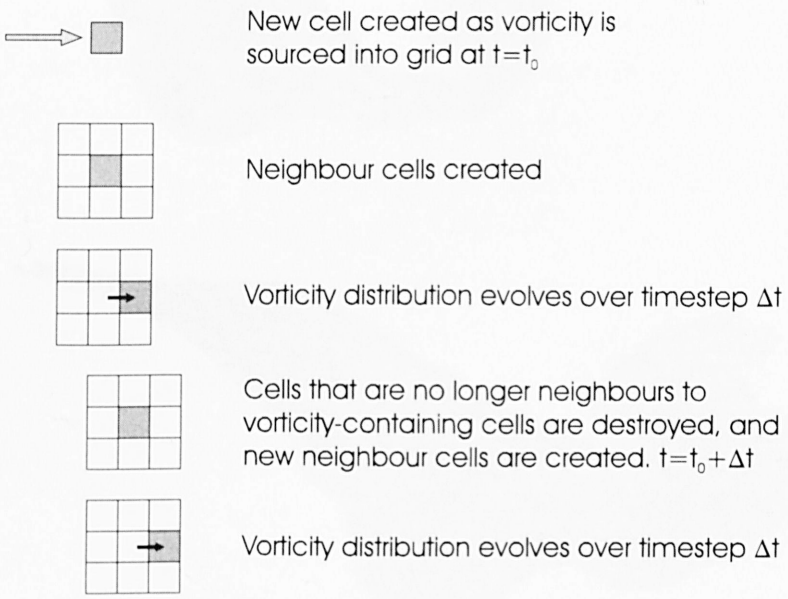


Figure 3.1: *Adaptive grid generation and destruction tracks regions of vorticity within the flow.*

Assuming that the velocity is known at every cell interface, this grid structure is sufficient to allow the VTM to evolve the flow according to equation (2.5). At successive timesteps, additional neighbour cells are generated around all vorticity-containing cells to allow the new vorticity distribution to evolve. Simultaneously, any cells that no longer contain vorticity are destroyed. This process of cell generation and destruction is repeated at every timestep to allow the flow to evolve freely. It can be seen that, at any point during the simulation, the solution domain, Ω, is simply defined as the support of the vorticity field, i.e. those regions of the flow where the vorticity field is non-zero. Regions of the flow which do not contain vorticity are ignored by the calculation, thereby reducing the required number of cells to a minimum. The Lagrangian nature of the method is now obvious since the resulting grid effectively tracks the vorticity distribution as it evolves through time.

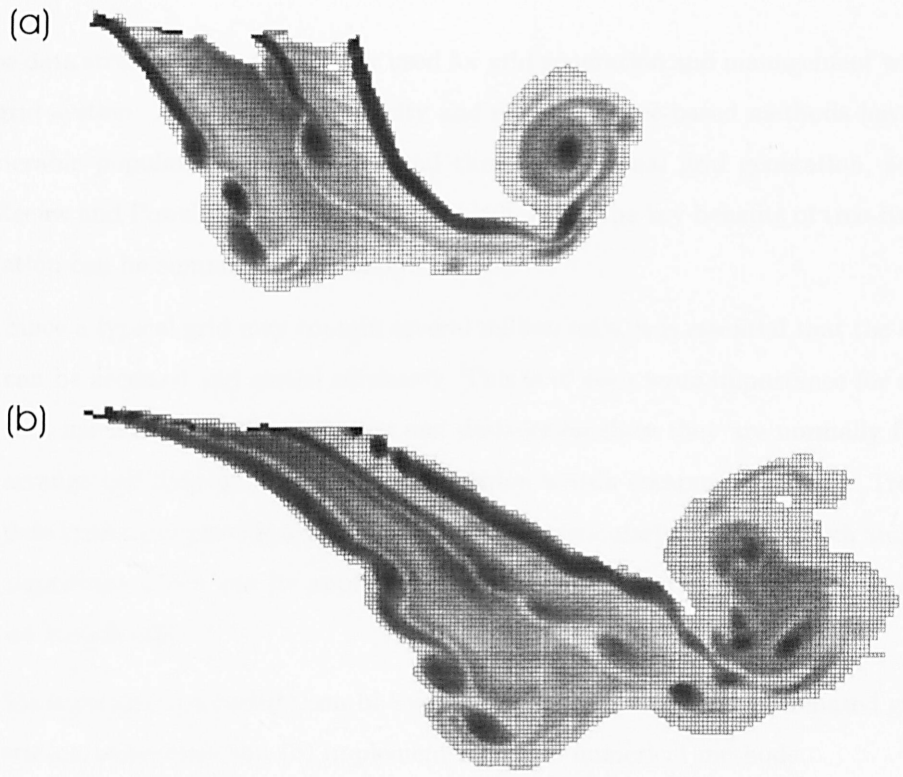


Figure 3.2: *Adaptation of the grid structure as the rotor wake evolves.*

Figure 3.2 shows the grid and wake structures, viewed on a vertical slice through the rotor hub at two points during a simulation of a four-bladed rotor in accelerating forward flight; the wake is visualised using contours of vorticity magnitude. The top image shows the wake and grid structures shortly after the startup of the rotor; the starting vortex of the rotor can be clearly seen to the right of the figure. The advance ratio or the rotor at this point is $\mu = 0.04$. The lower image shows the grid structure at a later time, by which point the forward speed of the rotor has increased to $\mu = 0.07$. These snapshots of the grid structure illustrate clearly how the grid structure has adapted to track the underlying vorticity distribution. It should be noted that the method can not be described as fully Lagrangian though since the computational cells are fixed in an Eulerian frame of reference, and are not themselves transported by the flow.

3.3 Octree Data Structure

Octree data structures are extensively used for grid generation and management within the new grid system. Due to their simplicity and efficiency, tree-based methods have gained considerable popularity for both two and three dimensional grid generation, see Wang [38], Zeeuw and Powell [39], and Berger *et al* [40], [41]. The key benefits of tree-based grid generation can be summarised as follows:

- Since a typical grid may contain several million cells, it is essential that the cell data can be accessed and sorted efficiently. This is of even more importance for methods that use adaptive cell generation and destruction since they are normally forced to arrange cell data in an unstructured fashion within computer memory. Tree-based data structures provide access to a number of particularly efficient search and sorting algorithms which can be applied easily to both structured and unstructured data, see Knuth [42].

- Their recursive structure can be exploited to (a) develop fully automated grid generation techniques and (b) implement recursive numerical methods.

- When applied to simple geometries, such as regular Cartesian grids, tree-based data structures provide a straightforward means by which to introduce grid adaptation and refinement.

In the case of the VTM, the octree system also provides the essential infrastructure required to evaluate the velocity field via the Fast Multipole Method. Significant improvements in efficiency and performance can therefore be achieved by exploiting the same octree data structure within both the grid system and the velocity calculation.

Generation of the octree data structure takes place as follows. At the lowest level of the octree lie the cells themselves. The next level of the octree is formed by collecting together the cells in eight neighbouring cell locations to form a parent cluster, as shown in figure 3.3. This process of clustering is repeated on each level of the octree until a level is reached on which there exists one single cluster which contains the entire computational domain.

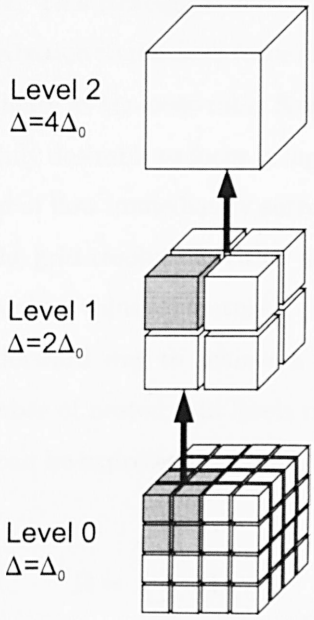


Figure 3.3: *Cell locations organised into an octree data structure.*

The octree is stored as a linked list of data structures. Each element in the octree contains links, or pointers, to its parent, up to six immediate neighbours and up to eight children. However, due to the adaptive nature of the grid, not all of an element's neighbours or children will always exist. Since the tree has a finite depth, at the lowest level of the tree, the elements are the actual cells and will not have any children. Similarly, the element at the root of the tree will not have a parent.

3.4 Nested Grids

As a consequence of utilising a boundary-free formulation, it is feasible that the growth of the grid structure will eventually exhaust the available computer memory, prohibiting the grid from growing any larger in size. From this point onwards, the grid has boundaries upon which boundary conditions must be applied for the simulation to proceed. Since the new grid formulation does not support the application of far-field boundary conditions, the simulation is forced to terminate prematurely.

The growth rate of the grid in terms of cell count can, however, be constrained by adapting the resolution of the grid. The vorticity close to rotor may be resolved on a high resolution grid, whilst the resolution can then be reduced systematically on moving away from the rotor into the far-wake. This strategy is certainly justified since the vorticity in the far-field has a minimal contribution to the near-rotor flows, and does not therefore need to be resolved with the same fidelity as the near-rotor flow. Indeed, from a computational efficiency standpoint, it is certainly desirable to focus computational effort on to the area of most interest, namely the region of flow immediately surrounding the rotor. Furthermore, the ability to enhance locally the grid resolution, either to expose fine-scale flow features or to improve accuracy, is certainly a valuable feature.

Arguably the most straightforward way to achieve a variable resolution capability is to partition the grid into a number of nested grid levels of varying resolution. Using this approach, the solution domain can be expressed as the union of a number of sub-domains,

$$\Omega = \bigcup_{i=0}^{N_g-1} \Omega_i \,, \tag{3.1}$$

where N_g is the number of nested grid levels, and the subset Ω_i contains all the vorticity located on grid level i.

The octree data structure presents a particularly convenient means with which to nest grids of varying resolution. First, the rotor is positioned within the lowest grid level, Ω_0, in which the vorticity-containing cells have side-length Δ_0 - equal to that of the underlying stencil. At some distance from the rotor, the resolution of the grid can be reduced by simply reducing the depth of the octree so that the vorticity-containing cells now lie on level 1 of the grid, Ω_1, and have side-length $2\Delta_0$. This process can then be repeated to

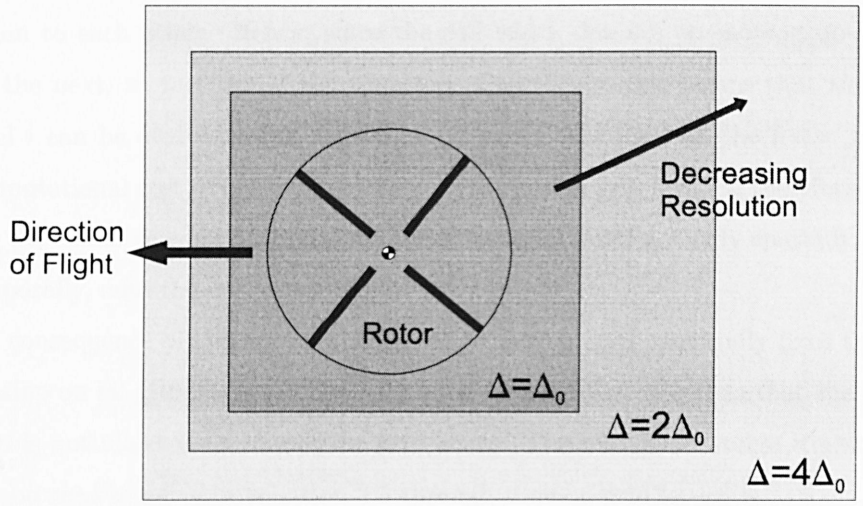


Figure 3.4: *The rotor is embedded within a nested grid structure that decreases in resolution with distance from the hub.*

generate any number of grid levels. A schematic representation of a computational domain with such a nested grid structure is shown in figure 3.4.

Since the cell width doubles on moving up a level of the tree, the width of a cell on grid level i is $2^i\Delta_0$. This exponential growth rate in cell size allows the growth rate of the grid, in terms of cell count, to be constrained to manageable levels. The rate at which computational storage is consumed by the simulation is therefore retarded and the wake structure is free to evolve over the course of a simulation (of finite duration) without ever encountering grid boundaries.

3.4.1 Courant-Friedrichs-Lewy Condition

A powerful feature of the nested grid approach relates to the maximum stable rate at which the computation can be advanced on each grid level. For the explicit WAF scheme, the stability requirement, expressed in terms of the timestep, cell size and local flow velocity, is set by the Courant-Friedrichs-Lewy (CFL) condition

$$\left|\frac{u\Delta t}{\Delta x}\right| \leq 1 \,. \tag{3.2}$$

The CFL condition essentially states that the timestep and cell width should vary in proportion to each other. Hence, since the cell width doubles on moving up from one level to the next, so too should the timestep. Practically, this means that the flow on grid level i can be evolved using a timestep 2^i times that used on the finest grid level. The computational cost of evolving the flow on the coarse grid levels is therefore reduced, allowing the available computational resources to be focussed not only spatially, but now also temporally, onto the near-rotor flow.

As a consequence of the above strategy, the timestep Δt_0 essentially fixes the size of the timestep on all grid levels. Hence, Δt_0 must be carefully chosen so that the CFL condition is not violated on any of the grid levels. The maximum stable timestep, $\Delta t_i^\star$, that can be used to advance equation 2.5 through time on grid level i is

$$\Delta t_i^\star = \frac{\Delta x}{\|u\|_i} , \tag{3.3}$$

where

$$\|u\|_i = \max_{\Omega_i} |u| . \tag{3.4}$$

Since the cell width doubles on moving up a level of the tree, equation 3.3 can be expressed as

$$\Delta t_i^\star = \frac{2^i \Delta_0}{\|u\|_i} . \tag{3.5}$$

Furthermore, since $\Delta t_i^\star = 2^i \Delta t_0^\star$, the maximum value of $\Delta t_0^\star$ is effectively dictated by the minimum value of $\Delta t_i^\star$ given by equation 3.5. $\Delta t_0^\star$ can therefore be expressed as

$$\Delta t_0^\star = \min_{i \in N_g} \frac{\Delta_0}{\|u\|_i} = \frac{\Delta_0}{\|u\|} , \tag{3.6}$$

where $\|u\|$ is the maximum absolute velocity in the entire solution domain. Equation 3.6 provides a rigorous upper limit on the timestep Δt_0 that can be used to evolve the solution through time.

3.4.2 Grid Level Boundaries

Due to the different spatial and temporal resolutions used on the various nested grid levels, great care must be taken to preserve the accuracy of the solution near to the interfaces separating neighboring grid levels. In particular, it is essential that advection of vorticity across a grid interface conserves not only vorticity, but also the second order accuracy and TVD properties of the WAF scheme.

Berger and Leveque [43] developed a strategy for achieving conservation and second order accuracy at grid interfaces. The method described below extends their approach to preserve also the local TVD properties of the solution.

First, a small overlap region is introduced between two adjacent grid levels at the grid interface. The structure of the overlap for a one-dimensional grid is illustrated in figure 3.5.

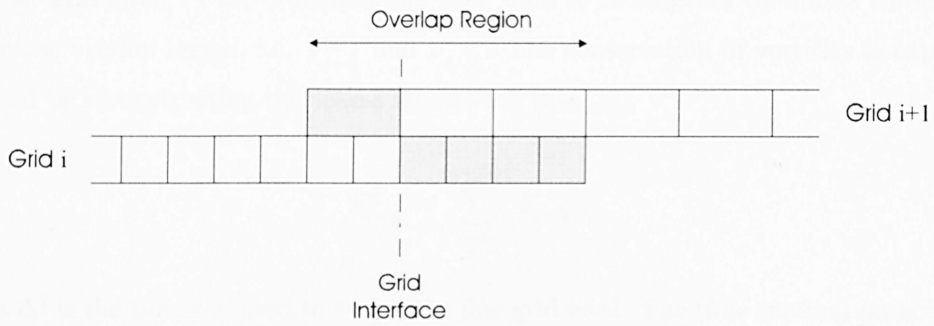


Figure 3.5: *Overlapping of adjacent grid levels for a one-dimensional grid; shaded cells represent ghost cells.*

Extending the same approach to the full three-dimensional case leads to the grid structure as shown in figure 3.6. These overlapping cells, or *ghost* cells, provide all the necessary cell structure to maintain the required solution properties.

Figure 3.7(a) shows the underlying cell structure at the grid interface whilst figures 3.7(b) and (c) show the representation of the same interface as seen by the coarse and fine grid levels respectively.

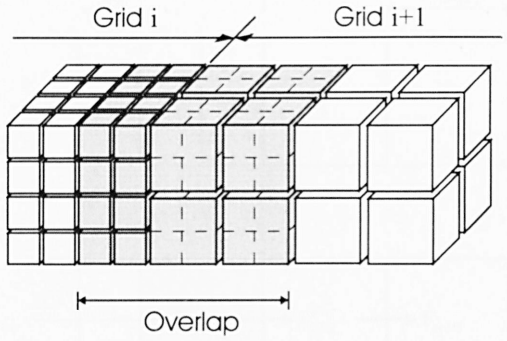


Figure 3.6: *Overlapping of the grid level boundaries provides both second order accuracy and monotonicity; shaded cells represent ghost cells.*

From a known vorticity distribution at time t_0, the ghost cells are initialised by making a copy of the vorticity field from the underlying grid cells. Next, all intercell fluxes on the finer grid level, $\hat{F}$, are evaluated and then used to reconstruct the fluxes throughout the coarse overlap region, i.e. $F^*_{i-\frac{1}{2}}$ and $F^*_{i-\frac{3}{2}}$. The conservation of vorticity is explicitly enforced by reconstructing the coarse fluxes such that

$$F^*_{i-\frac{1}{2}} = \sum_{t=t_0}^{t_0+2\Delta\hat{t}} \hat{F}_{i-\frac{1}{2}} \,, \tag{3.7}$$

where $\Delta\hat{t}$ is the timestep used to evolve the fine grid level. The time summation accounts for the fact that the fine grid level is evolved at twice the rate of the coarse level. Equation 3.7 effectively states that the fluxes of vorticity across the grid interface, as observed on both the coarse and fine grid levels, are identical.

Finally, the vorticity contained in the coarse cells either side of the interface at the next timestep can be evaluated by replacing the intercell flux in equation 2.11 with the appropriate reconstructed flux F^*. Taking for example the coarse cell i in figure 3.7(b), the left-flux $F_{i-\frac{1}{2}}$ is replaced with the reconstructed flux $F^*_{i-\frac{1}{2}}$ to yield

$$[\omega_i]^{n+1} = [\omega_i]^n - \frac{\Delta t}{\Delta x}(F_{i+\frac{1}{2}} - F^*_{i-\frac{1}{2}}) \,. \tag{3.8}$$

As discussed in section 2.4.3, the wave amplification functions used to make the solution TVD require data from the two cells either side of a cell interface. Since all the fluxes

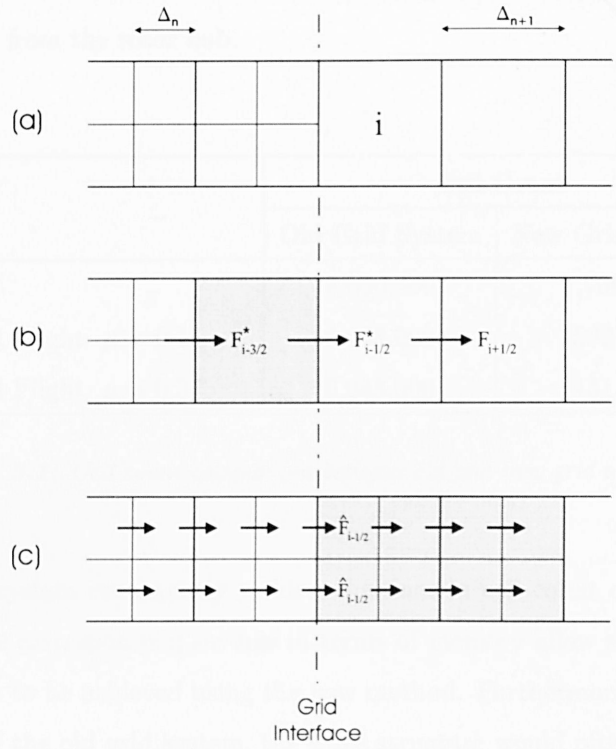


Figure 3.7: *Strategy for preserving vorticity conservation, second order accuracy and the TVD properties of the solution at grid interfaces. Shaded cells denote ghost cells.*

throughout the overlap region are evaluated upon the higher resolution grid level, it can be seen that the structure of the overlap region provides all the necessary data for the calculation of the wave amplification factors. Hence, the TVD properties, and also the second order accuracy, of the WAF scheme are preserved throughout the overlap region.

3.5 Grid Performance

A comparison of the new and old grid system, in terms of cell counts, for a number of representative rotor calculations is presented in table 3.1. The data presented for the new grid system is based upon a grid of resolution on the finest grid level of $\Delta x = 0.02R$, and four levels of grid refinement; the grid level boundaries are located at distances of $2R$, $4R$, and $6R$ from the rotor hub. The data presented for the original grid system is

based upon a grid resolution of $\Delta x = 0.02R$ with the grid boundary located a distance of approximately $3R$ from the rotor hub.

Case	Cell Count	
	Old Grid System	New Grid System
Hover	8,000,000	1,700,000
Forward Flight $\mu = 0.15$	6,048,000	592,700
Forward Flight $\mu = 0.37$	6,048,000	431,200

Table 3.1: *Cell count comparison between old and new grid systems.*

The new grid system consistently yields reductions in cell count of roughly an order of magnitude. The corresponding savings in terms of memory allow sizeable increases in the grid resolution to be achieved using the new method. Furthermore, as a result of the bounded nature of the old grid system, the wake structure would often be truncated. In contrast, by retaining all the vorticity in the flow, the rotor wake need never be truncated, leading to a more accurate description of the flow.

Figure 3.8 shows an example rotor wake generated by a four-bladed rotor at an advance ratio of $\mu = 0.12$. The grid consists of three nested levels, with transitions between levels located at $2.3R$ and $4R$. The resolution used on the finest grid level is $\Delta x = 0.016R$. The use of nested grid levels to progressively step down the resolution on moving away from the rotor into the far-wake can clearly be seen. Furthermore, by tracking the the entire vorticity distribution over the course of the simulation, the grid has been able to retain the entire wake history of the rotor, all the way back to the starting vortex produced by the impulsive start-up of the rotor at the beginning of the simulation.

Table 3.2 illustrates how the vast majority of cells are contained within the finest grid level, indicating the success of the grid nesting strategy at focussing the computational effort into modelling the most important region of the flow.

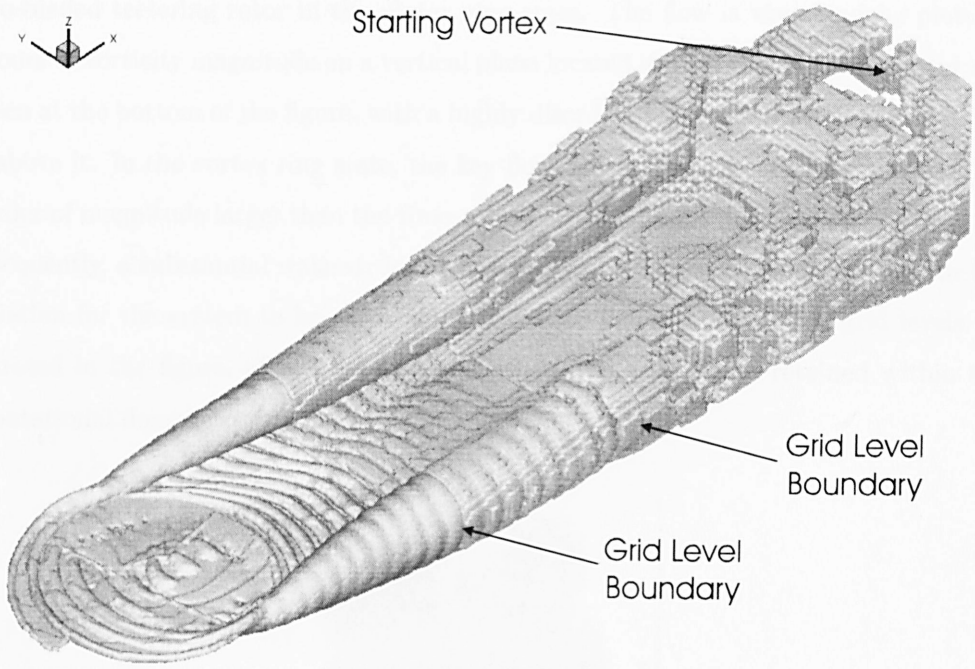


Figure 3.8: *Use of nested grid levels to reduce progressively the resolution into the far wake;* $\mu = 0.12, \Delta x_0 = 0.016R$

Grid Level	Cell Count	Cell Count as Percentage of Total
1	767,000	77.4%
2	150,000	15.2%
3	71,000	7.2%
4	2,000	0.2%
TOTAL	990,000	100.0%

Table 3.2: *Distribution of cells throughout grid levels.*

As a second example, figure 3.9 shows the calculated wake geometry generated by a two-bladed teetering rotor in the vortex ring state. The flow is visualised by plotting contours of vorticity magnitude on a vertical plane located at the rotor hub. The rotor can be seen at the bottom of the figure, with a highly disordered and unsteady wake streaming out above it. In the vortex ring state, the key flow features evolve on timescales roughly an order of magnitude larger than the timescales associated with the rotation of the rotor. Consequently, a substantial wake structure is formed which must be contained within the simulation for the system to be modelled accurately. The use of multiple grid levels, as illustrated in the figure, allows the entire length of the wake to be retained within the computational domain.

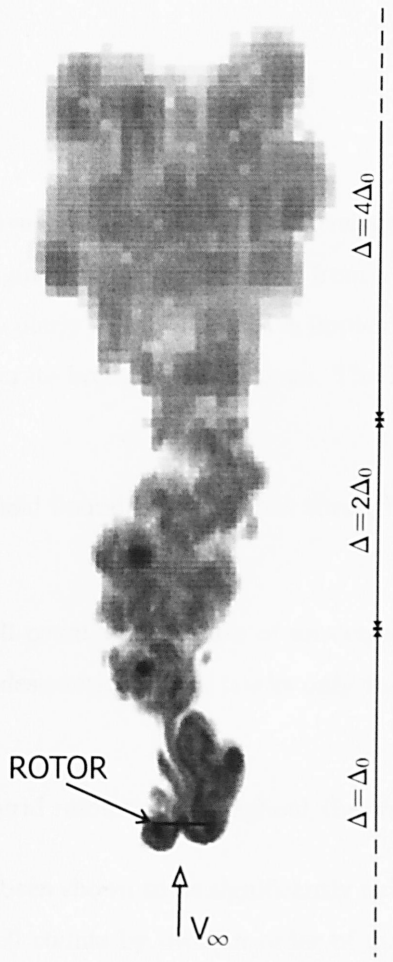


Figure 3.9: *Visualisation of the wake of a two-bladed teetering rotor in vortex ring conditions.*

In the example shown, a total of four nested grid levels are employed; the cell size on the finest grid level is $\Delta x = 0.10R$. The wake shown in the figure has a length of over 25 rotor radii but is captured using just 156,000 cells. 64% of the cells used by the simulation are contained within the finest grid level surrounding the rotor, showing how the method is able to concentrate computer resources into the the area of most interest.

Finally, due to the efficiency of the octree data structure, the computational cost of implementing an adaptive grid generation approach is minimal. The runtime required to implement the grid adaptation is typically less than 5% of the total runtime. These results highlight the point that the entire wake history can realistically be retained within the grid, through use of the boundary free formulation, at minimal extra cost compared to a bounded-grid approach.

3.6 Summary

The Semi-Lagrangian Adaptive Grid system has been developed to replace the grid system of the original VTM. The original grid system suffered from a number of limiting deficiencies, stemming from its particularly memory intensive implementation and the difficulties associated with deriving accurate boundary conditions. The key features of the new grid system include:

- the elimination of far-field boundary conditions through use of a boundary-free solution domain;
- the minimisation of cell count through use of an octree-based, adaptive approach to cell generation and destruction which tracks only those regions of the flow that contain vorticity;
- the ability to vary the grid resolution throughout the wake by using nested grids.

The new grid system has been shown to be significantly more efficient that the original system, typically reducing cell counts by over an order of magnitude, thus allowing the available computational resources to be used more effectively than in the original version of the VTM.

Chapter 4

Cartesian Fast Multipole Method

4.1 Introduction

Multipole methods are a family of approximate methods for evaluating potential fields. Systems that are governed by potential fields can generally be described in terms of a number of particles, each of which generates a force, or potential, at every other particle in the system. Simple examples of such systems include a collection of charged particles and their associated electrostatic potential field, or a collection of massive bodies and their induced gravitational field. For a system containing N particles, a total of N^2 particle-particle interactions therefore exist. The problem of evaluating the potential at each of the particles in the system is known as the N-body problem. Direct summation of all particle-particle interactions throughout the system leads to a computational algorithm with $\mathcal{O}(N^2)$ cost.

Multipole methods all employ some form of hierarchical decomposition of the solution domain to group together particles into clusters. This allows multiple long-range particle-particle interactions to be replaced by a smaller number of particle-cluster or cluster-cluster interactions. These interactions are approximated by describing the interaction in terms of a truncated algebraic series. A comprehensive review of multipole methods can be found in Pringle [44].

Arguably the first multipole method was developed by Appel [45] who used a simple monopole expansion to approximate multiple particle-cluster interactions. The method of Barnes and Hut [46] extended Appel's method by introducing arbitrary order mul-

tipole series expansions to approximate particle-cluster interactions. Methods based on the approximation of particle-cluster interactions are generally known as *Treecodes* due to their use of tree-based data structures for hierarchically decomposing the solution domain. Treecodes typically reduce the cost of the N-body problem to $\mathcal{O}(N \log N)$.

The computational cost can be reduced further however by making use of cluster-cluster interactions, which are once again approximated using a multipole series. The Fast Multipole Method (FMM), developed by Greengard and Rokhlin [47] [48], makes use of both particle-cluster and cluster-cluster interactions to reduce the cost of solving the N-body problem to just $\mathcal{O}(N)$. Although the original FMM of Greengard and Rokhlin was based upon Taylor series expansions of the interactions, a wide range of alternative multipole series can also be used. The choice of multipole series is often related to the most convenient coordinate system for the given problem. Later versions of the FMM replaced the Taylor series with spherical harmonics and their associated Legendre polynomials, [49]. More recently, Hrycak and Rokhlin [50] have demonstrated significant performance improvements using exponential series.

Multipole methods, and the FMM in particular, have gained popularity for modelling a wide range of potential field problems. Dehnen [51] used the FMM to model the evolution of large gravitational systems and also developed a version of the FMM which implicitly preserves the momentum of the system. Warren and Salmon, who also used the FMM to model large-scale gravitational systems for astrophysics [52], have made a number of valuable contributions to the development of multipole methods in general. They were the first to development a parallelised version of the FMM [53] which has been applied to generalised potential field problems, including Smooth Particle Hydrodynamics (SPH) and incompressible fluid dynamics [54]. They also carried out a rigorous error analysis of the Fast Treecode method [55]. Further examples of how the FMM has been applied to SPH problems include the work Hernquist [56], and Monaghan [57]. The FMM has also been used extensively to evaluate electrostatic and electromagnetic fields for (a) modelling molecular dynamics and quantum-mechanical systems for protein modelling [58] and molecular chemistry [59], (b) calculating the stiffness of materials [60], (c) structural modelling of nanostructures [61], and (d) extracting the capacitance and inductance properties of electronic components [62] [63].

Multipole methods were first used for modelling incompressible fluid flow by Anderson [64], who used a treecode-based method to calculate the velocity field induced by a collection of vortex particles. Lindsay and Krasny [65] used a Taylor-series based treecode to investigate the evolution and stability of vortex sheets, whilst Dracgicescu and Dragicescu developed a treecode for use within vortex filament methods [66]. More recently, Marshall et al used a treecode method within a grid-based CFD model to model the flow past a sphere at low Reynolds numbers [67].

This chapter presents an $\mathcal{O}(N)$ Cartesian Fast Multipole Method that has been integrated into the new version of the VTM for evaluating the velocity field throughout the grid system. The formulation presented here differs somewhat from standard FMM implementations; in that, instead of describing the system as a collection of discrete particles, a continuous grid-based description of the vorticity field is used. The octree-based nature of the adaptive grid system used in the new version of the VTM allows several pre-existing data structures to be shared by both the grid management and FMM algorithm, leading to more efficient use of computational resources. Finally, to reflect the inherent Cartesian structure of the computational grid used by the VTM, a Taylor-series formulation of the FMM has been developed.

4.2 Theory

The Cauchy-Stokes decomposition theorem [68] allows the velocity field of a flow to be split into an irrotational component and a rotational, or solenoidal, component. In the context of rotor simulations, the irrotational component is simply the free-stream velocity field, which is known at any point during the simulation. The rotational component is coupled to the vorticity field by the Biot-Savart relationship, stated previously in its differential form in equation 2.4, and its integral form in equation 2.20. This section presents the theory underlying the Fast Multipole Method, which is used within the new version of the VTM to evaluate the rotational velocity field throughout the flow. From this point onwards, the rotational velocity field will be referred to as simply the velocity field.

Defining the solution domain $\Omega \subset \mathbb{R}^3$ as the support of the vorticity field of the flow, at any point $\mathbf{x} \in \mathbb{R}^3$ the velocity $\mathbf{u}(\mathbf{x})$ induced by the vorticity contained in Ω can be evaluated as

$$\mathbf{u}(\mathbf{x}) = \int_{\Omega} \mathbf{K}(\mathbf{x}, \mathbf{y}) \times \omega(\mathbf{y}) \, \mathbf{dy} \, , \tag{4.1}$$

where the Biot-Savart kernel is defined as

$$\mathbf{K}(\mathbf{x}, \mathbf{y}) = -\frac{\mathbf{1}}{4\pi} \frac{(\mathbf{x} - \mathbf{y})}{|\mathbf{x} - \mathbf{y}|^{\mathbf{3}}} \, . \tag{4.2}$$

Within the VTM, the solution domain is populated throughout with N_Ω computational cells, V_i, such that

$$\Omega = \bigcup_{i=1}^{N_\Omega} V_i \, . \tag{4.3}$$

The integration in equation 4.1 can, therefore, be split into N_Ω integrations over the volume of each computational cell:

$$\mathbf{u}(\mathbf{x}) = \sum_{i=1}^{N_\Omega} \int_{V_i} \mathbf{K}(\mathbf{x}, \mathbf{y}) \times \omega(\mathbf{y}) \, \mathbf{dy} \, . \tag{4.4}$$

There is no straight-forward method with which to evaluate the velocity field induced by an isolated cell of vorticity. Although a series solution exists, it is far too expensive to implement numerically *. The integral in equation 4.4 can however be approximated using

$$\int_{V_i} \mathbf{K}(\mathbf{x}, \mathbf{y}) \times \omega(\mathbf{y}) \, d\mathbf{y} \approx \mathbf{K}^*(\mathbf{x}, \mathbf{y_c}) \times [\omega_i] \, , \tag{4.5}$$

where K^* is a regularised Biot-Savart kernel, y_c is the geometric centre of the cell volume, and $[\omega_i]$ is the total vorticity contained within cell i. The derivation of the regularised kernel is discussed in the following subsection.

*An analytic solution can be derived using the theory derived in section 4.2.3. A cell containing a uniform distribution of vorticity can be represented as a cluster containing an infinite number of infinitesimal cells, each containing equal vorticity. This description allows the velocity field induced by the cell to be written as the limit of a multipole series. This approach is not pursued any further here.

Equation 4.4 can therefore be approximated by

$$\mathbf{u}(\mathbf{x}) \approx \sum_{i=1}^{N_\Omega} \mathbf{K}^*(\mathbf{x}, \mathbf{y_c}) \times [\omega_i] \,, \tag{4.6}$$

which forms the starting point for the derivation of the Fast Multipole Method.

4.2.1 The Rosenhead-Moore Kernel

Regularised kernels were first used in vortex methods to remove the singularities in the velocity field which come about as result of the discontinuities in the curvature of the vorticity field, see Vanden-Broeck [69] and Krasny et al [70]. Representing the flow in terms of infinitesimal particles of vorticity (vortex singularities) generally leads to unstable numerical methods. By regularising the Biot-Savart kernel, the description of the flow in terms of vortex singularities is effectively transformed to one in which the vorticity of a particle is distributed over a small, but non-zero, region of space, thereby removing the singularities in the induced velocity field. A vast number of possibilities exist for defining the distribution of vorticity throughout the 'smoothed' particle, or blob. A review of some of the more popular formulations are discussed by Cottet and Koumoutsakos [71] and Chorin [68].

The regularised kernel developed by Rosenhead [72] and Moore [73] is used in the new version of the VTM to approximate the velocity field induced by a cell containing a uniform distribution of vorticity. Krasny used the Rosenhead-Moore kernel extensively in his study of vortex sheet dynamics and stability, see [74] and [75]. The Rosenhead-Moore kernel,

$$K_\delta(\mathbf{x}, \mathbf{y}) = -\frac{1}{4\pi} \frac{(\mathbf{x} - \mathbf{y})}{(|\mathbf{x} - \mathbf{y}|^2 + \delta^2)^{3/2}} \,, \tag{4.7}$$

makes use of an artificial smoothing parameter δ, which upon setting $\delta = 0$ restores the singular Biot-Savart kernel in equation 4.2. A comparison of the velocity fields generated by the singular Biot-Savart kernel and the regularised kernel of Rosenhead and Moore is shown in figure 4.1.

The smoothing parameter δ effectively sets the size of the vortex blob. The stationary points in the velocity field induced by an isolated vortex blob located at $x = 0$, evaluated

using the Rosenhead-Moore kernel are located at

$$\pm x_{sp} = \sqrt{\frac{\delta^2}{2}} \,, \tag{4.8}$$

where x_{sp} is the distance from centre of the blob. Hence, the location of the stationary points can be controlled through the choice of δ.

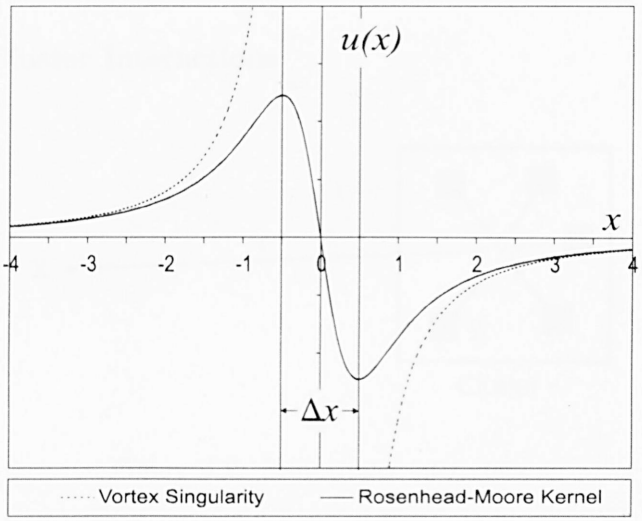


Figure 4.1: *Comparison of the Biot-Savart and Rosenhead-Moore kernels.*

By aligning the geometric centre of the cell with that of the blob, and positioning the stationary points to lie on the cell boundary, i.e. $x_{sp} = \Delta x/2$, the Rosenhead-Moore kernel can be used to approximate the velocity field induced by a cubic vorticity-containing cell. The required value of the smoothing parameter therefore becomes

$$\delta^2 = \frac{1}{2} \, (\Delta x)^2 \,. \tag{4.9}$$

It should be noted that the Rosenhead-Moore kernel is non-harmonic [†], which prevents the use of the Rosenhead-Moore kernel within the traditional multipole methods based upon the use of spherical harmonics.

[†]A harmonic function is defined as any real function with continuous second partial derivatives which satisfies Laplace's equation, $\nabla^2 u = 0$.

4.2.2 Point-Particle Interactions

A point-particle interaction is defined simply as the velocity induced at a point $\mathbf{x}$ by a vorticity containing cell, i, and is given by

$$\mathbf{u}_i(\mathbf{x}) = \mathbf{K}_\delta(\mathbf{x}, \mathbf{y}_i) \times [\omega_i] \,, \tag{4.10}$$

where $\mathbf{y}_i$ is the centre of cell i.

4.2.3 Point-Cluster Interactions

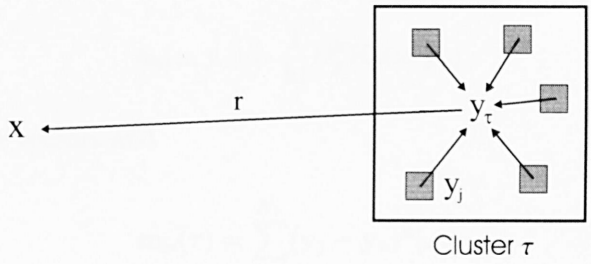


Figure 4.2: *Point-cluster interaction.*

A cluster is defined as a vorticity-containing region of the flow, $\tau \subseteq \Omega$, consisting of N_τ cells. The cell centres are located at $y_i, i \in [1, \ldots, N_\tau]$, and the vorticity-weighted centre of the cluster lies at y_τ. Using the Rosenhead-Moore kernel as the regularised Biot-Savart kernel, the velocity $\mathbf{u}_\tau$ induced by the vorticity contained in τ at a point $\mathbf{x}$ outside of τ can be approximated as

$$\mathbf{u}_\tau(\mathbf{x}) \approx \sum_{j=1}^{N_\tau} \mathbf{K}_\delta(\mathbf{x}, \mathbf{y}_j) \times [\omega_j] \,. \tag{4.11}$$

Expanding the right hand side of equation 4.11 in a Taylor series about the cluster centre leads to

$$\begin{aligned}
\sum_{j=1}^{N_\tau} \mathbf{K}_\delta(\mathbf{x}, \mathbf{y}_j) \times [\omega_j] &= \sum_{j=1}^{N_\tau} \mathbf{K}_\delta(\mathbf{x}, \mathbf{y}_\tau + (\mathbf{y}_i - \mathbf{y}_\tau)) \times [\omega_j] \\
&= \sum_{j=1}^{N_\tau} \sum_{k=0}^{\infty} \frac{1}{\mathrm{k!}} D_{\mathbf{y}}^{\mathrm{k}} \mathbf{K}_\delta(\mathbf{x}, \mathbf{y}_\tau)(\mathbf{y}_j - \mathbf{y}_\tau)^k \times [\omega_j] \\
&= \sum_{k=0}^{\infty} \frac{1}{\mathrm{k!}} D_{\mathbf{y}}^{\mathrm{k}} \mathbf{K}_\delta(\mathbf{x}, \mathbf{y}_\tau) \times \sum_{j=1}^{N_\tau} (\mathbf{y}_j - \mathbf{y}_\tau)^k [\omega_j] \,,
\end{aligned} \tag{4.12}$$

where $\mathbf{k}$ is the order of the Taylor series expansion. Note that the Taylor series expansion used in equation 4.12 is a three dimensional expansion. The index of each term of the Taylor series is therefore a vector, $\mathbf{k} = (k_1, k_2, k_3)$. Hence $D_{\mathbf{y}}^{\mathbf{k}} = \partial/\partial y_1^{k_1} \partial y_2^{k_2} \partial y_3^{k_3}$, $\mathbf{k}! = k_1!k_2!k_3!$ and $\mathbf{x}^{\mathbf{k}} = x_1^{k_1} x_2^{k_2} x_3^{k_3}$ where $k_i \geq 0$ and the subscripts 1, 2 and 3 refer to the Cartesian directions.

Truncation of the Taylor series in equation 4.12 after the $\mathbf{p}$'th term leads to

$$\mathbf{u}_\tau(\mathbf{x}) \approx \sum_{k=0}^{p} \mathbf{a}_{\mathbf{k}}(\mathbf{x}, \mathbf{y}_\tau) \times \mathbf{m}_{\mathbf{k}}(\tau) \,, \tag{4.13}$$

where

$$\mathbf{a}_{\mathbf{k}}(\mathbf{x}, \mathbf{y}_\tau) = \frac{1}{\mathbf{k}!} D_{\mathbf{y}}^{\mathbf{k}} \mathbf{K}_\delta(\mathbf{x}, \mathbf{y}_\tau) \tag{4.14}$$

are the Taylor series tensors and

$$\mathbf{m}_{\mathbf{k}}(\tau) = \sum_{j=1}^{N_\tau} (\mathbf{y}_j - \mathbf{y}_\tau)^{\mathbf{k}} [\omega_j] \tag{4.15}$$

are the vorticity moments. Equations 4.12 and 4.13 effectively decouple the point-cluster interaction into two independent components: the tensors and the moments. The tensors are simply the weighted derivatives of the Rosenhead-Moore kernel and are a function of the interaction distance alone. The moments simply describe the internal distribution of vorticity throughout the cluster, and are independent of the interaction distance.

4.2.4 Error Analysis

The error associated with the the truncation of the Taylor series in equation 4.13 after the $\mathbf{p}$'th term is given by the Lagrange Remainder of the Taylor series

$$\varepsilon_{\mathbf{p}} = \left| \sum_{k=p+1}^{\infty} \mathbf{a}_{\mathbf{k}}(\mathbf{x}, \mathbf{y}_\tau) \times \mathbf{m}_{\mathbf{k}}(\tau) \right| . \tag{4.16}$$

Using the mean-value theorem, this can be simplified to

$$\varepsilon_{\mathbf{p}} = \left| \, \mathbf{a}_{\mathbf{k+1}}(\mathbf{x}, \mathbf{y}^*) \times \mathbf{m}_{\mathbf{k+1}}(\tau) \, \right| , \tag{4.17}$$

where $\mathbf{y}^*$ is some pointed located in a circle of radius $d_\tau = \max|\mathbf{y}_j - \mathbf{y}_\tau|$, $j \in [1, \ldots, N_\tau]$, with its centre located at $\mathbf{y}^\tau$. This measure of the error is clearly not convenient since it requires calculation of additional terms in the Taylor series for its evaluation. Instead, a heuristic estimate of the error, based on the analysis of Lindsay and Krasny [65],

$$\varepsilon_{\mathbf{p}} \approx \max\left\{ \frac{(p_i+1)^2 \, d_\tau^{\mathbf{p}} \, |\mathbf{m_0}(\tau)|}{4\pi R^{(p_i+2)}} \, , \; i = 1,2,3 \right\} \tag{4.18}$$

is used, where $R = (|\mathbf{x} - \mathbf{y}_\tau|^2 + \delta^2)^{\frac{1}{2}}$. By specifying a required level of accuracy, $\varepsilon_{\mathbf{p}}$, equation 4.18 can be solved to determine the order at which to truncate the Taylor series for each cluster interaction.

4.2.5 Tensor Calculation

The tensors, $\mathbf{a_k}$, defined in equation 4.14 can be evaluated efficiently using a recursion formula which has been used previously by Lindsay and Krasny [65] and Dragicescu and Dragicescu [66]. The recursion formula is based on the properties of the regularised Newtonian potential,

$$\phi_\delta(\mathbf{x}, \mathbf{y}) = \frac{1}{4\pi} \frac{1}{(|\mathbf{x} - \mathbf{y}|^2 + \delta^2)^{1/2}} \, , \tag{4.19}$$

which can be written as the gradient of the Rosenhead-Moore kernel,

$$\mathbf{K}_\delta(\mathbf{x}, \mathbf{y}) = \nabla_{\mathbf{x}} \phi_\delta(\mathbf{x}, \mathbf{y}) = -\nabla_{\mathbf{y}} \phi_\delta(\mathbf{x}, \mathbf{y}) \, . \tag{4.20}$$

Defining the scaled derivatives of the Newtonian potential as

$$b_{\mathbf{k}}(\mathbf{x}, \mathbf{y}) = \frac{1}{\mathbf{k}!} D_{\mathbf{y}}^{\mathbf{k}} \phi_\delta(\mathbf{x}, \mathbf{y}) \tag{4.21}$$

with $b_0 = \phi_\delta(\mathbf{x}, \mathbf{y})$ and $b_{\mathbf{k}} = 0$ for $k_i < 0$, successive values of $b_{\mathbf{k}}$ are related by

$$\|\mathbf{k}\| R^2 b_{\mathbf{k}} \; - \; (2\|\mathbf{k}\| - 1) \sum_{i=1}^{3} (x_i - y_i) b_{\mathbf{k}-\mathbf{e}_i} \; + \; (\|\mathbf{k}\| - 1) \sum_{i=1}^{3} b_{\mathbf{k}-2\mathbf{e}_i} = 0 \tag{4.22}$$

where $R^2 = |\mathbf{x} - \mathbf{y}|^2 + \delta^2$, $\|\mathbf{k}\| = k_1 + k_2 + k_3$ and $\mathbf{e}_i$ is the i^{th} Cartesian basis vector. This result is derived in full by Krasny [65]. Having calculated all $\mathbf{b_k}$ up to the required order,

the Taylor series tensors $\mathbf{a_k}$ can be reconstructed using

$$\mathbf{a_k}(\mathbf{x}, \mathbf{y}) = -\sum_{i=1}^{3}(k_i + 1)b_{\mathbf{k}+\mathbf{e}_i}\mathbf{e}_i \,. \tag{4.23}$$

4.2.6 Moment Calculation

Consider a cluster, $\tau \subseteq \Omega$, which is partitioned into a number of smaller clusters, or child clusters, α, each of which contains N_α vorticity-containing cells. The total number of cells contained in τ is therefore $N_\tau = \sum_{\alpha\in\tau} N_\alpha$. The moments of cluster τ are

$$\mathbf{m_k}(\tau) = \sum_{j=1}^{N_\tau}(\mathbf{y}_j - \mathbf{y}_\tau)^{\mathbf{k}}[\omega_j] \,, \tag{4.24}$$

where $\mathbf{y}_\tau$ is the centre of τ. Splitting the summation in equation 4.24 into summations over each of τ's child clusters leads to

$$\begin{aligned} \mathbf{m_k}(\tau) &= \sum_{\alpha\in\tau}\sum_{j=1}^{N_\alpha}(\mathbf{y}_j - \mathbf{y}_\tau)^{\mathbf{k}}[\omega_j] \\ &= \sum_{\alpha\in\tau}\sum_{j=1}^{N_\alpha}((\mathbf{y}_j - \mathbf{y}_\alpha) + (\mathbf{y}_\alpha - \mathbf{y}_\tau))^{\mathbf{k}}[\omega_j] \,, \end{aligned} \tag{4.25}$$

which can be written as the binomial sum

$$\mathbf{m_k}(\tau) = \sum_{\alpha\in\tau}\sum_{\mathbf{n}=0}^{\mathbf{k}} \mathrm{C}_{\mathbf{n}}^{\mathbf{k}}(\mathbf{y}_\alpha - \mathbf{y}_\tau)^{\mathbf{k}}\ \mathbf{m_{k-n}}(\alpha) \,, \tag{4.26}$$

where $\mathbf{y}_\alpha$ are the centres of the child cluster, and $\mathrm{C}_{\mathbf{n}}^{\mathbf{k}} = \mathrm{C}_{n_1}^{k_1}\mathrm{C}_{n_2}^{k_2}\mathrm{C}_{n_3}^{k_3}$. Hence, the moments of a cluster can be written explicitly as a binomial sum of the moments of its children. When evaluating the moments of large clusters, equation 4.26 leads to a significant reduction in the computational cost compared to the direct method given by equation 4.24.

4.2.7 Cluster-Cluster Interactions

In section 4.2.3, the point-cluster interaction was defined in which the velocity induced at $\mathbf{x}_0$ by a cluster of vorticity-containing cells was approximated using a truncated Taylor series. A natural extension of the point-cluster approach involves the calculation of the derivatives of the velocity field about the point, $\mathbf{x}_0$, in addition to velocity itself. This extra information then allows the velocity field to be projected to other points near to $\mathbf{x}_0$.

Consider the two clusters in figure 4.3, in which the source cluster, τ, induces a velocity field throughout the target cluster. The centres of the source and target cluster are located at $\mathbf{y}_\tau$ and $\mathbf{x}_0$ respectfully.

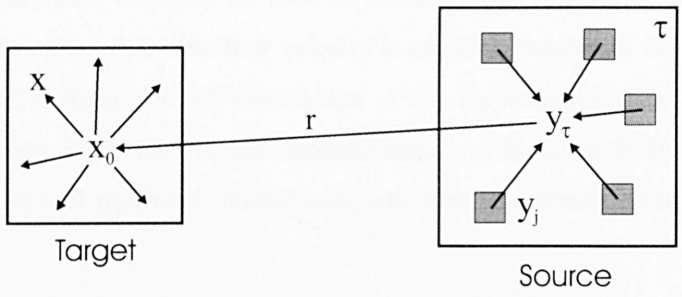


Figure 4.3: *Use of multipole expansions of vorticity and velocity field in a cluster-cluster interactions.*

The velocity induced by τ at $\mathbf{x_0}$ can be evaluated directly from equation 4.13. The derivatives of the velocity field at $\mathbf{x}_0$ can be obtained by differentiating equation 4.13 with respect to $\mathbf{x}_0$ to produce

$$D_{\mathbf{x}}^{\mathbf{n}}\mathbf{u}(\mathbf{x}_0) = (-1)^{\mathbf{n}} \sum_{\mathbf{k=n}}^{\mathbf{p}} \frac{\mathbf{k!}}{\mathbf{(k-n)!}}\, \mathbf{a_k}(\mathbf{x}_0, \mathbf{y}_\tau) \times \mathbf{m_{k-n}}(\tau)\,. \tag{4.27}$$

The velocity at a nearby point $\mathbf{x}$ can then be approximated by projecting the velocity field from $\mathbf{x_0}$ as

$$\mathbf{u}(\mathbf{x}) \approx \mathbf{u}(\mathbf{x}_0) + \sum_{\mathbf{k=1}}^{\mathbf{p}} \frac{1}{\mathbf{k!}}\, D_{\mathbf{x}}^{\mathbf{k}}\mathbf{u}(\mathbf{x}_0)(\mathbf{x}-\mathbf{x}_0)^{\mathbf{k}}\,. \tag{4.28}$$

In a similar fashion the derivatives of the velocity field can also be projected from $\mathbf{x_0}$ to $\mathbf{x}$ using

$$D_{\mathbf{x}}^{\mathbf{n}}\mathbf{u}(\mathbf{x}) \approx D_{\mathbf{x}}^{\mathbf{n}}\mathbf{u}(\mathbf{x}_0) + \sum_{\mathbf{k=n+1}}^{\mathbf{p}} \frac{1}{\mathbf{k-n!}}\, D_{\mathbf{x}}^{\mathbf{k}}\mathbf{u}(\mathbf{x}_0)(\mathbf{x}-\mathbf{x}_0)^{\mathbf{k-n}}\,. \tag{4.29}$$

It can be seen that equation 4.29 reduces to equation 4.28, and that equation 4.27 reduces to equation 4.13 for the case $\mathbf{n} = 0$.

4.3 Implementation

This section describes how the theory presented in the previous section is utilised by the FMM to efficiently evaluate the velocity field throughout the solution domain. It should be noted that the FMM can only be used to calculate the velocity at points within the grid structure. In cases where the flow velocity is required outside of the grid, a treecode algorithm is used instead. A full description of the implementation of the treecode is presented in section 4.3.3. Key to the implementation of both the FMM and treecode is the concept of *well separated* interactions, which will be presented in section 4.3.2.

4.3.1 Octree Data Structure

A crucial component of both the FMM and treecode algorithms is the hierarchical decomposition of the solution domain. The computational cells are first collected together to form clusters, which in turn are collected together to form larger clusters, and so on until the entire solution domain can be contained within a single cluster. Arguably the most efficient strategy available for generating the required hierarchy of clusters is to employ an octree data structure.

As highlighted in chapter 3, the octree data structures used to generate and manage the grid system in the VTM are perfectly suited for generating the hierarchy of clusters required to implement the FMM and treecode. The vast majority of FMM implementations found in literature are forced to generate a tree structure from scratch every time the algorithm is called. This is not the case for the VTM - the octree structure need only be modified to capture the changes in the spatial distribution of vorticity-containing regions of the flow. As a result, the dual use of the octree data structures by both the grid system and FMM generates valuable savings in terms of computational memory requirements and runtime. A detailed description of the octree generation process can be found in section 3.3.

4.3.2 Well Separated Interactions

All multipole methods rely upon a crucial characteristic of potential fields, namely that the strength of an interaction decays rapidly as the distance of the interaction increases. As a result, multiple long-range interactions can clustered together and approximated using a truncated multipole series. A criterion is therefore required which determines whether the loss of accuracy resulting from an approximation is acceptable. If an approximation for an interaction is valid, then the interaction is said to be *well separated.*

A minimum interaction distance is set by the requirement that the multipole expansions converge. As illustrated by figure 4.4, the multipole series used to approximate the velocity field induced by a cluster converges only at points exterior to a circle of radius $R_\tau = \max |\mathbf{y}_i - \mathbf{y}_\tau| \ , \ i = 1, \ldots, N_\tau$, with its centre located at $\mathbf{y}_\tau$.

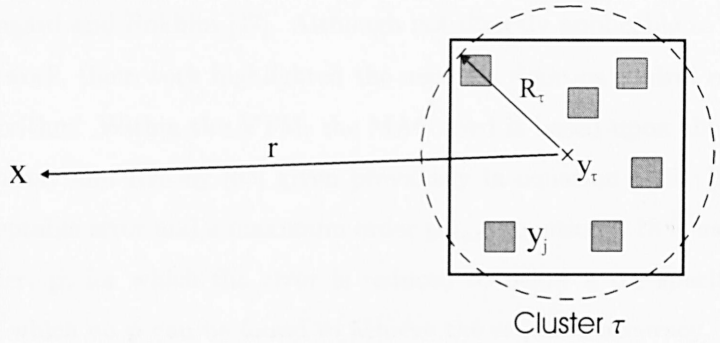


Figure 4.4: *Region of convergence of multipole series.*

The larger the distance of the interaction, the faster the rate of convergence of the multipole series, and hence the more accurate the multipole approximation becomes. The accuracy of an interaction is also a function of the cluster size, as defined by R_τ, and the magnitude of vorticity contained within the cluster. The condition which is used to decide whether a cluster interaction is well separated or not is known as the Multipole Acceptance Criteria (MAC).

Many different forms for the MAC have been proposed. For treecodes the MAC developed by Barnes and Hut [46] is arguably the most popular. It defines a well separated

interaction as one which satisfies

$$\mathbf{r} \geq \frac{R_\tau}{\theta} \,, \tag{4.30}$$

where $\mathbf{r} = |\mathbf{x} - \mathbf{y}_\tau|$ is the distance of the interaction, and $\theta < 1$ is a user specified parameter used to control the accuracy of the interaction. The smaller the value of θ, the more strict the criterion, and hence the number of multipole terms required to evaluate the velocity must increase.

Salmon and Warren [76] and Grama et al [77] both carried out in depth studies of the accuracy and efficiency achieved using a variety of MACs. They both concluded that the most effective approach was to base the MAC on an analytic measure of the interaction error rather than one based solely on the distance of the interaction.

A bounded analytic measure of the error of a truncated multipole series was first derived by Greengard and Rokhlin [47]. Although not directly applicable to the FMM presented in this work, their work highlighted the need for rigorous control of errors within any FMM algorithm. Within the VTM, the MAC used is based upon the error measure derived by Lindsay and Krasny [65] given previously in equation 4.18. By specifying a maximum acceptable error and a maximum order $\mathbf{p}_{max}$, equation 4.18 is used to establish the lowest order, $\mathbf{p}$, for which the error is reduced to below a pre-specified level. For interactions in which no $\mathbf{p}$ can be found to achieve the required accuracy, then the interaction is not considered to be well separated. The use of variable order approaches, such as this one, have been shown not only to minimise the computational cost of achieving the required accuracy, but to also reduce the standard deviation of the error throughout the solution domain [76], [77].

4.3.3 Fast Treecode

A limitation of the FMM is that the velocity can be evaluated only at locations contained within the grid structure, i.e. within the solution domain. Situations do arise however in which the velocity exterior to the solution domain is required. For example, it is feasible that a rotor blade will pass through a region of the flow which does not contain any vorticity, i.e. external to the solution domain. In order to calculate the aerodynamic loading of the blade, a method which allows the velocity to be evaluated outside of the

computational domain is therefore required. The Fast Treecode algorithm presented here is a multipole-based method which can be used to evaluate the velocity at any point in the flow, internal or external to the solution domain. The treecode makes use of the same underlying theory as the FMM and requires no additional information or code structure over that already available for the FMM.

The velocity induced at the point $\mathbf{x} = (x_1, x_2, x_3) \subset \mathbb{R}^3$ by all the vorticity contained in the solution domain is

$$\mathbf{u}(\mathbf{x}) = \sum_{i=1}^{N_\Omega} \mathbf{u}_i(\mathbf{x}) \,, \tag{4.31}$$

where $\mathbf{u}_i(\mathbf{x})$ is the velocity resulting from the point-particle interaction between $\mathbf{x}$ and the cell i. The treecode accelerates the summation in 4.31 by replacing suitable point-particle interactions with point-cluster interactions. The velocity at $\mathbf{x}$ can then be approximated as

$$\mathbf{u}(\mathbf{x}) \approx \sum_{\tau \in S_1} \mathbf{u}_\tau(\mathbf{x}) + \sum_{i \in S_2} \mathbf{u}_i(\mathbf{x}) \,, \tag{4.32}$$

such that $\Omega = S_1 \cup S_2$. S_1 is a set of well separated point-cluster interactions, and S_2 is the set of all point-particle interactions which are not suitable for approximation with point-cluster interactions. The generation of the interaction sets S_1 and S_2 and the evaluation of the point-cluster and point-cell interactions are implemented during a recursive sweep up and then down through the octree.

The upward sweep through the octree calculates the moments of every cluster in the octree. The sweep begins from those clusters which parent the computational cells. The moments of these clusters are evaluated using equation 4.15. The moments of the remaining clusters are evaluated by applying equation 4.26 to each cluster on moving upwards through the octree.

The downwards sweep of the octree starts from the root cluster, which by definition encapsulates the entire solution domain. If the root cluster is well separated from the point $\mathbf{x}$, as defined by the MAC, then only the point-cluster interaction between $\mathbf{x}$ and the root cluster interaction need to be evaluated to produce $\mathbf{u}(\mathbf{x})$. In this case, S_1 contains just one cluster, the root cluster, and S_2 is empty. If the root cluster is not well separated from $\mathbf{x}$, then the treecode descends down one level of the hierarchy of the octree and the MAC is tested on each of the cluster's children in turn. This process is repeated until a

cluster is located which satisfies the MAC, at which point the cluster is added to S_1 and the point-cluster interaction is evaluated using equation 4.13. Obviously, once a well separated cluster is located, the treecode does not need to descend any further down the relevant branch of the octree. If however the treecode reaches the bottom of a branch without identifying any well separated clusters, then no point-cluster interactions exist which can provide the required accuracy. These interactions must therefore be evaluated directly as point-particle interactions using equation 4.10. All such point-particle interactions are added to S_2. Once the downward sweep is concluded, the calculation of $\mathbf{u}(\mathbf{x})$ is complete. The velocity at any other point can then be evaluated by repeating the downwards sweep; the upwards sweep does not need to be repeated unless the underlying vorticity distribution has changed.

For a solution domain containing N computational cells, the set $S = S_1 \cup S_2$ contains $\mathcal{O}(\log N)$ interactions. Therefore, a total of $\mathcal{O}(N \log N)$ interactions must be evaluated to obtain the velocity throughout the entire solution domain.

4.3.4 Fast Multipole Method

As in the treecode algorithm, the first stage of the FMM involves an upward sweep through the octree, during which the moments of every cluster in the octree is calculated. The procedure is identical to the one used within the treecode (see section 4.3.3) and need not be described again here.

The second stage of the FMM involves a sweep back down the tree. This sweep is responsible for generating and refining the velocity field on each level of the tree. Unlike the treecode, which must perform a complete downward sweep N times to calculate the velocity at N different points, the FMM uses just one downward sweep to evaluate the velocity at all N points simultaneously.

A key feature of the FMM is the use of interaction lists to control the decomposition of the solution domain. The velocity field at any point within a cluster or cell can be considered as the sum of a near-field, an intermediate-field and a far-field component. Figure 4.5(a) illustrates how these components are used to construct a cluster's interaction list. For clarity the two-dimensional interaction sets have been shown, but the diagram extends easily to three dimensions. The near-field is defined as all the nearest neighbours

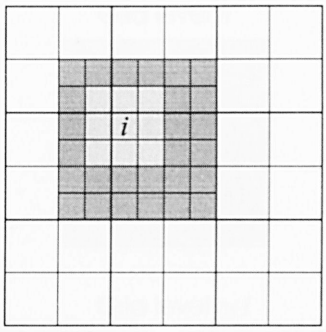


Figure 4.5: *Decomposition of the vorticity field in to the far field (white), intermediate field (dark grey), near field (light grey) of cluster i.*

of i. The intermediate-field contains all those clusters which are children of the nearest neighbours of i's parent and which are not contained within the near-field. All clusters which are not contained in the near- or intermediate-fields make up the far-field. A cluster's interaction list contains all those clusters contained within the cluster's intermediate-field. In three-dimensions, the interaction list contains a total of 189 clusters, and 27 in two-dimensions.

The implementation of the FMM is described as follows. Assume that the multipole expansion describing the velocity far-field is known for the cluster i on level n of the octree. The contribution from the intermediate-field is added by evaluating the cluster-cluster interactions contained within cluster i's interaction list. Note that the contributions from the near-field are not evaluated at this stage. The combined intermediate-field and far-field components of the velocity field are then translated to cluster i's children using equation 4.28. As illustrated in figure 4.6, this translated field is identical to the child cluster's far-field. This process of evaluation and translation is repeated on all clusters on level n of the grid, before descending to level $n-1$ and repeating the entire process.

The FMM starts its downwards descent of the octree from the root cluster. Note that both the far-field and intermediate-field component of the velocity field of the root cluster, and also its children, are by definition zero. This provides enough information to initiate the recursive descent of the octree, as described above. Once the lowest level of the octree has been reached, the far-field of every cell is known. The calculation is completed by adding the contributions from each cell's intermediate and near-fields, all of which are evaluated as point-cluster interactions using equation 4.13.

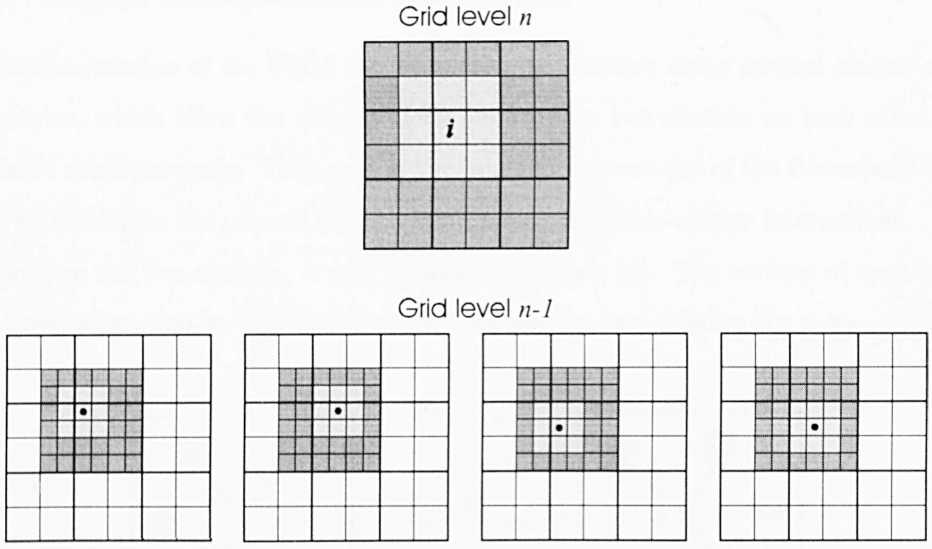


Figure 4.6: *Refinement of velocity field through hierarchical decomposition.*

Figure 4.7 illustrates the effective decomposition of the solution domain associated with the calculation of the velocity on the shaded cell using the FMM. The structure of the interaction lists can clearly be seen.

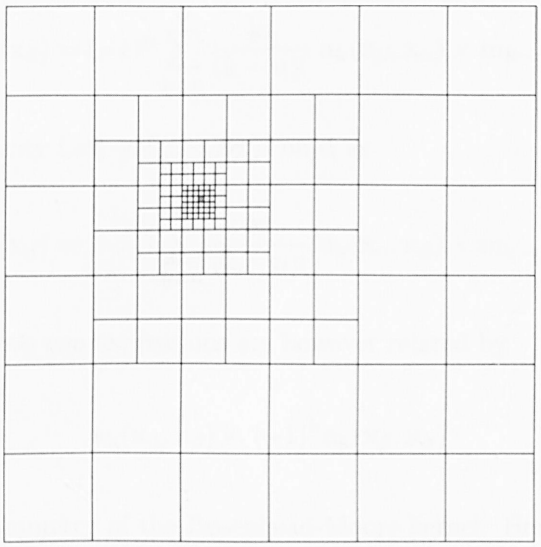


Figure 4.7: *Effective interaction list of the shaded cell*

4.3.5 Mutual Cluster-Cluster Interactions

The implementation of the FMM can be accelerated further using mutual cluster-cluster interactions, which allow the velocity fields induced by two clusters on each other to be calculated simultaneously. They exploit the inherent symmetries of the Rosenhead-Moore kernel to accelerate the process of evaluating multiple cluster-cluster interactions.

Consider the two clusters, α and β, shown in figure 4.8. The centres of each cluster are located at $\mathbf{x}_\alpha$ and $\mathbf{x}_\beta$ and the distance between the two clusters is $\mathbf{r} = \mathbf{x}_\beta - \mathbf{x}_\alpha$.

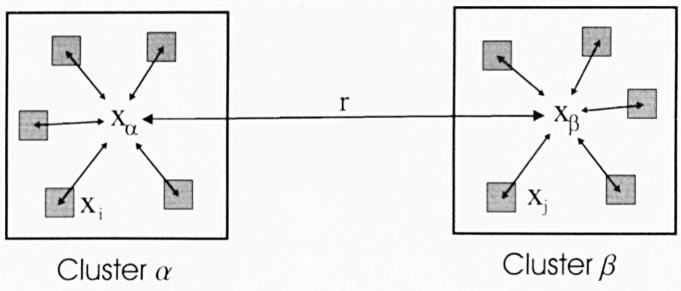


Figure 4.8: *Evaluation of the mutually induced velocity fields generated by two clusters.*

From equation 4.27 the velocity field induced by α on β can be expressed as

$$D^{\mathbf{n}}_{\mathbf{x}}\mathbf{u}(\mathbf{x}_\beta) = (-1)^{\mathbf{n}} \sum_{\mathbf{k}=\mathbf{n}}^{\mathbf{p}} \frac{\mathbf{k}!}{(\mathbf{k}-\mathbf{n})!}\, \mathbf{a}_{\mathbf{k}}(\mathbf{x}_\beta, \mathbf{x}_\alpha) \times \mathbf{m}_{\mathbf{k}-\mathbf{n}}(\alpha)\,, \tag{4.33}$$

and similarly, the velocity field induced by β on α as

$$D^{\mathbf{n}}_{\mathbf{x}}\mathbf{u}(\mathbf{x}_\alpha) = (-1)^{\mathbf{n}} \sum_{\mathbf{k}=\mathbf{n}}^{\mathbf{p}} \frac{\mathbf{k}!}{(\mathbf{k}-\mathbf{n})!}\, \mathbf{a}_{\mathbf{k}}(\mathbf{x}_\alpha, \mathbf{x}_\beta) \times \mathbf{m}_{\mathbf{k}-\mathbf{n}}(\beta)\,. \tag{4.34}$$

The tensors in the above two expressions are however related by

$$\mathbf{a}_{\mathbf{k}}(\mathbf{x}_\alpha, \mathbf{x}_\beta) = (-1)^{\mathbf{k}} \mathbf{a}_{\mathbf{k}}(\mathbf{x}_\beta, \mathbf{x}_\alpha) \tag{4.35}$$

due to the inherent symmetry of the Rosenhead-Moore kernel. Hence, by evaluating the interactions between clusters α and β simultaneously, rather than separately, the lengthy procedure associated with calculation of the Taylor series tensors (see section 4.2.5) can be reduced by a factor of two.

A consequence of using mutual cluster-cluster interactions within the FMM is that the interaction lists can be halved in size. All of the clusters marked with a cross in figure 4.9 can be removed from the interaction list because the contribution from those clusters will be accounted for when their own intermediate-field is evaluated. Using this approach in three dimensions, the number of clusters contained in the interaction list is reduced from 189 to 95, and from 27 to 14 in two dimensions.

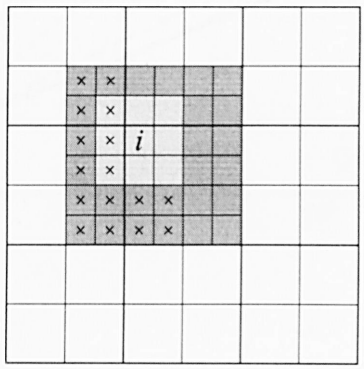


Figure 4.9: *Interaction list for cluster i using mutual cluster-cluster interactions; far field (white), intermediate field (dark grey), and near field (light grey).*

Dehnen [51], who first introduced the concept of mutual cluster-cluster interactions, found that they not only improved the performance of his algorithm, but also allowed him to preserve implicity the momentum of the system. Comparisons between the mutual cluster-cluster approach and the direct cluster-cluster approach, carried out using the new version of the VTM, have demonstrated the former method to produce speed improvements of roughly 40% with no loss in accuracy.

4.4 Computational Cost

The CPU time required to evaluate the velocity on all the cell interfaces within a computational domain consisting of N vorticity-containing cells is shown in figure 4.10. The data was produced on a PC equipped with a 2.0GHz Intel Pentium-4 CPU and 1 gigabyte of memory. The figure clearly demonstrates that the FMM quickly converges on its $O(N)$

Although the accuracy that can be attained by the FMM can be chosen arbitrarily by varying the order of the multipole expansion according to equation 4.18, it should be noted that the memory requirements of method scale with p^3. An upper bound on the accuracy is therefore imposed by the size of the available computer memory. Consequently, the multipole expansions used for the simulations presented in this work was limited to 2^{nd} order. Tests carried out on simple arrangements of vortex filaments indicate that this constraint corresponds to an mean error of $O(10^{-4})$.

theoretical cost as the number of cells contained in the computational domain is increased.

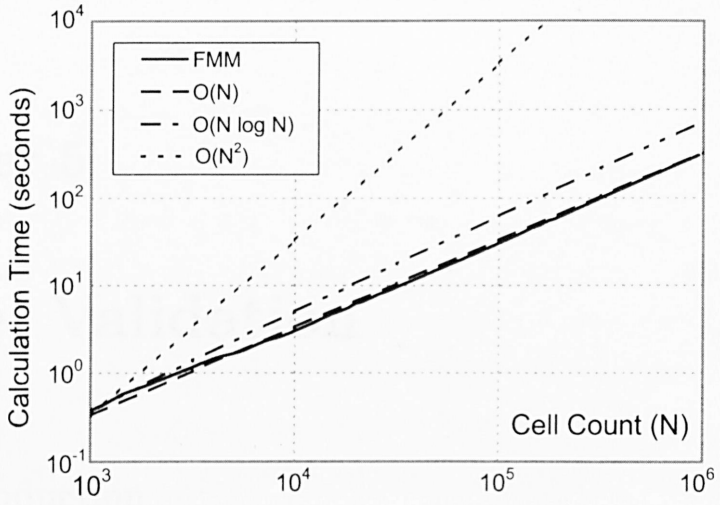


Figure 4.10: *Computational cost of the FMM.*

4.5 Summary

A Fast Multipole Method has been developed to evaluate the velocity field throughout the computational grid. For a grid containing N cells, the FMM allows the velocity field to be approximated on each of the N cells in $\mathcal{O}(N)$ operations. The accuracy of the algorithm is controlled rigorously through the application of an error criterion to all particle-cluster and cluster-cluster interactions. The performance of the algorithm has been further improved through the introduction of mutual cluster-cluster interactions, which allows multiple cluster-cluster interactions to be evaluated simultaneously.

In addition to the FMM, a fast treecode, of computational cost $\mathcal{O}(N \log N)$, has also been developed to allow the velocity at any point exterior to the computational grid to be calculated.

Octree data structures are used extensively within the new version of the VTM, playing a crucial role in the implementation of the grid system and in the velocity calculation.

Chapter 5

Model Validation

5.1 Introduction

This chapter describes the validation of the new version of the VTM against two well known sets of experimental data. The first set of experimental data was obtained by Caradonna and Tung [6], who measured the aerodynamic loading and wake geometry of a two-bladed rotor in hovering flight. The second set of experimental data was obtained by Harris [5], who studied the low-frequency dynamics of a four-bladed rotor in a wind tunnel environment over a range of foward flight speeds. His work identified a somewhat unexpected variation in lateral disc tilt with forward speed - a feature which many computational wake models have had difficulty in capturing accurately. Whitehouse and Brown [78] successfully predicted the variation in lateral disc tilt using the original version of the VTM however. Validation of the new version of the VTM against the Harris data set therefore provides an indication, not only of the accuracy of the model, but also of its performance relative to the original version of the VTM. This second validation exercise identified some particularly interesting flow physics which may provide an explanation of the physical mechanisms driving the variations in the lateral disc with forward speed. A detailed study of Harris' work, based on these observations, is presented separately in chapter 6.

5.2 Caradonna & Tung's Experimental Data

5.2.1 Experimental Setup

Caradonna and Tung's experimental work was one of the first to include simultaneous measurements of both the blade loading and the wake geometry for a rotor in hovering flight. The experiments were carried out in the US Army Aeromechanics Laboratory Hover Test Facility, which is equipped with special ducting to minimise recirculation of the flow within the test chamber. The experiments were performed using a simple two-bladed model helicopter rotor, into which were integrated sixty pressure tubes allowing the chordwise and radial pressure distributions on the blade to be measured. The locations of the tip vortices were acquired using hot-wire probes placed beneath the rotor. A number of tests were carried out covering a range of thrust conditions and rotational speeds. A detailed breakdown of the rotor geometry and operating conditions is shown in table 5.1.

Number of Blades	2
Rotor Radius (m)	1.143
Blade Chord (m)	0.1905
Blade Aspect Ratio	6
Blade Twist	0°
Tip Geometry	Rectangular
Aerofoil Section	NACA 0012
Rotational Speed (rpm)	650, 1250, 1750, 2279
Tip Mach Number	0.226, 0.434, 0.607, 0.794

Table 5.1: *Description of Caradonna and Tung's experimental setup.*

5.2.2 Numerical Simulations

Given that the Prandtl-Glauert compressibility correction used by the VTM cannot be guaranteed to provide a rigorous representation of the high Mach number and transonic features on the blade, only the $\Omega = 650$rpm ($M_{tip} = 0.226$) cases have been considered within the validation study.

All the numerical results were generated using 32 blade collocation points in a cosine distribution along each blade. The grid used four nested levels, with grid level boundaries located at $1.5R$, $3.0R$ and $6.0R$. The cell size on the finest grid level was $\Delta x = 0.025R$.

5.2.3 Blade Loading

Figures 5.1 and 5.2 compare the calculated lift coefficient and blade loading distributions along the rotor blade with the experimental data. The blade loading coefficient is defined as

$$C_{BL}(r) = C_L(r) \left(\frac{u(r)}{\Omega R} \right)^2 , \tag{5.1}$$

where $u(r)$ is the local flow velocity at the radial location $x/R = r$. Although the experimental data is relatively sparse, and the associated error does not appear to have been quantified in the original reference, the predictions from the VTM simulation are in close agreement with experiment, both in terms of magnitude and in terms of the general shape of the spanwise distributions.

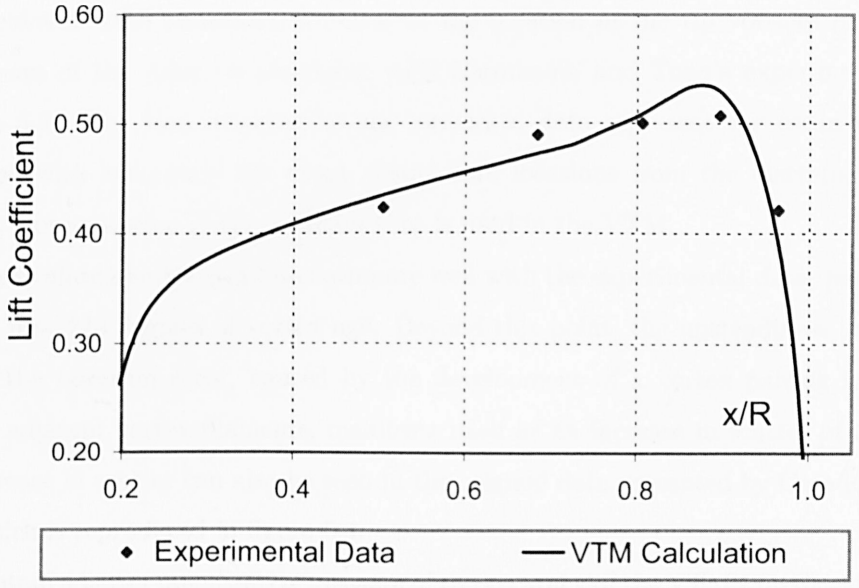


Figure 5.1: *Comparison between experimental and calculated lift coefficient:* $C_T = 0.0079, \Omega R = 150 ms^{-1}$.

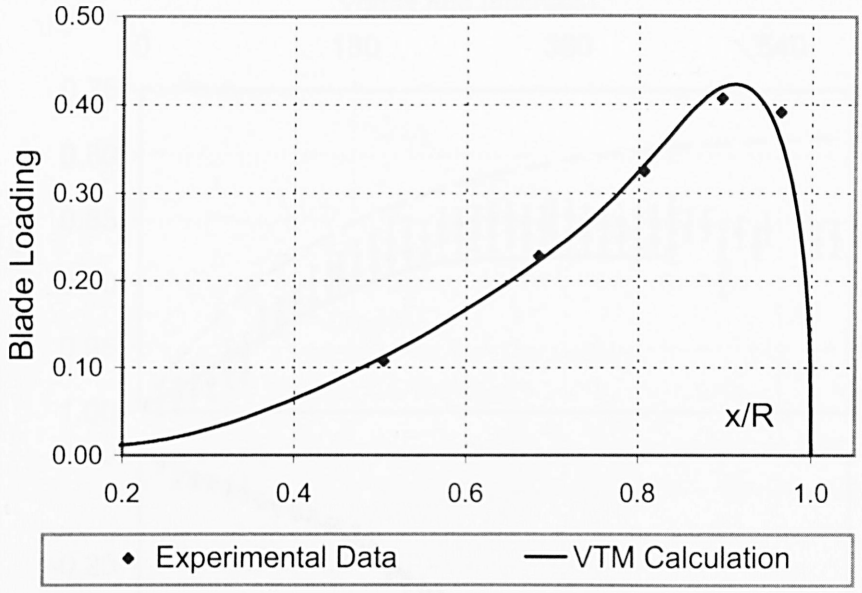


Figure 5.2: *Comparison between experimental and calculated loading coefficient:* $C_T = 0.0079, \Omega R = 150ms^{-1}$.

5.2.4 Wake Geometry

The calculated wake structure, in terms of the location of the tip vortices in the flow downstream of the rotor, is compared with Caradonna and Tung's experimental data in figure 5.3. The bars attached to the numerical data represent the estimated error associated with extracting the exact vortex core locations from the discrete, cellwise-constant representation of the vorticity that is used in the VTM.

The calculated vortex positions compare well with the experimental data, particularly over the first 270 degrees of vortex age. Beyond this point, the unsteadiness in the far-wake of the hovering rotor, caused by the development of a vortex pairing instability between adjacent vortex filaments, manifests itself as an increase in scatter of the data. This increase in scatter can also be seen in the original data presented by Caradonna and Tung which is reproduced in figure 5.4.

To obtain a better quantitative measure of the accuracy of the VTM's predictions of the wake geometry, figure 5.3 also includes a comparison against Kocurek and Tangler's widely-used empirical wake trajectory [79]. Although the predictions of the VTM lie between the experimental data and the predictions of Kocurek and Tangler's empirical model, the axial vortex locations produced by both experiment and the VTM are consistent with

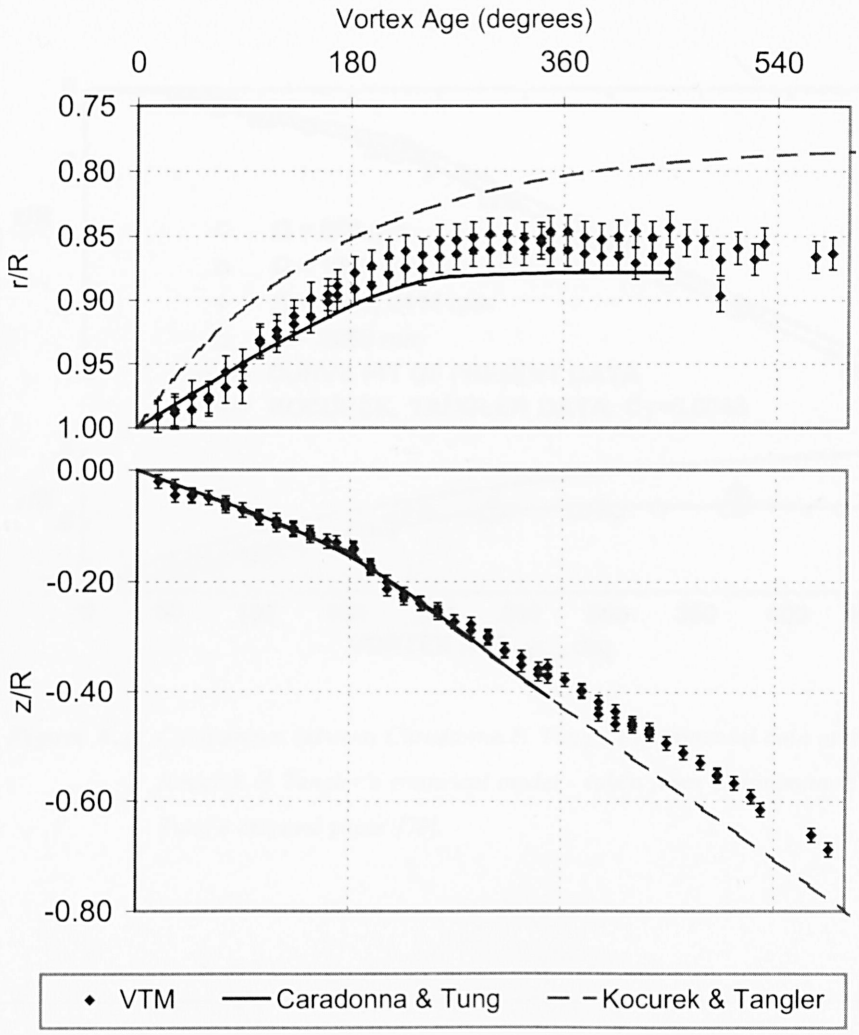


Figure 5.3: *Comparison in wake geometry between Caradonna & Tung's experimental data and VTM prediction.*

an over-prediction of the contraction rate of the wake by Kocurek & Tangler's model. It is however possible that the experimental data may be contaminated by the presence of the rotor support tower, or more likely, by the inadequate far-field boundary conditions provided by the design of the test facility.

Figure 5.5 shows three example snap-shots of the calculated wake structure produced during the VTM's simulation of Caradonna & Tung's rotor, visualised here by plotting contours of vorticity magnitude on a vertical plane through the rotor hub. The development of the vortex pairing instability in the far wake of the rotor, mentioned previously in association with the scatter in the observed tip vortex locations, can be seen clearly.

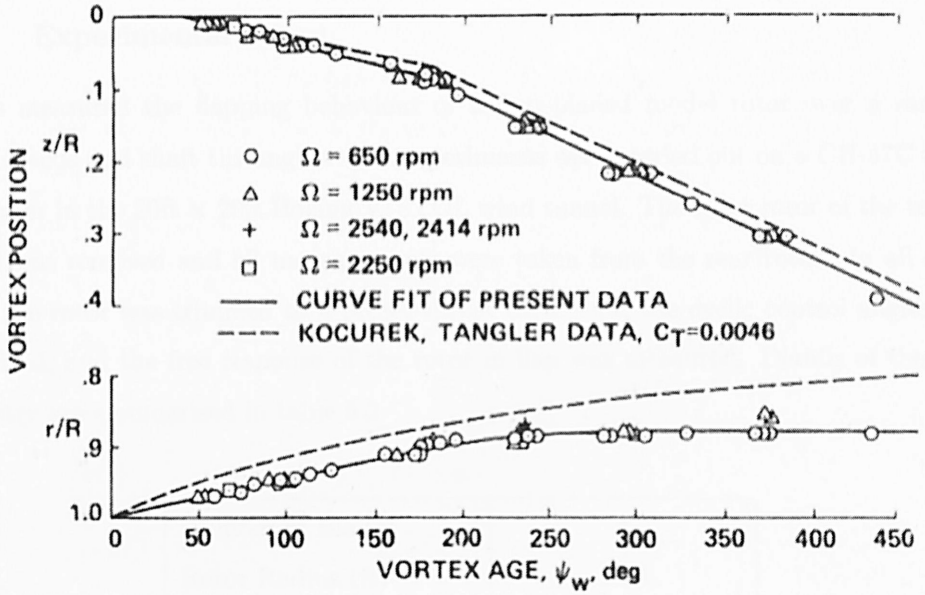


Figure 5.4: *Comparison between Caradonna & Tung's experimental data and Kocurek & Tangler's empirical model - taken from Caradonna & Tung's original paper [79].*

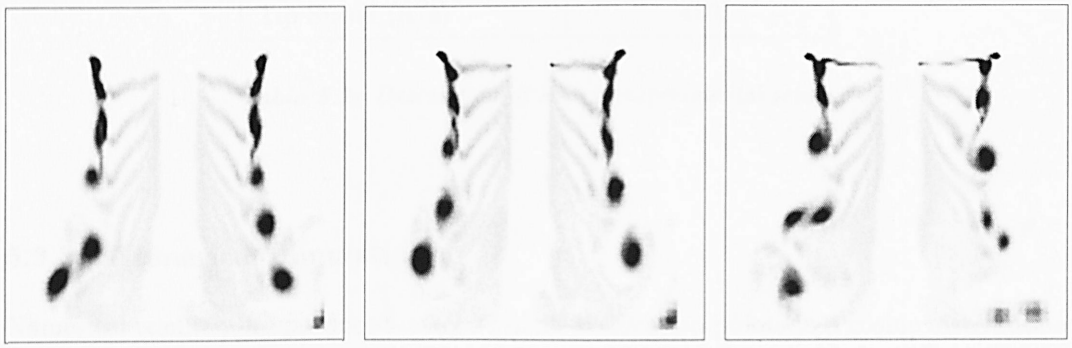


Figure 5.5: *Visualisations of the predicted wake geometry.*

5.3 Harris' Experimental Data

5.3.1 Experimental Setup

Harris measured the flapping behaviour of a four-bladed model rotor over a range of flight speeds and shaft tilt angles. The experiments were carried out on a CH-47C model helicopter in the 20ft × 20ft Boeing V/STOL wind tunnel. The front rotor of the tandem model was removed and all measurements were taken from the rear rotor. In all of the tests, the rotor was trimmed to a preset thrust coefficient, the cyclic control angles were held fixed, and the free response of the rotor in flap was measured. Details of the rotor geometry are summarised in table 5.2.

Number of Blades	4
Rotor Radius (ft)	2.73
Blade Chord (ft)	0.191
Solidity	0.0892
Blade Twist	-9.14°
Tip Geometry	Rectangular
Root Cut-out (ft)	0.525
Aerofoil Section	V23010-1.58
Tip Speed (ft/s)	450

Table 5.2: *Description of Harris' experimental setup.*

5.3.2 Numerical Simulations

Numerical results were produced using 20 blade collocation points in a cosine distribution along each blade, and by resolving the rotor radius across 25 computational cells at the finest grid level. When using the new version of the VTM, four levels of grid expansion were used, with transitions between grid levels positioned at $2R$, $6R$ and $10R$ from the rotor hub. To investigate the convergence of the results, three further simulations were carried out using the new version of the VTM, but with the number of collocation points increased to 32 and the underlying grid resolution increased to resolve the rotor radius across 62.5 cells.

5.3.3 Disc Tilt

Figure 5.6 compares the lateral and longitudinal disc tilts measured by Harris' with the predictions of both the old and new versions of the VTM. The error bars in figure 5.6 represent the experimental error of the data, estimated by Harris to be ±0.25°.

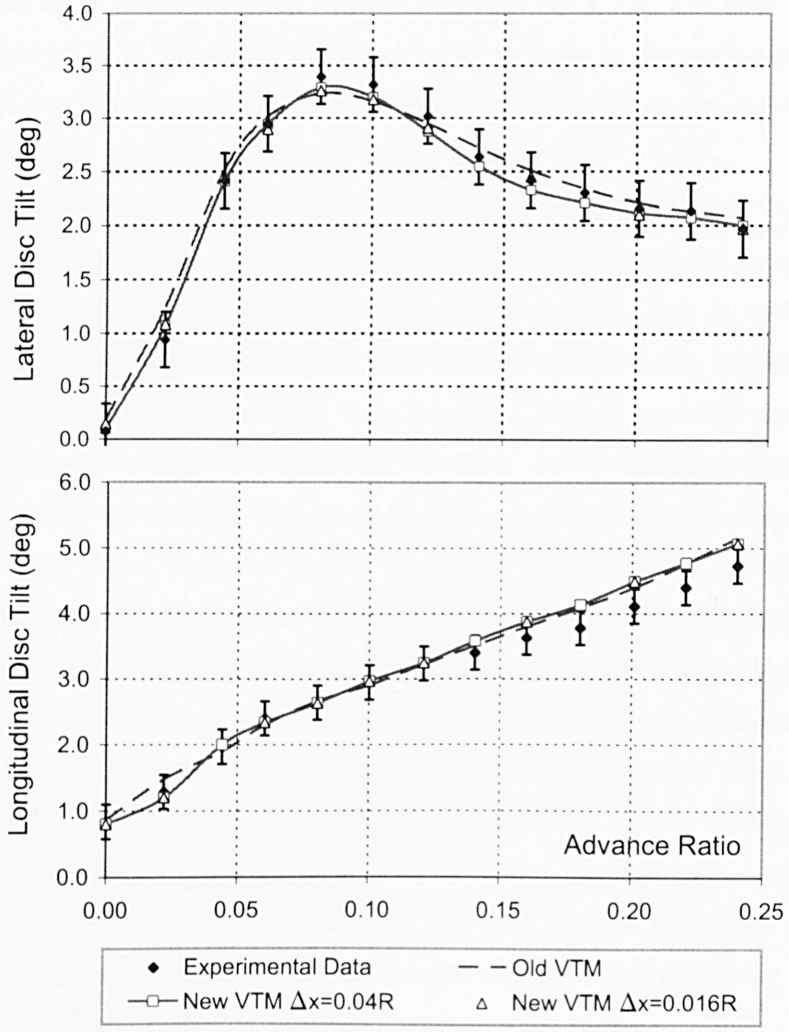


Figure 5.6: *Comparison of new and old versions of the VTM against Harris' experimental data: lateral disc tilt (top), longitudinal disc tilt (bottom).*

Simulating Harris' experiments has proven to be a significant challenge to computational methods in the past, but both old and new versions of the VTM show good agreement with the experimental data for both the lateral and the longitudinal tilt of the

rotor. Although marginally lower than the experimental values, the values of the lateral disc tilt predicted by the new version of the VTM lie within the experimental error bounds over the full range of flight speeds.

The new version of the VTM produces somewhat improved correlation than the old version at low forward speeds. The overall trend in lateral disc tilt over the speed range is also captured more accurately using the new version of the VTM. The poor performance of the original VTM at low speed, which can be seen clearly in the over prediction of the longitudinal disc tilt below $\mu = 0.04$, is believed to originate from the contamination of the solution by the boundary conditions on the vorticity field.

The consistent behaviour between the two versions of the code in slightly over-predicting the longitudinal tilt at high forward speed ($\mu > 0.20$) is indicative of a deficiency in the present blade aerodynamic model at high advance ratio, most likely in its treatment of the post-stall lift variation in the reverse-flow region on the retreating side of the rotor.

Figure 5.7 compares the predicted wake structures, for the $\mu = 0.12$ case, produced using grid resolutions of $\Delta x = 0.04R$ and $\Delta x = 0.016R$. The visualisation of the wake produced using the lower resolution grid shows some distinctly under-resolved flow structures compared to the higher resolution result. The effect of the different spatial resolutions is clearly visible in the aerodynamic loading of the blades, as shown in figure 5.8. The BVI features in the blade loading distribution only become exposed in the high resolution predictions. In spite of its lack of spatial resolution, the low resolution simulation still predicts almost identical rotor flapping as the high resolution simulation. This observation can be explained as follows. Since the flapping behaviour of a rotor blade is controlled primarily by the integrated aerodynamic moment about the flap hinge, only the gross features of the inflow distribution need to be captured in order to predict the flapping behaviour of the rotor. The fine scale features in the inflow are effectively filtered out when the aerodynamic loading is integrated over the blade radius.

The vorticity conserving approach employed by the VTM guarantees that the distribution and strength of the vorticity present within the wake is largely independent of grid resolution. The gross features of the wake-induced inflow distribution can therefore be captured accurately even at very low resolutions. Consequently, in cases where only the low-frequency dynamics of the rotor are required, these results suggest that the VTM can be run at significantly lower resolutions than are required, for example, for modelling rotor vibration or acoustics.

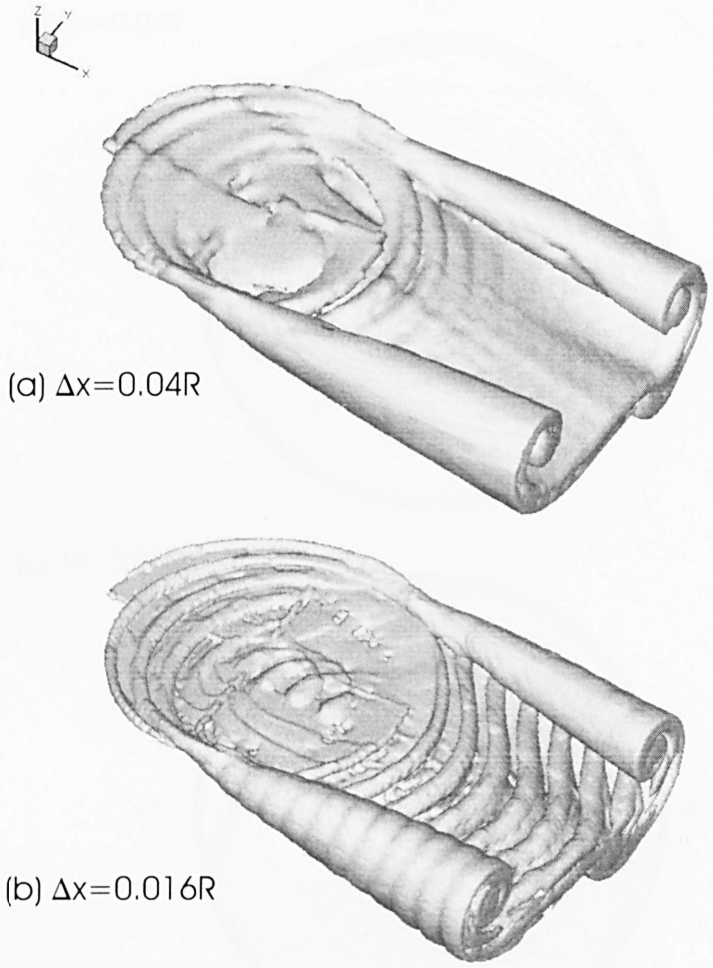


Figure 5.7: *Wake structure for the $\mu = 0.12$ case, resolved using cell sizes of (a) $\Delta x = 0.04R$, and (b) $\Delta x = 0.016R$.*

5.4 Summary

The new version of the VTM has been validated against two sets of experimental data. The first set of experimental data, produced by Caradonna and Tung, includes measurements of the aerodynamic loading of the rotor as well as measurements of the wake geometry, in terms of tip vortex locations, for a rotor in hover. The spanwise distribution of aerodynamic loading along the rotor blade is predicted well by the new version of the VTM, both in terms of magnitude and in terms of the shape of the distribution. The axial de-

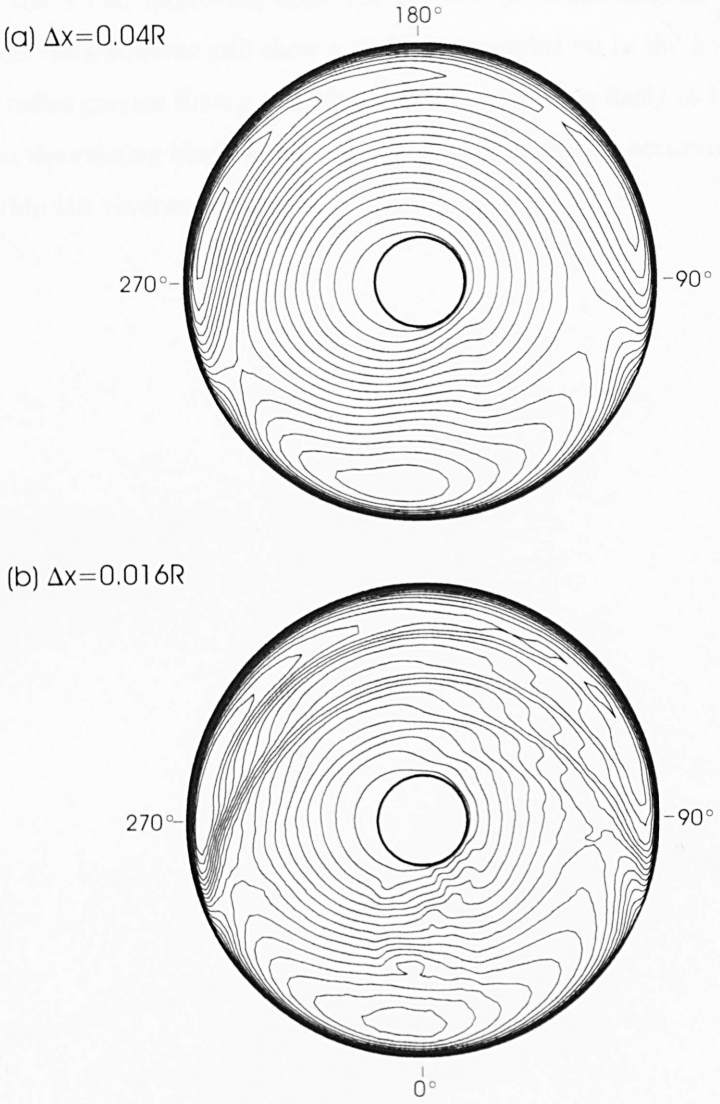


Figure 5.8: *Comparison of predicted blade loading using grid resolutions of (a) $\Delta x = 0.04R$, and (b) $\Delta x = 0.016R$.*

scent rate and vertical descent rate of the tip vortices is captured accurately over the first 270 degrees of wake age, beyond which the radial contraction rate appears to be slightly over-predicted.

The second set of experimental data, produced by Harris, investigates the free response of an articulated rotor with fixed control inputs over a range of forward flight conditions. The variation in disc tilt of the rotor over the speed range is accurately captured by the

new version of the VTM, improving upon the predictions of the original version of the VTM. The model does however still show a slight over-prediction in the longitudinal disc tilt at advance ratios greater than $\mu = 0.20$; a deficiency which is likely to be attributable to deficiencies in the existing blade aerodynamic model in capturing accurately the loading of the rotor within the reverse flow region.

Chapter 6

A Detailed Study of Harris' Experimental Work

6.1 Introduction

In the previous chapter, a validation exercise was carried out against the experimental data of Harris [5]. This case has proven to be a significant challenge to computational methods in the past; however, both versions of the VTM show good agreement with Harris' experimental data for the variation of both the lateral and the longitudinal tilt of the rotor with forward speed.

As shown in figure 6.1, prediction codes using simple wake models, such as low-order inflow models or prescribed wake models, have, in general, significantly under-predicted the lateral disc tilt at low advance ratios. Only those models which capture the free evolution of the wake system have successfully matched Harris' experimental data.

The physical mechanisms which drive the variation in lateral disc tilt are, however, not thoroughly understood. Johnson [80] and Quackenbush [81] both carried out detailed studies of Harris' experiments using vortex-filament free-wake methods, and identified the wake structures which they believed were responsible for the high level of lateral flapping of the rotor at low advance ratio.

Johnson first highlighted the important role played by the wake geometry in determining the lateral flapping of the rotor at low advance ratio. He observed how the tip vortices held a position close to the rotor disc rather than descending rapidly below the rotor, as is predicted by simple wake models. He demonstrated that the presence of these vortices

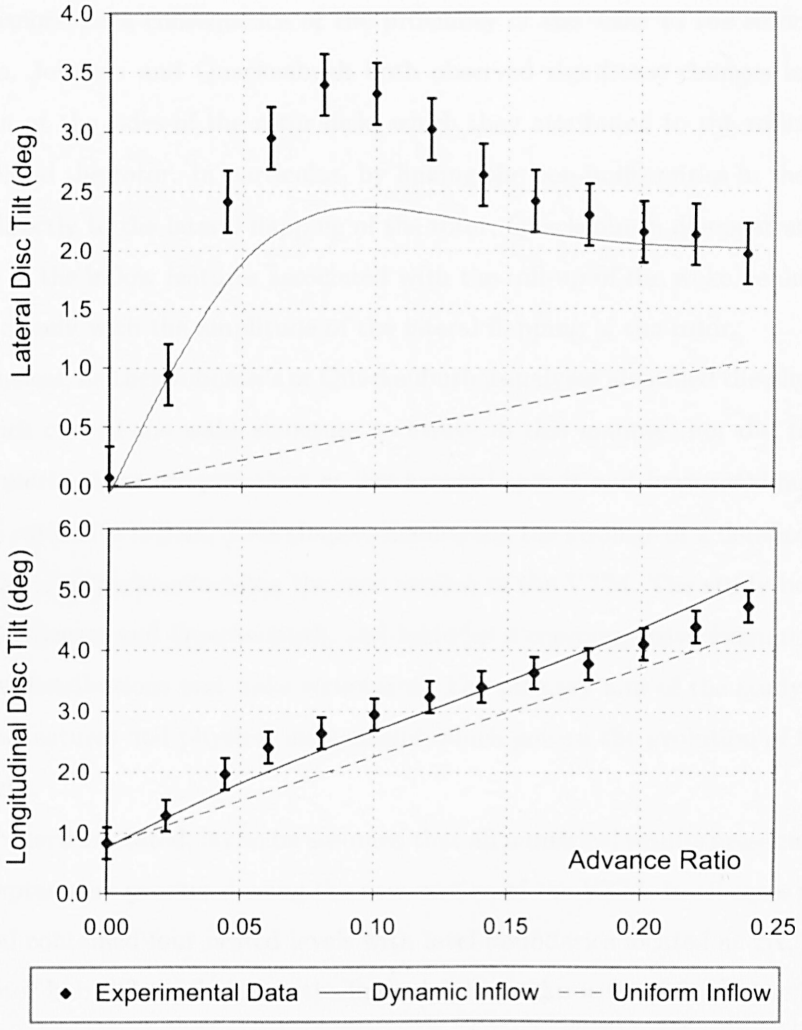


Figure 6.1: *Lateral disc tilt predictions using a uniform inflow model and a three-mode dynamic inflow model.*

close to the rotor disc introduced non-uniformities in the inflow distribution, increasing the downwash over the rear of the rotor disc and thus increasing the lateral flapping of the rotor.

Quackenbush later reinforced Johnson's conclusions by investigating the effect of climb velocities on lateral flapping. In climb, the tip vortices tended to be convected downstream, away from the rotor, thus reducing the lateral flapping. In descent, the vortices were held closer to the rotor, thus augmenting the effect. Indeed, it was observed that the maximum lateral disk tilt shifted to higher advance ratios for climbing flight and to lower advance ratios in descending flight.

Furthermore, as a consequence of the proximity of the wake to the rotor at low advance ratio, Johnson and Quackenbush both observed significant changes in the inflow distribution at the sides of the rotor disk, which they attributed to the rolling up of tip vortices behind the rotor. In particular, by linking the non-uniformities in the inflow distribution directly to the lateral flapping of the rotor, Quackenbush demonstrated how the magnitude of the inflow features associated with the roll-up of the wake behind the rotor correlated closely with the amplitude of the lateral flapping of the rotor.

Nevertheless, neither Johnson's or Quackenbush's analyses identified the physical mechanisms which caused the wake structure to evolve in this manner, nor did they explain why these mechanisms are prevalent at low forward speeds and have maximum effect at an advance ratio of $\mu = 0.08$. This chapter documents the findings of a detailed numerical study of Harris' experiments using the new version of the VTM. The study builds on the analyses of Johnson and Quackenbush, and includes a comprehensive examination of the rotor inflow distributions and wake structures. The primary aim of the study is to identify the flow features and physical mechanisms which govern the evolution of the wake in forward flight.

Unless otherwise stated, it can be assumed that all numerical results presented throughout this chapter were produced using the new version of the VTM. In all cases the computational grid contained four nested levels with level boundaries located at 2R, 4R and 8R from the rotor hub. The cell size on the finest level was $\Delta x = 0.016R$ and the blade aerodynamics were captured using 32 collocation points, distributed in a cosine distribution, along each blade.

6.2 Flap Dynamics

The equation of motion describing the flap dynamics of a rotor blade [82], which can be derived by considering the effect of the inertial, centrifugal and aerodynamic moments acting about the blade flap hinge, can be written as

$$\ddot{\beta} + \Omega^2 \beta = \frac{1}{I_\beta} \int_0^1 F_z(r) r \, dr \, , \tag{6.1}$$

where $F_z(r)$ is the aerodynamic force generated by the blade acting normal to the blade, and I_β is the moment of inertia of the blade about the flap hinge. In deriving equation 6.1, it has been assumed that (a) the blades are rigid, (b) the flap hinge of the blade is located at the rotor hub, (c) there is no coupling of the lag or feather motion with the flap motion, and (d) there is no mechanical stiffness or damping about the flap hinge.

A general solution of equation 6.1 can be derived by expressing the flap angle of the blade, in terms of azimuth location, using a Fourier series expansion:

$$\beta(\psi) = \beta_0 + \beta_{1c} \cos\psi + \beta_{1s} \sin\psi + \text{higher order terms} \, . \tag{6.2}$$

In steady flight conditions the coefficients of the series are time-invariant. Under these conditions, the coefficients in the Fourier expansion can be evaluated by multiplying equation 6.1 by the series of operators, 1, $\cos\psi$, $\sin\psi$, ..., and integrating over a rotor revolution to yield the sequence

$$\frac{1}{2\pi} \int_0^{2\pi} (\ddot{\beta} + \Omega^2 \beta) \, d\psi = \frac{1}{2\pi I_\beta} \int_0^{2\pi} \int_0^1 F_z(r) r \, dr \, d\psi \, , \tag{6.3}$$

$$\frac{1}{\pi} \int_0^{2\pi} (\ddot{\beta} + \Omega^2 \beta) \cos\psi \, d\psi = \frac{1}{\pi I_\beta} \int_0^{2\pi} \int_0^1 F_z(r) r \cos\psi \, dr \, d\psi \, , \tag{6.4}$$

$$\frac{1}{\pi} \int_0^{2\pi} (\ddot{\beta} + \Omega^2 \beta) \sin\psi \, d\psi = \frac{1}{\pi I_\beta} \int_0^{2\pi} \int_0^1 F_z(r) r \sin\psi \, dr \, d\psi \, . \tag{6.5}$$

$$\vdots$$

For the purpose of analysing Harris' data, in which only the first harmonics of the rotor flapping response are of interest, the higher order terms can be neglected.

Substitution of the general solution into this sequence and performing the integration leads to

$$\frac{1}{2\pi I_\beta}\int_0^{2\pi}\int_0^1 F_z(r)r\ dr\ d\psi = \beta_0 \tag{6.6}$$

$$\frac{1}{\pi I_\beta}\int_0^{2\pi}\int_0^1 F_z(r)r\cos\psi\ dr\ d\psi = 0 \tag{6.7}$$

$$\frac{1}{\pi I_\beta}\int_0^{2\pi}\int_0^1 F_z(r)r\sin\psi\ dr\ d\psi = 0\ . \tag{6.8}$$

These results demonstrate how the first harmonics of the inertial and centrifugal terms on the left hand side of equation 6.1 cancel exactly. Crucially, this leads to the requirement that the first harmonics of the aerodynamic forcing on a rotor in equilibrium must be zero. The orientation of the rotor disc in space, defined by the values of β_{1c} and β_{1s}, is driven simply by the requirement for zero net aerodynamic moment about the rotor hub, whilst the coning of the rotor, β_0, is driven by the mean aerodynamic force being generated by the rotor.

For small angles of incidence, F_z can be assumed to be equal to the lift being generated by the blade. Assuming linear aerodynamics, the lift can be expressed as

$$F_z(r) = \frac{1}{2}\rho ac\,(u_\mathsf{T}^2\theta - u_\mathsf{P}u_\mathsf{T})\ , \tag{6.9}$$

where u_T and u_P are the velocity components tangential and perpendicular to the disc plane, and α is the aerofoil's angle of incidence, as shown in figure 6.2.

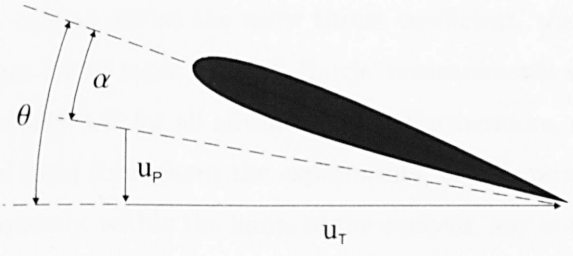


Figure 6.2: *Definition of aerofoil flow angles.*

To first order, the tangential velocity component can be written as the sum of the rotational and freestream velocity, whist the perpendicular velocity component can be written as the sum of the wake-induced inflow, the flap velocity and the freestream component:

$$u_{\mathsf{T}} = \Omega r + \mu \sin\psi \tag{6.10}$$

$$u_{\mathsf{P}} = \lambda(r,\psi) + r\dot{\beta} + \beta\mu\cos\psi \; . \tag{6.11}$$

Substituting these definitions into equation 6.7 and equation 6.9 leads to

$$\beta_{1s}(1+\frac{\mu^2}{2}) = \theta_{1c}(1+\frac{\mu^2}{2}) + \frac{4\beta_0\mu}{3} + \frac{4}{\pi}\int_0^{2\pi}\int_0^1 \lambda(r,\psi)r^2\cos\psi \; dr \; d\psi \; , \tag{6.12}$$

after some manipulation, where β_{1s} is the first sine harmonic of the flapping motion and θ_{1c} is the first cosine harmonic of the pitch-control input.

Equation 6.12 can be further simplified to

$$\beta_{1s}(1+\frac{\mu^2}{2}) = \theta_{1c}(1+\frac{\mu^2}{2}) + \frac{4\beta_0\mu}{3} + 4\int_0^1 \lambda_{1c}(r)r^2 \; dr \; , \tag{6.13}$$

where $\lambda_{1c}(r)$ is the first cosine harmonic of the inflow distribution at the radial location r. It can be seen, therefore, that the lateral flapping response of the rotor is driven primarily by the longitudinal variation in inflow, the lateral cyclic and the coning contribution to the blade incidence.

The coning of the rotor, as shown by Prouty [83],

$$\beta_0 = \frac{2}{3}\gamma\frac{C_T/\sigma}{a} - \frac{mgR^2}{2I_\beta\Omega^2} \; , \tag{6.14}$$

is a function of the rotor thrust and the inertial properties of the blade. Since Harris' experiments were all carried out at the same thrust coefficient, the coning of the rotor should remain constant for all cases. Indeed, Harris' measurements show that the coning of the rotor was nominally 3.3° for all advance ratios. Furthermore, since all the controls of the rotor were held fixed throughout the experiments, the θ_{1c} term in equation 6.12 is also constant. Consequently, within the limits of the analysis, any non-linear variations in lateral tilt with advance ratio must originate from the first cosine harmonic of the inflow distribution.

6.3 Inflow Distribution

A reconstruction of each term of equation 6.13, using the inflow distributions predicted by the VTM model, is shown in figure 6.3.

Although discrepancies between the reconstructed flapping and the experimental results still exist, these results strongly suggest that the variation in lateral flapping seen in Harris' data is likely to be accountable to the cosine variation in the inflow distribution, as predicted by equation 6.13. Indeed, discrepancies between the reconstructed flapping and the experimental results are to be expected due to the simplicity of equation 6.13 and the various assumptions made in its derivation.

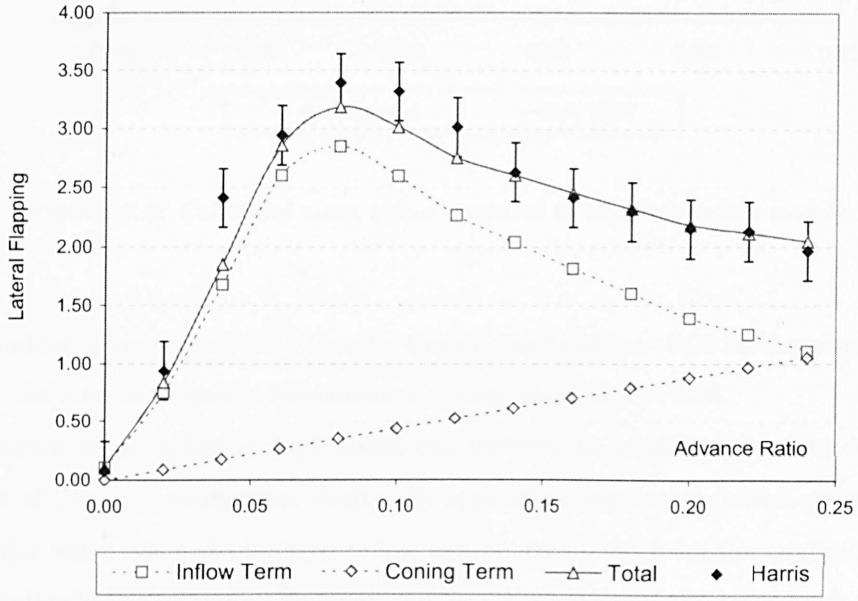


Figure 6.3: *Components of lateral flapping according to equation 6.13.*

Figure 6.4 compares the mean inflow, λ_0, given by Glauert's forward-flight extension to momentum theory [84],

$$\lambda_0 = \frac{C_T}{2\sqrt{\mu^2 + \lambda_0^2}}, \tag{6.15}$$

with that predicted by the VTM simulations. Up to an advance ratio of $\mu = 0.08$ the mean inflow predicted by the VTM and Glauert's theory agree closely. However, above

$\mu = 0.08$ the calculated inflow diverges abruptly from the momentum theory result, with the VTM predicting a considerably larger mean inflow.

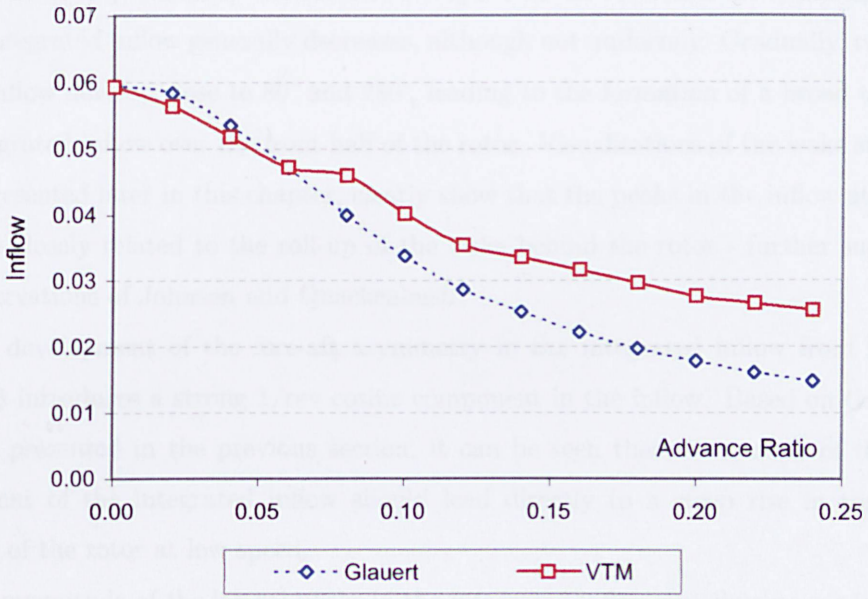


Figure 6.4: *Calculated mean inflow compared to Glauert's inflow model.*

The sudden divergence from Glauert's theory results at $\mu = 0.08$ further supports the idea that the flow undergoes a fundamental change close to $\mu = 0.08$.

The excess mean inflow at high speed can however be explained by considering the derivation of Glauert's momentum theory. By approximating a rotor in high speed forward as a circular wing, the wake induced inflow can be calculated from the analytic solution for an elliptically loaded wing. However, due to the rotation of the rotor blades and the influence of the root cut-out the loading of the rotor is far from elliptic. Consequently, for a conventional rotor in high speed flight, it is sensible to expect Glauert's model to underpredict the wake induced inflow.

Figures 6.5 and 6.6 show the variation in the radially integrated inflow,

$$\int_0^1 \lambda(r, \psi)\, dr\,, \tag{6.16}$$

with azimuth for each advance ratio. In hover the integrated inflow is effectively constant around the azimuth (the weak 4/rev component seen in the signal originates from the

longitudinal cyclic input $\theta_{1s} = 0.73°$ which was applied to the rotor at all advance ratios during Harris' experiments). As the forward speed of the rotor increases, the magnitude of the integrated inflow generally decreases, although not uniformly. Gradually, two peaks in the inflow develop close to 80° and 280°, leading to the formation of a broad trough in the integrated inflow over the front half of the rotor. Visualisations of the wake structure, to be presented later in this chapter, clearly show that the peaks in the inflow at 80° and 280° are closely related to the roll-up of the wake behind the rotor - further supporting the observations of Johnson and Quackenbush.

The development of the fore-aft asymmetry in the integrated inflow from hover to $\mu = 0.08$ introduces a strong 1/rev cosine component in the inflow. Based on the simple analysis presented in the previous section, it can be seen that the growth of the 1/rev component of the integrated inflow should lead directly to a steep rise in the lateral flapping of the rotor at low speed.

The magnitude of the lateral peaks in the integrated inflow distribution are largest at an advance ratio of $\mu = 0.08$. As the forward speed of the rotor is increased past $\mu = 0.08$ the integrated inflow continues to decrease in magnitude, particularly over the rear of the disk. As a consequence of the reduction in inflow over the rear of the disk, the strength of the 1/rev component slowly diminishes, leading to the drop off in lateral flapping above $\mu = 0.08$.

Interestingly, figures 6.5 and 6.6 show that the amplitude of the peaks in the inflow distribution at 80° and 280° does indeed vary with the lateral flapping of the rotor, as proposed by Quackenbush. Whether or not these roll-up features force directly the lateral flapping of the rotor can be confirmed by expressing the inflow contribution to the lateral flapping in equation 6.12 as

$$\int_0^1 \lambda_{1c}(r) r^2 \, dr = \int_0^{2\pi} J(\psi) \, d\psi = \int_0^{2\pi} \int_0^1 I(r, \psi) \, dr \, d\psi \, , \tag{6.17}$$

where

$$J(\psi) = \int_0^1 I(r, \psi) \, dr \, , \tag{6.18}$$

and

$$I(r, \psi) = \lambda(r, \psi) r^2 \cos\psi \, . \tag{6.19}$$

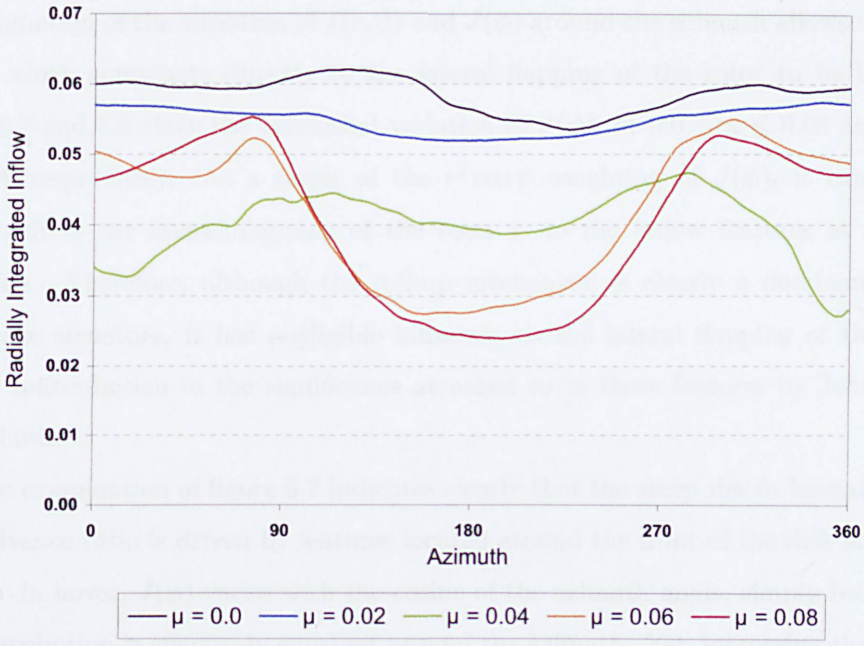


Figure 6.5: *Integrated inflow plotted as a function of azimuth,* $0 \leq \mu \leq 0.08$.

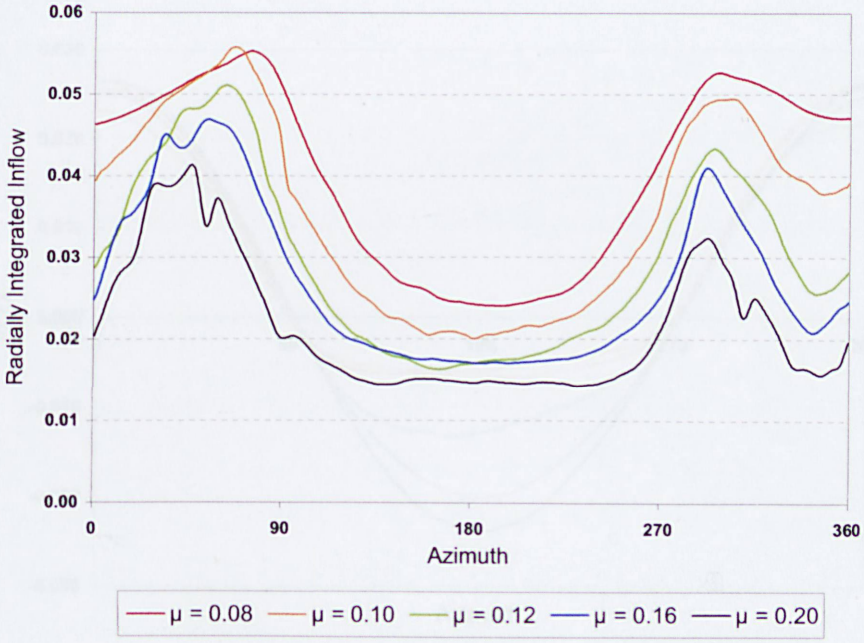


Figure 6.6: *Integrated inflow plotted as a function of azimuth,* $0.08 \leq \mu \leq 0.20$.

Examination of the variation of $I(r, \psi)$ and $J(\psi)$ around the azimuth allows the inflow features which contribute directly to the lateral flapping of the rotor to be identified. Figures 6.7 and 6.8 show the azimuthal variation of $J(\psi)$ for $0.0 \leq \mu \leq 0.08$ and $0.08 \leq \mu \leq 0.20$ respectively. As a result of the $r^2 \cos\psi$ weighting of $J(\psi)$, it can be seen how insensitive the lateral flapping of the rotor is to the inflow features at the sides of the disk. Therefore, although the roll-up mechanism is clearly a dominant feature of the wake structure, it has negligible influence on the lateral flapping of the rotor - in direct contradiction to the significance attached to to these features by Johnson and Quackenbush.

Closer examination of figure 6.7 indicates clearly that the steep rise in lateral flapping at low advance ratio is driven by features located around the front of the disk and not at the sides. In hover, $J(\psi)$ varies with the cosine of the azimuth angle, simply because the inflow distribution is effectively constant around the azimuth. Yet, increasing the forward speed of the rotor by even a small amount leads to a significant decrease in the magnitude of $J(\psi)$ between 90° and 270°.

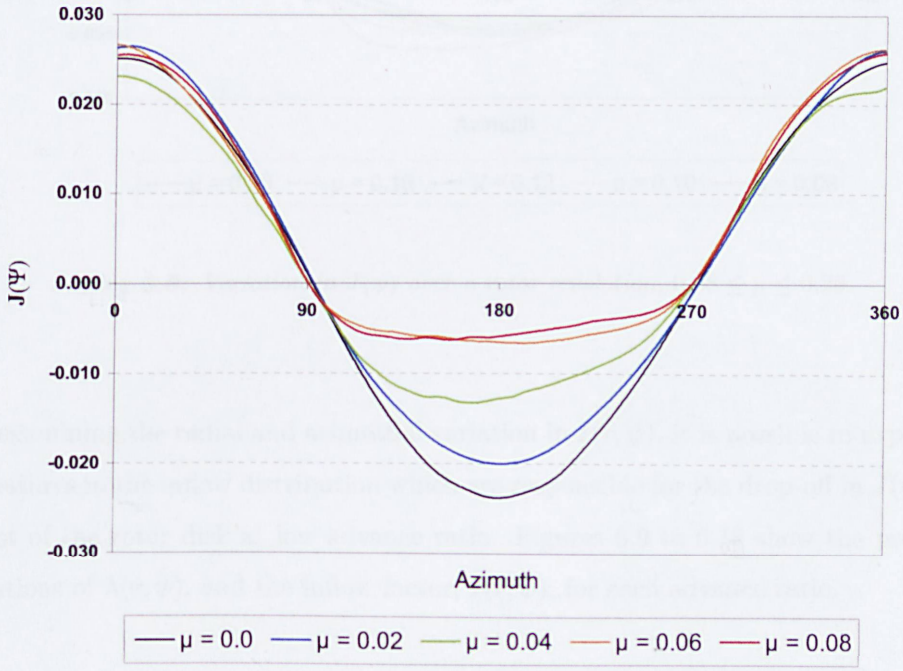


Figure 6.7: *Variation in $J(\psi)$ over a rotor revolution, $0.0 \leq \mu \leq 0.08$.*

Beyond $\mu = 0.08$ no further drop off in $J(\psi)$ over the front of the rotor disk is seen. Instead, a gradual reduction in $J(\psi)$ develops over the rear of the disk. The distinct change in the way $J(\psi)$ varies with advance ratio, influencing only the front of the disk below $\mu = 0.08$ and only the rear of the disk above $\mu = 0.08$, suggests that the flow surrounding the rotor undergoes a marked change in character close to $\mu = 0.08$. Further analysis of the inflow distributions and wake structures, presented later in this chapter, suggests strongly that this is indeed the case.

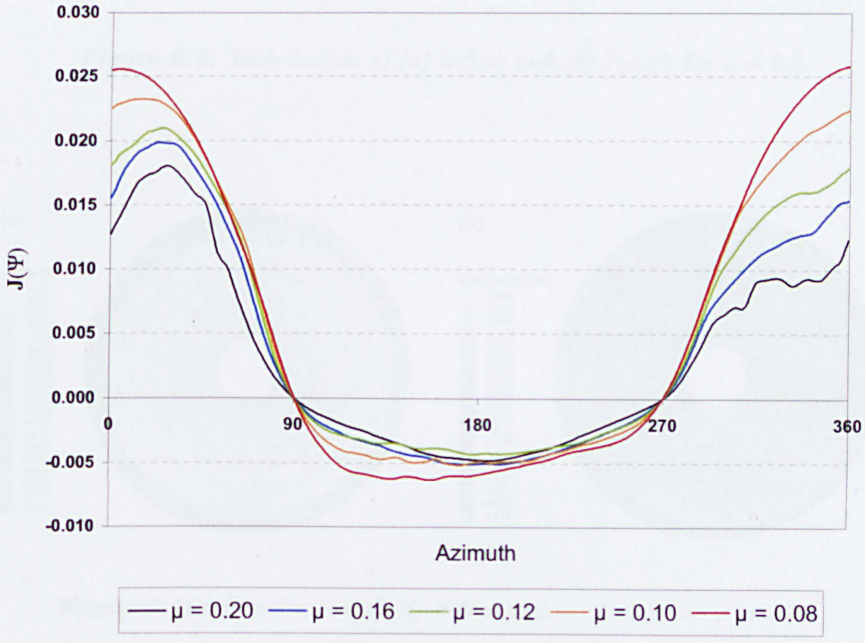


Figure 6.8: *Variation in $J(\psi)$ over a rotor revolution, $0.08 \leq \mu \leq 0.20$.*

By examining the radial and azimuthal variation in $I(r, \psi)$, it is possible to expose the exact features in the inflow distribution which are responsible for the drop-off in $J(\psi)$ over the front of the rotor disk at low advance ratio. Figures 6.9 to 6.18 show the predicted distributions of $\lambda(r, \psi)$, and the inflow factor, $I(r, \psi)$, for each advance ratio.

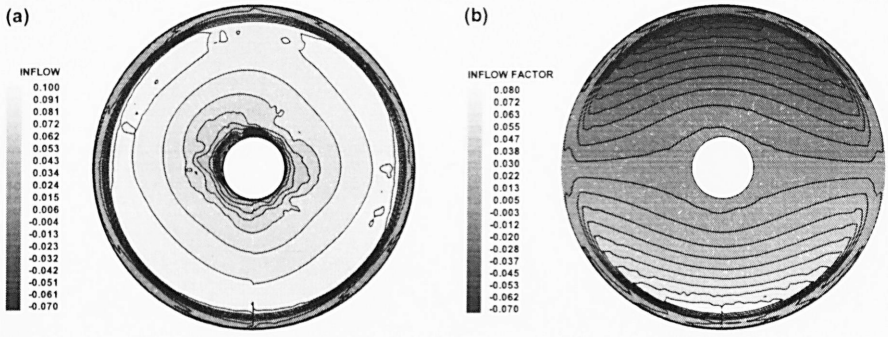


Figure 6.9: *Distribution of (a) inflow and (b) $I(r, \psi)$ for $\mu = 0.0$.*

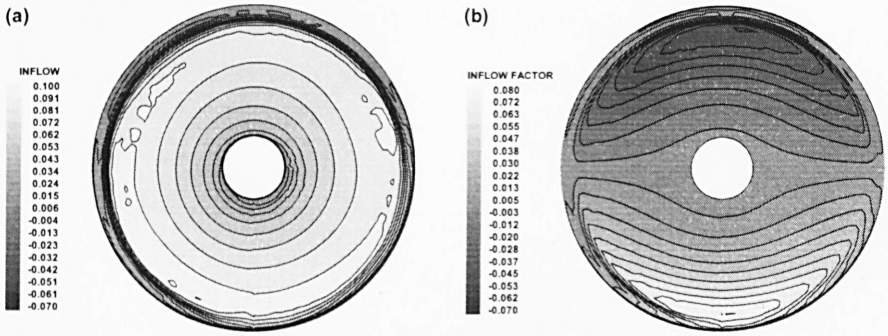


Figure 6.10: *Distribution of (a) inflow and (b) $I(r, \psi)$ for $\mu = 0.02$.*

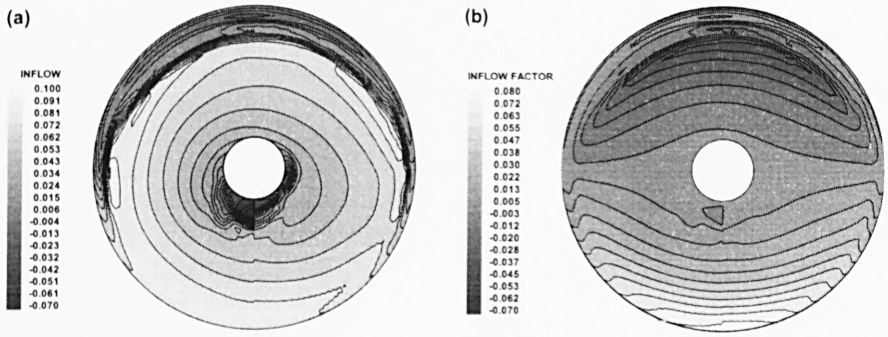


Figure 6.11: *Distribution of (a) inflow and (b) $I(r, \psi)$ for $\mu = 0.04$.*

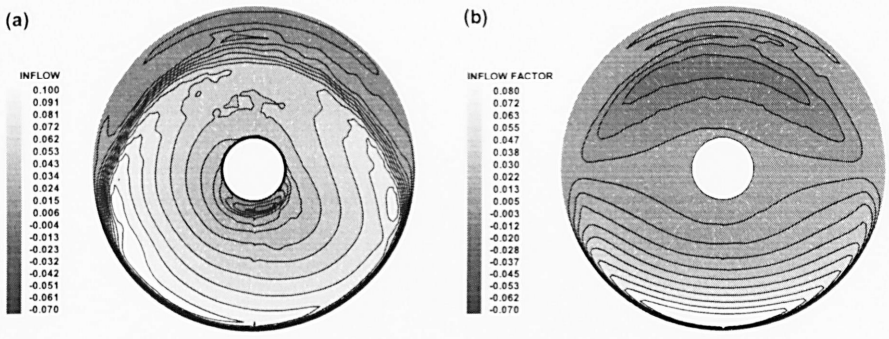


Figure 6.12: *Distribution of (a) inflow and (b) $I(r, \psi)$ for $\mu = 0.06$.*

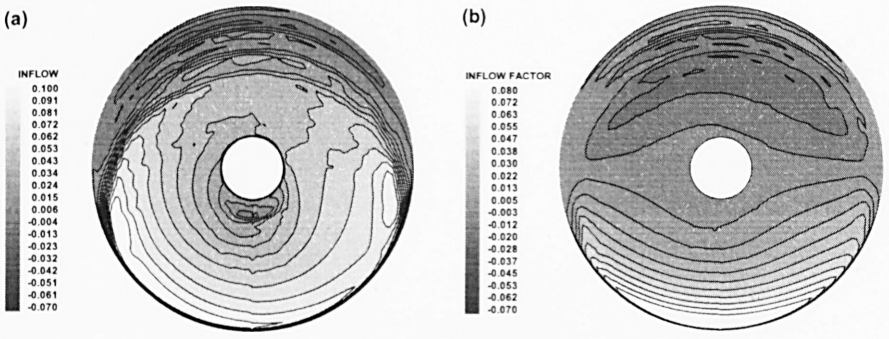


Figure 6.13: *Distribution of (a) inflow and (b) $I(r, \psi)$ for $\mu = 0.08$.*

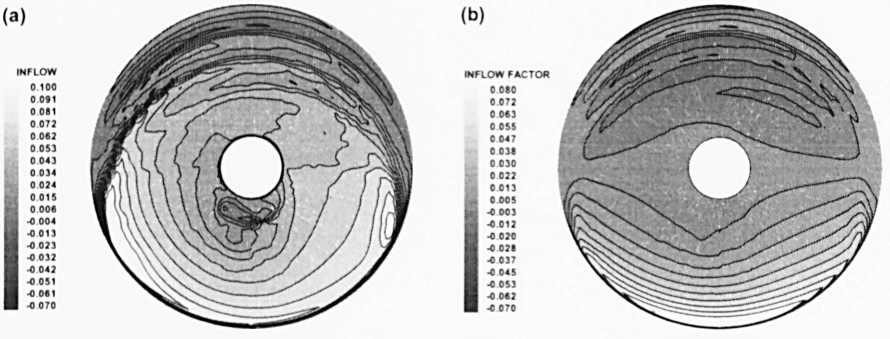


Figure 6.14: *Distribution of (a) inflow and (b) $I(r, \psi)$ for $\mu = 0.10$.*

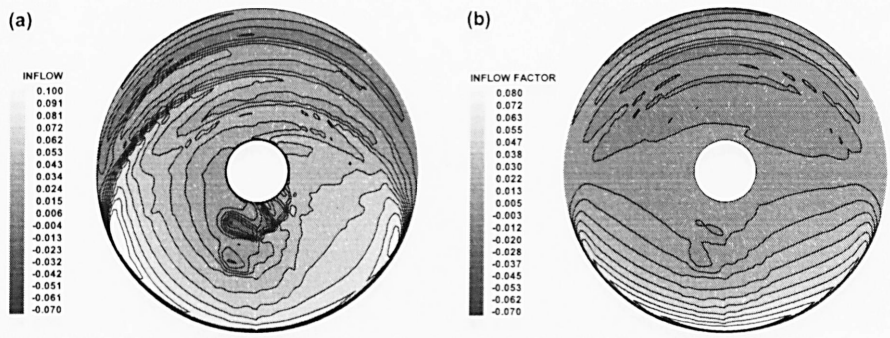


Figure 6.15: *Distribution of (a) inflow and (b) $I(r, \psi)$ for $\mu = 0.12$.*

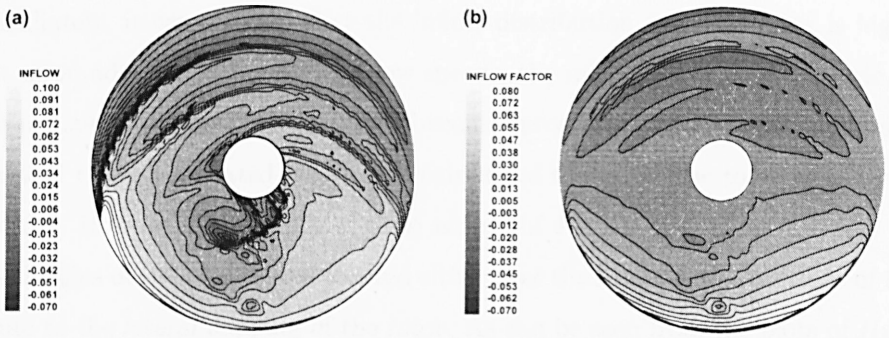


Figure 6.16: *Distribution of (a) inflow and (b) $I(r, \psi)$ for $\mu = 0.16$.*

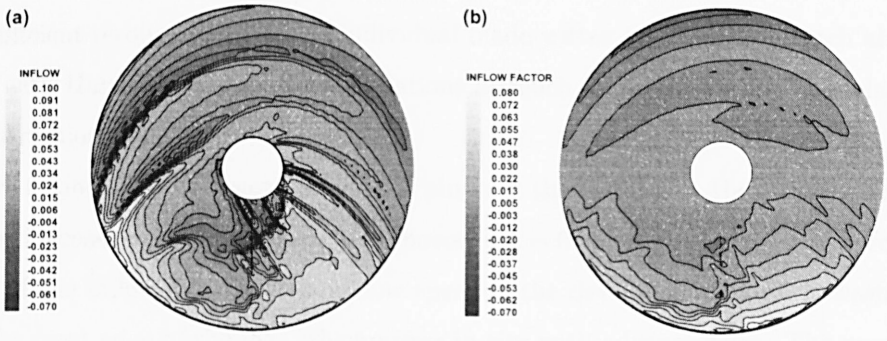


Figure 6.17: *Distribution of (a) inflow and (b) $I(r, \psi)$ for $\mu = 0.20$.*

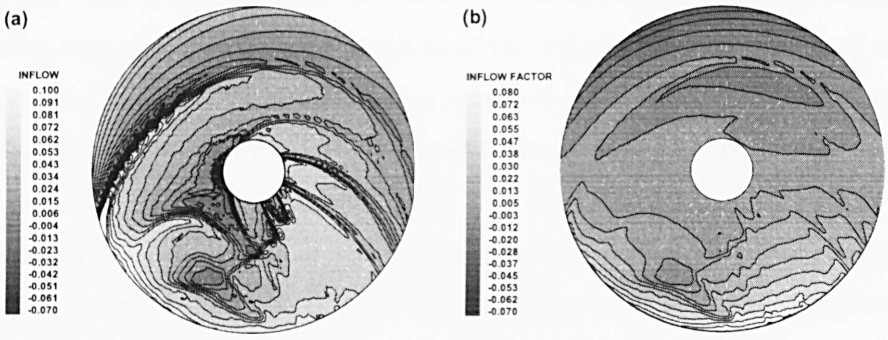


Figure 6.18: *Distribution of (a) inflow and (b) $I(r, \psi)$ for $\mu = 0.24$.*

Immediately, it can be seen that the inflow distribution over the rotor is highly dependent upon advance ratio. At very low speeds, the inflow is nearly symmetric, but as the forward speed is increased the inflow becomes progressively dominated by a series of BVI-induced ridges associated with the proximity of the rotor disc to vortical structures in the wake. However, due to the $r^2 \cos\psi$ nature of $I(r, \psi)$, only those features located towards the tips of the blades, and located either over the front or rear portions of the disc contribute to the lateral flapping of the rotor. As can be seen from the plots of $I(r, \psi)$, in which much of the fine detail of the inflow distribution is effectively filtered out, the lateral flapping of the rotor is more sensitive to the subtle variations in the gross inflow features, rather than the high-frequency features associated with individual BVI. The fact that the results from the low resolution VTM simulations (presented in chapter 5), which do not have sufficient resolution to resolve individual blade vortex interactions, match almost as closely with Harris' results as the calculations at much higher resolution is explained by this observation.

More importantly, it is now possible to pinpoint the features in the inflow which drive the steep increase in lateral flapping from hover to $\mu = 0.08$. Arguably the most prominent feature of the inflow distributions at low speed is the development of an upwash region along the front edge of the disk which grows in size with advance ratio. The presence of the upwash region at the front of the disk leads directly to the drop off in the magnitude of $I(r, \psi)$ with forward speed, which in turn leads to the characteristic changes in $J(\psi)$ over the front of the disk shown in figure 6.7.

The fact that the upwash region extends round the sides of the rotor disk suggests that the upwash may also be linked to the roll-up of the wake at the lateral edges of the rotor disk. This may explain the correlation that Quackenbush saw between the magnitude of the peaks in the inflow distribution, associated with the wake roll-up, and the magnitude of the lateral flapping of the rotor.

The presence of an upwash at the front of the rotor disk can be seen clearly in the resultant structure of the wake. Figure 6.19 shows the wake structure, visualised using contours of vorticity magnitude on a vertical slice through the rotor hub, for a range of advance ratios. In figures 6.19(a), (b) and (c) the tip vortices generated at the front of the disk can be seen to rise above the rotor disk under the influence of the upwash at the front of the rotor, before being pulled back through the rotor under the effect of the mean downwash.

A subtle feature present in figures 6.19(c) and (d), but not (a) and (b), is the kink in the underside of the wake as it passes beneath the rotor hub. Since the vortices contained in the underside of the wake originate from the front of the disk, their trajectories will be strongly coupled to the strength and size of the upwash region at the front of the disk. Indeed, the formation of the kink in the wake structure appears to coincide with the emergence of the 1/rev variation in the inflow at $\mu = 0.08$ (see figures 6.5 and 6.6). Over the front of the disk the inflow is relatively low in magnitude compared to that seen over the rear of the disk. Hence, as the wake convects from the front to the back of the rotor, it sees a sudden increase in the downwash beneath the rotor, leading to the formation of the kink in the wake structure. Furthermore, the fact that the tip vortices are transported upwards first by the upwash at the front of the disk then downwards by the mean downwash at the rear of the disk implies that the wake will remain in the vicinity of the rotor for longer than it would if the upwash region was not present. This explains, to an extent, why the wake tends to flatten, or 'hang up close' to the rotor, as observed by Johnson and Quackenbush. By remaining close to the rotor at high speed, the proximity of the wake to the rotor will naturally lead to a net increase in the inflow seen by the rotor, as observed previously in figure 6.4.

Arguably the most general observation that can be made regarding the wake structures shown in figure 6.19 relates to their stability. At low advance ratio the wake structures are much more unsteady and are less well ordered than those at high advance ratio. In figures

6.19(a) and (b) the products of instabilities in the flow can be seen clearly in the form of vortex pairing and vortex merging in the wake a small distance below and behind the rotor. Yet in figures 6.19(c) and (d) these features do not manifest until far downstream of the rotor. A detailed analysis of the wake structures, presented later in this chapter, certainly suggests that the stability of the wake structure may explain why the peak lateral flapping occurs at an advance ratio of $\mu = 0.08$.

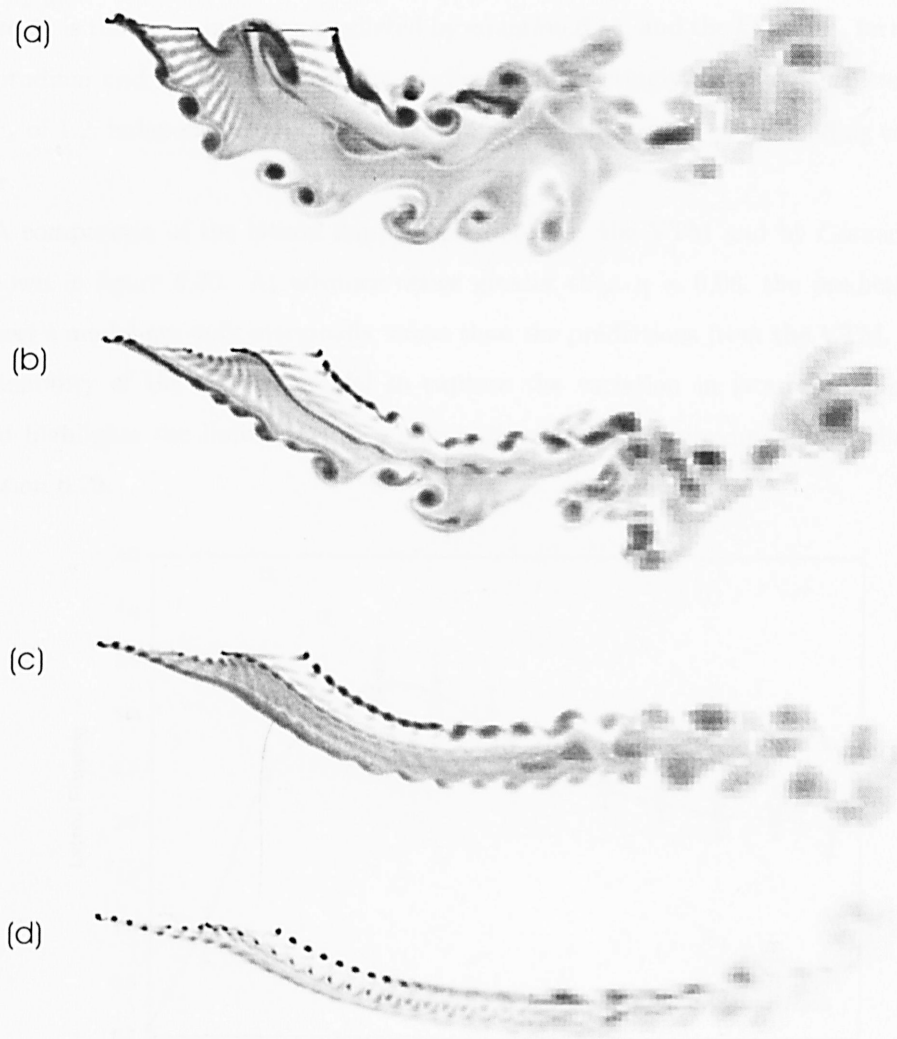


Figure 6.19: *Visualisations of the wake geometry on a vertical slice through rotor hub at various advance ratios: (a) $\mu = 0.04$ (b) $\mu = 0.06$ (c) $\mu = 0.08$ (d) $\mu = 0.10$.*

6.4 Linear Inflow Models

It is interesting to note that the lateral flapping of the rotor at high forward speed, $\mu > 0.08$, can be predicted accurately by assuming the inflow distribution to vary linearly from the front to the back of the disk. This approach was first proposed by Glauert [84], who defined the inflow distribution as

$$\lambda(r, \psi) = \lambda_0(1 + k_x r \cos\psi + k_y r \sin\psi) \,, \tag{6.20}$$

where λ_0 is the mean inflow as predicted by equation 6.15, and the k_x and k_y terms are the longitudinal and lateral linear inflow gradients. Interestingly, Glauert suggested a value for k_x of 1.2, independent of μ, which generates a small upwash at the leading edge of the rotor.

A comparison of the lateral flapping predicted by the VTM and by Glauert's model is shown in figure 6.20. At advance ratios greater than $\mu = 0.08$, the predictions from Glauert's model are only marginally worse than the predictions from the VTM. However, the inability of the Glauert model to capture the variation in lateral flapping at low speed highlights the limitations of a simple linear inflow approximation of the form of equation 6.20.

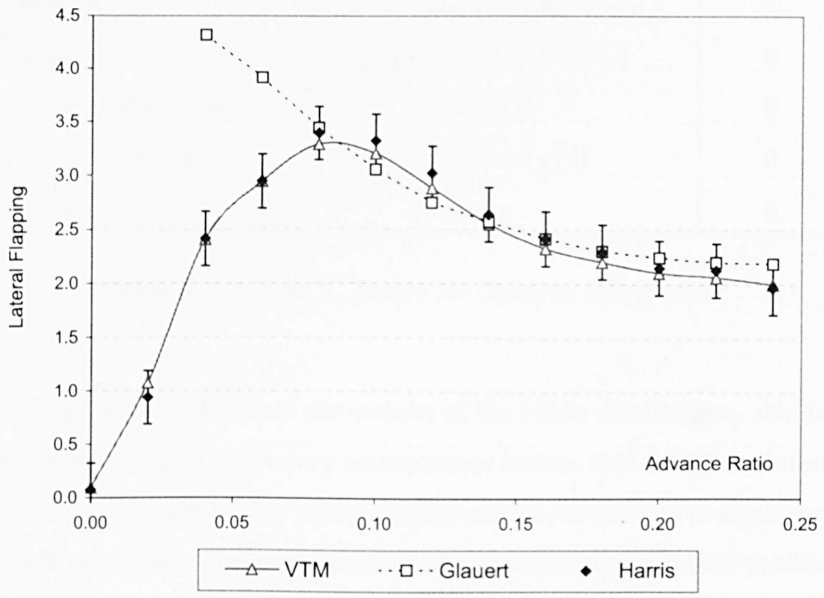


Figure 6.20: *Comparison between the predictions of the VTM and Glauert's model ($k_x = 1.35$, $k_y = 0.0$).*

Numerous extensions to Glauert's model have been developed in an attempt to account for the higher-order non-linear components. These methods express k_x and k_y as functions of wake skew angle, χ, and advance ratio; the expressions used by some of the most popular linear-inflow models are listed in table 6.1. A useful overview of these methods can be found in Leishman [85] and further information regarding the derivation of these methods can be found in Johnson [82]. The value of k_x given by each of these models is plotted as a function of advance ratio in figure 6.21; the effective value of k_x inferred from Harris' experimental results is also plotted.

In general, these models are derived from simple descriptions of the wake structure, such as prescribed vortex wake models, in which the mutual distortion effects of the vortical structures in the wake are neglected. Although most of these models improve upon the predictions of Glauert's original model, it can be seen from figure 6.21 that none of the models are able to predict accurately the lateral flapping over the full range of forward speeds.

Author(s)	k_x	k_y
Coleman et al.[86]	$\tan(\chi/2)$	0
Drees [87]	$(4/3)(1-\cos\chi-1.8\mu^2)/\sin\chi$	-2μ
Payne [88]	$(4/3)(\mu/\lambda_0/(1.2+\mu/\lambda_0)$	0
White & Blake [89]	$\sqrt{2}\sin\chi$	0
Pitt & Peters [90]	$(15\pi/23)\tan(\chi/2)$	0
Howlett [91]	$\sin^2\chi$	0

Table 6.1: *k_x and k_y factors for Glauert's inflow model.*

By including the first harmonic component of the inflow distribution, the linear inflow models are able to capture the primary aerodynamic feature that drives the lateral flapping of the rotor, and consequently they achieve significant improvements in accuracy compared to uniform inflow models. However, analysis of the inflow distributions predicted by the VTM suggests that the assumption of a linear variation in inflow along the rotor radius is certainly not adequate. For example, the upwash region seen at the front edge of the

rotor at low speed flight, which is believed to drive the rapid increase in lateral flapping at low speed, can not be resolved faithfully using a linear inflow assumption.

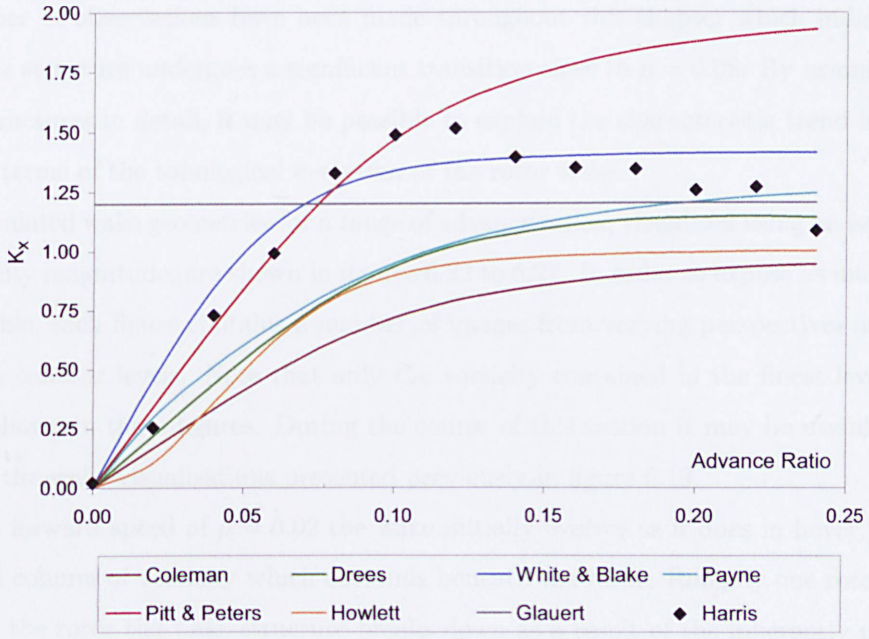


Figure 6.21: *Comparison of k_x for the methods presented in table 6.1.*

Furthermore, by describing the system in terms of a wake skew angle and a mean inflow, the linear inflow models make a number of assumptions regarding the structure of the wake and its induced velocity field. These models rely upon Glauert's theory to evaluate the mean inflow. As demonstrated earlier in section 6.3, the mean inflow seen by the rotor diverges from Glauert's result above $\mu = 0.08$. Furthermore, as can be seen from the wake structures shown in figure 6.19, it is difficult to define rigorously a wake skew angle for a real helicopter wake, particularly at high forward speed. Methods which describe the wake system in terms of simple geometric measures, such as wake skew angle, therefore run the risk of missing out some of the subtle yet important features of the rotor wake.

The fact that none of the linear inflow models predicts successfully the lateral flapping of the rotor over the full range of flight speeds suggests that the distortion of the wake by its own self-induced velocity field, and the high-order variation in inflow along the rotor radius need to be captured for the lateral flapping of the rotor to be predicted accurately.

6.5 Wake Topology

A number of observations have been made throughout this chapter which indicate that the wake structure undergoes a significant transition close to $\mu = 0.08$. By examining the wake structures in detail, it may be possible to explain the characteristic trend in Harris' data in terms of the topological evolution of the rotor wake.

Calculated wake geometries for a range of advance ratios, visualised using an iso-surface of vorticity magnitude, are shown in figures 6.22 to 6.27. In order to expose as much detail as possible, each figure contains a number of images from varying perspectives and using different contour levels. Note that only the vorticity contained in the finest level of the grid is shown in these figures. During the course of this section it may be useful to refer back to the wake visualisations presented previously in figure 6.19.

At a forward speed of $\mu = 0.02$ the wake initially evolves as it does in hover, forming a helical column of vorticity which descends beneath the rotor. Roughly one rotor radius beneath the rotor the wake structure breaks down as a result of the inherently unsteady dynamics of rotor wakes at low speed; these dynamics or instabilities in the wake manifest through vortex pairing and vortex merging mechanisms (see figure 6.22). Consequently, the far wake is a highly unsteady flow, dominated by highly complex and contorted vortical structures.

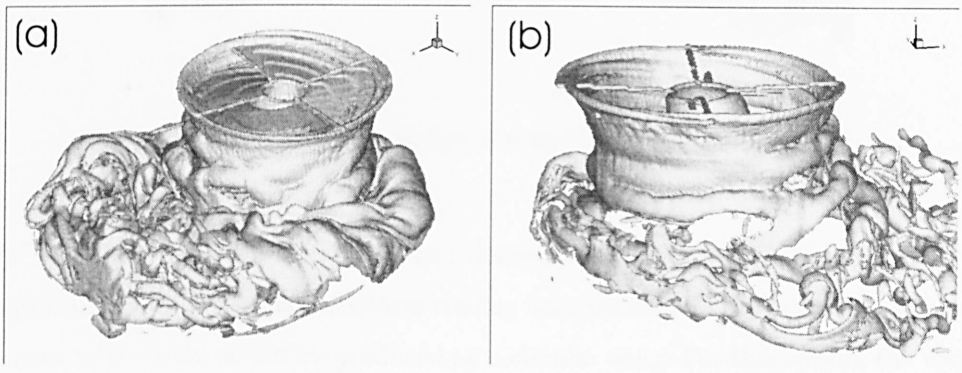


Figure 6.22: *Visualisation of wake structure at* $\mu = 0.02$.

Increasing the forward speed to $\mu = 0.04$ leads to significant changes in the overall topology of the wake. Behind the rotor the wake is highly unstructured, consisting of irregular and distorted vortical structures. Although aspects of the tubular hover-like wake can still be seen, the wake is arguably dominated by the roll-up of the wake at the sides of the disk into two large counter-rotating vortical structures. The integrity of these structures, however, is particularly weak and does not appear to persist far downstream of the rotor.

The effects of the upwash region on the wake structure can be seen in figures 6.23(b) and 6.22(b) in which the vortices located at the front of the disc are convected initially up over the front of the disk before being pulled back through the rotor by the mean downwash. Indeed, this feature can be seen at all advance ratios, as expected from the inflow maps shown previously in section 6.3. Figure 6.23(b) shows a similar effect occurring behind the root cut-out of the rotor, in which the root vortices are convected some distance above the rotor before being pulled back through the rotor.

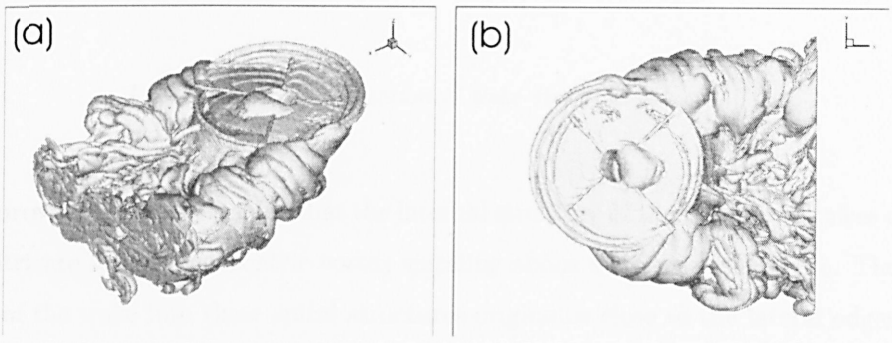


Figure 6.23: *Visualisation of wake structure at* $\mu = 0.04$.

At $\mu = 0.08$ the wake acquires a well defined structure which is dominated by the formation of two large vortical structures trailing from the sides of the rotor disk, somewhat analogous to the wake structure produced by a circular wing. For this reason, the vortical structures generated by the roll-up of the wake from the sides of the rotor will be referred to as wing-tip vortices. Nearly all of the unsteadiness seen at lower speeds has disappeared to yield a regular and periodic wake structure. This apparent onset of a stable, wing-like structure coincides with the maximum lateral flapping experienced by the rotor in forward flight (see figure 6.1).

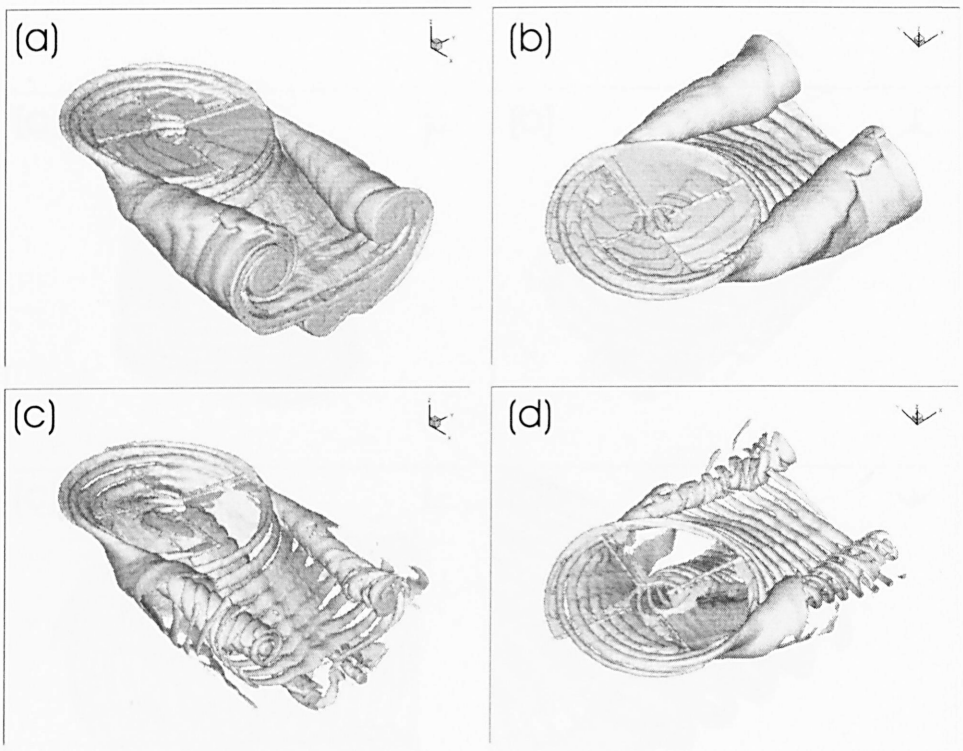


Figure 6.24: *Visualisation of wake structure at* $\mu = 0.08$.

Figures 6.24(c) and (d) show that the internal structure of the wing-tip vortices consists of an intricate series of concentric vortex spiraling about a strong central core. The initial roll-up of the wake into these spiral structures originates close to the lateral edges of the disk, at roughly 80° and 280°azimuth. The peaks seen in the inflow distribution at the sides of the disk (see figures 6.5 and 6.13), identified by both Johnson and Quackenbush, appear as a direct consequence of this roll-up process.

Increasing the forward speed further produces no obvious changes in the overall geometry of the wake. The wake structure remains stable and is dominated, as at $\mu = 0.08$, by the roll-up of the wake behind the rotor into the wing-tip vortices. Although the dimensions of the wing-tip vortices do however vary with advance ratio, becoming progressively tighter as the advance ratio is increased, they are topologically identical at all advance ratios $\mu \geq 0.08$. In fact, it appears that the topology of the entire wake structure remains unchanged for advance ratios greater than $\mu = 0.08$.

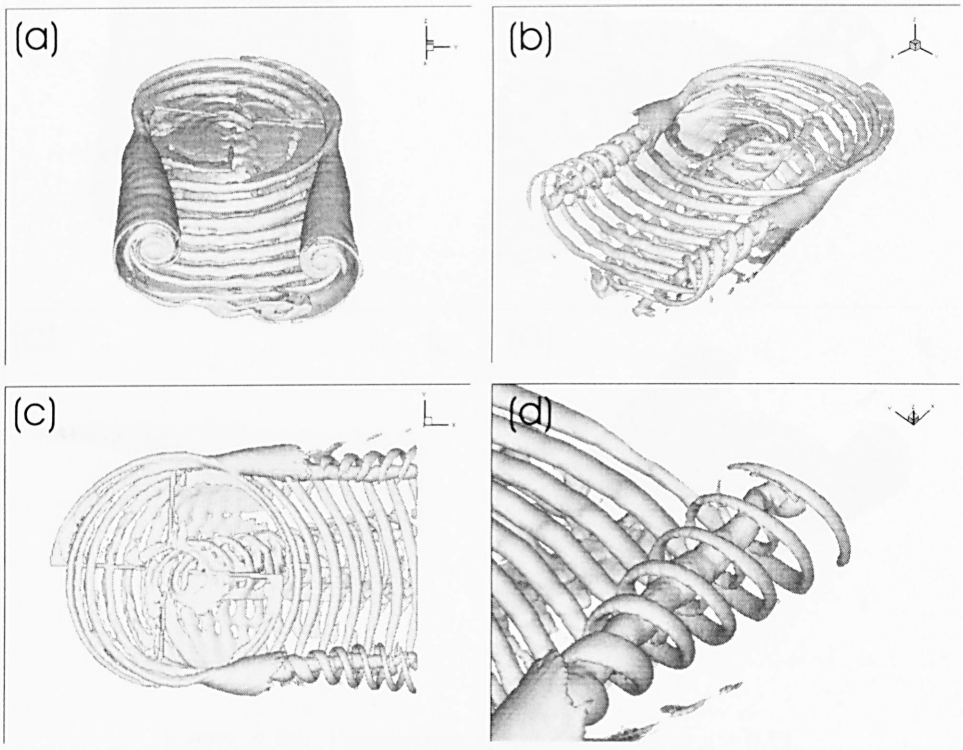


Figure 6.25: *Visualisation of wake structure at* $\mu = 0.10$.

The internal structure of the wing-tip vortices is exposed particularly well in figures 6.25(d) and 6.26(b). The outermost spirals forms from the roll-up of the underside of the wake, i.e. from those vortices produced at the front of the rotor disk. The innermost spirals forms from the roll-up of the top-side of the wake, i.e. from those vortices produced at the rear of the rotor disk.

A more subtle feature of the wake, which is present at all of the forward flight cases where $\mu \geq 0.08$, is the formation of a strong vortex emanating from the root of the advancing blade. This vortex can be seen clearly in figure 6.26(c) sitting below the main wake structure. The strength of the vortex grows with advance ratio; however, its contribution to the overall evolution of the wake is not entirely clear.

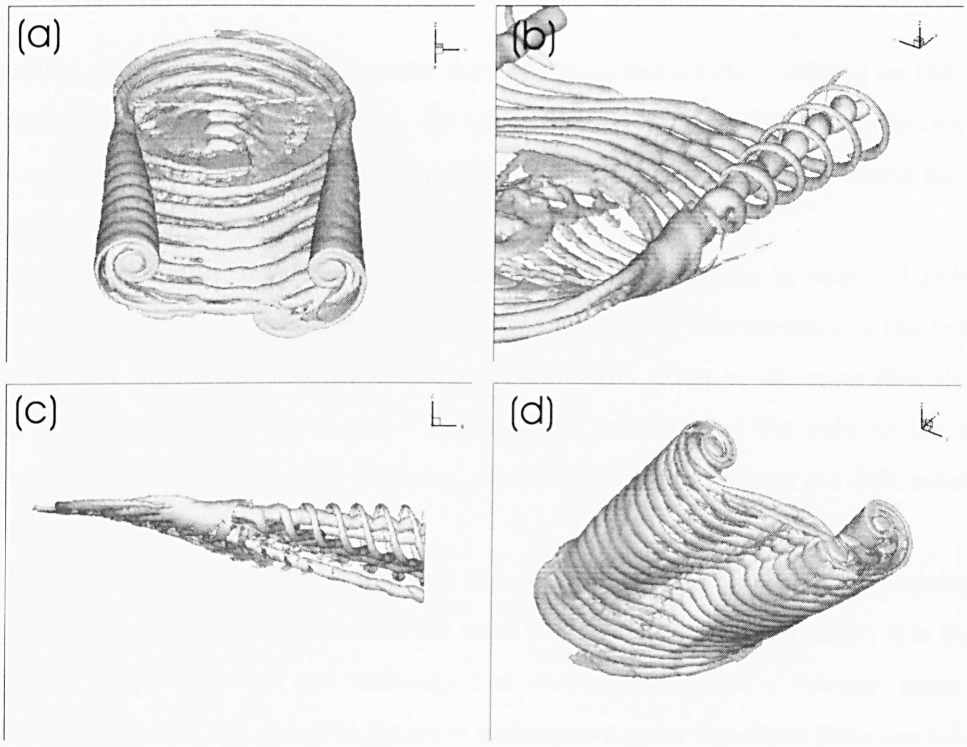


Figure 6.26: *Visualisation of wake structure at* $\mu = 0.12$.

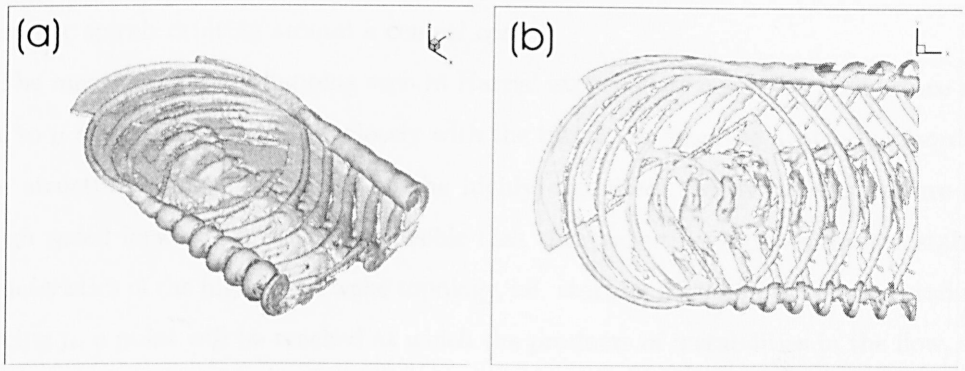


Figure 6.27: *Visualisation of wake structure at* $\mu = 0.16$.

6.6 Summary

A detailed study of Harris' experimental data has been carried out, building on the work of Johnson [80] and Quackenbush [81]. By examining in detail the inflow distribution and wake structure at each advance ratio, the key flow features controlling the lateral flapping of a rotor in forward flight have been identified.

Arguably the most important flow feature driving the variation in lateral flapping is the growth of an upwash region at the front of the rotor disk. The presence of the upwash at the leading edge of the disk forces the wake to remain closer to the rotor disk than it would if the upwash was not present. The resulting proximity of the wake to the rotor increases the mean inflow seen by the rotor, particularly over the rear of the disk, resulting in high levels of lateral flapping.

The trend seen in the lateral flapping can be explained, in part, by the topological evolution of the wake. Below $\mu = 0.08$ the wake has no well defined topology; it is highly disordered, highly distorted and unsteady, but retains elements of a tubular, hover-like wake. Between hover and $\mu = 0.08$ the wake undergoes a gross transition from the tubular wake seen in hover, to the flat, rolled-up, wing-like wake seen at high forward speed. Above $\mu = 0.08$ the wake acquires a well defined topology; dominated by the roll-up of wake behind the rotor into two distinct wing-tip-like vortices. The internal structure of these wing-tip vortices has been shown to be highly intricate, consisting of a number of concentric spirals orbiting around a central core.

The maximum lateral flapping seen in Harris' experiments occurs at an advance ratio close to $\mu = 0.08$. This coincides closely with the transition from the unsteady, disordered wake structure seen at low speed to the highly organised, steady wake structure seen in high speed forward flight. It is plausible that this transition is driven by the stability characteristics of the high speed wake topology, i.e. starting from high speed and gradually reducing μ, a point will be reached at which the products of instabilities in the flow, such as vortex pairing and vortex merging, are no longer convected downstream sufficiently fast to preserve the overall structure of the wake.

Chapter 7

Vibration Prediction

The helicopter industry as a whole lacks the capability to predict accurately the vibration levels of helicopter rotors. The AHS dynamics workshop, performed in 1996, carried out a blind comparison of various state-of-the-art prediction methods used throughout industry and academia. In their analysis of the workshop results, [1], Hansford and Vorwald remarked that none of the methods considered could predict the vibration levels to within 50% of flight test data.

Hansford and Vorwald also analysed the improvements in accuracy produced as the complexity of the models was systematically increased. In this way, they were able to identify those modelling strategies which resulted in the largest improvements in accuracy. Their analysis suggested that the largest improvements in accuracy were related to improvements in the fidelity of the aerodynamic modelling of the rotor, and most significantly, to the introduction of free-wake models.

This chapter presents an assessment of the new version of the VTM in terms of its ability to improve the accuracy of vibration prediction. The chapter begins with an analysis of the effects of blade twist on the aerodynamic forcing of the rotor system. In an attempt to improve the hover performance of their rotors, helicopter manufacturers are incorporating larger amounts of twist into the design of their rotor blades. The optimisation of the rotor for hover is achieved at a cost to the performance in forward flight. The relationship between blade twist and vibratory loads is not thoroughly understood however, mainly because the wake models employed for analysing rotor vibration do not have sufficient fidelity to capture the changes to the wake structure as blade twist is varied. Hence, the

ability of the VTM to capture the effects of blade twist on the aerodynamic forcing of the rotor system will provide an indication of its ability to improve the accuracy of vibration predictions.

Two of the most significant forward flight conditions, as far as rotor vibration is concerned, are found at transitional ($\mu \approx 0.15$) and high ($\mu > 0.3$) speeds. At transitional advance ratios, the aerodynamic loading of the rotor is dominated by numerous BVIs which excite the high-frequency dynamics of the rotor. At high speed however, the rotor vibration is driven by the strong asymmetry of the aerodynamic loading around the azimuth.

In an attempt to assess the actual improvements that can be gained from the introduction of the VTM into a vibration analysis, the VTM has been coupled with an industry-standard structural dynamics model called R150, which was developed by Westland Helicopters Ltd. (WHL). A further motivation for coupling the VTM with R150 was to gain further understanding of the relationship between blade twist and rotor vibration, thereby allowing blade twist to be used more effectively as a design parameter. The second half of the chapter documents the initial results from this integration task, and presents a number of recommendations to further improve the performance of the integrated R150-VTM code.

The AHS dynamics workshop considered two flight conditions, one at $\mu = 0.15$ and another at $\mu = 0.37$. The numerical results of the various prediction methods were compared against flight test data, produced using the Lynx XZ170 research aircraft. A detailed description of the aircraft can be found in [93] and a basic description of the main rotor geometry is provided in table 7.1.

For consistency, all of the numerical simulations presented throughout this chapter are based upon the XZ170 main rotor. Furthermore, all results presented correspond to either the $\mu = 0.15$ or $\mu = 0.37$ flight conditions considered in the AHS dynamics workshop. In all cases the main rotor is trimmed to specified rotor thrust and hub moments. The trim conditions for each of the advance ratios are listed in table 7.2.

Number of Blades	4
Rotor Radius (ft)	21.0
Blade Chord (ft)	1.296
Blade Aspect Ratio	16.2
Blade Twist	8°
Root Cut-out (ft)	5.943
Tip Geometry	Rectangular
Aerofoil Sections	NPL9618, NPL9615, NPL9617
Hub Design	Semi-rigid
Tip Speed (ft/s)	700

Table 7.1: *Description of the rotor of the Lynx XZ170 Main Rotor.*

	$\mu = 0.15$	$\mu = 0.37$
Rotor Thrust (lbs)	8662.0	9284.0
M_{1c} (lbs ft)	-19020.0	-6858.0
M_{1s} (lbs ft)	-3792.0	-20820.0

Table 7.2: *Trim conditions for each of the flight conditions used by the AHS dynamics workshop.*

7.1 Sensitivity to Blade Twist

Blade twist plays a crucial role in governing not only the aerodynamic loading of the rotor, but also the vibration levels. The modifications to the aerodynamic loading and wake structure associated with changes in blade twist can lead to significant alterations to the vibration levels of the rotor. Modern rotor designs are incorporating larger levels of blade twist in an attempt to improve hover performance. However, the design tools used by industry do not, in general, have the ability to capture the effects of blade twist on vibration levels. As described in the introduction of this chapter, this deficiency is believed

to stem from the simplicity of the wake models used for analysing rotor vibration. The performance benefits resulting from increases in blade twist are therefore achieved without a solid understanding of the implications for rotor vibration.

As a first step in analysing the potential improvements in vibration prediction that might be achieved by improved wake modelling, this section analyses the ability of the VTM to capture the effects of blade twist on the aerodynamic loading of the rotor. The XZ170 rotor, with 8° of linear twist, is used as a baseline from which to introduce parametric changes in the blade twist; the blade twist was varied from 6° to 20° in 2° increments (only linear twist distributions have been considered for this initial study). The study assumes that the rotor blades are rigid and hence any structural response originating from the flexibility of the blades is ignored. Both the $\mu = 0.15$ and $\mu = 0.37$ cases from the AHS dynamics workshop are analysed in this study. In all cases the blade aerodynamics were resolved using 32 collocation points, arranged in a cosine distribution along the blade, and the the cell size on the finest grid level was $\Delta x = 0.025R$.

Figure 7.1 show the calculated time-histories of rotor thrust over a single revolution for blade twists ranging from 6°to 20° at an advance ratio of $\mu = 0.15$. It can be seen that increases in blade twist lead to significant increases in the magnitude of the thrust oscillations experienced by a blade. A Fourier analysis of the thrust time-history is shown in figure 7.2 in which the magnitudes of each harmonic are plotted relative to the values for the blade with 8° twist. As the twist is increased the strength of the N/rev harmonic appears to increase almost linearly with the twist of the blade. For the blade with 20° twist, the strength of the N/rev harmonic is so strong that the high-frequency component of the signal can barely be seen.

Figures 7.3 and 7.4 show the thrust time-history and its Fourier decomposition for the high speed case. In contrast to the low speed case, at $\mu = 0.37$ it appears that no significant changes to the thrust history can be seen as the twist is increased. However, as shown in the harmonic analysis of the thrust, the frequency components above N/rev are clearly sensitive to changes in the blade twist, and the changes in the strength of these components will ultimately lead to modifications to the vibratory loading of the rotor.

These results clearly show how sensitive the aerodynamic loading of the blade is to variations in blade twist.

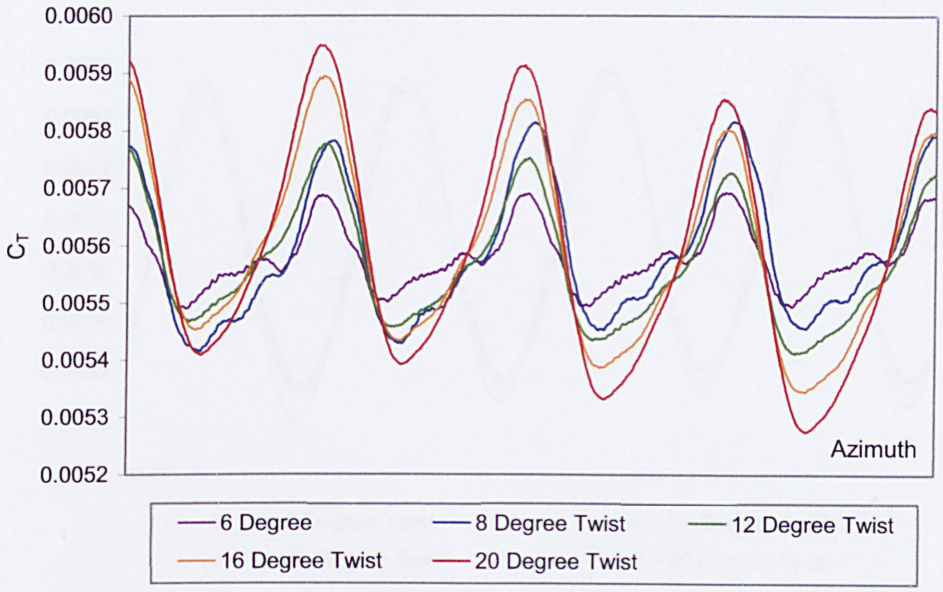


Figure 7.1: *Variation in rotor thrust due to changes in blade twist,* $\mu = 0.15$.

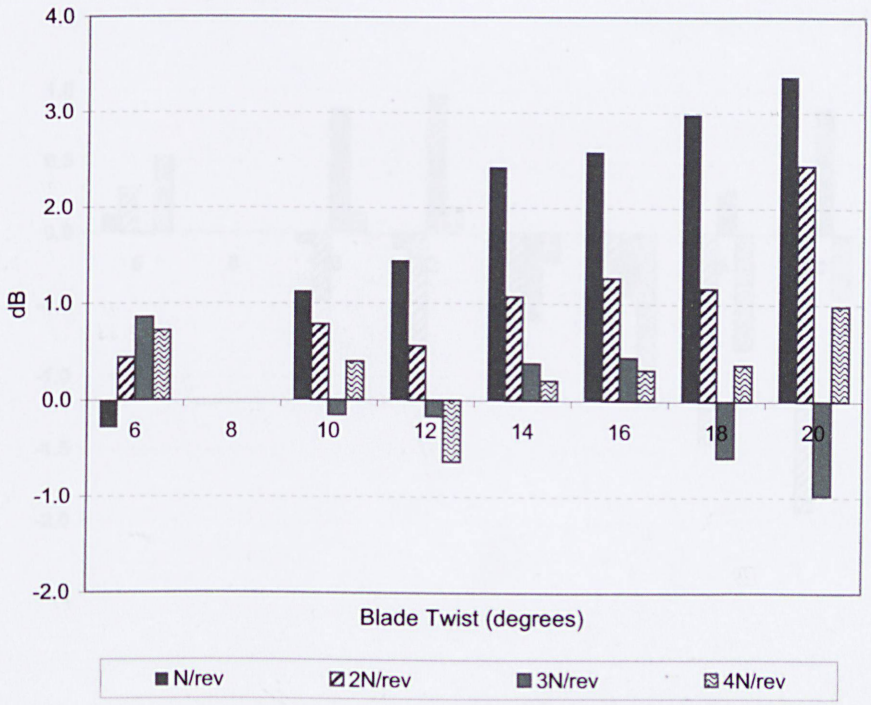


Figure 7.2: *Harmonic content of rotor thrust relative to 8° blade,* $\mu = 0.15$.

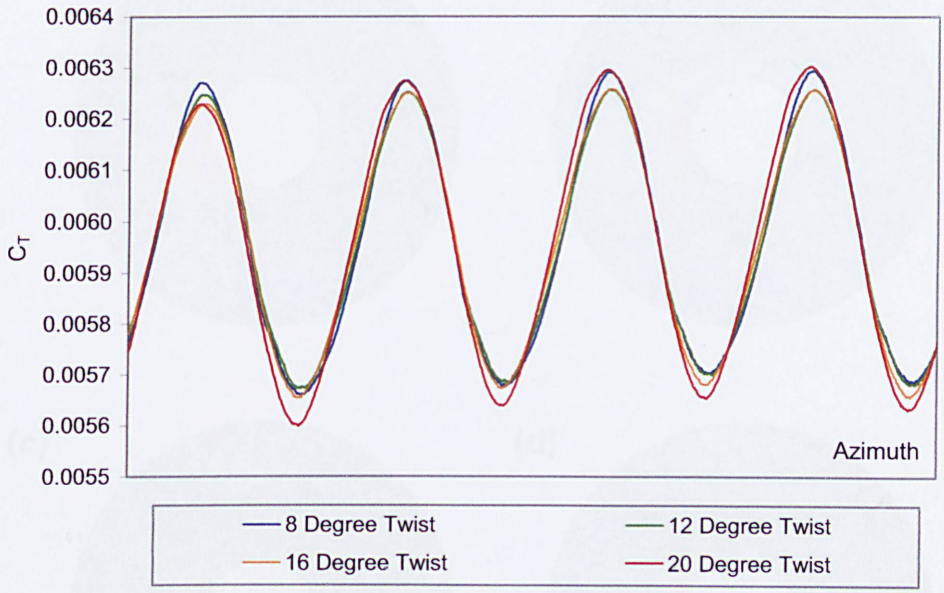


Figure 7.3: *Variation in rotor thrust due to changes in blade twist,* $\mu = 0.37$.

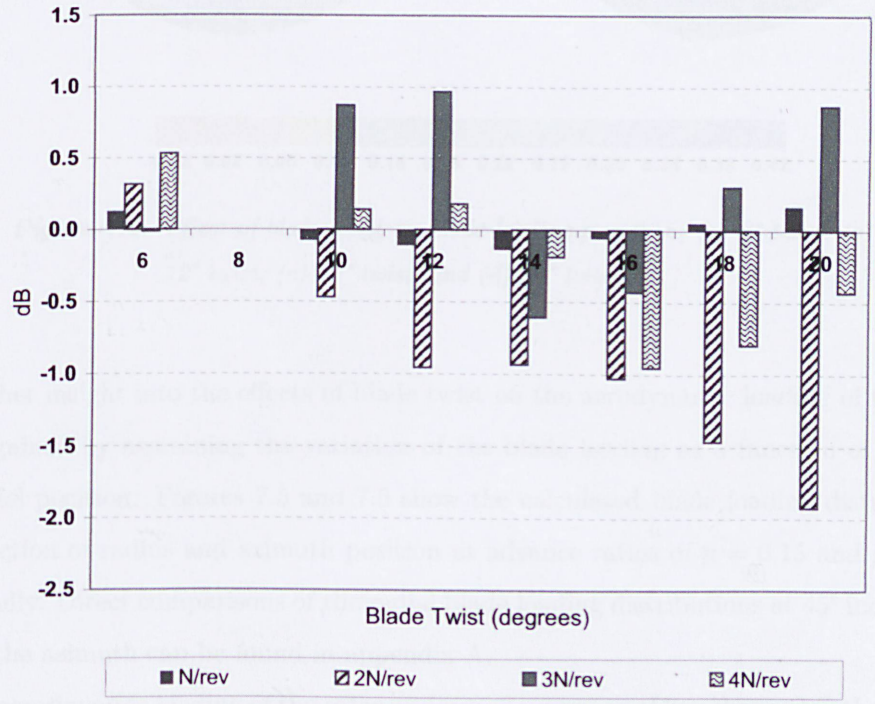


Figure 7.4: *Harmonic content of rotor thrust relative to 8° blade,* $\mu = 0.37$.

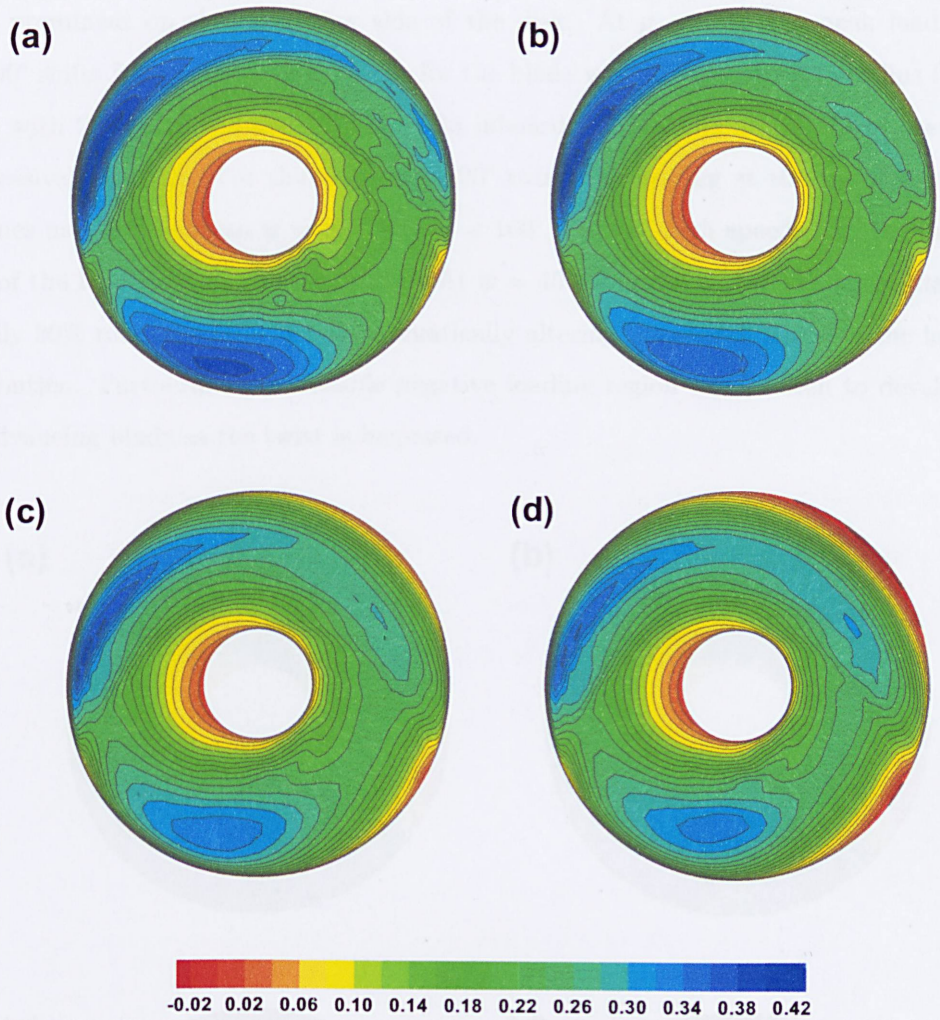


Figure 7.5: *Effect of blade twist on blade loading $\mu = 0.15$; (a) 8° twist, (b) 12° twist, (c) 16° twist, and (d) 20° twist.*

Further insight into the effects of blade twist on the aerodynamic loading of the rotor can be gained by examining the variation of the blade loading as a function of azimuth and radial position. Figures 7.5 and 7.6 show the calculated blade loading distributions as a function of radius and azimuth position at advance ratios of $\mu = 0.15$ and $\mu = 0.37$ respectfully. Direct comparisons of the radial blade loading distributions at 45° increments around the azimuth can be found in appendix A.

The aerodynamic loading of the rotor undergoes a number of key changes as the twist of the blade is increased. The primary effect of increasing blade twist, as might be expected, is to shift the aerodynamic loading of the blade inboard - an effect which appears to be

more prominent on the advancing side of the disk. At $\mu = 0.15$ the peak loading at $\psi = 90°$ shifts from roughly 95% radius for the blade with 8° twist, to 70% radius for the blade with 20° twist. As the loading shifts inboard, the loading at the tip of the blade progressively reduces. For the blade with 20° twist, the loading at the tip of the blade becomes negative between $\psi = 100°$ and $\psi = 160°$. For the high speed case, the inboard shift of the loading is more pronounced. At $\psi = 45°$ the peak in the loading shifts from roughly 80% radius to 50% radius, dramatically altering the overall shape of the loading distribution. Furthermore, a sizeable negative loading region can be seen to develop on the advancing blade as the twist is increased.

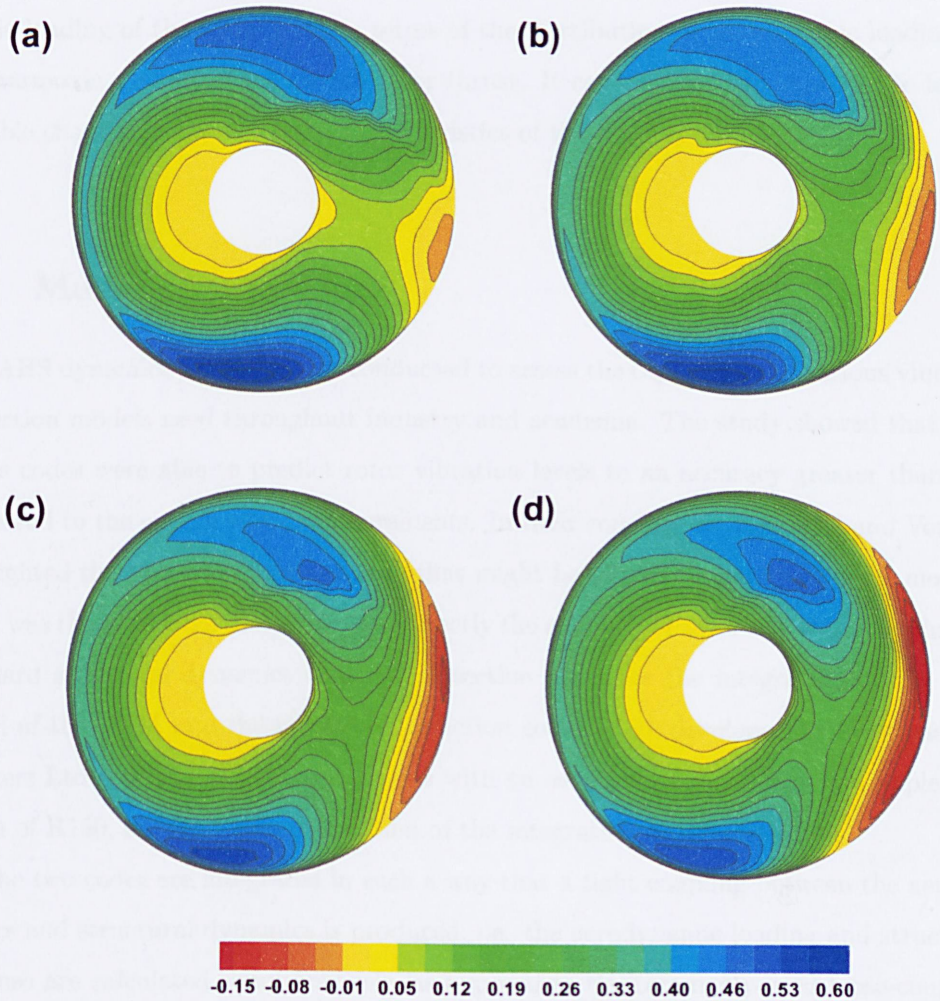


Figure 7.6: *Effect of blade twist on blade loading $\mu = 0.37$; (a) 8° twist, (b) 12° twist, (c) 16° twist, and (d) 20° twist.*

Arguably a more significant effect, as far as vibration is concerned, is the gradual reduction in the magnitude of the loading peaks associated with BVI with increase in blade twist. For the baseline blade at $\mu = 0.15$, four strong BVIs can be seen over the front of the disc. However, by increasing the twist to 20°, only two BVIs can been seen in the predicted blade loading distributions. Similarly, at high speed the dominant BVI located between $\psi = 90°$ and $\psi = 180°$ weakens significantly as the blade twist is increased.

These tests confirm that the new version of the VTM does indeed have the ability to capture the effect of blade twist on the aerodynamic loading of the rotor. The study has shown that increases in blade twist bring about significant modifications to the aerodynamic loading of the rotor, both in terms of the distribution of aerodynamic loading and the harmonic content of the overall rotor thrust. It can therefore be expected to lead to sizeable changes in the vibration characteristics of the rotor system.

7.2 Model Development

The AHS dynamics workshop was conducted to assess the capabilities of various vibration prediction models used throughout industry and academia. The study showed that none of the codes were able to predict rotor vibration levels to an accuracy greater than 50% compared to the experimental measurements. In their conclusions, Hansford and Vorwald highlighted the potential improvements that might be offered by improved wake models.

It was these findings that motivated directly the coupling of the VTM with an industry-standard structural dynamics code. This section describes the integration of the wake model of the VTM into the vibration prediction code, R150, developed by Westland Helicopters Ltd. (WHL). The section begins with an overview of the theory and implementation of R150, followed by a description of the integration of the two codes.

The two codes are integrated in such a way that a tight coupling between the aerodynamics and structural dynamics is produced, i.e. the aerodynamic loading and structural response are calculated simultaneously, as opposed to the commonly-used loose-coupling approach which iterates independent aerodynamic and structural dynamic calculations to converge towards the required solution. Although the loose-coupling approach is popular due to its straightforward implementation, it is not as robust as the tight-coupling

approach. In manoeuvring flight or in cases where large portions of the rotor is stalled, the loose-coupling approach may have difficulty converging onto a stable solution. Tight coupling between the aerodynamic loads and structural response of the rotor is not only more physically representative, but it also avoids any convergence issues and can therefore be applied to arbitrary flight conditions.

7.2.1 Structural Dynamic Model

R150 models the structural dynamics of the rotor using a modal approach. The structural response of the rotor is calculated by first linearising the equations of motion of the system and then decoupling the resulting equations using an eigenvalue analysis - the eigenvalues and eigenmodes represent the natural frequencies and mode shapes of the system. The resulting set of linear equations describe the system in terms of a number of modal degrees of freedom. For simple systems, the dynamics of the system can be modelled accurately using just a small number of modes. A detailed description of the underlying theory and implementation can be found in [94], [95] and [96].

For the structural design of the rotor system, the frequencies of most interest, as far as the structural design of the helicopter is concerned, are generally in the range 2/rev to 2N/rev. If the structural dynamics of the rotor system are be assumed to be linear, these frequency components can be captured using a relatively small number of modes. In the case of R150, the Lynx rotor system is described using a total of eight coupled modes; four flap, three lag and one torsion. This description of the modes is however slightly misleading. For example, although the first flap mode is dominated by the flap deformation, it is also includes small pitch and lag deformations. The approach is therefore able to capture the coupled pitch-flap-lag dynamics of the rotor blades. Although the mode shapes and natural frequencies can be extracted from experimental measurements, they are normally evaluated from a separate numerical analysis of the blade dynamics. Once the mode shapes and the aerodynamic forcing of the system are known, the modal equations of motion are discretised and marched through time using an explicit scheme.

R150 models only the dynamics of a single blade and its associated control linkages. It also assumes that the rotor hub is rigid; the structural response of the fuselage is therefore

neglected. This is somewhat inconsistent with a more modern view which considers the dynamics of the rotor and the fuselage to be inseparable. The Coupled Rotor-Fuselage Model (CRFM) is a much more sophisticated model used by WHL for structural loads prediction, see [94], [95] and [96]. In addition to capturing the coupled rotor-fuselage dynamics, it also includes a sophisticated pilot model for analysing vibrational loads in manoeuvring flight, as well as for analysing flight dynamics. However, the underlying theory and implementation of the structural dynamic model within R150 and the CRFM are very similar. The decision to integrate the VTM with R150, rather than the CRFM, was taken simply to avoid the added complexity of the CRFM.

7.2.2 R150-VTM Integration

This section describes the integration of the VTM wake model into R150. The combined R150-VTM code uses the original R150 code as the platform for the integration, with the blade aerodynamic model and wake model of the VTM being linked into the code structure of R150. At the start of a timestep the aerodynamic loading calculated by the VTM wake model and blade aerodynamic model, described in terms of sectional lift, drag and moment coefficients, is passed to R150. The modal forcing induced by the aerodynamic loading is calculated and used to force the structural dynamics of the rotor. The structural response of the blade, described in terms of its position and velocity at a number of points along the span, is then passed back to the VTM. The blade loading at the end of the timestep is then calculated, the trailed and shed vorticity is sourced into the computational grid, and the structure of the wake is evolved. This process is repeated until the rotor achieves the required trim state; typically ten revolutions of the rotor are required to achieve trim.

7.2.2.1 Implementation

Several major modifications to the VTM were required in order to overcome some of the differences in structure between the two codes. Arguably the most significant difference is that R150 models the dynamics of just a single blade, whereas the VTM uses a multi-blade approach. This problem is resolved by storing the position and velocity data for the R150 'reference' blade at each azimuthal station. The dynamics of the remaining blades are then reconstructed from the stored data, lagged by an azimuth angle of $2\pi i/N_b$, where i is

the blade number and N_b is the number of blades. However, the aerodynamic loading of each blade is calculated independently for each blade - the aerodynamic coupling between the blades is therefore captured completely. Note that this approach can only be applied when the steady-state solution is required, and hence one of the major advantages of the VTM, its ability to capture the unsteady evolution of the rotor wake, is sacrificed.

The current version of R150 is constrained in both its spatial and temporal resolution. The number of collocation points that can be used along the blade to represent the blades aerodynamics is fixed at 25, and the azimuthal resolution is limited to either 1° or 5° increments. The timesteps employed by the VTM are typically 0.25°; this level of resolution is required primarily to capture accurately the unsteady aerodynamics of the blades. The use of excessively large timesteps reduces the accuracy of the blade aerodynamic model. Furthermore, the fastest stable rate at which the vorticity transport equation can be evolved is governed by the Courant-Friedrichs-Lewy condition, shown previously in equation 3.3. Ideally, the timestep should be allowed to vary in proportion to the cell size used in the computation. The restriction of a large, fixed timestep limits the maximum grid resolution that can be achieved using the coupled code.

7.2.2.2 Blade Aerodynamics

The blade aerodynamic model used by the VTM does not model the aerofoil pitching moments because it is normally assumed that the blades have infinite torsional stiffness. For the prediction of vibration this assumption is no longer valid. Indeed, the unsteady aerodynamics of the rotor blades are known to play an important role in the aeroelastics of helicopter rotors [97]. The aerofoil pitching moments provide torsional damping, which, if neglected, will lead to high-frequency torsional deformations which may destabilise the simulation. Accordingly, the blade aerodynamic model was upgraded to include a simple model to predict the pitching moments. The model is derived from quasi-steady thin aerofoil theory [85] and expresses the pitching moment as

$$C_m(\alpha, \dot{\alpha}, \dot{h}, M) = C_{m0} + C_m^C(\alpha, \dot{\alpha}) + C_m^I(\dot{\alpha}, \dot{h}, M) \,, \tag{7.1}$$

where C_{m0} is the static pitching moment, C_m^C is the circulatory pitching moment, and C_m^I is the impulsive (added mass) pitching moment produced from changes in blade incidence

and plunge rate. A detailed description of the calculation of each term can be found in Beddoes [36] and Leishman [85].

7.2.2.3 Fuselage Aerodynamics

The aerodynamic interaction between the fuselage and the rotor is known to modify to the vibration levels on the rotor, particularly the magnitude and phasing of the 2/rev aerodynamic forcing. A simple source-based representation of the fuselage aerodynamics exists within R150 and is retained within the R150-VTM code. However, due to incompatibilities between the fuselage model and the wake model of the VTM, the model does not currently account for the deformation of the wake by the fuselage. Only the fuselage upwash seen by the rotor is captured. In spite of its weaknesses, the use of the fuselage model within the R150-VTM has yielded improvements in the phasing of the loading in the two AHS dynamics workshop cases.

7.3 AHS Dynamics Workshop

Having integrated the VTM into the R150 structural dynamics model, the predictions of the resulting R150-VTM code were compared directly against the Lynx XZ170 flight test data as well as the predictions of the original R150 model.

Hansford and Vorwald's study constrained its analysis to just two forward flight conditions; $\mu = 0.15$ and $\mu = 0.37$. In order to limit the contamination of the vibration measurements from the structural response of the fuselage and manoeuvre loads, each test was carried out to 'performance standard' *. Each rotor blade was fitted with a total of 15 strain gauges, taking measurements of the flapwise and lagwise bending moments at seven locations along the blade radius, and one further gauge to measure the loading within the pitch link. The hub loads could not be measured directly on the aircraft and were therefore reconstructed using the method of Strain Modal Synthesis (SMS) [98].

*Performance Standard: the rotor loading and forward speed are held constant over the two minute duration of the test, during which measurements of rotor speed, rotor torque and aircraft altitude must remain steady.

7.3.1 Convergence Study

Before comparing the predictions of the R150-VTM code with the flight test data, a convergence study was carried out to evaluate the sensitivity of the solutions to the resolution of the computational grid. The convergence tests were carried out on the high speed case ($\mu = 0.37$) analysed in the AHS dynamics workshop. The resolution of the computational grid was varied from 10 cells per radius ($\Delta x = 0.10R$) to 50 cells per radius ($\Delta x = 0.02R$).

As demonstrated previously in Chapter 5, the gross features of the aerodynamic loading can be captured accurately using very low resolutions, whereas the fine-scale loading features, associated with BVIs, are only exposed using higher grid resolutions. The results of this study are consistent with this observation.

The aerodynamic loading of the rotor produced in the high speed flight condition is dominated by a single BVI located between $\psi = 90°$ and $\psi = 180°$, see figure 7.6. Figure 7.7 shows the distribution of the predicted normal force coefficient along the blade radius at $\psi = 135°$. Using a grid resolution of 10 cells per radius ($\Delta x = 0.10R$), the strong BVI at 65% radius is not exposed at all. As the resolution is increased to 50 cells per radius ($\Delta x = 0.02R$), the BVI feature is resolved more sharply .

However, in regions of the azimuth where no strong BVI exist, for instance at $\psi = 45°$, shown in figure 7.8, the blade loading is predicted accurately using all of the resolutions considered by the study.

The convergence properties of the VTM are governed strongly by the compatibility between the resolution of the blade aerodynamic model and the resolution of the computational grid. All the vorticity contained in the computational grid originates from the blade aerodynamic model, and the resolution of that model therefore dictates the range of length-scales of the vortical structures entering the wake. For a fixed number of collocation points, the predicted blade loading will converge as the grid resolution is increased. Once the resolution of the grid becomes sufficient to resolve all the length scales of the flow, the solution will become insensitive to further increases in grid resolution. For the case studies here, in which the blade loading is calculated at 25 stations along the blade radius, the results suggest that a grid resolution close to $\Delta x = 0.02R$ is required to obtain convergence. It is therefore essential that the resolution of the blade aerodynamic model and the computational grid are matched to ensure that the level of detail achieved by the blade aerodynamic model is preserved when the information is transferred into the computational grid, and visa versa.

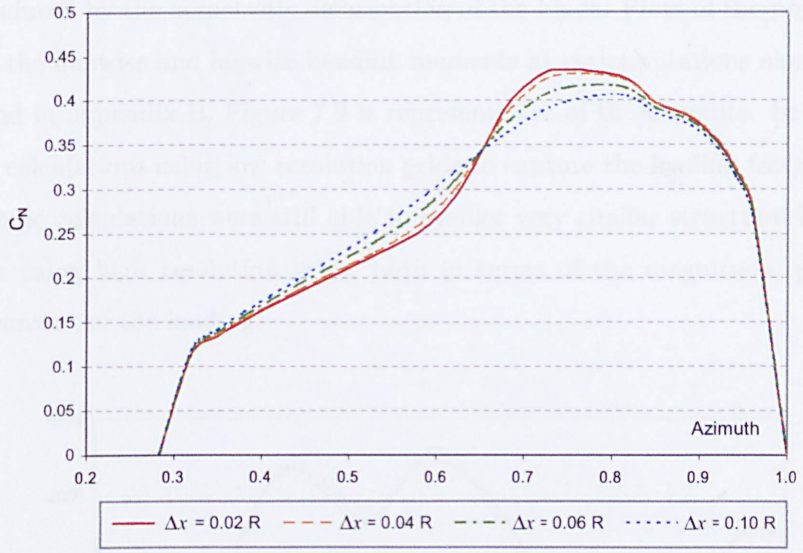


Figure 7.7: *Sensitivity of blade loading to grid resolution* $\psi = 135$, $\mu = 0.37$.

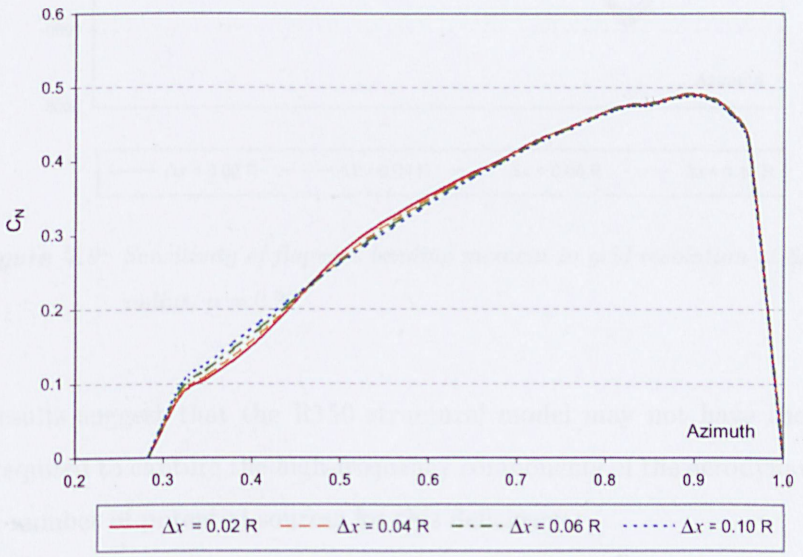


Figure 7.8: *Sensitivity of blade loading to grid resolution* $\psi = 45$, $\mu = 0.37$.

The sensitivity of the predicted structural loading to changes in the grid resolution has also been investigated by examining the predicted flapwise and chordwise bending moments induced by the aeroelastic deformation of the blade. Plots of the predicted time histories of the flapwise and lagwise bending moments at various stations along the blade can be found in appendix B. Figure 7.9 is representative of these results. In spite of the inability of calculations using low resolution grids to capture the loading features induced by BVIs, these calculations were still able to predict very similar structural loads as the calculations using high resolution grids, both in terms of the magnitude, phasing and frequency content of the loading.

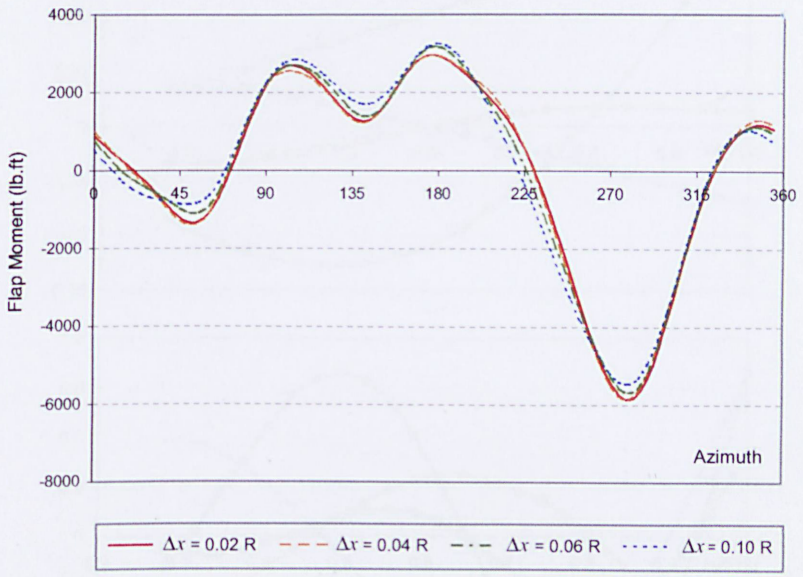


Figure 7.9: *Sensitivity of flapwise bending moment to grid resolution at 64% radius, $\mu = 0.37$.*

These results suggest that the R150 structural model may not have the fidelity or sensitivity required to capture the high-frequency components of the aerodynamic forcing. There are a number of potential sources for this deficiency.

Firstly, the current version of the R150-VTM code allows the aerodynamic loading to be sampled at only 25 points along the blade. The aerodynamic forcing of each structural

mode is then calculated as

$$\int_0^1 w(r)F_a(r)\ dr\ , \tag{7.2}$$

where $F_a(r)$ is the aerodynamic loading distribution along the blade and $w(r)$ is the mode shape. The flap components of the eight mode shapes used by R150 are shown in figure 7.10.

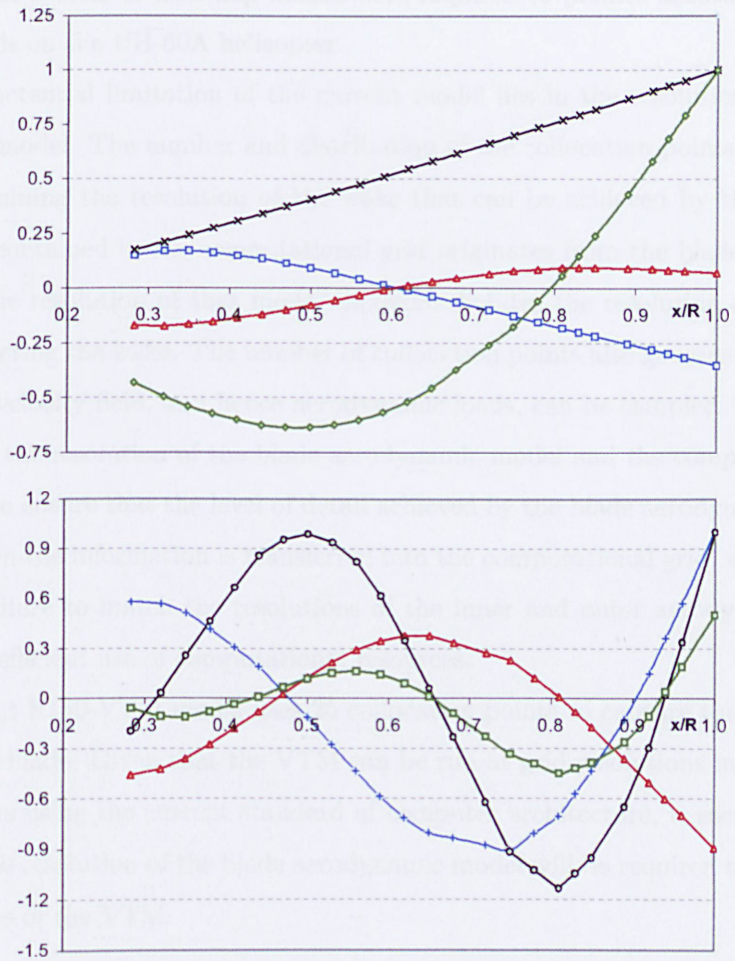


Figure 7.10: *Flap components of the R150 mode shapes.*

Arguably, these mode shapes only have sufficient spatial resolution to extract the gross features of the radial loading distribution, i.e. the aerodynamic loading features induced by BVIs will be of such a small scale compared to the modal wavelength, that their contribution to forcing of the low-order structural modes will be minimal. Hence,

for a structural model which uses only low-order modes, once convergence on the low-order components of the aerodynamic loading has been achieved, the dynamic response of the rotor will be largely insensitive to further increases in grid resolution. In order to capture the aerodynamic forcing originating from BVIs, additional modes will need to be introduced. For instance, in a recent publication by Datta and Chopra [99] [100], it was found that a total of nine flap modes were required to predict accurately the 4/rev vibratory loads on the UH-60A helicopter.

Another potential limitation of the current model lies in the resolution of the blade aerodynamic model. The number and distribution of the collocation points play a crucial role in determining the resolution of the wake that can be achieved by the model. All the vorticity contained in the computational grid originates from the blade aerodynamic model, and the resolution of that model therefore dictates the resolution of the vortical structures entering the wake. The number of collocation points also governs the resolution at which the velocity field, and hence aerodynamic loads, can be sampled. It is therefore essential that the resolution of the blade aerodynamic model and the computational grid are matched to ensure that the level of detail achieved by the blade aerodynamic model is preserved when the information is transferred into the computational grid, and vise versa. Ultimately, failure to match the resolutions of the inner and outer aerodynamic models leads to an inefficient use of computational resources.

The current R150-VTM model uses 25 collocation points to capture the aerodynamic loading of the blade. Given that the VTM can be run at grid resolutions in excess of 100 cells per radius using the current standard of computer architecture, it seems likely that increases in the resolution of the blade aerodynamic model will be required to fully exploit the capabilities of the VTM.

7.3.2 High Speed Case

No direct measurements of the aerodynamic loading of the blades were made during the flight tests. The only on-blade measurements available were the flapwise and lagwise bending moment distributions. Figures C.35 to C.39, found in appendix C1, compare the predicted and measured flapwise bending moments as a function of azimuth at a number of radial positions. The corresponding lagwise bending moment comparisons are shown in

figures C.40 to C.42, also to be found in appendix C1.

In general, the VTM produces improvements over the predictions of the original R150 model for both the flapwise and lagwise bending moments. The R150-VTM code appears to capture the phasing and frequency content of the loading more accurately than the original R150 code. However, the overall results are quite mixed. None of the predictions correlate well with the flight test data over a full rotor revolution; at any radial position, it is generally found that the loading is predicted very well over part of the azimuth, but not very well over the remainder.

Figures 7.11 and 7.12, respectively, show arguably the best and worst correlations between the R150-VTM predictions and the flight test data.

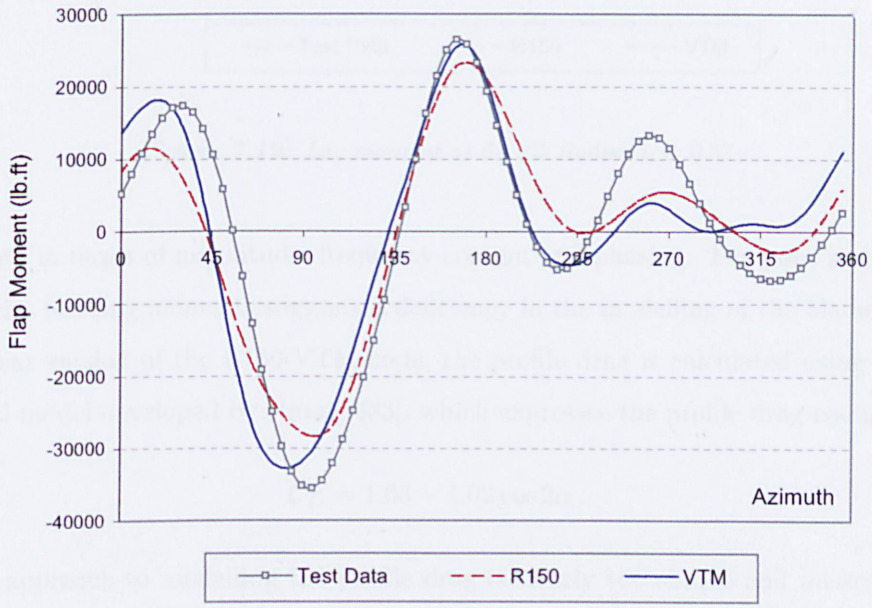


Figure 7.11: *Flap moment at 3.2% Radius* $\mu = 0.37$.

In figure 7.11, it can be seen that the R150-VTM code produces very good predictions over the first 225° of the azimuth, particularly in terms of the magnitude of the loading, although a small 15° phase lag is present on the advancing blade.

The predicted lagwise bending moments are in general less well predicted than the flapwise bending moments. Figure 7.12 shows the lagwise bending moment predictions at 64% radius. Other than the pseudo-agreement at $\psi = 180$, the overall correlation is very

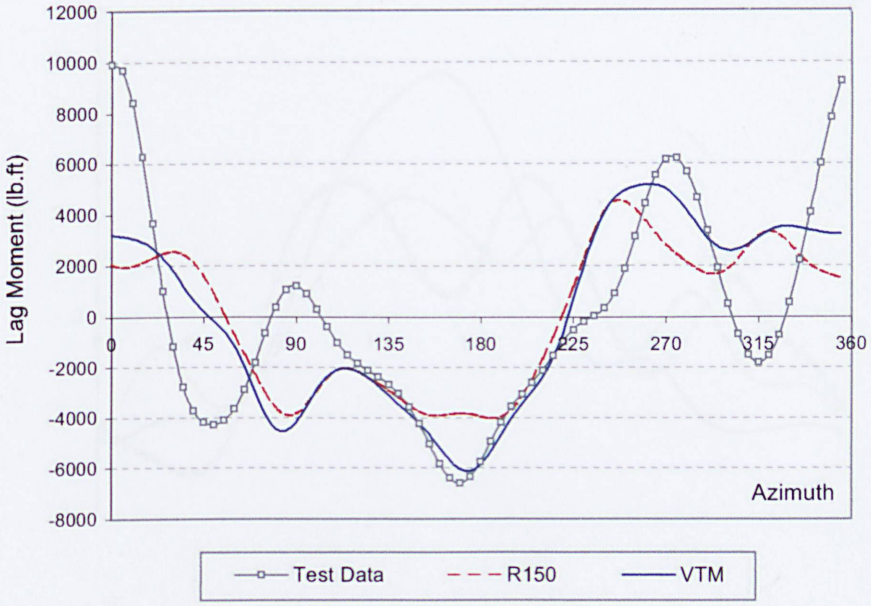


Figure 7.12: *Lag moment at 64.0% Radius* $\mu = 0.37$.

poor, both in terms of magnitude, frequency content and phasing. The poor prediction of the lagwise bending moments suggests a deficiency in the modelling of the blade drag. In the current version of the R150-VTM code, the profile drag is calculated using a simple empirical model developed by Prouty [83], which expresses the profile drag coefficient as

$$C_D = 1.03 - 1.02 \cos 2\alpha \, . \tag{7.3}$$

This approach to modelling the profile drag is clearly too simple and misses out the subtle variations in drag with incidence and Mach number. The use of real aerofoil data should significantly improve the accuracy of the lagwise bending moment predictions.

Another area which is likely to benefit from improvements in the modelling of the blade aerodynamics is the prediction of the control rod loads. Figure 7.13 compares the predicted control loads with the original R150 predictions and the flight test data.

The structural loads experienced by the control rods are largely governed by the torsional loading of the blades, and hence are particularly sensitive to the aerodynamic pitching moments generated by the blade. It is believed that the strong 1/rev component seen in the R150-VTM predictions is associated with a deficiency in the modelling of the aerofoil pitching moments. The current version of the R150-VTM model assumes that the static

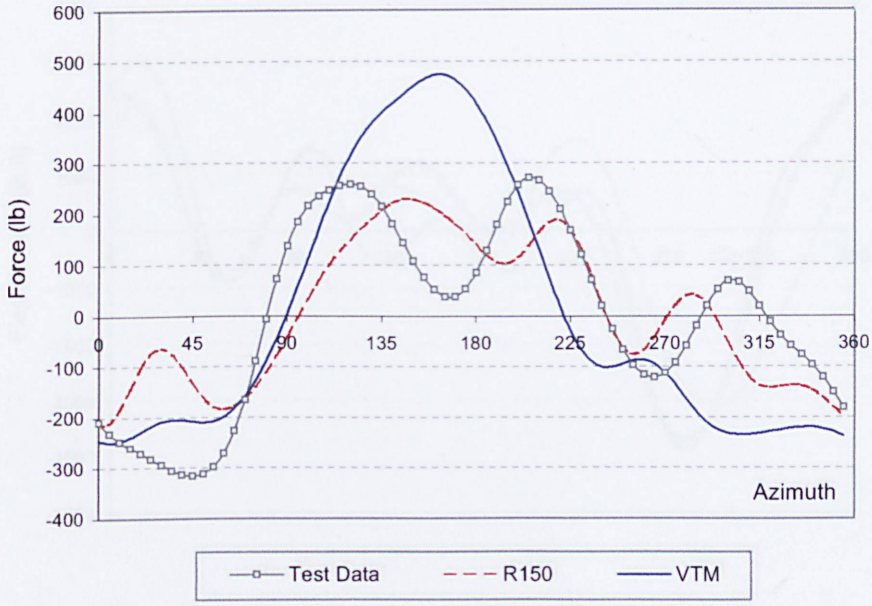


Figure 7.13: *Control loads* $\mu = 0.37$.

component of the pitching moment coefficient is constant for all operating conditions, see equation 7.1. In reality, the pitching moment of an aerofoil is sensitive to changes to the incidence of the aerofoil as well as to Mach number. Upgrading the blade aerodynamic model to reflect these dependencies should significantly improve the accuracy of the control rod load predictions.

7.3.3 Low Speed Case

Figures C.44 to C.48, to be found in appendix C2, compare the predicted and measured flapwise bending moments as a function of azimuth at a number of radial positions. The corresponding lagwise bending moment comparisons are shown in figures C.49 to C.51, also to be found in appendix C2.

The results from the low speed case largely support the conclusions reached in the previous section. At some radial positions the bending moments are predicted very well over certain portions of the azimuth. For example, at 64% radius, the predicted bending moments correlate very closely with the flight test data between 270° and 90°, as shown in figure 7.14. However, accurate correlation with the flight test data over a complete revolution is not achieved at any of the radial stations.

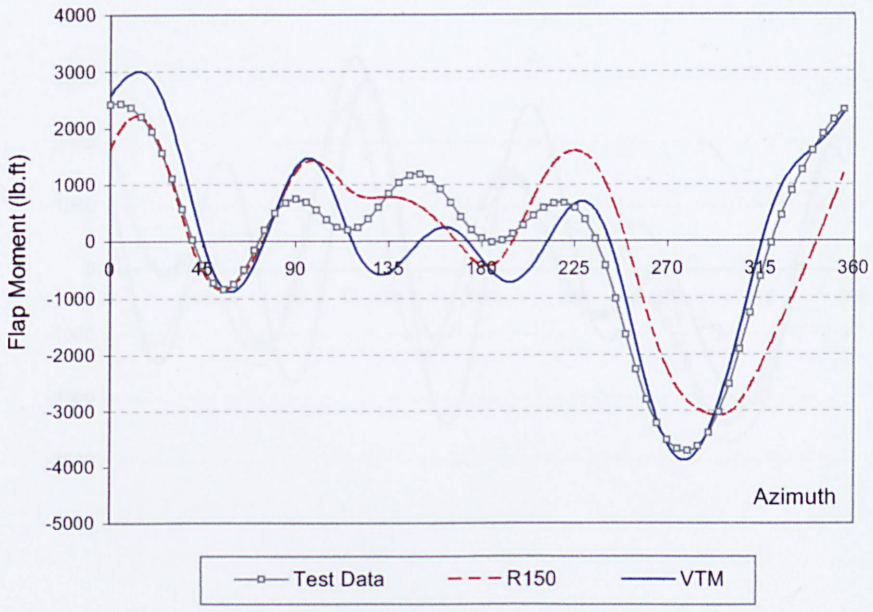


Figure 7.14: *Flap moment at 64.0% Radius* $\mu = 0.15$.

A particularly curious result can be seen in the predicted bending moments at 31% radius, shown in figure 7.15, in which the signal is contaminated by a strong 5/rev component. This high frequency contamination of the predicted loading was also experienced by some of the free wake models that were evaluated during the AHS dynamics workshop. The natural frequency of the first torsion mode and third flap mode of the Lynx blade are very close to 5/rev. When forced at close to its resonant frequency, the magnitude of a mode's response is dictated by the level of damping of the mode. For the torsional mode, the damping is provided almost entirely from the aerodynamic pitching moments. Hence, poor prediction of high frequency components of the aerodynamic forcing will induce significant errors in the predicted structural response of the rotor. The high frequency contamination of the predictions seen in figure 7.15 indicates that, once again, deficiencies exist in the blade aerodynamic model.

Examination of the predicted control rod loads at $\mu = 0.15$, shown in figure 7.16, again shows a dominant 1/rev component in the predicted loading, as seen in the high speed case, further highlighting the need for a more accurate modelling of the aerofoil pitching moments.

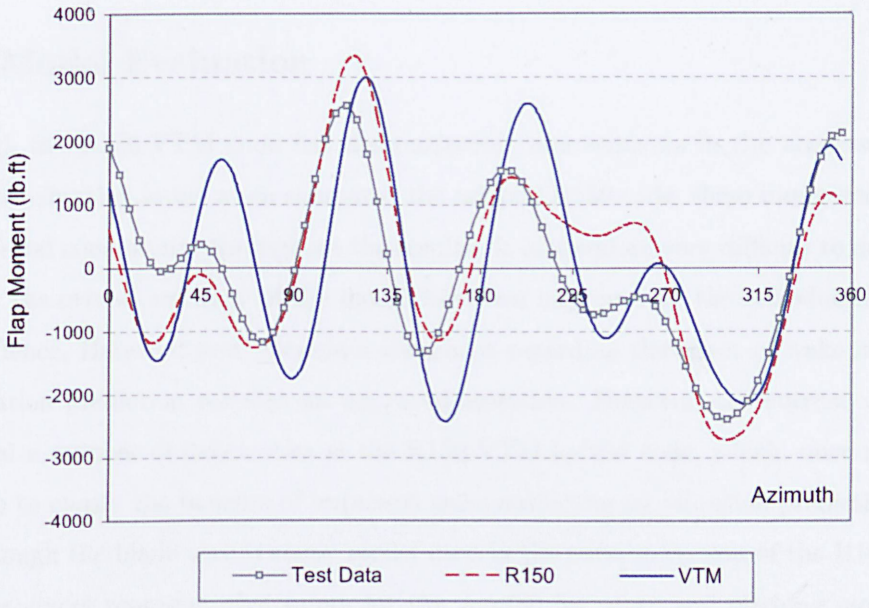


Figure 7.15: *Flap moment at 31.0% Radius* $\mu = 0.15$.

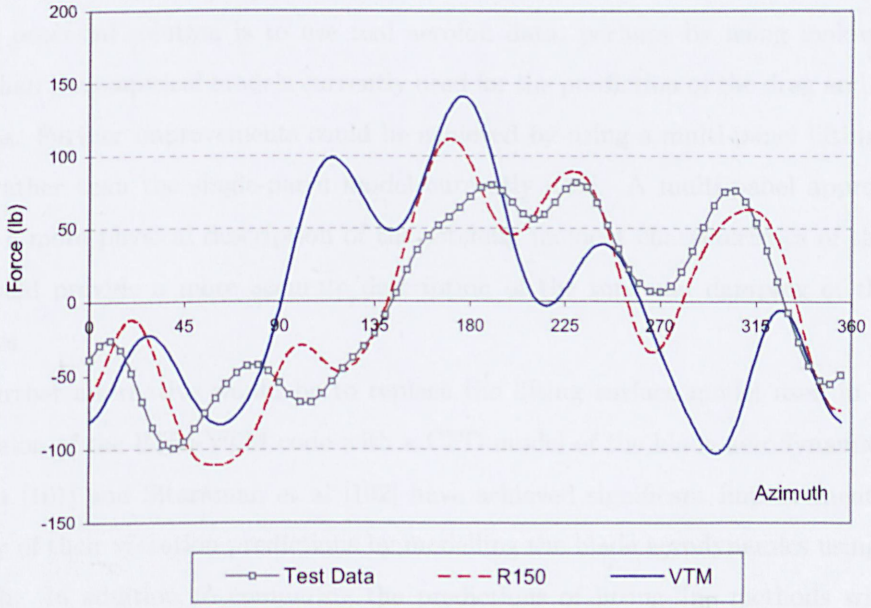


Figure 7.16: *Control loads* $\mu = 0.15$.

7.4 Model Evaluation

Although the R150-VTM code has demonstrated improvements in the accuracy of the predicted vibration levels when compared the original R150 code, these improvements are not achieved consistently throughout the results. It is therefore very difficult to determine whether the overall accuracy of the model has been improved by the introduction of the VTM. Hence, Hansford and Vorwald's statement regarding the effect of wake modelling on vibration prediction remains an unproved assertion. However, the current work has identified a number of deficiencies in the R150-VTM hybrid code, which, once removed, will help to clarify the benefits of improved wake modelling on vibration prediction.

Although the blade aerodynamic model used in the current version of the R150-VTM model produces representative values for the aerofoil lift, drag and pitching moment, it appears that a more accurate approach is needed to capture accurately the sectional drag and pitching moments. Indeed, these findings support the views of Bousman [2] who highlighted the importance of accurate prediction of aerofoil pitching moments for vibration prediction.

One potential solution is to use real aerofoil data, perhaps by using look-up tables rather than the empirical models currently used for the prediction of the drag and pitching moments. Further improvements could be achieved by using a multi-panel lifting surface model rather than the single-panel model currently used. A multi-panel approach will provide a more physical description of the pitching moment characteristics of the blade, and should provide a more accurate description of the torsional damping of the blade dynamics.

A further alternative would be to replace the lifting surface model used in the current version of the R150-VTM code with a CFD model of the blade aerodynamics. Both Potsdam [101] and Sitaraman et al [102] have achieved significant improvements in the accuracy of their vibration predictions by modelling the blade aerodynamics using a CFD approach. In addition to comparing the predictions of lifting-line methods with CFD methods, Sitaraman et al also compared the predictions of two different CFD-based approaches. The first used two-dimensional CFD to model the sectional aerodynamics along the length of the blade. The second used three-dimensional CFD modelling of the entire blade. They discovered that the use of full blade CFD improved the phasing of the rotor vibration compared to the sectional approach, suggesting that the three-dimensional flow

effects present on the rotor play an important role in driving rotor vibration.

There are also deficiencies in current version of the R150-VTM code in terms of the modelling of the fuselage aerodynamics. Although the primary interference effects of the fuselage are captured by the model, inclusion of the wake deformation effects are certain to bring about improvements in the accuracy of the aerodynamic forcing of the rotor. Realistically, this can only be achieved by incorporating a comprehensive fuselage model into the VTM wake model.

In terms of the structural model, the results of the convergence study suggest that a more complete basis of structural modes is required to capture the fine-scale features of the aerodynamic loading induced by BVIs. The inability of the structural model to capture the contributions from the fine-scale loading features will significantly constrain the accuracy of the vibration predictions that can be achieved using the current model.

Additionally, it should be noted that the modal approach is not capable of capturing the non-linear dynamics of the rotor system, i.e. the changes to the mode shapes and natural frequencies resulting from deformations of the blade. It would therefore be sensible to assess the implications of the assumption that the dynamics are linear by employing an approach which has the fidelity to capture all of the non-linearities present in the structural dynamics of the rotor system.

Even if the structural dynamics of the rotor system can be modelled legitimately using a linear model, the non-linearities present within the fluid dynamics of the system will be sufficient to introduce coupling between the structural modes. Given that the evolution of the flow surrounding the rotor is governed by the Navier-Stokes equations, linear changes in the structural dynamics of the rotor will induce non-linear variations in the wake structure, aerodynamic loading and ultimately the forcing of the structural dynamics. For example, introduction of additional torsion modes will alter the description of the twist of the blade. As demonstrated in section 7.1, modifications to the twist of blade will bring about gross changes in both the loading of the blade and the wake structure, which will, in turn, modify the aerodynamic forcing of all the structural modes. In order for these effects to be captured accurately, a comprehensive description of the blade dynamics is required. This can only be achieved with the introduction of additional structural modes. Indeed, it is highly unlikely that the torsional deformations of the blade can be described adequately using just a single mode, as used by most industry standard models.

Finally, in order to develop accurate analysis tools it is essential that the experimental data used to validate new codes is designed so that any deficiencies of a code can be easily identified. Most of the conclusions and recommendations made throughout this chapter have been based on intuition and experience rather than on solid evidence. Since no experimental measurements of the aerodynamic loading on the blades were obtained during the flight tests, it is impossible to state conclusively whether the deficiencies in the R150-VTM model originate from the modelling of the aerodynamics or the modelling of the structural dynamics. The Lynx flight test data is also far too complex and inadequately defined for it to be used to assess the performance and accuracy of individual components of the numerical model. For example, the R150-VTM is only capable of modelling the dynamics of a single blade attached to a fixed hub. In contrast, the flight test data contains contributions from the multi-body dynamics of the full aircraft and the aerodynamic interference of the fuselage and the tail rotor. It is impossible to quantify how these additional factors manifest within the experimental data, nor whether the assumptions made by the R150-VTM code are valid in this respect.

If the deficiencies of the R150-VTM model are to be overcome, and if a sophisticated understanding of the physics of rotor vibration is to be acquired, a more methodical and scientific approach to code validation and development must be employed. Experiments must be well conditioned, and designed in such a way to allow the individual components of a model to be scrutinised independently. The current situation, in which the complexity of the experimental setup forces the modeller to assess the performance of his/her code in its entirety, rather than in terms of its constituent parts, is far from ideal.

7.5 Summary

Future rotor designs are likely to incorporate high levels of blade twist in an attempt to improve hover performance and lift capability, possibly leading to unwanted increases in vibration levels generated by the rotor in forward flight. It is therefore essential that any vibration prediction tool is able to capture the effects of blade twist on the aerodynamic loading of the rotor. The VTM has successfully demonstrated that it can capture the effects of blade twist, and has identified the primary changes to the aerodynamic loading of the rotor induced by increases in blade twist.

The helicopter industry as a whole suffers from an inability to predict accurately the vibration levels of rotors. In order to assess the potential improvements that can be gained from coupling a CFD-based wake model with a structural dynamics model, the VTM has been coupled with Westland's in-house dynamics code, R150. The resulting R150-VTM code has been validated against the same flight test data as was analysed by Hansford and Vorwald during the AHS dynamics workshop. Although the R150-VTM model appears to produce some improvements in the prediction of the vibratory loading of the rotor, inconsistencies in the results do not allow any conclusive statements regarding the benefits of improved wake modelling to be made. The coupled R150-VTM has the potential to provide significant insight into the physics and modelling requirements of rotor vibration.

The results of the validation study suggest that the current model contains a number of deficiencies, but due to the nature of the flight test data, it is not possible to pinpoint the specific deficiencies of the code. It is believed however that further improvements in the accuracy of the predictions might be achieved through improvements in the blade aerodynamic model and through introduction of additional structural modes.

Chapter 8

Conclusions

The primary objective of this research was to develop a sophisticated computational fluid dynamic (CFD) model for simulating the aerodynamics of helicopter rotors. The model, based on the Vorticity Transport Model (VTM) of Brown [4], describes the flow in terms of a time-dependent vorticity distribution - an approach which provides a particularly faithful representation of the complex vortical structures present within rotor wakes. A number of limitations within the original VTM have been overcome through the introduction of a new adaptive grid system and efficient velocity calculation.

A semi-Lagrangian adaptive grid system has been developed which employs adaptive cell generation and destruction to track regions of the vorticity in the flow. Most significantly, the adaptive nature of the new grid system allows all the vorticity in the flow to be retained within the solution domain throughout the entire calculation, eliminating the need for far-field boundary conditions. The approach also incorporates nested grid levels to vary the resolution of the grid throughout the computational domain, allowing the available computational resources to be focussed onto the region of most interest. Compared to the grid system used in the original version of the VTM, the new grid system typically produces a reduction in cell count by an order of magnitude.

The method used in the original version of the VTM to evaluate the velocity field throughout the solution domain has been replaced with the Cartesian Fast Multipole Method (FMM). For a grid consisting of N vorticity-containing cells, the FMM allows the velocity to be evaluated at each of the N cells in $\mathcal{O}(N)$ operations, compared to the $\mathcal{O}(N \log N)$ cost of the method of cyclic reduction used in the original version of the VTM.

The new version of the VTM has been validated against two sets of experimental data. The first set of experimental data, produced by Caradonna and Tung, tested the VTM's ability to predict the aerodynamic loading of the rotor as well as measurements of the wake geometry, in terms of tip vortex locations, for a rotor in hover. The second set of experimental data, produced by Harris, tested the VTM's ability to predict the low-frequency dynamics of an articulated rotor with fixed control inputs over a range of forward flight conditions.

The validation of the VTM against Harris' experimental work was later extended to investigate the fundamental physical mechanisms associated with the evolution of the rotor wake in forward flight. The study identified the existence of an upwash region over the front edge of the rotor, which is responsible, almost entirely, for the steep rise in lateral flapping between hover and $\mu = 0.08$. Close to $\mu = 0.08$, a distinct change in the structure of the wake is seen, from the tubular, hover-like wake seen at low speed, to the flat, rolled-up, wing-like wake seen in high speed forward flight. The transition between these two regimes coincides with the maximum lateral flapping of the rotor and also an abrupt increase in the mean inflow produced by the rotor. The transition is believed to be related to the stability characteristics of the rotor wake. At low speed the products of instabilities are held close to the rotor and introduce significant unsteadiness into the flow. Above $\mu = 0.08$, the growth rate of the products of instabilities is significantly reduced by the effect of the larger freestream velocity, leading to a highly-ordered and steady wake geometry. A detailed analysis of the stability characteristics of the flow field, along with further analysis of the associated wake topologies, could provide an invaluable insight into the physical process governing the evolution of rotor wakes in general.

A further aim of this work was to investigate the potential benefits that a comprehensive model of the rotor aerodynamics, such as the VTM, might have on the accuracy of rotor vibration predictions. A parametric study investigating the effects of blade twist on the aerodynamic forcing of the rotor was first carried out. The study illustrated that the VTM is indeed capable of capturing the link between blade twist and the high-frequency dynamics of the rotor system. Variations to the blade twist have been shown to introduce significant changes in the harmonic content of the aerodynamic forcing of the structural dynamics.

In order to assess the ability of the enhanced version of the VTM to improve the

accuracy of vibration predictions, the VTM was integrated with an industry-standard structural dynamics code (R150). Validation of the R150-VTM hybrid code against flight test data indicated some improvements in the accuracy of the predicted vibration levels compared to the existing prescribed wake model. However, inconsistencies in the results do not allow any definitive conclusions regarding the potential benefits of improved wake modelling to be made. The study identified a number of limitations and deficiencies in the R150-VTM code which, if addressed, could dramatically improve the fidelity and accuracy of the model.

In the author's opinion, the most significant limitation relates to the number of modes used to describe the structural response of the rotor. Even if the structural dynamics of the system can be modelled legitimately using a linear model, the non-linearities present within the fluid dynamics of the system will be sufficient to introduce coupling between the structural modes. In order for the non-linearities in the fluid dynamics, and hence the coupling of the structural modes, to be captured accurately, a comprehensive description of the blade dynamics is required. This can only be achieved with the introduction of additional structural modes. This deficiency of the R150-VTM code, explains to an extent why the predicted structural response of the rotor appears to be insensitive to changes in the grid resolution used to capture the rotor wake.

A number of the limitations of the R150-VTM code relate to the modelling of the blade aerodynamics and fuselage aerodynamics. A deficiency in the modelling of the aerofoil properties is the most likely source of the the poor prediction of the lag response of the rotor, as well as the over-prediction of the 1/rev component of the pitch link loads. Improvements in the modelling of the sectional aerofoil properties should bring about improvements in the accuracy of the predicted structural loads. The use of real aerofoil data, through the introduction of look-up tables, will eliminate some of the deficiencies in the prediction of aerofoil pitching moments and drag coefficients present in the current model. Specifically, this should lead to improvements in the prediction of the torsional damping, the control loads and the lag response of the rotor. Major improvements may however require full CFD modelling of the blade aerodynamic, rather than the current lifting surface approach. Although considerably more expensive and challenging to implement than the lifting surface approach, full-blade CFD has the potential to model faithfully the complex flow features seen on rotor blades, including blade vortex interactions, dynamic stall and

radial flow effects.

The work presented in this thesis has demonstrated how the improvements in the fidelity and efficiency of the VTM can be exploited to provide further insight into the physics of rotor aerodynamics. Once the remaining limitations of the VTM are removed, the code will provide a powerful base from which to tackle the challenging problems of rotor vibration, acoustics and interactional aerodynamics.

Bibliography

[1] Hansford, R. E. and Vorwald, J., "Dynamics Workshop on Rotor Vibratory Loads Prediction," *Journal of the American Helicopter Society,* Vol. 43, No. 1, January 1998, pp. 76-87.

[2] Bousman, W. G., "Putting the Aero Back into Aeroelasticity," *Eigth Annual ARO Workshop on Aeroelasticity of Rotorcraft Systems,* University Park, PA, October 1999.

[3] Caradonna, F. X., "Developments and Challenges in Rotorcraft Aerodynamics," *38th AIAA Aerospace Sciences Meeting,* AIAA 2000-0109, January 2000.

[4] Brown, R. E., "Rotor Wake Modeling for Flight Dynamic Simulation of Helicopters," *AIAA Journal,* Vol. 38, No. 1, 2000, pp. 57-63.

[5] Harris, F. D., "Articulated Rotor Blade Flapping Motion at Low Advance Ratio," *Journal of the American Helicopter Society,* Vol. 17, No. 1, 1972, pp. 41-48.

[6] Caradonna, F. X. and Tung, C., "Experimental and Analytical Studies of a Model Helicopter Rotor in Hover," *Vertica,* Vol. 5, 1981, pp. 149-161.

[7] Line, A. J. and Brown, R. E., "High Resolution Wake Modelling using a Semi-Lagrangian Adaptive Grid Formulation," *29th European Rotorcraft Forum,* Friedrichshafen, Germany, September 2003.

[8] Line, A. J. and Brown, R. E., "Fuselage and Tail-Rotor Interference Effects on Helicopter Wake Development in Descending Flight," *60th Annual Forum of the American Helicopter Society,* Baltimore, June 2004.

[9] Brown, R. E. and Line, A. J., "Developments and Challenges in Rotorcraft Aerodynamics," *38th AIAA Aerospace Sciences Meeting,* AIAA 2000-0109, January 2000.

[10] Brown, R. E. and Houston, S. S., "Comparison of Induced Velocity Models for Helicopter Flight Mechanics," *AIAA Journal of Aircraft,* Vol. 37, No. 4, 2000, pp. 623-629.

[11] Brown, R. E., et al., "Blade Twist Effects on Rotor Behaviour in the Vortex Ring State," *60th Annual American Helicopter Society Forum,* Baltimore, Maryland, June 2004.

[12] Brown, R. E., Line, A. J. and Ahlin, G. A., "Fuselage and Tail-Rotor Interference Effects on Helicopter Wake Developments in Descending Flight," *28th European Rotorcraft Forum,* Bristol, September 2002.

[13] Whitehouse, G. R. and Brown, R. E., "Modeling the Mutual Distortions of Interacting Helicopter and Aircraft Wakes," *AIAA Journal of Aircraft,* Vol. 40, No. 3, 2003, pp. 440-449.

[14] Brown, R. E., "Numerical Solution to the Two-Dimensional Navier-Stokes Equations Using Viscous-Convective Operator Splitting," *M.Sc. Thesis,* College of Aeronautics, Cranfield Institute of Technology, 1990.

[15] Harlow, F. H. and Welsh, J. E.,"Numerical Calculation of Time Dependent Viscous Incompressible Flow with Free Surface," *Phyics of Fluid* Vol. 8, 1965, pp. 2182-2189.

[16] Ferziger, J. H. and Peric, M.,"Computational Methods for Fluid Dynamics," *Springer-Verlag,* 2002, 3rd Edition.

[17] Peyret, R.,"Handbook of Computational Fluid Mechanics," *Academic Press,* 1996.

[18] Toro, E. F., "A Weighted Average Flux Method for Hyperbolic Conservation Laws," *Proceedings of the Royal Society of London, Series A: Mathematical and Physical Sciences,* Vol. 423, No. 1864, 1989, pp. 401-418.

[19] Toro, E. F., "Some Aspects of Shock Capturing Methods for Gas Dynamics," *College of Aeronautics Report, Cranfield Institute of Technology,* No. 9112, June 1991.

[20] Harten, A., "High Resolution Schemes for Hyperbolic Conservation Laws," *Journal of Computational Physics,* No. 49, 1983, pp. 357-393.

[21] Toro, E. F., "TVD Regions for the Weighted Average Flux (WAF) Method as Applied to a Model Hyperbolic Conservation Law," *College of Aeronautics Report, Cranfield Institute of Technology,* No. 8907, June 1989.

[22] Bilett, S. J. and Toro, E. F., "Restoring Monoticity of Slowly-Moving Shocks Computed with Gudunov-Type Schemes," *College of Aeronautics Report, Cranfield Institute of Technology,* No. 9207, March 1992.

[23] Strang, G., "On the Construction and Comparison of Finite Difference Schemes," *SIAM Journal of Numerical Analysis,* Vol. 5, 1968, pp. 995-1011.

[24] Billet, S. J. and Toro, E. F., "On WAF-Type Scheme for Multi-Dimensional Hyperbolic Conservation Laws," *Journal of Computational Physics,* Vol. 130, 1997, pp. 1-24.

[25] Toro, E. F. and Billet, S. J., "Multidimensional WAF-type Schemes for Model Conservation Laws," *College of Aeronautics Report, Cranfield Institute of Technology,* No. 9312, September 1993.

[26] Schumann, U. and Sweet, R. A., "A Direct Method for the Solution of Poisson's Equation with Neumann Boundary Conditions on a Staggered Grid of Arbitrary Size," *Journal of Computational Physics,* Vol. 20, No. 2, 1976, pp. 171-182.

[27] Swarztrauber P. N. and Sweet, R. A., "The Fourier and Cyclic Reduction Methods for Solving Poisson's Equation," *Handbook of Fluid Dynamics and Fluid Machinery,* John Wiley & Sons, New York, 1996.

[28] Weissinger, J., "The Lift Distribution of Swept-Back Wings," *NACA Technical Memorandum,* No. 1120, March 1947.

[29] DeYoung, J., "Theoretical Additional Span Loading Characteristics of Wings with Arbitrary Sweep, Aspect Ratio and Taper Ratio," *NACA Technical Note,* No. 1491, December 1947.

[30] Stevens, V. I., "Theoretical Basic Span Loading Characteristics of Wings with Arbitrary Sweep, Aspect Ratio and Taper Ratio," *NACA Technical Note,* No. 1772, December 1948.

[31] Corrigan, J. and Shillings, J. J., "Empirical Model for Stall Delay Due to Rotation," *American Helicopter Society Aeromechanics Specilist Conference,* San Franciso, CA, January 1994.

[32] Du, Z. and Selig, M. S., "The Effect of Rotation on the Boundary Layer of a Wind Turbine Blade," *Windpower Conference,* Bakersfield, CA, 1998.

[33] Du, Z. and Selig, M. S., "A 3-D Stall Delay Model for Horizontal Axis Wind Turbine Performance Prediction," *ASME/AIAA Joint Wind Energy Symposium,* Austin, Texas, June 1997.

[34] Corten, G. P., "Inviscid Stall Model," *European Wind Energy Conference,* Copenhagen, Denmark, July 2001.

[35] Beddoes, T. S., "A synthesis of Unsteady Aerodynamic Effects including Stall Hysteresis," *Vertica,* Vol. 1, pp. 113-123, 1976.

[36] Beddoes, T. S., "Representation of Airfoil Behaviour," *Vertica,* Vol. 7, No. 2, pp. 183-197, 1987.

[37] Beddoes, T. S., "Practical Computation of Unsteady Lift," *Vertica,* Vol. 8, No. 1, pp. 55-71, 1984.

[38] Wang, Z. and Wang, Z., "The Level Set Method on Adaptive Cartesian Grid for Interface Capturing," *42nd Aerospace Sciences Meeting & Exhibit,* Reno, Nevada, January 2004.

[39] De Zeeuw, D. and Powell, K. G., "An Adaptively Refined Cartesian Mesh Solver for Euler Calculations," *Journal of Computational Physics,* Vol. 104, 1993, pp. 56-68.

[40] Berger, M. J. and Aftosmis, M. J., "Aspects (and Aspect Ratios) of Cartesian Mesh Methods," *Proceedings of the 16th International Conference on Numerical Methods in Fluid Dynamics,* Arcachon, France, July 1998.

[41] Berger, M. J. and Colella, P., "Local Adaptive Mesh Refinement for Shock Hydrodynamics," *Journal of Computational Physics,* Vol. 82, 1989, pp. 62-84.

[42] Knuth, D. E., "The Art of Computer Programming: Vol 1-3," *Addison Wesley Press,* November 1998.

[43] Berger, M. J. and Leveque, R. J., "Adaptive Mesh Refinement using Wake-Propagation Algorithms for Hyperbolic Systems," *SIAM Journal of Numerical Analysis,* Vol. 35, No. 6, pp. 2298-2316, 1998.

[44] Pringle, G. J., "Numerical Study of Three-Dimensional Flow using Fast Parallel Particle Algorithms," *PhD Thesis, Dept. Mathematics, University of Edinburgh,* 1994.

[45] Appel, A. W., "An efficient program for many-body simulation," *SIAM Journal of Sci. Statist. Comput.,* Vol. 6, pp. 85-103, 1985.

[46] Barnes, J. E. and Hut, P. "A Hierarchical O(N log N) Force-Calculation Algorithm," *Nature,* Vol. 324, No. 446, 1986.

[47] Greengard, L. and Rokhlin V., "A Fast Algorithm for Particle Simulations," *Journal of Computational Physics,* Vol. 73, No. 1, pp. 325-348, 1987.

[48] Greengard, L. and Rokhlin, V., "A Fast Algorithm for Particle Simulations," *Journal of Computational Physics,* Vol. 135, pp. 280-292, 1997.

[49] Cheng, H., Greengard, L. and Rokhlin, V., "A Fast Adaptive Multipole Algorithm in Three Dimensions," *Journal of Computational Physics,* Vol. 155, pp. 468-498, 1999.

[50] Hrycak, T. and Rokhlin, V., "An Improved Fast Multipole Algorithm for Potential Fields," *SIAM Journal of Scientific Computing,* Vol. 19, No. 6, pp. 1804-1826, November 1998.

[51] Dehnen, W, "A Very Fast and Momentum-Conserving Tree-Code," *Max-Planck-Institute of Astronomy Report,* No. 3209, May 2000.

[52] Warren, M. S. and Salmon, J. K., "Astrophysical N-Body Simulations Using Hierarchical Tree Data Structures," *IEEE Comput. Soc. Press,* pp. 570-576, 1992.

[53] Warren, M. S. and Salmon, J. K., "A Portable Parallel Particle Program ," *Computer Physics Communications,* Vol. 87, pp. 266-290, 1995.

[54] Winckelmans, G. S., et al, "Application of Fast Parallel and Sequential Treecodes to Computing Three-Dimensional Flows with the Vortex Element and Boundary Element Methods," *ESAIM Proceedings,* Vol. 1, pp. 225-240, 1996.

[55] Warren, M. S. and Salmon, J. K., "Skeletons from the Treecode Closet ," *Journal of Computational Fluid Dynamics,* Vol. 111, pp. 136-155, 1994.

[56] Hernquist, L. and Katz, N., "Treesph: A unification of SPH with the hierarchical tree method," *Journal of Asptrophysics,* Vol. 70, p. 419, 1989.

[57] Monaghan, J. J., "Particle methods for hydrodynamics," *Computer Physics Reports,* Vol. 3, p. 71, 1985.

[58] Kong, Y, "Multipole Electrostatic Methods for Protein Modeling with Reaction Field Treatment," *PhD Thesis, Washington University,* August 1997.

[59] Ding, H., et al., "Atomic Level Simulations on a Million Particles: The Cell Multipole Method for Coulomb and London Nonbond Interactions," *Journal of Chemical Physics,* Vol. 97, 1992.

[60] Yuhong, F., et al., "A Fast Solution Method for Three-Dimensional Many-Particle Problems of Linear Elasticity ," *International Journal for Numerical Methods in Engineering,* Vol. 42, pp. 1215-1229, 1998.

[61] Nakano, A., et al., "Atomistic Simulation of Nanostructured Material," *IEEE Computational Science & Engineering,* Vol. 5, No. 68, 1998.

[62] Nabors, K. and White, J., "FastCap: A Multipole Accelerated 3-D Capacitance Extraction Program," *IEEE Transactions on Computer Aided Design,* Vol. 10, No. 11, November 1991.

[63] Kamon, N, et al., "FASTHENRY: A Multipole Accelerated 3-D Inductance Extraction Program," *IEEE Transactions on Microwave Theory and Techniques,* Vol. 42, No. 9, Septemeber 1994.

[64] Anderson, C. R., "A method of local corrections for computing the velocity field due to a distribution of vortex blobs," *Journal of Computational Physics,* Vol. 62, pp. 11-123, 1986.

[65] Krasny R. and Lindsay, K., "A Particle Method and Adaptive Treecode for Vortex Sheet Motion in Three-Dimensional Flow," *Journal of Computational Physics,* Vol. 172, pp. 879-907, 2001.

[66] Dragicescu, C. I. and Dragicescu, M. D., "A Fast Algorithm for Vortex Blob Interactions," *Journal of Computational Physics,* Vol. 116, pp. 69-78, 1995.

[67] Marshall, J. S., et al, "Vorticity Transport on a Lagrangian Tetrahedral Mesh," *Journal of Computational Physics,* Vol. 161, pp. 85-113, 2000.

[68] Chorin, A. J., "Vorticity and Turbulence ," *Springer Verlag ,* November 1997.

[69] Vanden-Broeck, J. M., "Rosenhead's Point Vortex Approximation Revisited," *Physics of Fluids,* Vol. 5, No. 11, Novermber 1993.

[70] Krasny R., Lindsay, K. and Nitsche, M., "Simulations of Vortex Sheet Roll-Up: Chaos, Azimuthal Waves, Ring Merger," *Physics of Fluids,* Vol. 5, No. 11, Novermber 1993.

[71] Cottet, G. H. and Koumoutsakos P. D., "Vortex Methods: Theory and Applications," *Cambridge University Press,* 2000.

[72] Rosenhead, L., "The Spread of Vorticity in the Wake behind a Cylinder," *Proceedings of the Royal Society London,* Series A, Vol. 127, No. 590, 1930.

[73] Moore, D. W., "Finite Amplitude Wave on Aircraft Trailing Vortices," *Aero. Quarterly,* Vol. 23, No. 307, 1972.

[74] Krasny R., "A Study of Sinularity Formation in a Vortex Sheet by the Point-Vortex Approximation," *Journal of Fluid Dynamics,* Vol. 167, No. 65, 1986.

[75] Krasny R., "Desingularisation of Periodic Vortex Sheet Roll-Up," *Journal of Computational Physics,* Vol. 65, No. 292, 1986.

[76] Salmon, J. K. and Warren, M. S., "Skeletons from the Treecode Closet," *Journal of Computational Physics,* Vol. 111, pp. 136-155, 1994.

[77] Grama, A., Sarin, V. and Sameh, A., "Improving Error-Bounds for Multipole-Based Treecodes," *SIAM Journal on Scientific Computing,* Vol. 21, No. 5, pp. 1790-1803, 2000.

[78] Whitehouse, G. R. and Brown, R. E., "Helicopter Rotor Response to Wake Encouters in Ground Effect," 59^{th} *American Helicopter Society Annual Forum,* Pheonix, Arizona, May 2003.

[79] Kocurek, J. D. and Tangler, J. L, "A Prescribed Wake Lifting Surface Hover Performance Analysis," *Presented at the 32nd Annual Forum of the American Helicopter Society,* Washington DC, May 1976.

[80] Johnson, W., "Comparison of Calculated and Measured Helicopter Rotor Lateral Flapping Angles," *NASA TM 81213, AVRADCOM TR 80-A-11,* 1980.

[81] Quackenbush, T. R., "Computational Studies in Low Speed Rotor Aerodynamics" *AHS Specialist's Meeting on Aerodynamics and Aeroacoustics,* Arlington, Texas, 1987.

[82] Johnson, W., "Helicopter Theory," *Dover Publications,* 1994.

[83] Prouty, R. W., "Helicopter Performance, Stability, and Control," *Robert E. Krieger Publishing Company,* 1986.

[84] Glauert H., "A General Theory of the Autogiro," *ARC R & M,* No. 1111, 1926.

[85] Leishman, J. G., "Principles of Helicopter Aerodynamics," *Cambridge University Press,* 2000.

[86] Coleman, R. P., et al, "Evaluation of the Induced Velocity Fields of an Idealized Helicopter Rotor," *NACA ARR L5E10,* 1945.

[87] Drees, J. M., "A Theory of Airflow through Rotors and its Application to Some Helicopter Problems," *J. Helicopter Association, Great Britain,* Vol. 3, No. 2, 1949.

[88] Payne, P. R., "Helicopter Dynamics and Aerodynamics," *Pitman & Sons, London* 1959.

[89] White, F. and Blade, B. B., "Improved Method of Predicting Helicopter Control Response and Gust Sensitivity," *35th Annual Forum of the American Helicopter Society,* Washington DC, 1979.

[90] Pitt, D. M. and Peters, D. A. "Theoretical Prediction of Dynamics Inflow Derivatives," *Vertica,* No. 5, 1981.

[91] Howlett, J. J., "UH-60A Blackhawk Engineering Simulation Program: Vol. 1 - Mathematical Model," *NASA CR-66309,* 1981.

[92] Wang, J. M., "Challenges in Rotor Dynamics Correlation," *54th Annual Forum of the American Helicopter Society,* Washington D.C., May 1998.

[93] Lau, B. H., et al, "Performance and Rotor Loads Measurements of the Lynx XZ170 Helicopter with Rectangular Blades," *NASA Technical Momorandum,* No. 104000, May 1993.

[94] Hansford, R. E., "The Development of the Coupled Rotor-Fuselage Model (CRFM)," *48th Annual Forum of the American Helicopter Society,* Washington DC, June, 1992.

[95] Juggins, T. W., "Coupled Rotor Fuselage Mode Shapes - A Tool un Understanding Helicopter Response," *48th Annual Forum of the American Helicopter Society,* Washington DC, June, 1992.

[96] Chan, W. Y. F., et al., "Results of Initial Aircraft Manoeuvre Simulation of the Coupled Rotor Fuselage Model (CRFM)," *55th Annual Forum of the American Helicopter Society,* Montreal, May, 1999.

[97] Byham, G. M. and Beddoes, T.S., "The Importantce of Unsteady Aerodynamics in Rotor Calculations," *AGARD Paper,* CP-227.

[98] McKenzie, K. T. and Howell, D.A.S., "The Prediction of Loading Actions on High Speed Semi-Rigid Rotor Helicopters," *AGARD Specialists Meeting on Helicopter Loads Prediction Methods,* Milan, Italy, March 1973.

[99] Datta, A. and Chopra, I., "Validation and Understanding of UH-60A Vibratory Loads in Steady Level Flight," *60th Annual Forum of the American Helicopter Society,* Baltimore, June, 2004.

[100] Datta, A., et al., "Analysis Refinements for Prediction of Rotor Vibratory Loads in High Speed Forward Flight," *60th Annual Forum of the American Helicopter Society,* Baltimore, June, 2004.

[101] Potsdam, M., at el., "Rotor Airloads Prediction using Loose Aerodynamic/Structural Coupling," *60th Annual Forum of the American Helicopter Society,* Baltimore, June, 2004.

[102] Sitaraman, J., et al., "Fundamental Understanding and Prediction of Rotor Vibratory Loads in High Speed Forward Flight," *29th European Rotorcraft Forum,* Friedrichshafen, Germany, 2003.

[103] Hamm, J., "The Development of Helicopter Pilot Models to Control Engineering Simulations," *RAeS Airspace Flight Simulation Conference,* 1994.

Appendix A:

VTM-R150 Twist Study

A1. High Speed Case $\mu = 0.37$

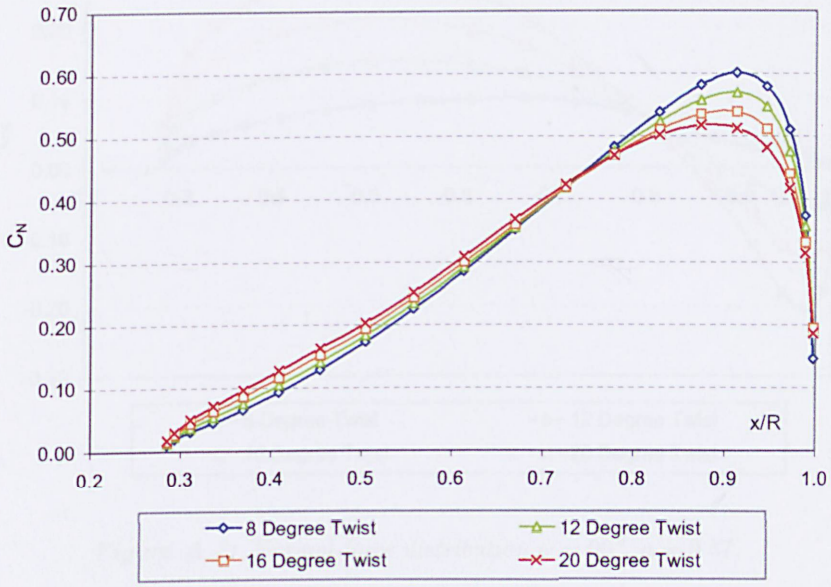


Figure A.1: *Normal force distribution* $\psi = 0°$, $\mu = 0.37$.

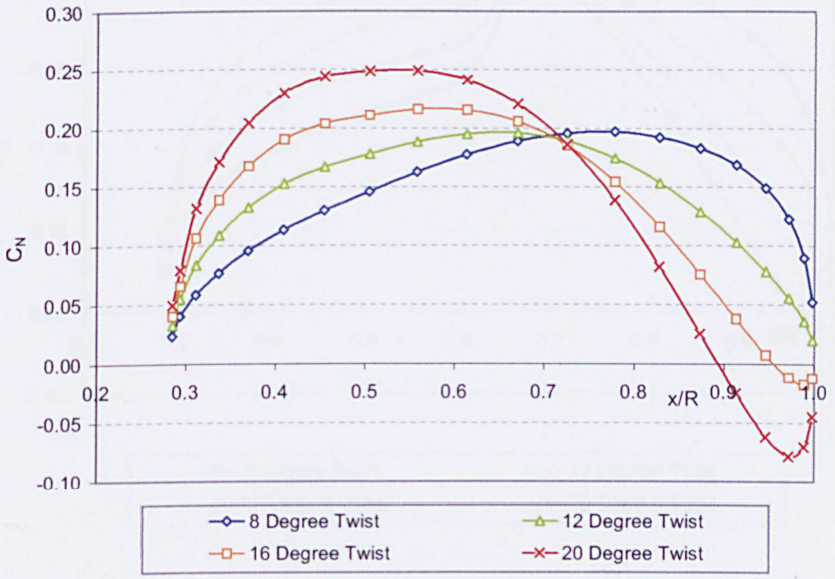


Figure A.2: *Normal force distribution* $\psi = 45°$, $\mu = 0.37$.

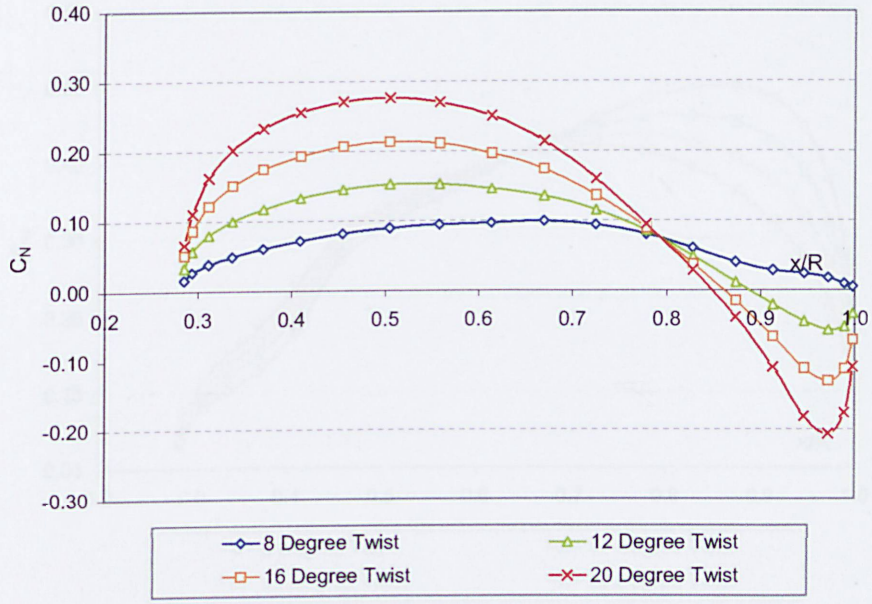


Figure A.3: *Normal force distribution* $\psi = 90^\circ$, $\mu = 0.37$.

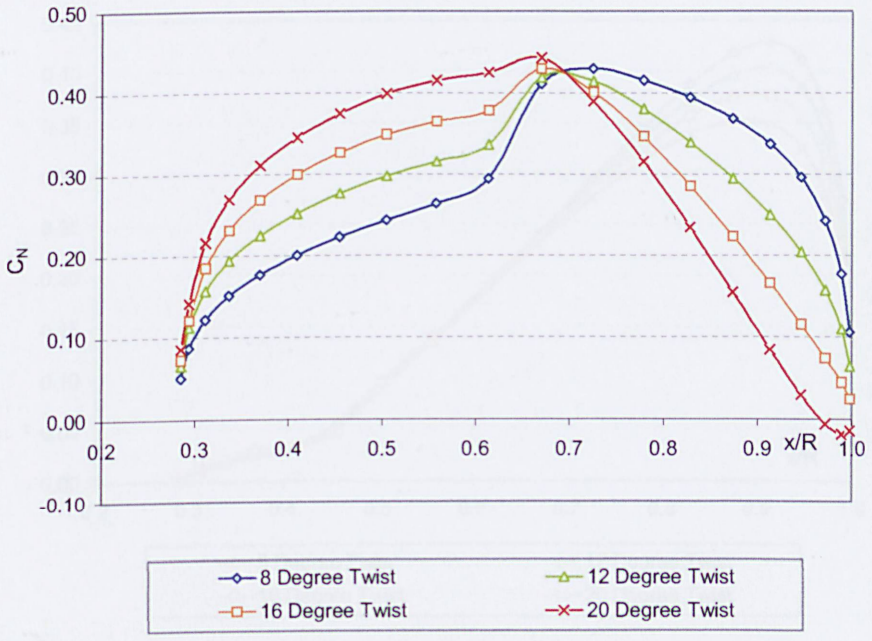


Figure A.4: *Normal force distribution* $\psi = 135^\circ$, $\mu = 0.37$.

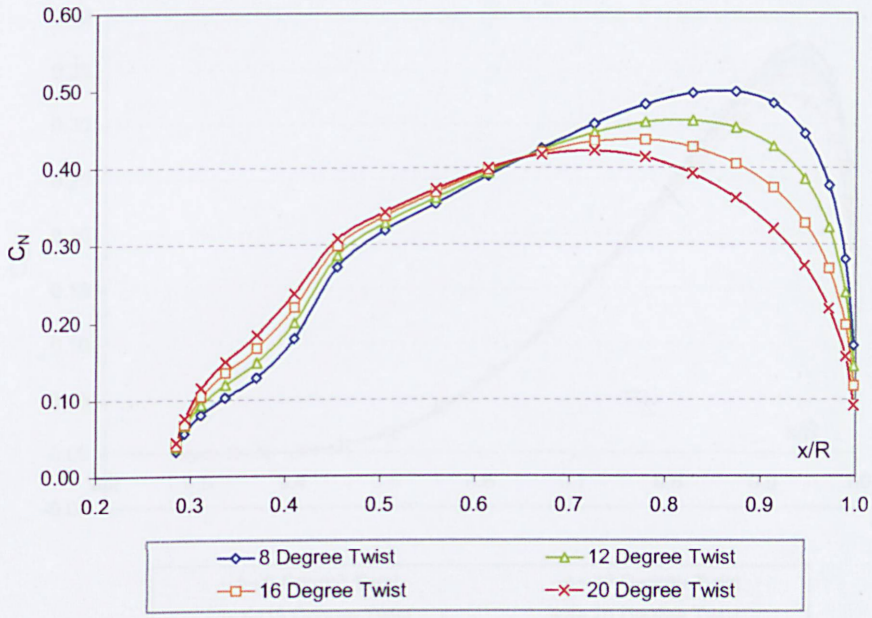


Figure A.5: *Normal force distribution* $\psi = 180^\circ$, $\mu = 0.37$.

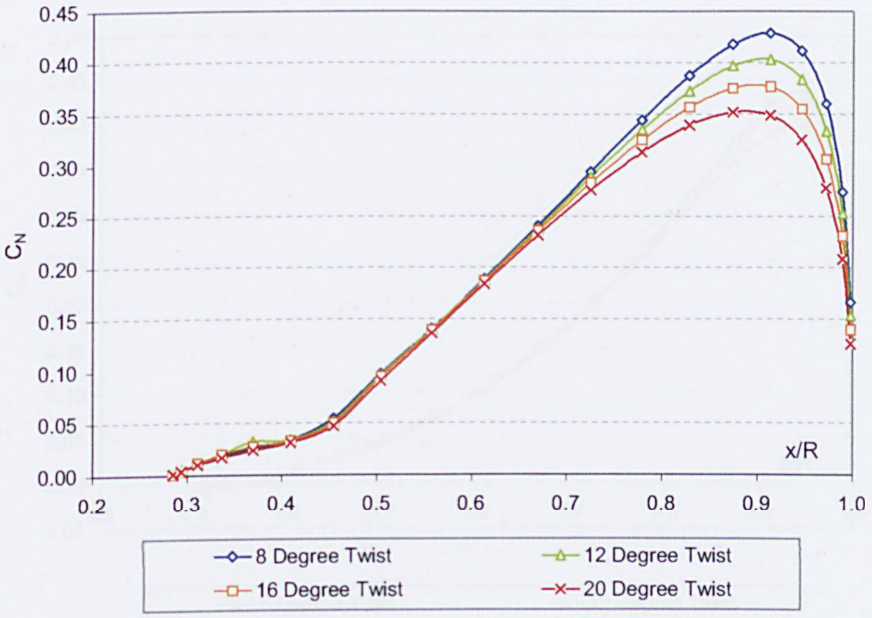


Figure A.6: *Normal force distribution* $\psi = 225^\circ$, $\mu = 0.37$.

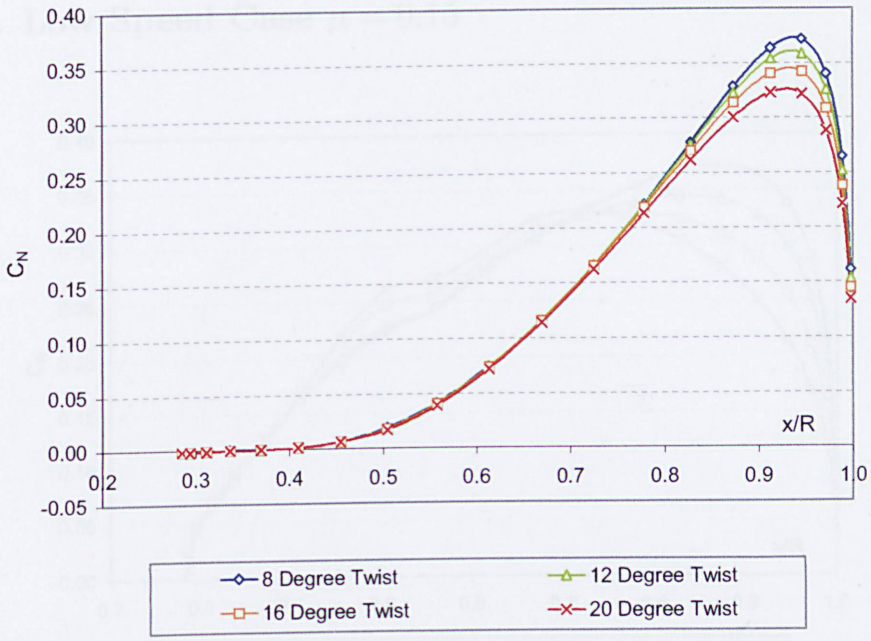


Figure A.7: *Normal force distribution* $\psi = 270°$, $\mu = 0.37$.

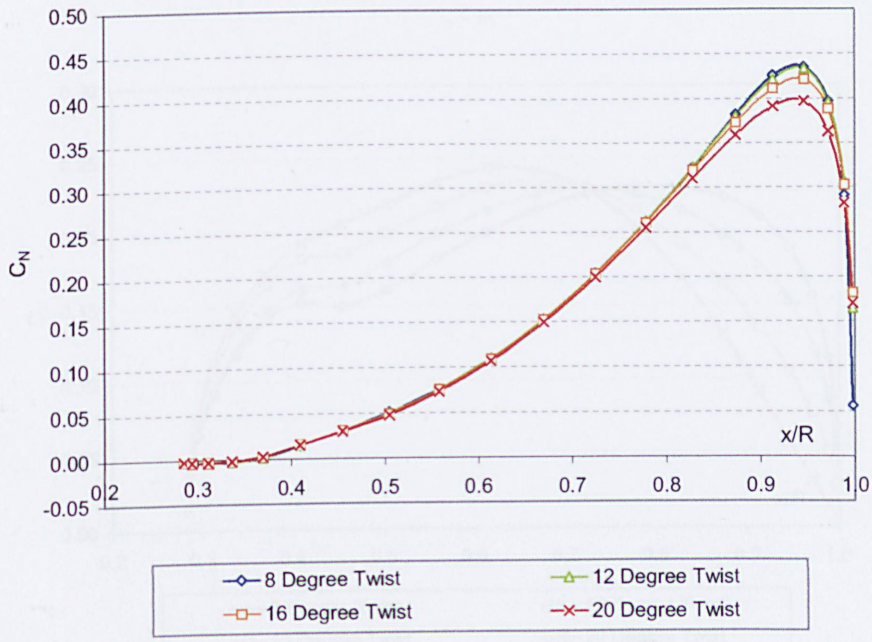


Figure A.8: *Normal force distribution* $\psi = 315°$, $\mu = 0.37$.

A2. Low Speed Case $\mu = 0.15$

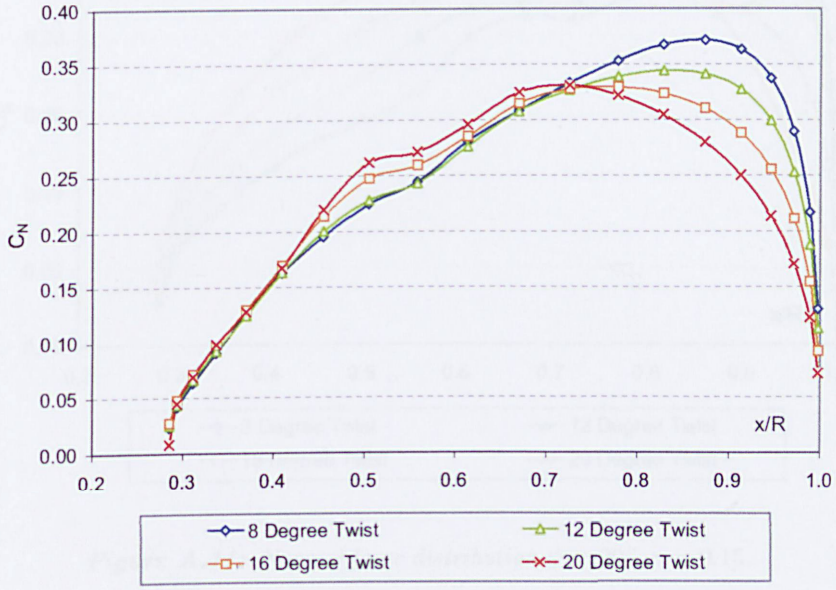


Figure A.9: *Normal force distribution* $\psi = 0°$, $\mu = 0.15$.

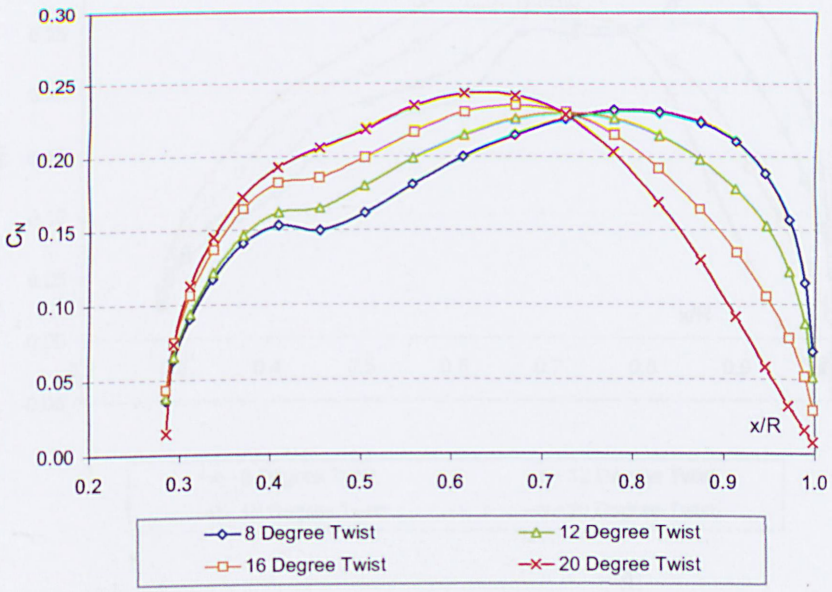


Figure A.10: *Normal force distribution* $\psi = 45°$, $\mu = 0.15$.

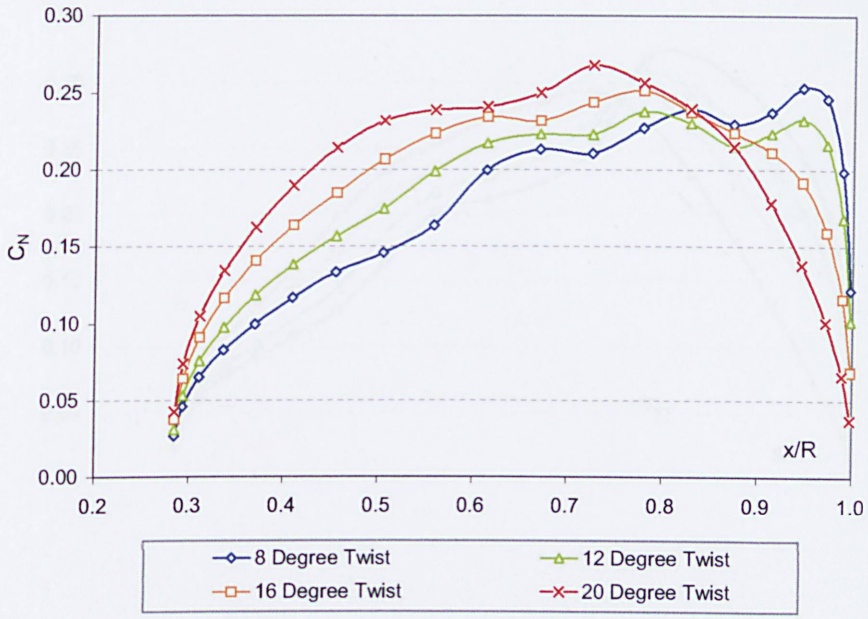


Figure A.11: *Normal force distribution* $\psi = 90°$, $\mu = 0.15$.

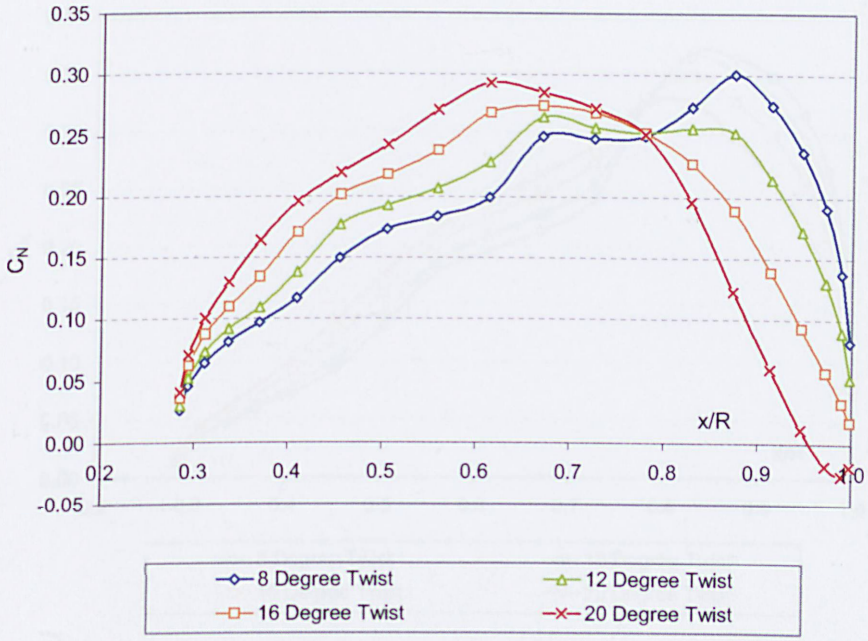


Figure A.12: *Normal force distribution* $\psi = 135°$, $\mu = 0.15$.

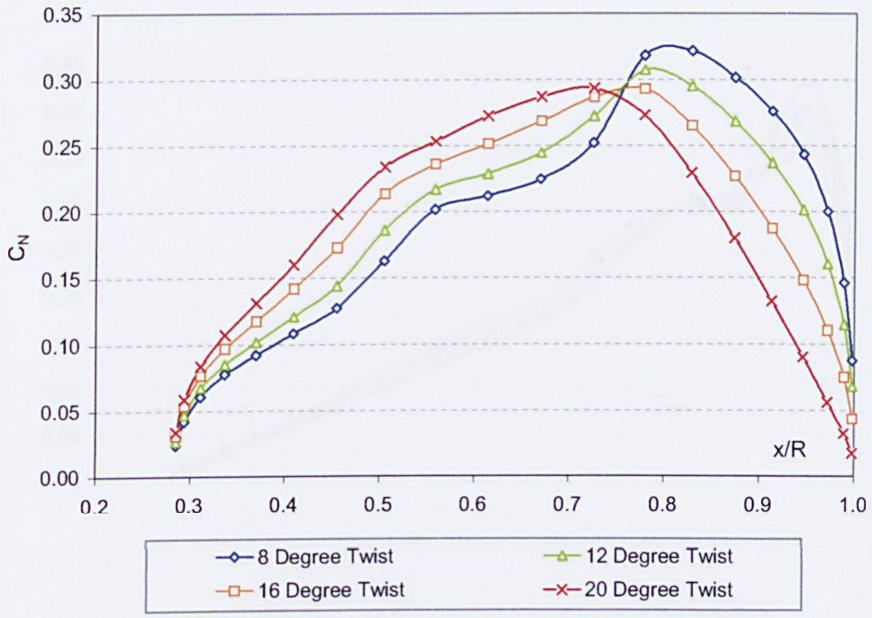


Figure A.13: *Normal force distribution* $\psi = 180°$, $\mu = 0.15$.

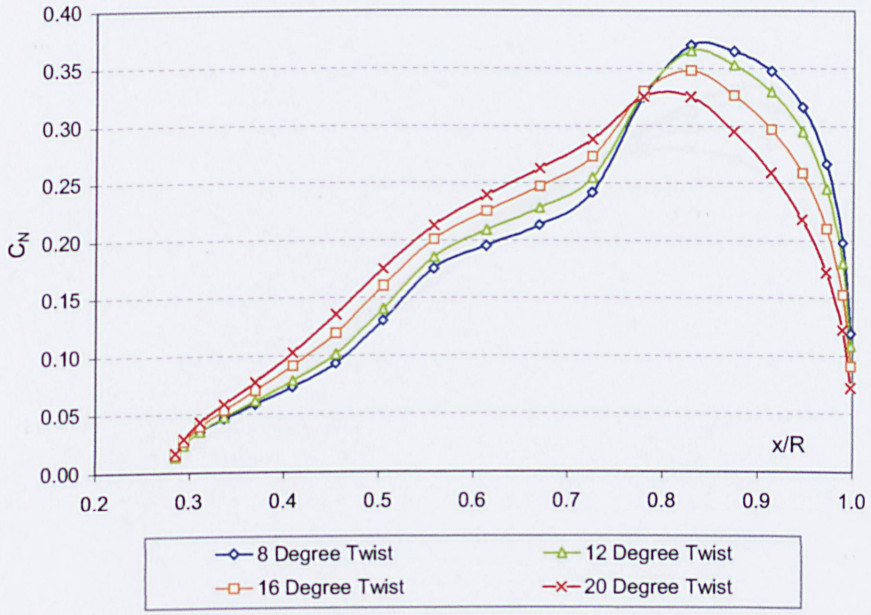


Figure A.14: *Normal force distribution* $\psi = 225°$, $\mu = 0.15$.

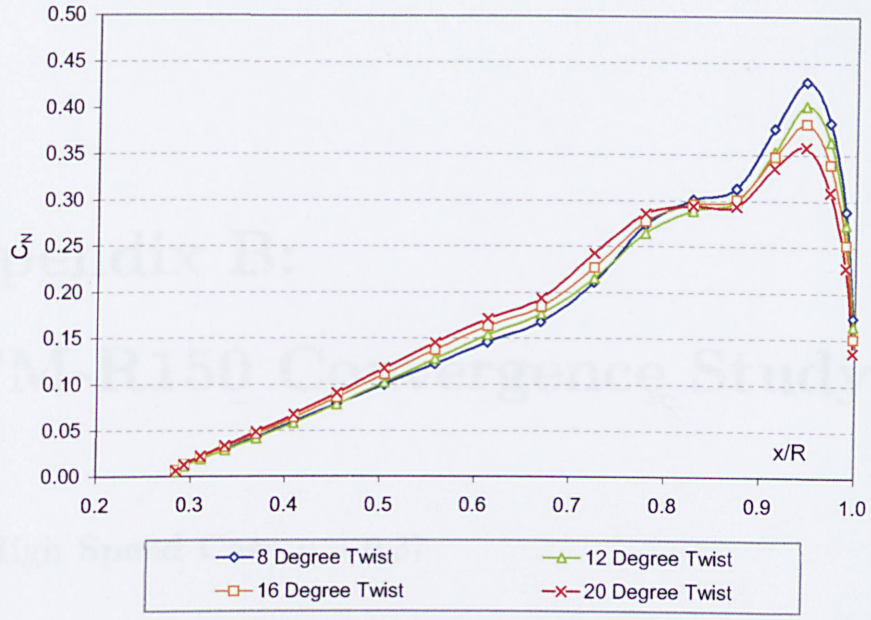


Figure A.15: *Normal force distribution* $\psi = 270°$, $\mu = 0.15$.

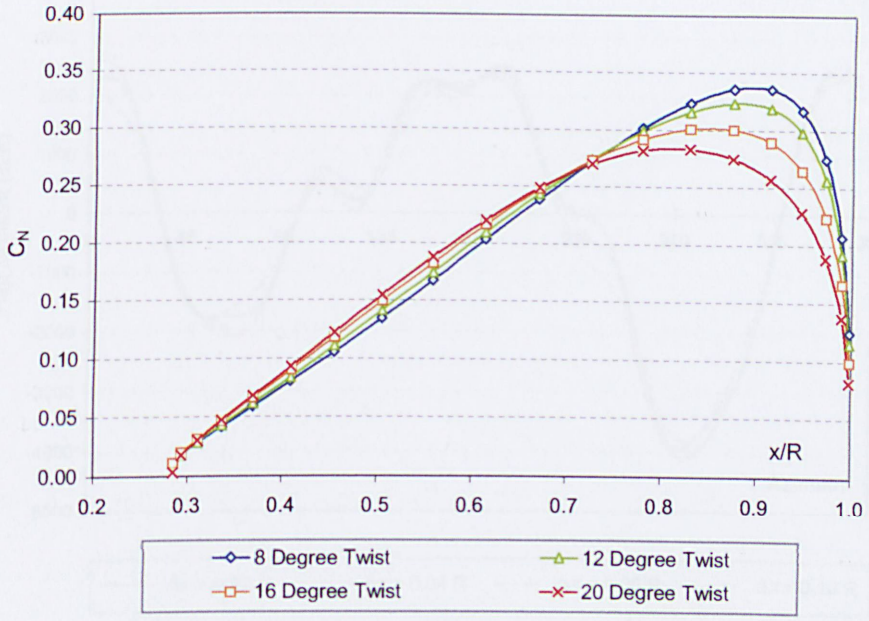


Figure A.16: *Normal force distribution* $\psi = 315°$, $\mu = 0.15$.

Appendix B:

VTM-R150 Convergence Study

B1. High Speed Case $\mu = 0.37$

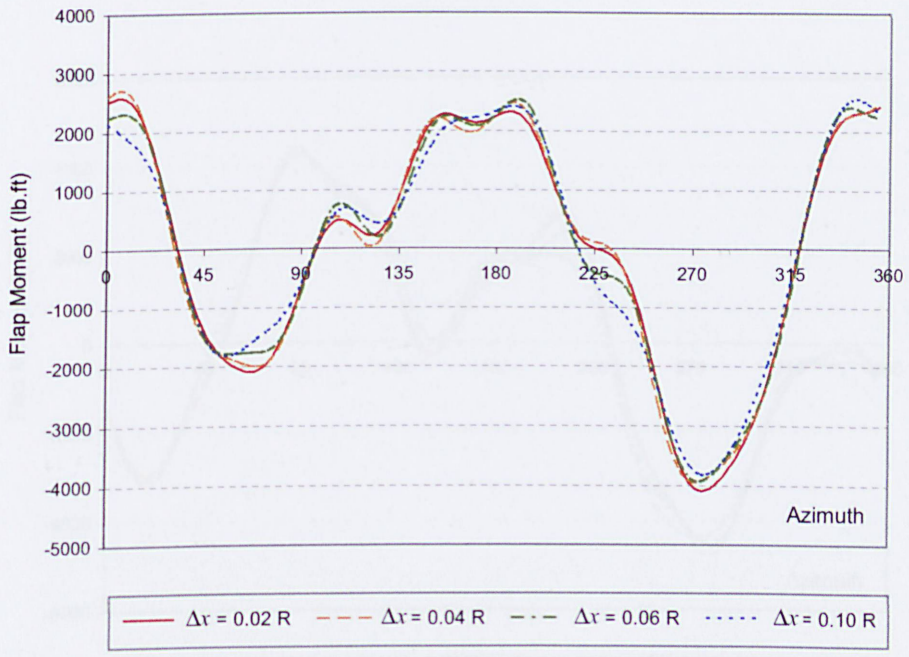


Figure B.17: *Predicted flap moment at 81.0% Radius* $\mu = 0.37$.

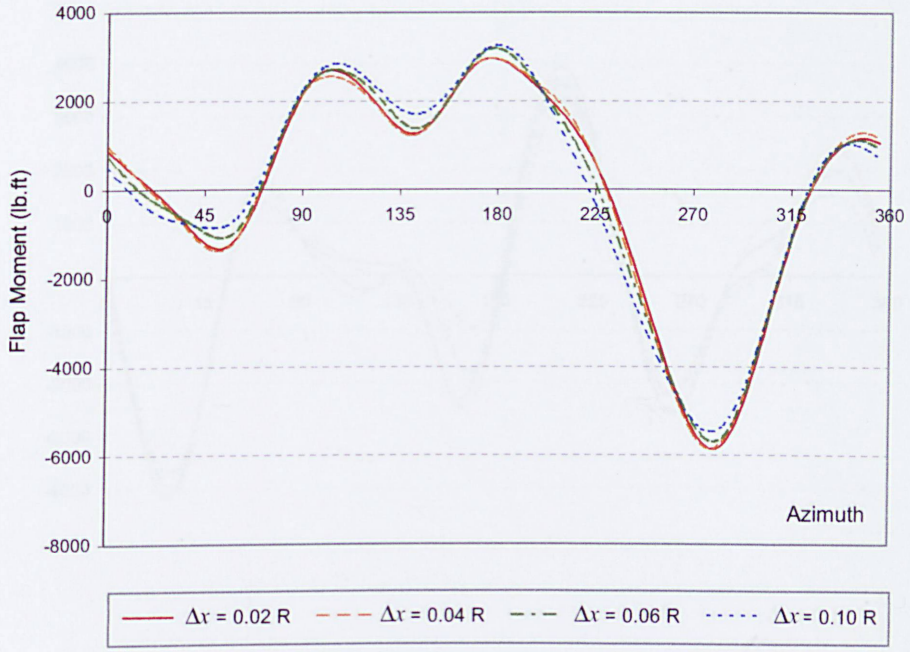


Figure B.18: *Predicted flap moment at 64.0% Radius* $\mu = 0.37$.

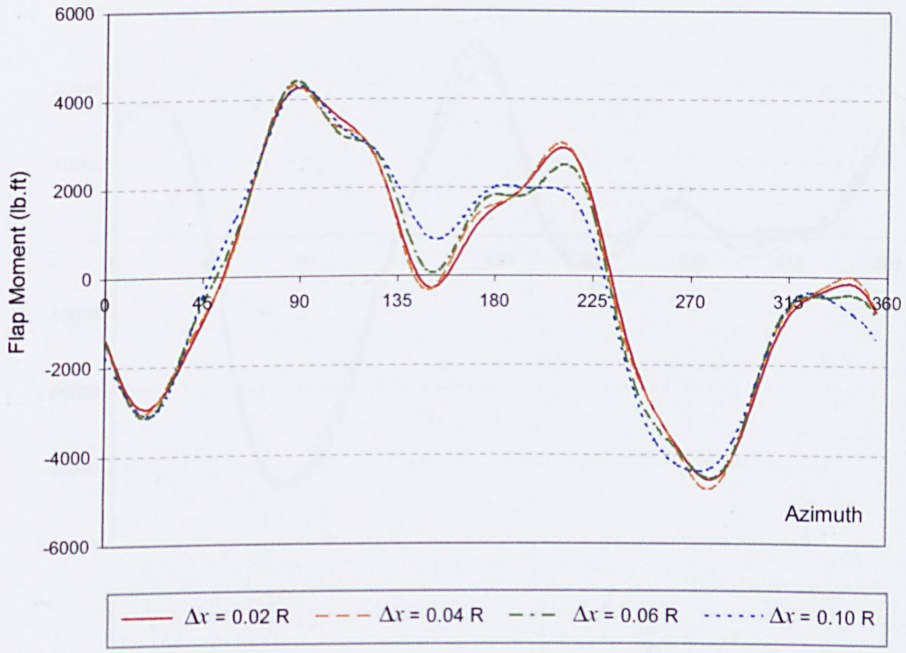


Figure B.19: *Predicted flap moment at 48.0% Radius* $\mu = 0.37$.

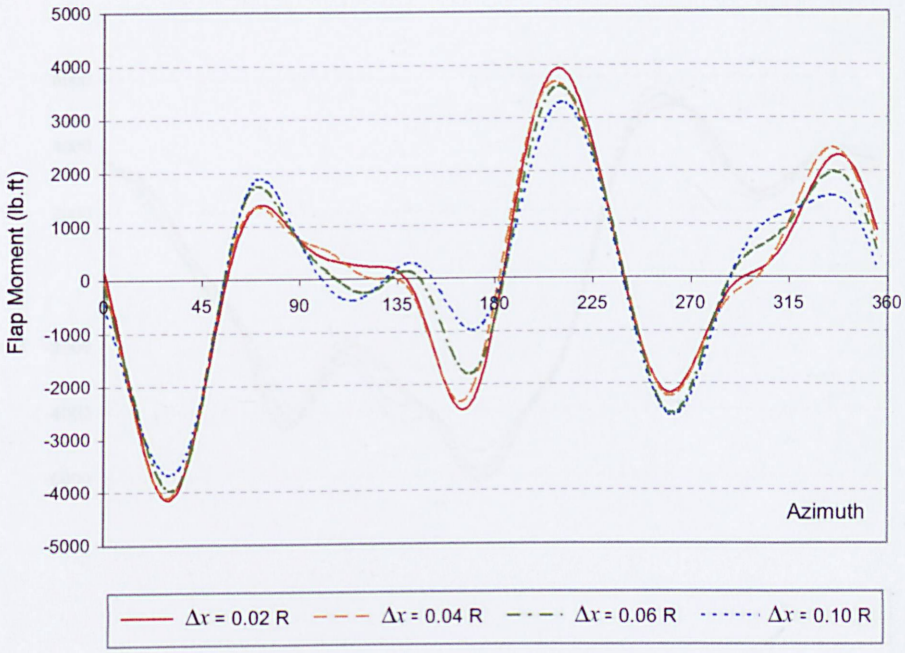


Figure B.20: *Predicted flap moment at 31.0% Radius* $\mu = 0.37$.

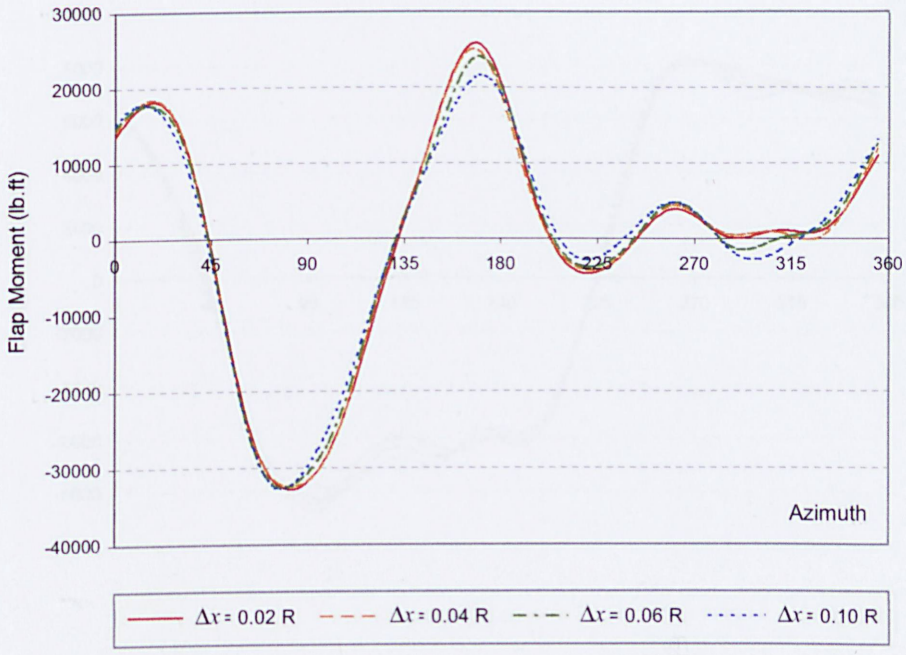


Figure B.21: *Predicted flap moment at 3.2% Radius* $\mu = 0.37$.

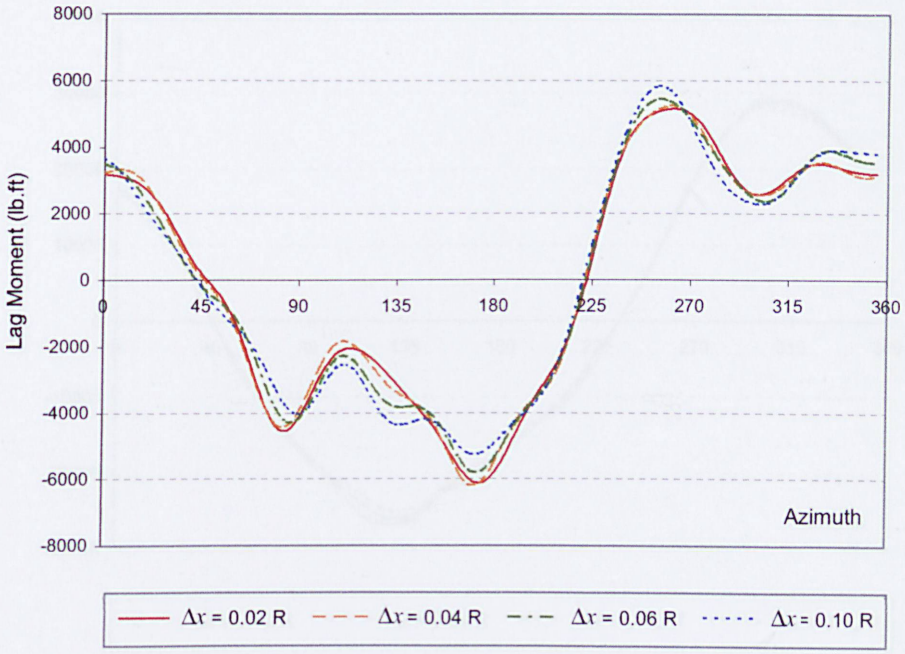


Figure B.22: *Predicted lag moment at 64.0% Radius* $\mu = 0.37$.

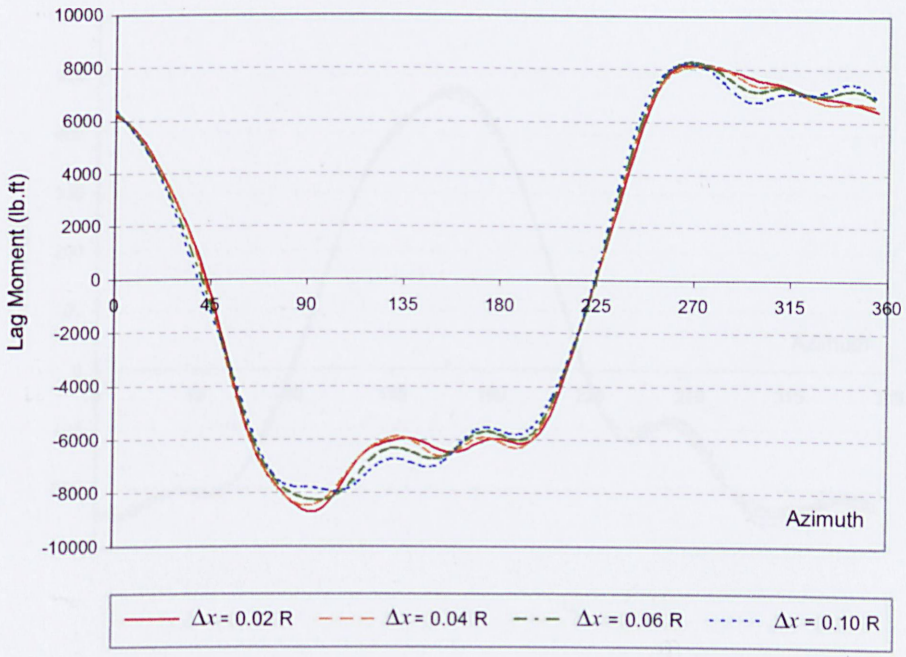


Figure B.23: *Predicted lag moment at 31.0% Radius* $\mu = 0.37$.

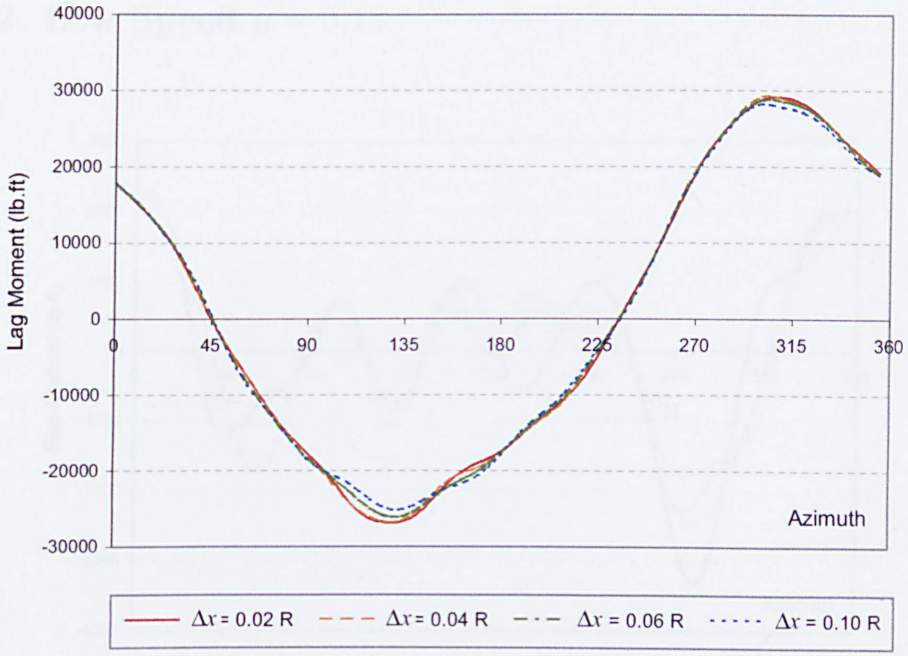


Figure B.24: *Predicted lag moment at 6.8% Radius* $\mu = 0.37$.

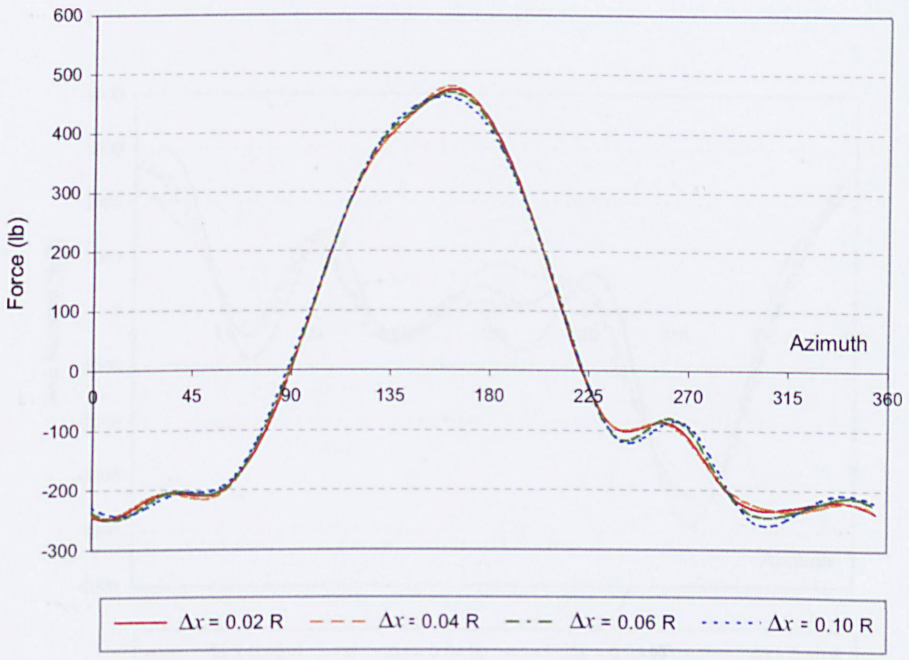


Figure B.25: *Predicted control loads* $\mu = 0.37$.

B2. Low Speed $\mu = 0.15$

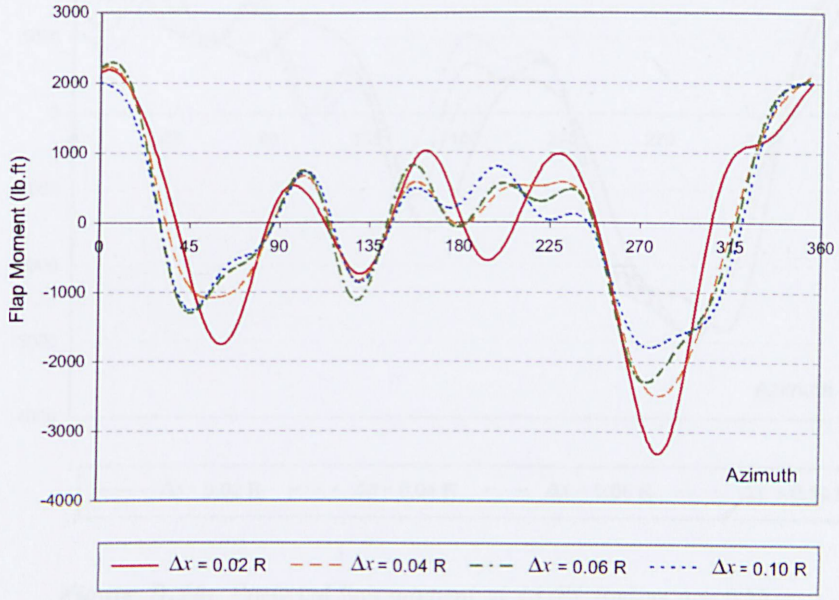


Figure B.26: *Predicted flap moment at 81.0% Radius* $\mu = 0.15$.

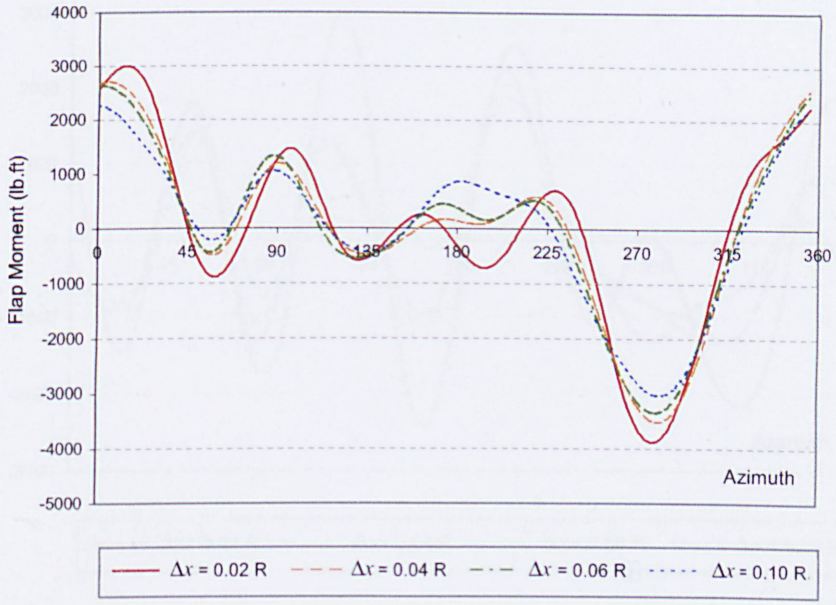


Figure B.27: *Predicted flap moment at 64.0% Radius* $\mu = 0.15$.

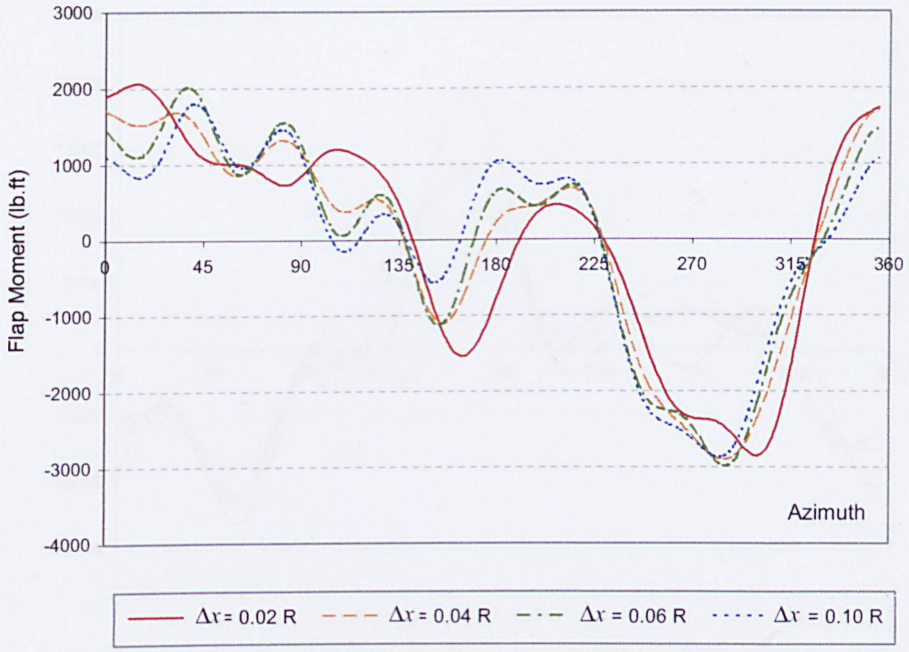


Figure B.28: *Predicted flap moment at 48.0% Radius* $\mu = 0.15$.

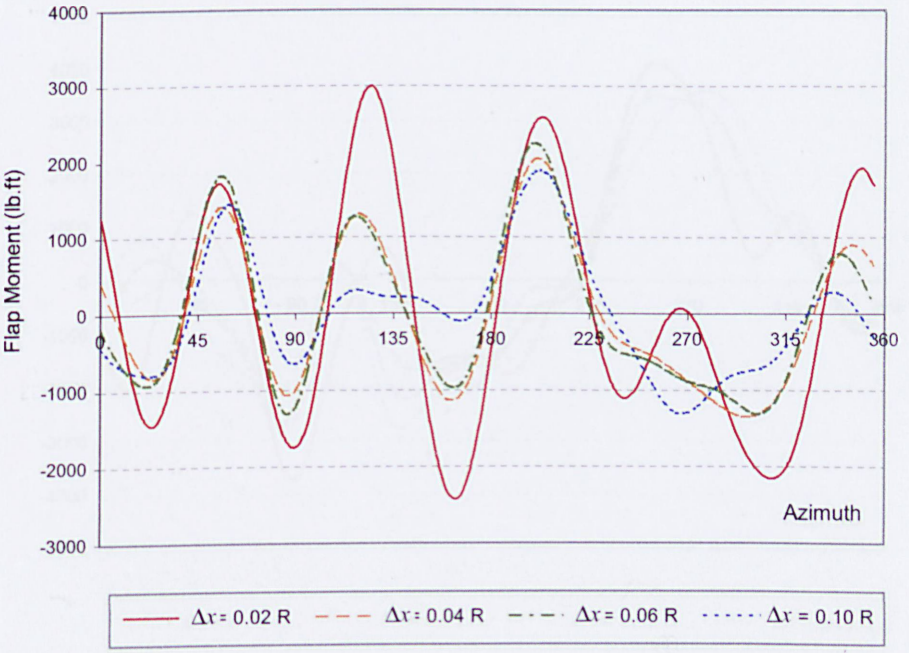


Figure B.29: *Predicted flap moment at 31.0% Radius* $\mu = 0.15$.

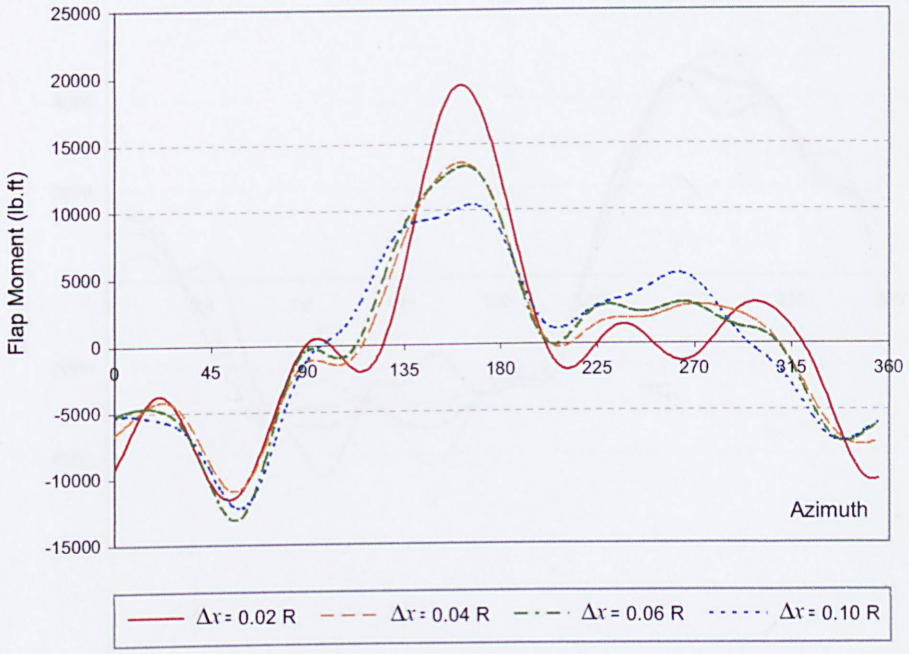


Figure B.30: *Predicted flap moment at 3.2% Radius* $\mu = 0.15$.

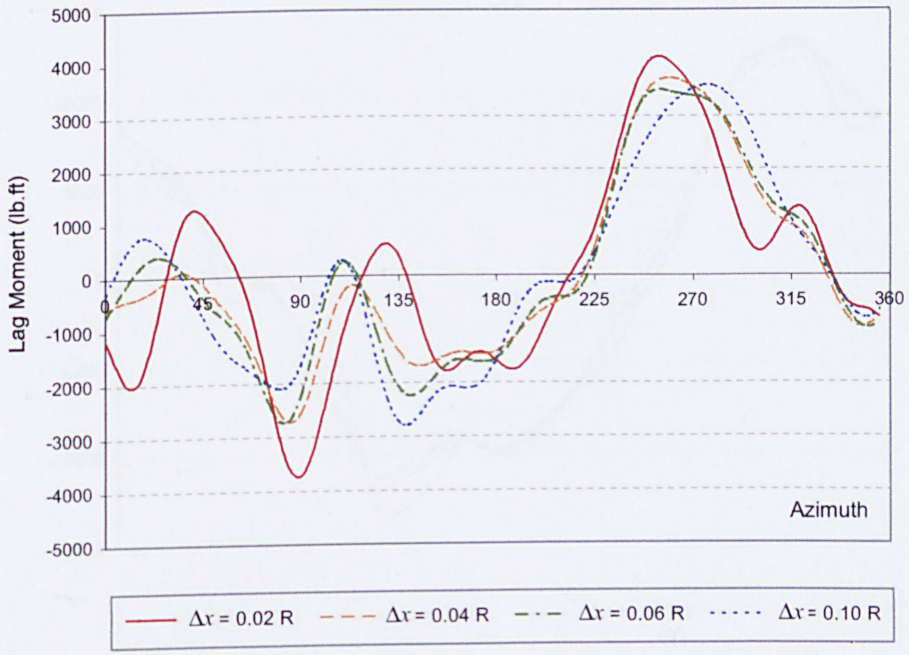


Figure B.31: *Predicted lag moment at 64.0% Radius* $\mu = 0.15$.

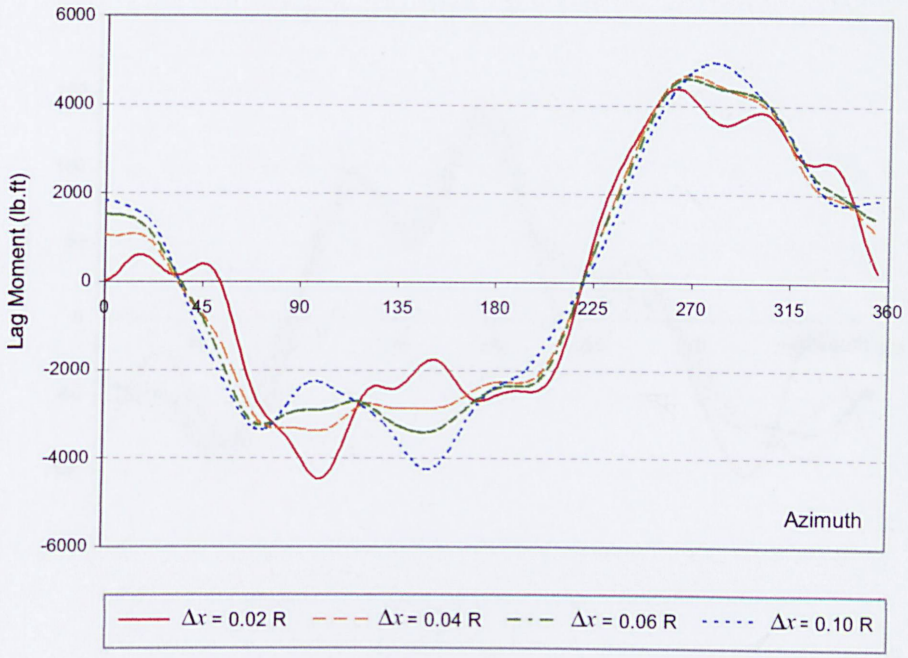


Figure B.32: *Predicted lag moment at 31.0% Radius* $\mu = 0.15$.

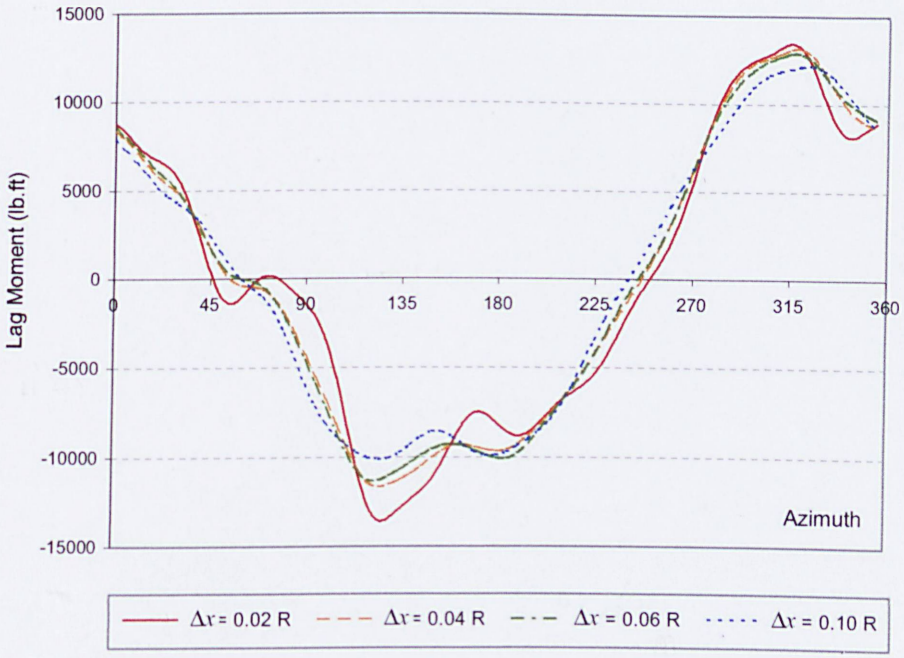


Figure B.33: *Predicted lag moment at 6.8% Radius* $\mu = 0.15$.

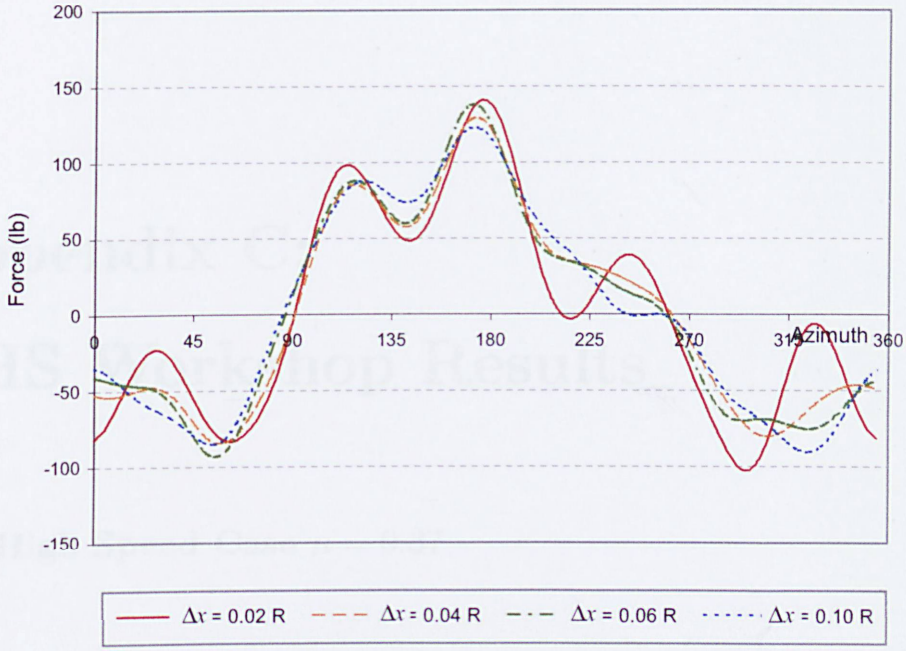


Figure B.34: *Predicted control loads* $\mu = 0.15$.

Appendix C:

AHS Workshop Results

C1. High Speed Case $\mu = 0.37$

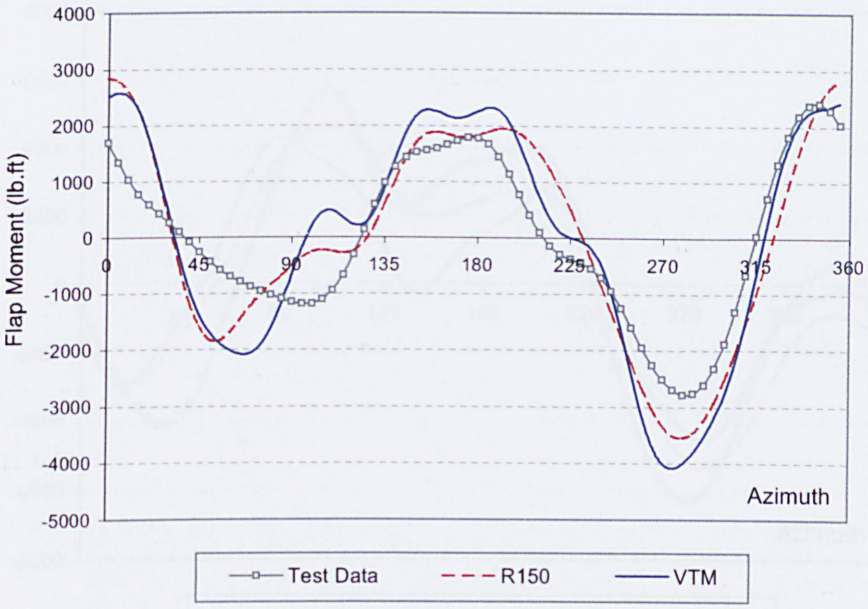


Figure C.35: *Flap moment at 81.0% Radius* $\mu = 0.37$.

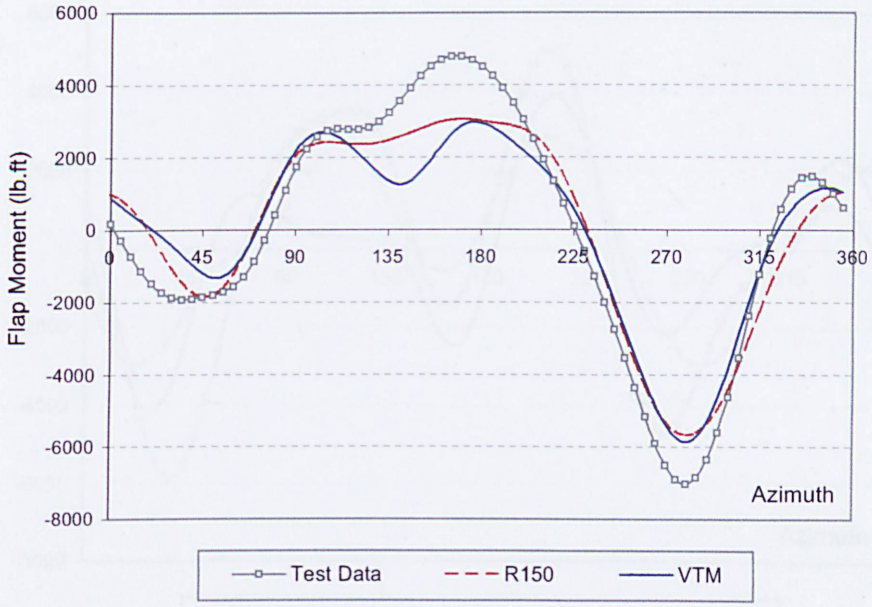


Figure C.36: *Flap moment at 64.0% Radius* $\mu = 0.37$.

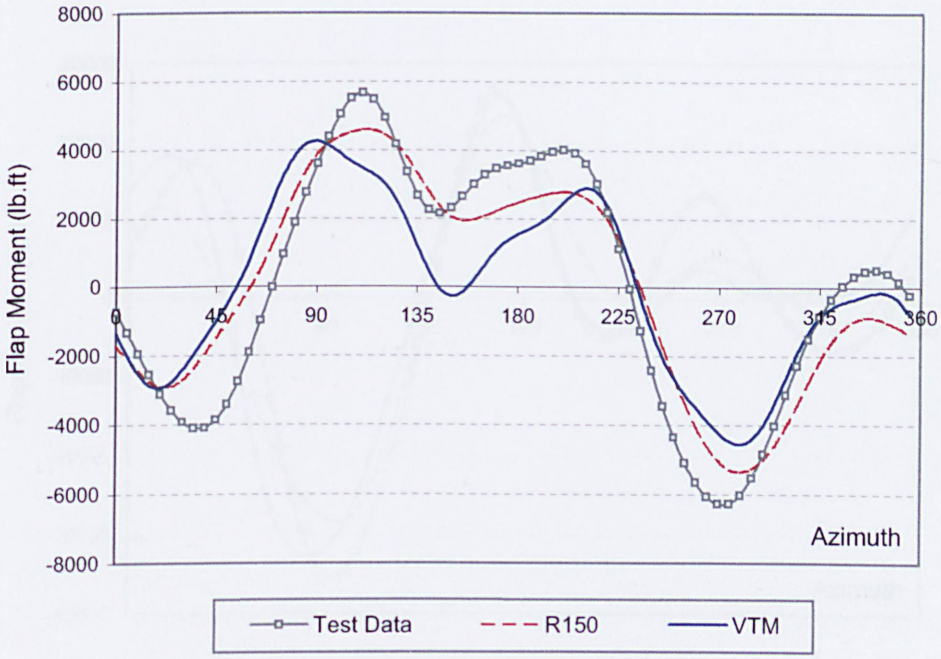


Figure C.37: *Flap moment at 48.0% Radius* $\mu = 0.37$.

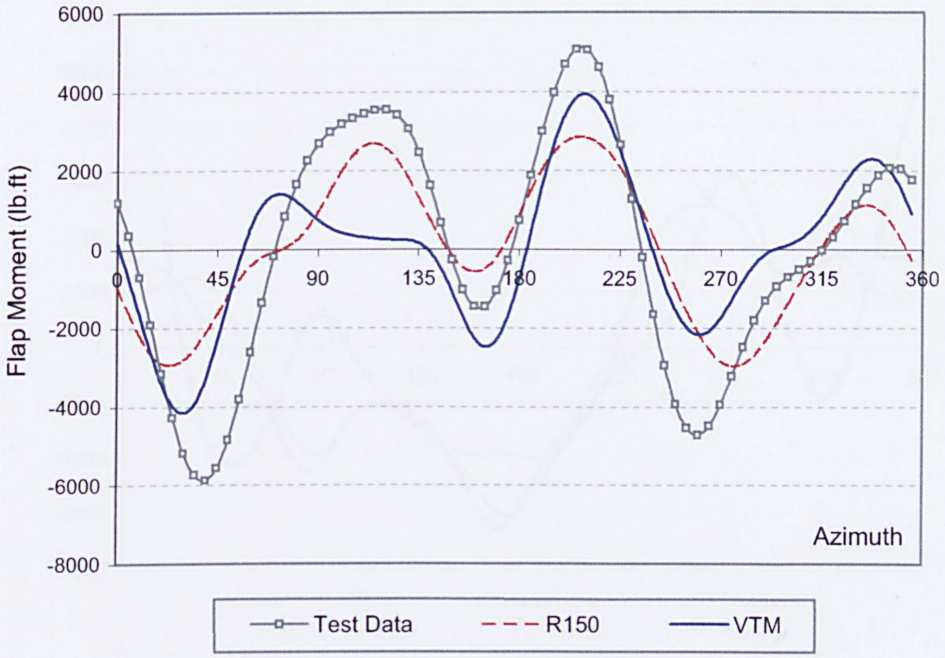


Figure C.38: *Flap moment at 31.0% Radius* $\mu = 0.37$.

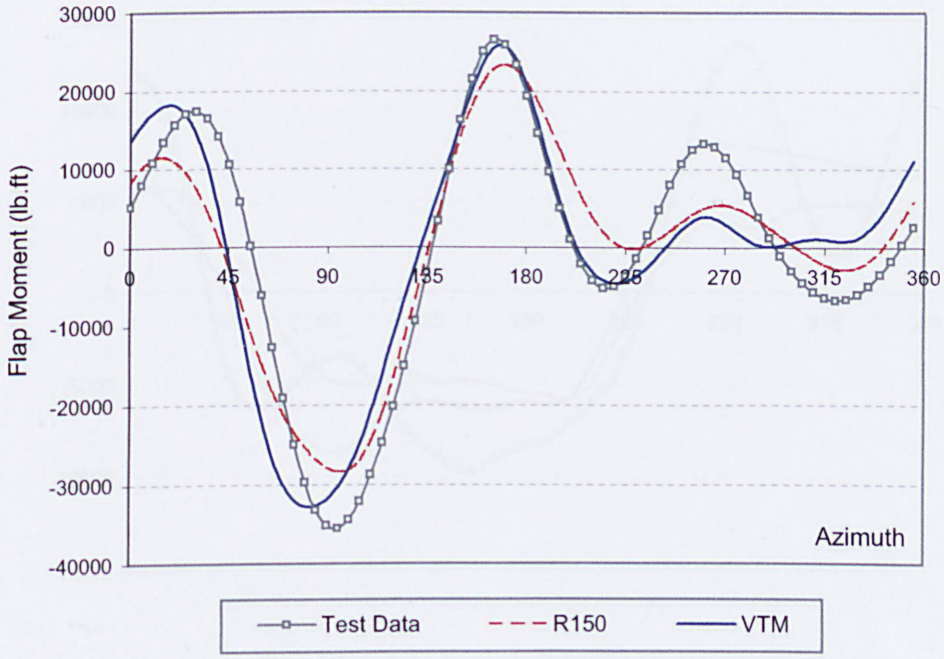


Figure C.39: *Flap moment at 3.2% Radius* $\mu = 0.37$.

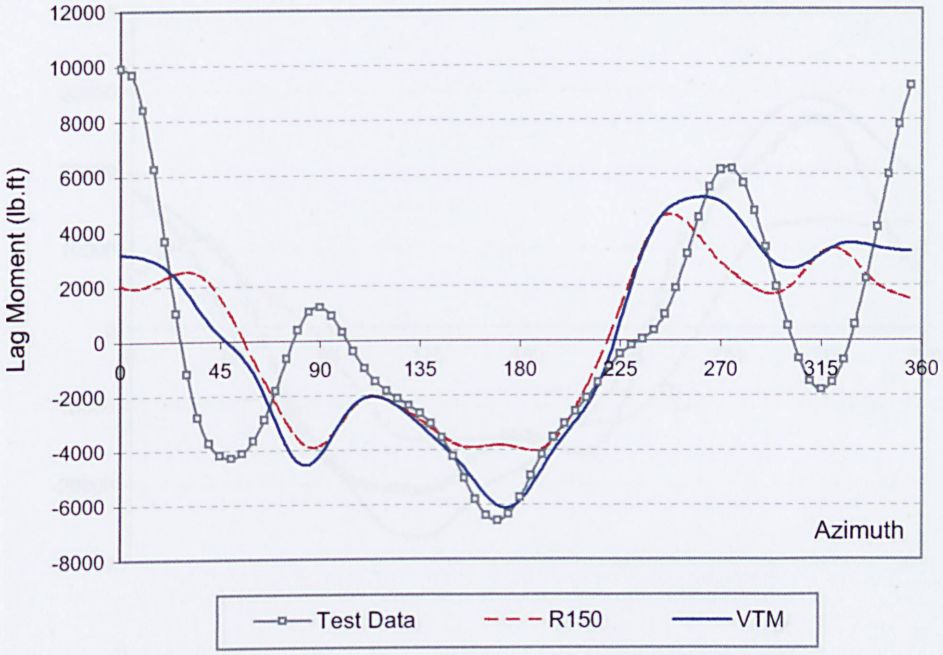


Figure C.40: *Lag moment at 64.0% Radius* $\mu = 0.37$.

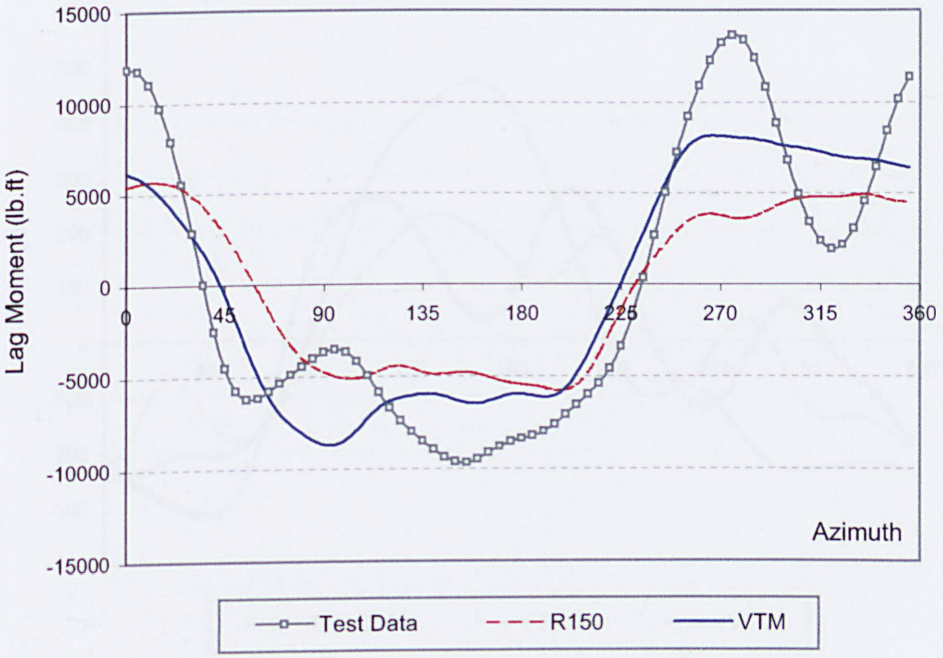


Figure C.41: *Lag moment at 31.0% Radius* $\mu = 0.37$.

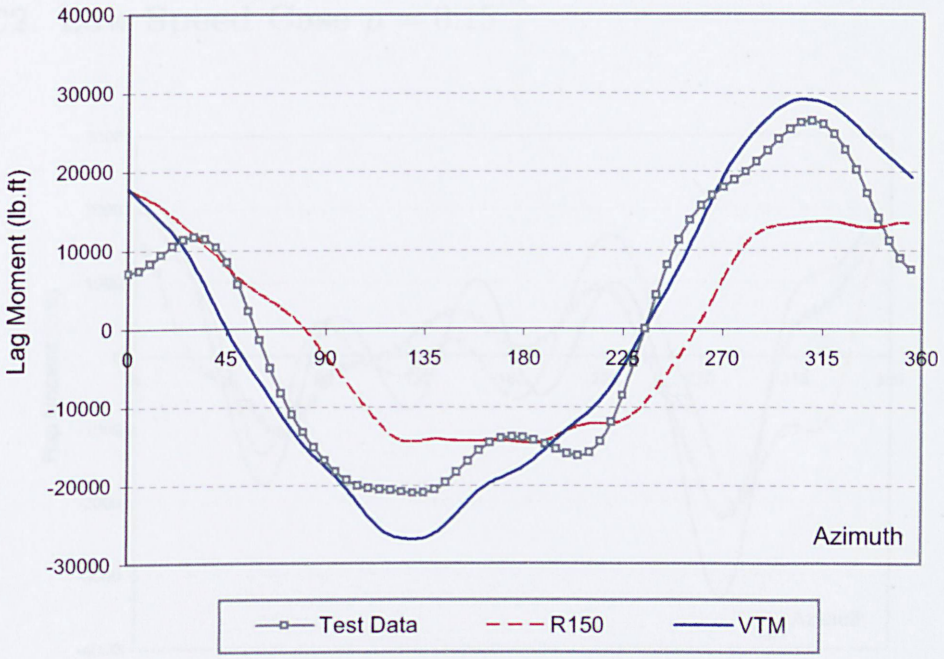


Figure C.42: *Lag moment at 6.8% Radius* $\mu = 0.37$.

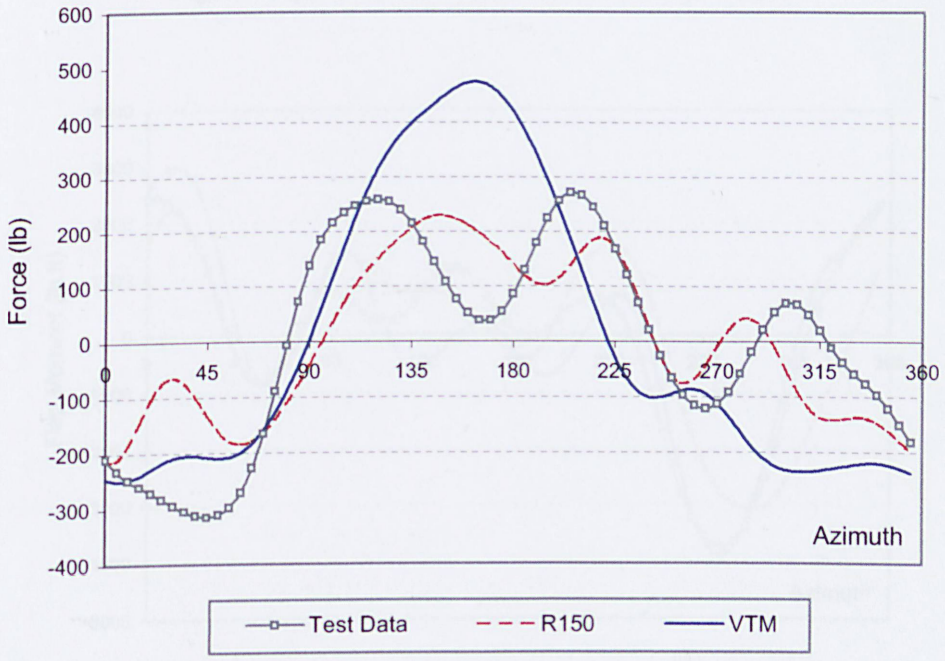


Figure C.43: *Control loads* $\mu = 0.36$.

C2. Low Speed Case $\mu = 0.15$

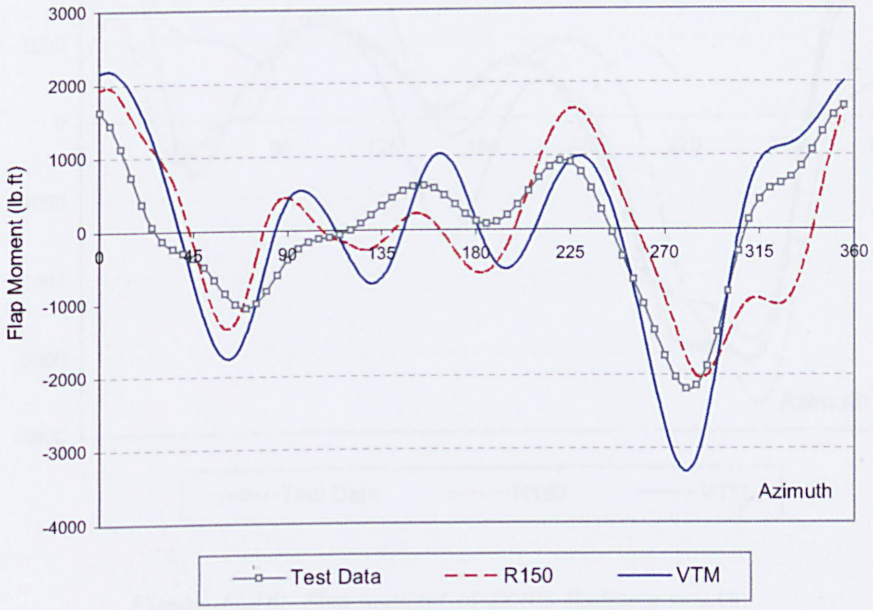


Figure C.44: *Flap moment at 81.0% Radius* $\mu = 0.15$.

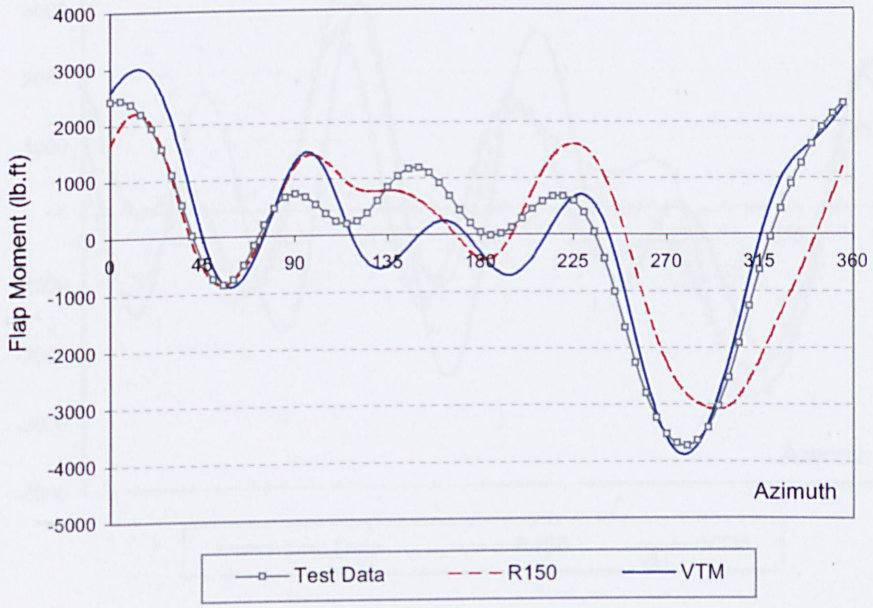


Figure C.45: *Flap moment at 64.0% Radius* $\mu = 0.15$.

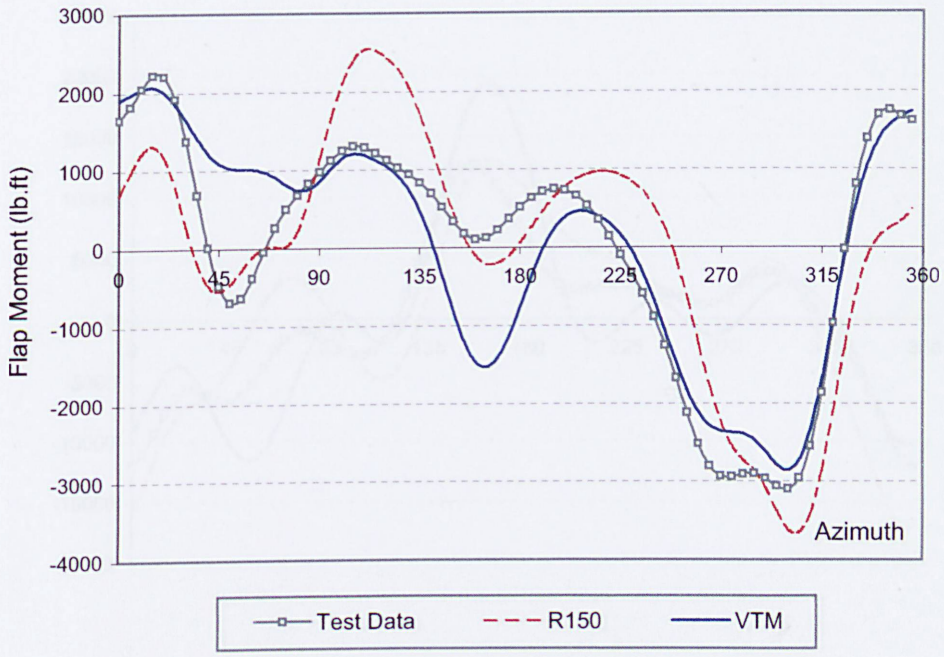


Figure C.46: *Flap moment at 48.0% Radius* $\mu = 0.15$.

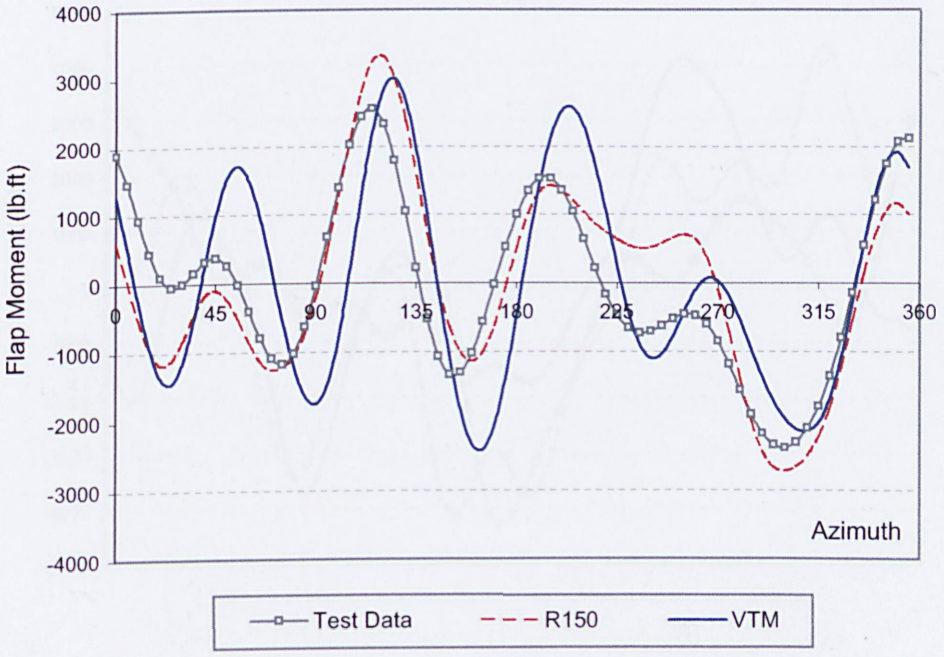


Figure C.47: *Flap moment at 31.0% Radius* $\mu = 0.15$.

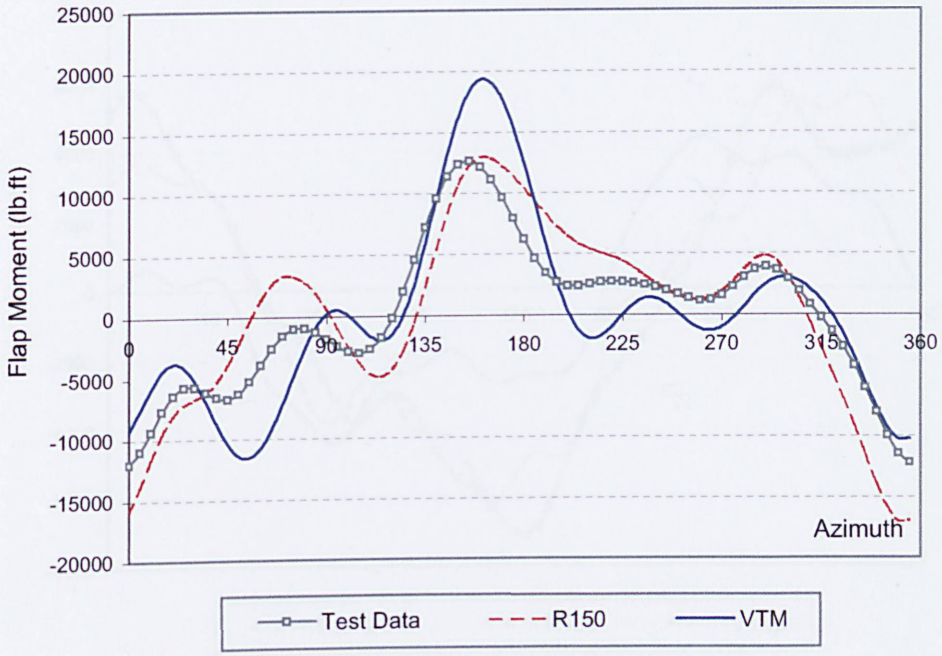


Figure C.48: *Flap moment at 3.2% Radius* $\mu = 0.15$.

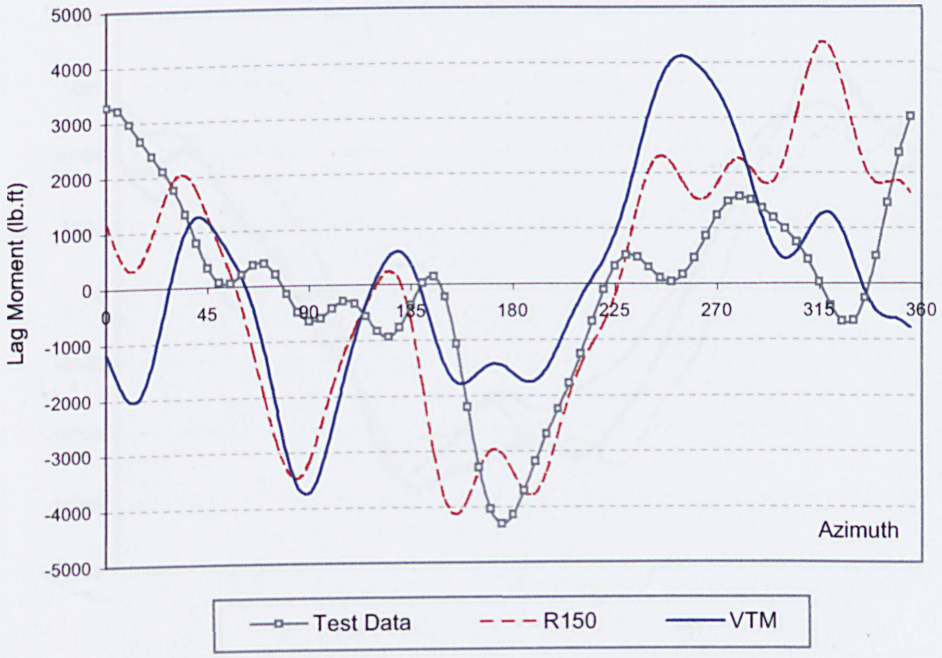


Figure C.49: *Lag moment at 64.0% Radius* $\mu = 0.15$.

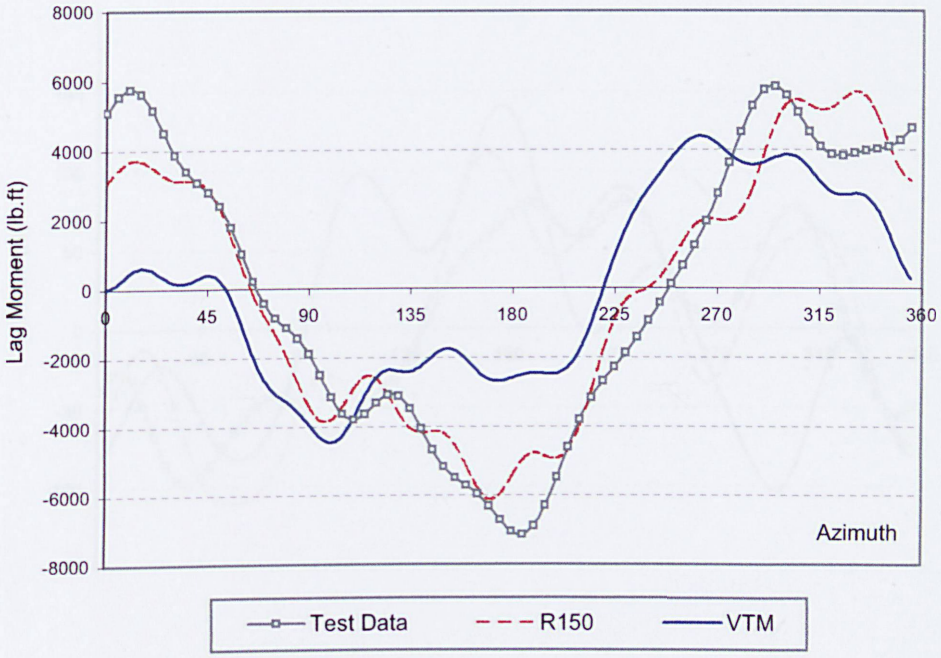


Figure C.50: *Lag moment at 31.0% Radius* $\mu = 0.15$.

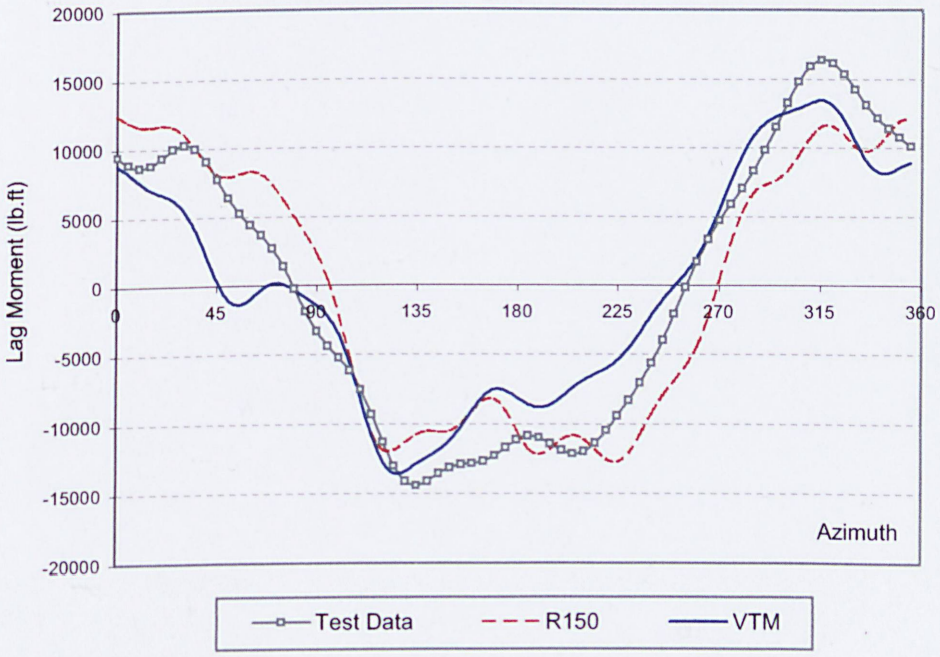


Figure C.51: *Lag moment at 6.8% Radius* $\mu = 0.15$.

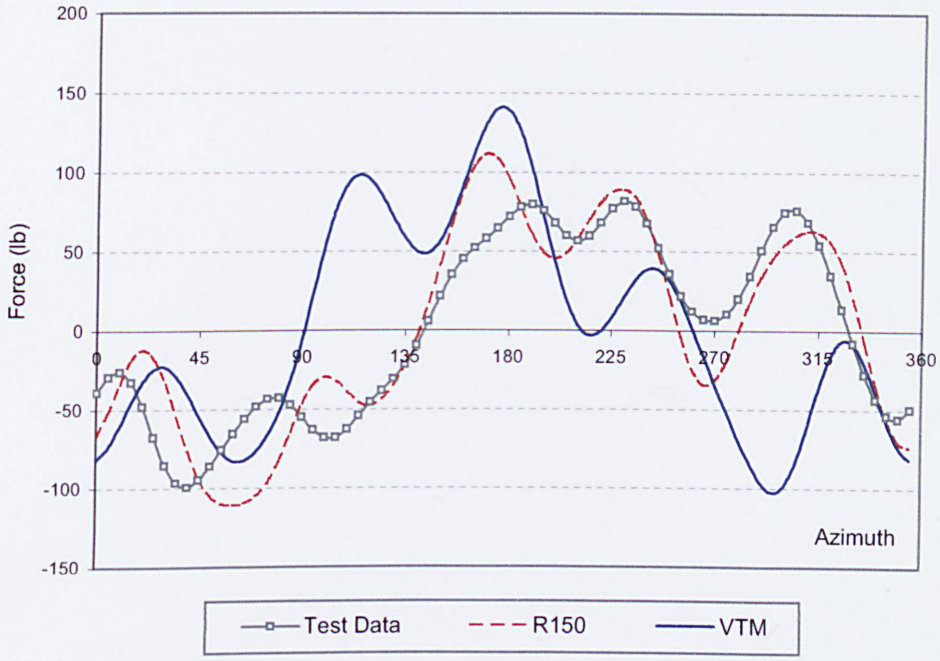


Figure C.52: *Control loads* $\mu = 0.15$.